Universität Hamburg
DER FORSCHUNG | DER LEHRE | DER BILDUNG

From *ab initio* to downfolded lattice models: Exploring charge density wave physics

Dissertation
zur Erlangung des Doktorgrades
an der Fakultät für Mathematik, Informatik und Naturwissenschaften
Fachbereich Physik
der Universität Hamburg

vorgelegt von

Arne Hilwert Paul Schobert

Hamburg

2023

Gutachter/innen der Dissertation:	Prof. Dr. Tim Wehling Dr. Mariana Rossi
Zusammensetzung der Prüfungskommission:	Prof. Dr. Daniela Pfannkuche Prof. Dr. Tim Wehling Dr. Mariana Rossi Prof. Dr. Daria Gorelova Prof. Dr. Michael Rübhausen
Vorsitzende der Prüfungskommission:	Prof. Dr. Daniela Pfannkuche
Datum der Disputation:	02.04.2024
Vorsitzender des Fach-Promotionsausschusses PHYSIK:	Prof. Dr. Markus Drescher
Leiter des Fachbereichs PHYSIK:	Prof. Dr. Wolfgang J. Parak
Dekan der Fakultät MIN:	Prof. Dr.-Ing. Norbert Ritter

Abstract

This dissertation explores downfolded models in condensed matter physics, emphasizing their role in understanding the interplay between electronic and lattice degrees of freedom, particularly within the low-energy domain.

The research demonstrates that downfolded lattice models accurately reproduce Born-Oppenheimer potential energy surfaces of *ab initio* methods, while offering computational speedups of multiple orders of magnitude. This enables extensive molecular dynamics simulations and insights into charge density wave physics in real materials.

Through collaborations between experiment and theory, the work challenges the understanding of conventional charge density wave physics by revealing nonlinear mode-mode coupling in materials like monolayer 1T-VS_2. It also confirms the existence of a charge density wave with unconventional electronic gap features in monolayer 1H-NbS_2. Furthermore, it demonstrates how molecular dynamics simulations can be employed to determine the transition temperature of the charge density wave phase transition in monolayer 1H-TaS_2.

In summary, this research advances charge density wave physics through interdisciplinary collaboration, while providing downfolded lattice models as a valuable tool for understanding dynamics and thermodynamics for systems beyond the charge density wave phenomenon. It opens avenues for exploring phase transitions, correlations, and quantum phenomena, showcasing the transformative potential of downfolded lattice models.

Zusammenfassung

Diese Dissertation erforscht heruntergefaltete Modelle in der Festkörperphysik und betont ihre Rolle bei der Verständigung des Zusammenspiels zwischen elektronischen und Gitterfreiheitsgraden, insbesondere im niederenergetischen Bereich.

Die Forschung zeigt, dass heruntergefaltete Gittermodelle Born-Oppenheimer-Potentialenergieflächen von *ab initio*-Methoden reproduzieren können und dabei rechentechnische Geschwindigkeitssteigerungen von mehreren Größenordnungen erreichen. Dies ermöglicht umfangreiche Molekulardynamiksimulationen und Einblicke in die Physik der Ladungsdichtewellen in realen Materialien.

Durch Kollaborationen zwischen Experiment und Theorie stellt diese Arbeit das Verständnis von konventioneller Ladungs-dichtewellen-Physik in Frage, indem sie nichtlineare Moden-Moden-Kopplungen in Materialien wie Monolage-1T-VS_2 aufdeckt. Sie bestätigt auch die Existenz einer Ladungsdichtewelle mit unkonventionellen elektronischen Bandlückenmerkmalen in Monolage-1H-NbS_2. Außerdem zeigt sie auf, wie mit Hilfe von Molekulardynamik-Simulationen die Übergangstemperatur des Phasenübergangs zur Ladungsdichtewelle von einer Monolage-1H-TaS_2 bestimmt werden kann.

Zusammenfassend trägt diese Forschung zur Fortentwicklung der Ladungsdichtewellen-Physik durch interdisziplinäre Zusammenarbeit bei und stellt heruntergefaltete Gittermodelle als wertvolles Werkzeug zur Verfügung, um Dynamik und Thermodynamik von Systemen jenseits des Ladungsdichtewellen-Phänomens zu verstehen. Sie eröffnet Möglichkeiten zur Erforschung von Phasenübergängen, Korrelationen und Quantenphänomenen und zeigt das transformative Potenzial heruntergefalteter Gittermodelle auf.

Preface

This preface provides an overview of all publications that form the basis for this cumulative dissertation, including further publications that are not part of the dissertation. Additionally, it mentions conference talks, posters, and participations accomplished during the doctoral phase.

Publications

This cumulative dissertation will be based on the following publications (1. – 4.). The author's individual contributions to each publication will be stated at the beginning of their respective dedicated chapters.

4. T. Knispel, J. Berges, **A. Schobert**, E. G. C. P. van Loon, W. Jolie, T. O. Wehling, T. Michely, J. Fischer, *Unconventional charge-density-wave gap in monolayer NbS_2,* [accepted for publication in Nano Letters], arXiv:2307.13791

3. **A. Schobert**, J. Berges, E. G. C. P. van Loon, M. A. Sentef, S. Brener, M. Rossi, and T. O. Wehling, *Ab initio electron-lattice downfolding: potential energy landscapes, anharmonicity, and molecular dynamics in charge density wave materials,* [submitted to SciPost Phys.], arXiv:2303.07261

2. C. van Efferen, J. Berges, J. Hall, E. G. C. P. van Loon, S. Kraus, **A. Schobert**, T. Wekking, F. Huttmann, E. Plaar, N. Rothenbach, K. Ollefs, L. M. Arruda, N. Brookes, G. Schönhoff, K. Kummer, H. Wende, T. O. Wehling, and T. Michely *A full gap above the Fermi level: the charge density wave of monolayer VS_2,* Nat. Commun. **12**, 6837 (2021), arXiv:2101.01140

1. **A. Schobert**, J. Berges, T. O. Wehling, and E. G. C. P. van Loon, *Downfolding the Su-Schrieffer-Heeger model,* SciPost Phys. **11**, 079 (2021), arXiv:2104.09207

Further publications

Published before doctoral phase:

F1. J. Berges, E. G. C. P. van Loon, **A. Schobert**, M. Rösner, and T. O. Wehling, *Ab initio phonon self-energies and fluctuation diagnostics of phonon anomalies: Lattice instabilities from Dirac pseudospin physics in transition metal dichalcogenides,* Phys. Rev. B **101**, 155107 (2020), arXiv:1911.02450

Talks

5. **A. Schobert**, J. Berges, M. A. Sentef, E. G. C. P. van Loon, S. Brener, M. Rossi, and T. O. Wehling, *Nailing down charge-density-wave phase-transition temperatures with downfolding approaches*,
DPG Spring Meeting, Dresden, Germany (26–31 March 2023)

4. **A. Schobert**, J. Berges, M. A. Sentef, M. Rossi, E. G. C. P. van Loon, S. Brener, and T. O. Wehling, *Electronically driven anharmonicities in low-energy lattice models: Affordable molecular dynamics of charge-density-wave systems*,
DPG Autumn Meeting, Regensburg, Germany (4–9 September 2022)

3. **A. Schobert**, J. Berges, E. G. C. P. van Loon, M. A. Sentef, and T. O. Wehling, *Electronically-driven anharmonicity in charge-density-wave materials*,
DPG Autumn Meeting, Online (27 September – 01 October 2021)

2. J. Berges, E. G. C. P. van Loon, **A. Schobert**, M. Rösner, and T. O. Wehling, *Ab initio phonon self-energies and fluctuation diagnostics of phonon anomalies: Lattice instabilities from Dirac pseudospin physics in transition metal dichalcogenides*,
APS March Meeting, Online (15–19 March 2021)

1. **A. Schobert**, J. Berges, E. G. C. P. van Loon, M. A. Sentef, and T. O. Wehling, *Electronically-driven anharmonicities in charge-density-wave materials*,
APS March Meeting, Online (15–19 March 2021)

Posters

5. **A. Schobert**, J. Berges, M. A. Sentef, M. Rossi, E. G. C. P. van Loon, S. Brener, and T. O. Wehling, *Electronically driven anharmonicities in low-energy lattice models: Affordable molecular dynamics of charge-density-wave systems*,
Psi-K Conference 2022, EPFL, Lausanne, Switzerland (22–25 August 2022)

4. **A. Schobert**, J. Berges, E. G. C. P. van Loon, M. A. Sentef, and T. O. Wehling, *Electronically-driven anharmonicity in charge-density-wave materials*,
International CECAM Workshop "Capturing Anharmonic Vibrational Motion in First-Principles Simulations", Online (6–8 December 2021)

3. J. Berges, E. G. C. P. van Loon, **A. Schobert**, M. Rösner, and T. O. Wehling, *Ab initio phonon self-energies and fluctuation diagnostics of phonon anomalies: Lattice instabilities from Dirac pseudospin physics in transition metal dichalcogenides*,
"2021 Virtual School on Electron-Phonon Physics and the EPW code", Online (14–18 June 2021)

2. **A. Schobert**, J. Berges, E. G. C. P. van Loon, M. A. Sentef, and T. O. Wehling, *Electronically-driven anharmonicity in charge-density-wave materials*,
"2021 Virtual School on Electron-Phonon Physics and the EPW code", Online (14–18 June 2021)

1. J. Berges, E. G. C. P. van Loon, **A. Schobert**, M. Rösner, and T. O. Wehling, *Ab initio phonon self-energies and fluctuation diagnostics of phonon anomalies: Lattice instabilities from Dirac pseudospin physics in transition metal dichalcogenides,* DPG Spring Meeting SurfaceScience21, Online (1–4 March 2021)

Participations

3. Jülich Workshop "Autumn School on Correlated Electrons: Simulating Correlations with Computers", Online (20-24 September 2021)

2. BYRD Workshop "Good Scientific Practice", Online (17-18 May 2021)

1. IMPRS-UFAST core course "Solid State Physics", Online (22-26 February 2021)

Contents

List of Figures

1

Introduction

Matter, in the form of solids and molecules, emerges from the interplay between two fundamental constituents: electronic and nuclear degrees of freedom. These constituents hold the key to the remarkable properties exhibited by materials, such as charge density waves (CDW) [1], (super)conductivity [2], metal–insulator transitions [3] and magnetism [4]. The foundation for understanding these phenomena lies in the solid state Hamiltonian (see Sec. 2). This theoretical construct, which can be simply written in a single line, encapsulates the underlying physics governed in materials.

However, unlocking the secrets encoded within this Hamiltonian is no simple task. The complexity arises from three formidable challenges: (i) the intertwined dynamics of electrons and nuclei, (ii) the staggering number of particles involved ($\sim 10^{23}$ electrons per cm^3), and (iii) the quantum nature of matter, resulting in an astonishingly vast Hilbert space. Tackling these challenges with the help of creative approximations is a pursuit at the forefront of materials science.

One of these approximations to tackle (i) is the so-called Born-Oppenheimer approximation (see Sec. 2.1). It is the simplest way of decoupling the dynamics of electrons and nuclei. It is justified in the sense that electrons are much lighter than the nuclei, leading to different timescales in their dynamics. As a result, the electronic motion can be approximated as instantaneous compared to the slower nuclear motion. This justifies the assumption that the electronic and nuclear motions can be treated as decoupled.

Decoupling the Schrödinger equations leaves a purely electronic problem, with the nuclear coordinates entering as parameters. Still, the remaining task is due to (ii) and (iii) a complex many-body problem. It is at this point, where two overarching methodologies have emerged as essential avenues of exploration: *ab initio* and model approaches.

Density functional theory (DFT – see Sec. 3.1) is one of the most widely used *ab initio* approaches. It transforms the complex many-body problem into a single-particle problem, which is solved self-consistently and gives access to accurate Born-Oppenheimer potential energy surfaces. DFT has an undeniable success, as evidenced by its inclusion among the top 100 most cited papers [5] and its recognition through the Nobel Prize [5]. However, the unknown exchange-correlation functional and the *a priori* unknown orbital composition of the electronic structure renders this method intransparent — much like a black box [6]. Additionally, despite the availability of supercomputers, it is not feasible to simulate much more than a few hundred atoms with traditional DFT (cubic scaling). Albeit, linear-scaling DFT can improve this number [7]. Lastly, DFT fails to represent the physics of strongly-correlated compounds [8].

The aforementioned disadvantages of DFT are circumvented in model approaches at the expense of additional approximations. Model approaches often rely on the tight-binding approximation [9–21].

In these approaches the orbital composition is predefined and specifically tailored for each individual material by constructing a model Hamiltonian that consists of a few orbitals per atom only. Additionally there are often restrictions on the form of the interaction tensor (e.g. purely local, density-density only, ...). Hence, there is, on one hand, a gain in understanding of chemical bonding through this method. On the other hand, this rigid construct poses an obstacle, meaning that *transferability* is restricted. Transferability entails applying the model Hamiltonian to a different material or scenario and expecting to yield similarly good results. On another note, this method shows significantly greater speed compared to DFT, enabling the simulation of a far larger number of atoms. This acceleration in computational efficiency arises from the small Hilbert space on which the model operates and also often from being effectively non-interacting, hence a simple matrix diagonalization suffices.

In concluding the comparison between purely model and *ab initio* approaches, it is evident that DFT excels in accurately predicting Born-Oppenheimer potential energy surfaces for relatively small and weakly-correlated systems, without prior knowledge of the chemical bonding. On the other hand, model approaches explicitly revolve around constructing a model Hamiltonian, which could potentially lack transferability. Nevertheless, thanks to a substantial computational advantage, these methods can be effectively applied to multiscale modelling [22].

It might come as no surprise that there are methods aiming to combine both the DFT-accuracy and the ability to simulate as many atoms as the pure model-based approaches. Various strategies have emerged in different domains. These include the creation of multiscale coarse-grained models, utilization of machine-learning models [23–27], and the development of (density functional) tight binding potentials [28–36]. These approaches involve defining models through the calibration of semiempirical or "machine learned" parameter functions, often derived from DFT reference data.

This dissertation follows a different approach. It is well-established that numerous physical phenomena are primarily governed by the characteristics of the low-energy electronic band structure. This assertion can be illustrated through examples such as superconductivity [37, 38] or charge density waves [39]. In scenarios of this nature, it becomes sensible to divide the electronic subspace into distinct high-energy and low-energy sectors. This division sets the stage for the application of a technique known as *downfolding* [40].

In essence, downfolding involves the mapping of the solid-state Hamiltonian onto a low-energy lattice model. This can be done by the utilization of Wannier functions, which build a bridge between *ab initio* and model approaches. These functions form a localized basis set in which all the components of the lattice model can be expressed, including the single-electron term (see Sec. 3.2), electron-phonon (see Sec. 5.2) and electron-electron interactions (see Sec. 6.1). The resulting low-energy lattice model effectively captures the nuances of the low-energy sector, while the contributions from high-energy bands are either neglected or implicitly taken into account by partially screened quantities. Methods for the derivation of model parameters include the constrained random phase approximation (cRPA – see Sec. 6.3.1) [41–47], constrained density functional perturbation theory (cDFPT – see Sec. 4.2.1) [39, 48–51], and the constrained functional renormalization group [52–54].

As previously mentioned, CDWs exemplify a specific phenomenon situated within the realm of dominant low-energy physics. CDWs manifest as a consequence of spontaneous structural phase transitions occurring in metals. These phase transitions result in a reduction of crystal lattice symmetry, accompanied by the emergence of a superstructure.

It is widely recognized that the behavior of CDWs is often significantly dictated by the low-energy bands near the Fermi level. The quintessential model for comprehending this phenomenon is the Peierls model (see Sec. 10.2), which has a variant known as the SSH model. This model will be studied in the *first publication* of this dissertation (see Ch. 11).

In this study, the two-band model (per doubled unit cell) will be downfolded onto a single-band effective model. The aim of this study will be to investigate the applicability of a downfolding technique on an analytically solvable model, given the unclear limitations of this technique – specifically focussing on two key quantities: the electronic structure and the Born-Oppenheimer potential energy surfaces. The findings will reveal that the downfolded model accurately reproduces both the potential energy surface and electronic dispersion. It is noteworthy that, by construction, the downfolded model captures spectral weight solely within the target space. The results give confidence in using downfolding methods for studying CDWs, as it aligns with the primary aim of the SSH model, which is to describe CDW physics in a simplified way.

In this model, static atomic displacements lead to a gap opening at the Fermi level. This gap contributes to an overall energy gain within the electronic sector. This energy gain can be substantial enough to outweigh the elastic energy costs inherent to atomic displacements.

However, this simple model may not necessarily apply to real-world materials, as demonstrated in the *second publication* of this dissertation (see Ch. 12). Chapter 12 presents a collaborative investigation between theory and experiment regarding the CDW in monolayer 1T-VS_2. The findings illustrate that the CDW, observed in scanning tunneling microscopy (STM) experiments, does not conform to the conventional Peierls type. Instead, non-linear mode-mode coupling is responsible for the CDW, resulting in a full gap *above* the Fermi level.

Notably, a subsequent study by another research group, conducted after this publication, revealed a CDW with a different lattice periodicity as seen in STM images. This group identified a gap opening *at* the Fermi level, suggesting a Fermi-surface mechanism as the driving force. This controversy, discussed in Section 12.2, underscores the importance of comprehending the low-energy physics within CDW materials.

To this end, the following observations will be stated. It is well-established that the necessary electronic energy gain to trigger a CDW can be disrupted by manipulating the low-energy sector, e.g. through the introduction of electronic temperature (commonly referred to as *smearing* in DFT calculations) [55] or doping [56]. Moreover, materials that were previously non-CDW hosts, such as MoS_2, can develop CDWs when subjected to doping [57]. These examples underscore a crucial point: CDWs are overwhelmingly influenced by low-energy physics. This characteristic renders them applicable to strategies like downfolding, which focus on modeling the low-energy behavior of materials.

The development of the aforementioned downfolded lattice models will be the purpose of the *third publication* of this dissertation (see Ch. 13). Chapter 13 introduces three different downfolding strategies, which are based on constraining and unscreening techniques. These models will proven effective in reproducing Born-Oppenheimer potential energy surfaces of diverse CDW materials with a similar accuracy as DFT. This circumstance enables molecular dynamics simulations that achieve a computational speed up of more than *five orders* of magnitude as compared to purely *ab initio* calculations. Remarkably, this acceleration in computation speed is achieved without a significant compromise in accuracy.

As a demonstration of this new method, classical and path integral replica exchange molecular dynamics simulations are conducted for a monolayer of TaS_2. Notably, these simulations are performed with a large system that were previously unattainable through purely *ab initio* methods. The insights derived from these simulations shed light on the influence of thermal and quantum fluctuations on the CDW transition.

A new light on the CDW transition will be given in the *fourth publication* of this dissertation (see Ch. 14) as well. The publication provides clear experimental evidence of a CDW in monolayer

1H-NbS_2. While the study focuses less on the origin of said CDW, it explores the unique CDW gap that comes with low-energy peaks. These peaks are not solely of electronic origin but likely involve combined electron-phonon quasiparticles in its emergence.

In conclusion, it can be stated that through the development of *ab initio* based downfolded lattice models this dissertation will contribute to the exploration and understanding of electron-lattice coupled systems, such as charge density waves and beyond.

Outline

Chapters 2–10: Theoretical Background and Phenomena

Chapters 2–10, delve into the theoretical foundation and the phenomena under investigation in this dissertation. Chapter 2 provides the fundamental *ab initio* solid state Hamiltonian and the Born-Oppenheimer approximation to decouple electronic and nuclear degrees of freedom. Chapters 3–6 provide a comprehensive exploration of the origin and significance of the constituents within the downfolded lattice models. Specifically, these encompass the following: the undistorted electronic Wannier Hamiltonian (Ch. 3), the interatomic force constants (Ch. 4), the electron-phonon coupling (Ch. 5), and lastly, the electron-electron interactions (Ch. 6).

Chapters 7 introduces fundamental concepts in statistical mechanics, such as free energy and entropy, which are imperative for conducting molecular dynamics simulations (Ch. 8).

Subsequently, Chapter 9 delves into the critical concept of anharmonicity.

Chapter 10 is dedicated to discussing the charge density wave, a particular physical phenomenon to which the downfolded models will be applied to and which are intrinsically associated with anharmonicity. This chapter serves as the culmination of our exploration of the theoretical background.

Chapters 11–14: Research Publications

Chapters 11–14 are dedicated to the presentation and discussion of the four publications that form the core of this cumulative dissertation. Each chapter begins with a statement on the personal contributions to the publication, followed by an discussion on how the publication can be located within the scientific landscape and ends with the publication itself.

Chapter 15: Conclusion

The final chapter, Chapter 15, provides a comprehensive summary of the conclusions drawn throughout the development and application of downfolded models in the study of charge density waves.

2

Ab initio Hamiltonian

The general Hamiltonian of interacting electrons and nuclei in the position representation and atomic units, where in particular $m_\mathrm{e} = e = 1$ and $e^2/4\pi\varepsilon_0 = 1$, reads

$$H_\mathrm{FP} = T_e + T_k + V_{ee} + V_{ek} + V_{kk} \tag{2.1}$$

$$= -\sum_i \frac{\Delta_i}{2} - \sum_k \frac{\Delta_k}{2M_k} + \sum_{i<j} \frac{1}{|\boldsymbol{r}_i - \boldsymbol{r}_j|} - \sum_{ik} \frac{Z_k}{|\boldsymbol{r}_i - \boldsymbol{R}_k|} + \sum_{k<l} \frac{Z_k Z_l}{|\boldsymbol{R}_k - \boldsymbol{R}_l|}, \tag{2.2}$$

where $\boldsymbol{r}_i$ and $\boldsymbol{R}_k$ are electronic and nuclear positions, Δ_i and Δ_k are the corresponding Laplace operators, and Z_k and M_k are atomic numbers and nuclear masses. This Hamiltonian is also called "first-principles (FP) Hamiltonian", since only fundamental laws (i.e., the Schrödinger equation, Coulomb potential, etc.) and fundamental constants (elementary charges etc.) enter. It accounts for full atomic scale and chemical details. Numerical treatments leading directly from this Hamiltonian to physical results are called *ab initio*.

2.1. Born-Oppenheimer approximation

The Born-Oppenheimer approximation [58] is a fundamental concept in quantum mechanics that is used to simplify the first-principles Hamiltonian (Eq. 2.1). The electronic structure calculations which will be presented throughout this dissertation are all based on this approximation. The assumption is that the electronic motion is much faster than the nuclear motion, due to their vastly different masses. Specifically, the Born-Oppenheimer approximation assumes that the electroncs follow the nuclei instantaneously.

In this approximation, the kinetic energy of the nuclei will be treated as a perturbation:

$$H = H_0 + T_k \quad \text{with} \quad H_0 = T_e + V_{ee} + V_{ek} + V_{kk}. \tag{2.3}$$

In the remaining electronic Hamiltonian H_0, the positions of the nuclei $\boldsymbol{R}$ will enter as parameters only. By assuming that the electronic Hamiltonian can be solved in the following manner,

$$H_0\, \phi_\alpha(\boldsymbol{r}, \{\boldsymbol{R}\}) = \varepsilon_\alpha(\boldsymbol{R})\, \phi_\alpha(\boldsymbol{r}, \{\boldsymbol{R}\}), \tag{2.4}$$

the full wave function can be represented in the basis of the electronic wave functions,

$$\Psi(\boldsymbol{r}, \boldsymbol{R}) = \sum_\alpha \phi_\alpha(\boldsymbol{r}, \{\boldsymbol{R}\}) \chi_\alpha(\boldsymbol{R}). \tag{2.5}$$

Inserting the full wave function into the full Hamiltonian yields,

$$H\Psi(\boldsymbol{r},\boldsymbol{R}) = \sum_{\alpha} \left[H_0 + T_k\right] \phi_\alpha(\boldsymbol{r},\{\boldsymbol{R}\})\chi_\alpha(\boldsymbol{R}). \tag{2.6}$$

Here, the Laplace operator $\Delta_{\boldsymbol{R}}$ of the kinetic energy term T_k will act on the nuclear coordinates of the wave functions, leading essentially to the terms $\phi\nabla^2\chi + 2\nabla\phi\nabla\chi + \chi\nabla^2\phi$. In the Born-Oppenheimer approximation, the last two terms are neglected, which leaves a *decoupled* Schrödinger equation for the nuclei

$$\left[T_k + \varepsilon_\alpha(\boldsymbol{R})\right]\chi_\alpha(\boldsymbol{R}) = E\chi_\alpha(\boldsymbol{R}). \tag{2.7}$$

Thus, solving the many-body Schrödinger equation has been transformed into a two step process. First, the electronic Schrödinger equation (2.4) is solved for fixed nuclear positions $\boldsymbol{R}$. Then, the nuclei are allowed to move in a potential $\varepsilon_\alpha(\boldsymbol{R})$ defined by the electrons.

3

Electrons

This dissertation primarily focuses on the development of downfolded lattice models, which characterize the low-energy behavior of the electronic subspace when atoms are displaced. It is equally crucial to describe the state without any displacements – the undistorted state. This undistorted electronic structure is based on Kohn-Sham energy states, accessible through density functional theory (Sec. 3.1), and can serve as the natural starting point for the models. By employing Wannier functions (Sec. 3.2), these Kohn-Sham eigenvalues can be efficiently mapped onto a model Hamiltonian with a localized basis.

3.1. Density functional theory

This section is inspired by Ref. [59].

Density functional theory (DFT) is a comprehensive theory, which not only provides the electronic structure of a material, but also vibrational properties, due to the extension of the density functional perturbation theory (see Sec. 4.2), and especially the total energy by design of all constituents. It allows to find a ground state solution of the isolated Born-Oppenheimer Hamiltonian (Eq. 2.3). This is possible due to the Hohenberg and Kohn theorems [60], which prove that the ground state energy E is uniquely linked to the ground state electron density $n(\boldsymbol{r})$.

The idea of Hohenberg and Kohn motivates to express the total energy as a functional of the electron density

$$E[n] = T[n] + \int d\boldsymbol{r}\, V_{\text{ext}}(\boldsymbol{r}) n(\boldsymbol{r}) + \frac{1}{2} \int d\boldsymbol{r} \int d\boldsymbol{r}' \frac{n(\boldsymbol{r}) n(\boldsymbol{r}')}{|\boldsymbol{r} - \boldsymbol{r}'|} + E_{\text{xc}}[n], \tag{3.1}$$

where the first term is the kinetic energy

$$T[n] = -\frac{1}{2} \sum_{i=1}^{N_e} \int d\boldsymbol{r}\, \psi_i^*(\boldsymbol{r}) \Delta \psi_i(\boldsymbol{r}), \tag{3.2}$$

which implicitely depends on the electron density via

$$n(\boldsymbol{r}) = \sum_{i=1}^{N_e} f(\varepsilon_i) |\psi_i(\boldsymbol{r})|^2. \tag{3.3}$$

The second term in Eq. (3.1) is the external potential, which describes the Coulomb attraction by the static nuclei. Next to it is the density-density interaction or the so-called Hartree term, which describes a classical electrostatic Coulomb repulsion. The last term is the so-called exchange-correlation (XC) functional, which includes all many-body effects that have not been addressed yet. The exact form of this term is not known as it would require to solve the full many-body problem. However, there are some well-known approximations, which will be discussed in Sec. 3.1.1.

With the help of the variational method, it is possible to find the ground state of the total energy functional (Eq. 3.1). The aim is to minimize the energy under the constraint that the single-particle wave functions $\psi_i(\boldsymbol{r})$ are normalized

$$\delta_{\psi_i^*}\left\{E[n(\boldsymbol{r})] - \sum_{j=1}^{N_e} \varepsilon_j\Big(\int d^3r\,|\psi_j(\boldsymbol{r})|^2 - 1\Big)\right\} = 0. \tag{3.4}$$

This leads to the **Kohn-Sham equations** [61]

$$\left\{-\frac{1}{2}\Delta + V_{\text{ext}}(\boldsymbol{r}) + \frac{1}{2}\int d^3r'\,\frac{n(\boldsymbol{r})}{|\boldsymbol{r}-\boldsymbol{r'}|} + \frac{\delta E_{\text{XC}}\{n(\boldsymbol{r})\}}{\delta n(\boldsymbol{r})}\right\}\psi_i(\boldsymbol{r}) = \varepsilon_i\psi_i(\boldsymbol{r}), \tag{3.5}$$

$$\left\{-\frac{1}{2}\nabla^2 + V_{\text{SCF}}(\boldsymbol{r})\right\}\psi_i(\boldsymbol{r}) = \varepsilon_i\psi_i(\boldsymbol{r}), \tag{3.6}$$

with the effective single-particle potential

$$V_{\text{SCF}}(\boldsymbol{r}) = V_{\text{ext}}(\boldsymbol{r}) + \frac{1}{2}\int d^3r'\,\frac{n(\boldsymbol{r})}{|\boldsymbol{r}-\boldsymbol{r'}|} + \frac{\delta E_{\text{XC}}\{n(\boldsymbol{r})\}}{\delta n(\boldsymbol{r})}. \tag{3.7}$$

To conclude, DFT allows to solve the complex many-body problem by transforming it to an auxiliary single-particle problem, which is a dramatic simplification. Although, in the upcoming sections, it will be demonstrated that the solution is more complex than it appears at first glance – due to the use of sophisticated XC functionals and so-called pseudopotentials.

3.1.1. Exchange-correlation functionals

This section is inspired by Ref. [62]. This reference tries to answer the question: "Which functional should I choose?". The outcome is that there is no definitive answer to the question of which exchange-correlation functional to choose. Instead, experience and benchmarking are necessary to determine the best approach for a specific property and system.

As shown above, DFT is an exact approach in principle, yielding the exact ground-state energy and density. However, practical implementation requires approximating the XC functional. The quality of the results depends on the accuracy of this approximation. Several classes of functionals have been developed to tackle this approximation challenge, including the local density approximation (LDA) [61], generalized gradient approximation (GGA) [63, 64], and the widely used Perdew-Burke-Ernzerhof (PBE) functional [65, 66].

The LDA is the simplest form of XC functional, approximating the XC energy solely based on the local electron density:

$$E_{\text{XC}}^{\text{LDA}}[n(\boldsymbol{r})] = \int d^3r\,n(\boldsymbol{r})\varepsilon_{\text{XC}}(n(\boldsymbol{r})). \tag{3.8}$$

While LDA provides reasonable accuracy for many systems, including the ones discussed in this dissertation, it often results in an overestimation of molecular binding energies, which is deemed an unacceptable level of error for chemical applications [62].

To overcome the limitations of LDA, the GGA class of functionals introduces an additional term that accounts for the density gradient:

$$E_{\mathrm{XC}}^{\mathrm{GGA}}[n(\boldsymbol{r})] = \int d^3r\, n(\boldsymbol{r})\varepsilon_{\mathrm{XC}}(n(\boldsymbol{r}), \nabla n(\boldsymbol{r})). \tag{3.9}$$

By considering not only the electron density but also its spatial variation, GGA functionals can better describe molecular systems, surfaces, and chemical reactions.

In the pursuit of higher accuracy, the PBE functional emerged as a popular choice. It belongs to the GGA family but stands out due to its simple formulation, where all parameters are fundamental constants [65].

The development of XC functionals can be viewed as a progression on Jacob's ladder [67], where each rung represents an increasing level of accuracy and complexity. LDA stands at the bottom rung, GGA stands a step higher, and PBE, with its aforementioned simplification, represents a notable advancement. Researchers continue to climb this ladder, exploring and developing novel functionals to address the limitations of existing approaches.

3.1.2. Solving the Kohn-Sham equations: Basis sets and pseudopotentials

This section is inspired by Ref. [59].

In practical calculations, the Kohn-Sham wave functions will be expressed in a basis set. In the context of a periodic lattice structure, it is often advantageous to expand the wave functions using plane waves

$$\langle \boldsymbol{r}|n\boldsymbol{k}\rangle = \psi_{n\boldsymbol{k}}(\boldsymbol{r}) = \frac{1}{\sqrt{V}} \sum_{\boldsymbol{G}} c_{n,\boldsymbol{k}+\boldsymbol{G}}\, e^{i(\boldsymbol{k}+\boldsymbol{G})\boldsymbol{r}}, \tag{3.10}$$

which is the approach taken by the DFT code from Quantum ESPRESSO [68]. However, it is crucial that the wave functions remain orthogonal to the core states of the inner electrons. This requirement leads to the emergence of short-wave oscillations near the core region, a property that standard plane waves cannot satisfy. To address this, the orthogonalized plane waves (OPW) method [69] is employed, aiming to construct plane waves that are orthogonal to the inner core states.

In this approach, it is assumed that the inner core states do not overlap with their counterpart from other unit cells. This means that the atomic eigenfunctions $\varphi_l(\boldsymbol{r}-\boldsymbol{R})$ correspond to discrete eigenvalues E_l. The core states will therefore be

$$\Psi_{l\boldsymbol{k}}^{c}(\boldsymbol{r}) = \langle \boldsymbol{r}|\Psi_{l\boldsymbol{k}}^{c}\rangle = \frac{1}{\sqrt{N}} \sum_{\boldsymbol{R}} e^{i\boldsymbol{k}\boldsymbol{R}} \varphi_l(\boldsymbol{r}-\boldsymbol{R}), \tag{3.11}$$

which leads to the orthogonal plane waves

$$\left|\Psi_{n\boldsymbol{k}}^{b}\right\rangle = |\boldsymbol{k}\rangle - \sum_{l<n} |\Psi_{l\boldsymbol{k}}^{c}\rangle\langle\Psi_{l\boldsymbol{k}}^{c}|\boldsymbol{k}\rangle \tag{3.12}$$

with the free plane wave $|\boldsymbol{k}\rangle$. By multiplying from the left with an inner core state $\langle\Psi^c_{m\boldsymbol{k}}|$, the orthogonality can be seen: $\langle\Psi^c_{m\boldsymbol{k}}|\Psi^b_{n\boldsymbol{k}}\rangle = 0$.

In principle, the "*all-electron*" treatment with OPWs works and has been applied [70]. However, it requires a large basis set size to model the oscillations of the inner core states and the final basis set is not transferable to other systems. With the knowledge that the core electrons in atoms are tightly bound and less involved in most chemical reactions, the all-electron method might be a computational overkill for most systems. Thus, it is beneficial to work in these situations with so-called *pseudopotentials*.

The influence of the projector $P_{\boldsymbol{k}} = \sum_{l<n} |\Psi^c_{l\boldsymbol{k}}\rangle\langle\Psi^c_{l\boldsymbol{k}}|$ on the free plane wave $|\boldsymbol{k}\rangle$ can also be expressed as a potential. To that end, one can assume Schrödinger equations such as

$$H|\Psi_{n\boldsymbol{k}}\rangle = \varepsilon_n(\boldsymbol{k})|\Psi_{n\boldsymbol{k}}\rangle \quad \text{and} \quad H|\Psi^c_{l\boldsymbol{k}}\rangle = E_l|\Psi^c_{l\boldsymbol{k}}\rangle. \tag{3.13}$$

The ansatz for the left Schrödinger equation is a linear combination of orthogonal plane waves,

$$|\Psi_{n\boldsymbol{k}}\rangle = (1 - \sum_{l<n} |\Psi^c_{l\boldsymbol{k}}\rangle\langle\Psi^c_{l\boldsymbol{k}}|)|\Phi_{\boldsymbol{k}}\rangle = (1 - \sum_{l<n} |\Psi^c_{l\boldsymbol{k}}\rangle\langle\Psi^c_{l\boldsymbol{k}}|) \sum_{\boldsymbol{G}} a_{\boldsymbol{kG}}|\boldsymbol{k}+\boldsymbol{G}\rangle. \tag{3.14}$$

This leads to an effective Schrödinger equation for the linear combination of plane waves,

$$\left[H + \sum_{l<n} (\varepsilon_n(\boldsymbol{k}) - E_l)|\Psi^c_{l\boldsymbol{k}}\rangle\langle\Psi^c_{l\boldsymbol{k}}|\right]|\Phi_{\boldsymbol{k}}\rangle = \varepsilon_n(\boldsymbol{k})|\Phi_{\boldsymbol{k}}\rangle \tag{3.15}$$

with the effective potential, called *pseudopotential* V_{ps}

$$V_{\text{ps}} = V + \sum_{l<n} (\varepsilon_n(\boldsymbol{k}) - E_l)|\Psi^c_{l\boldsymbol{k}}\rangle\langle\Psi^c_{l\boldsymbol{k}}|. \tag{3.16}$$

Due to the projector being inside of the pseudopotential V_{ps}, it is not a real potential (scalar function of spatial coordinates) anymore, but rather an operator. Additionally, the energies $\varepsilon_n(\boldsymbol{k})$ are inside the term of the potential as well, which makes it a non-trivial eigenvalue problem that has to be solved.

There are various types of pseudopotentials used in DFT calculations, including the Hartwigsen-Goedecker-Hutter pseudopotentials [71, 72], ultra-soft pseudopotentials [73], and optimized norm-conserving pseudopotentials [74].

Hartwigsen-Goedecker-Hutter pseudopotentials are a popular choice in many electronic structure codes. The distinctive features of these pseudopotentials are the complete analytical form, where at most, seven parameters are needed to fix these potentials [71]. Additionally, the all-electron wave function and the pseudo wave function do not coincide after some radial distance. Instead the wave functions approach each other exponentially.

Ultra-soft pseudopotentials are another type commonly employed in DFT calculations. These pseudopotentials are designed to be smooth and well-behaved, ensuring accurate description of the electron wavefunctions. The term “ultra-soft” refers to the smoothness of the pseudopotential, which is achieved by relaxing the constraint of *norm-conservation*. Instead a generalized eigenvalue problem has to be solved. These pseudopotentials were designed to yield the lowest possible energy cutoff for the plane wave basis set.

Lastly, the optimized norm-conserving pseudopotentials are designed to keep norm-conservation and present an extension to the standard norm-conserving pseudopotentials [75].

This dissertation focuses especially on the description of charge density waves. The phenomenon itself will be discussed in Chapter 10. However, here, their dependence on the XC functionals will

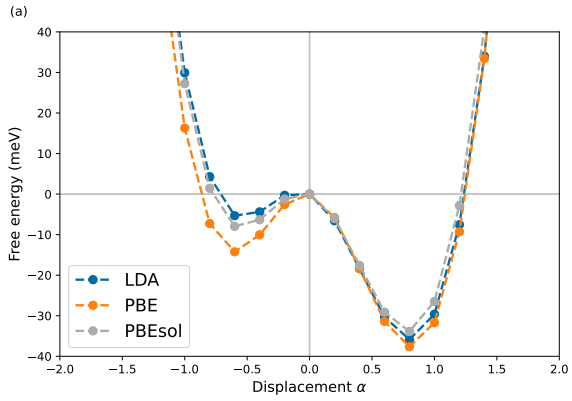

Figure 3.1: For a prototypical CDW displacement, DFT calculations were performed using QUANTUM ESPRESSO for monolayer 1H-TaS_2. The LDA (blue), PBE (orange) and PBEsol (gray) XC functionals and norm-conserving pseudopotentials from the PSEUDODOJO table are applied. (Computational details concerning this Fig. can be found in App. A.3.1)

be shown. As a prototypical example, Fig. 3.1 illustrates the utilization of DFT calculations to gain an understanding of the relevant energy scales. LDA (blue), PBE (orange) and PBEsol (gray) XC functionals and optimized norm-conserving pseudopotentials from the PSEUDODOJO table[74, 76] are applied. It is evident that all XC functionals yield consistent qualitative results. This signifies that a charge density wave is consistently identified within the framework of DFT across all instances. Nevertheless, there exist quantitative differences on the order of a few meV.

To conclude, the chemical accuracy of the chosen XC functional might yield a few percent of accuracy on the overall energy scale. If achieving such precision is the goal, performing benchmarks becomes essential. However, if the existence of the physical phenomenon itself is prioritized, then the significance of the various XC functionals diminishes.

3.2. Wannier functions

This section is inspired by Ref. [77].

Wannier functions are a set of localized functions used to describe the electronic states in a periodic solid material. They were introduced as an alternative representation of the Bloch electronic wavefunctions in a crystalline system [78]. Wannier functions have proven to be a powerful tool in condensed matter physics and materials science for understanding the electronic structure based on localized chemical orbitals.

To understand the concept of Wannier functions, it is insightful to consider a crystal with a periodic potential described by the periodic lattice vector $\boldsymbol{R}$. The electronic wavefunctions in this crystal can be written as Bloch wavefunctions, given by:

$$\psi_{n\boldsymbol{k}}(\boldsymbol{r}) = e^{i\boldsymbol{k}\boldsymbol{r}} u_{n\boldsymbol{k}}(\boldsymbol{r}), \tag{3.17}$$

where $\boldsymbol{k}$ is the crystal momentum, n denotes the band index, $\boldsymbol{r}$ is the position vector, and $u_{n\boldsymbol{k}}(\boldsymbol{r})$ is a periodic function with the same periodicity as the lattice.

The key idea behind Wannier functions is to find a set of localized and orthogonal functions that have the same information as the Bloch wavefunctions. Mathematically, the Wannier function $|\boldsymbol{R}n\rangle$ associated with the band n and the lattice vector $\boldsymbol{R}$ is given by the Fourier transform of the Bloch wavefunction in Dirac bra-ket notation:

$$|\boldsymbol{R}n\rangle = \frac{V}{(2\pi)^3}\int_{BZ} d\boldsymbol{k}e^{-i\boldsymbol{k}\boldsymbol{R}}|\psi_{n\boldsymbol{k}}\rangle, \tag{3.18}$$

where the integral extends over the Brillouin zone, and V is the real-space primitive cell volume.

One of the significant advantages of Wannier functions is that they provide a natural basis for studying the electronic properties of solids. They allow for a more intuitive understanding of electron-electron or electron-phonon interactions. This is because the electronic degrees of freedom can be represented with atomic-like orbitals. In the following this will be demonstrated with the so-called *tight-binding* formalism.

The matrix elements of an electronic Hamiltonian can be represented with the Wannier functions defined in Eq. (3.18), as

$$H_{\alpha\beta}(\boldsymbol{R}) = \langle \boldsymbol{R}\alpha|H|\boldsymbol{0}\beta\rangle := t_{\alpha\beta}(\boldsymbol{R}). \tag{3.19}$$

The magnitude of $t_{\alpha\beta}(\boldsymbol{R})$ represents the amplitude for an electron to move from orbital β located at the origin $\boldsymbol{0}$ to orbital α located at lattice site $\boldsymbol{R}$. Larger $t_{\alpha\beta}$ values indicate a higher probability of electrons hopping between adjacent sites, earning them the name hopping matrix elements. With a Fourier transform, the matrix elements in $\boldsymbol{k}$-space can be obtained via

$$t_{\alpha\beta}(\boldsymbol{k}) = \sum_{\boldsymbol{R}} t_{\alpha\beta}(\boldsymbol{R})e^{i\boldsymbol{k}\boldsymbol{R}}, \tag{3.20}$$

which leads to the momentum representation of the electronic Hamiltonian in second quantization:

$$H = \sum_{\boldsymbol{k}\alpha\beta} t_{\alpha\beta}(\boldsymbol{k})c^{\dagger}_{\alpha}c_{\beta}. \tag{3.21}$$

Solving the Hamiltonian yields the original eigenvalues that correspond to the Bloch wavefunctions. Interestingly, this mapping procedure can be done in a way that only parts of the original Hilbert space are reconstructed – e.g. the low-energy bands near the Fermi level. Thus, Wannier functions can be used to construct effective model Hamiltonians for describing the low-energy physics of materials, enabling the study of complex systems using simplified models.

The Wannier Hamiltonian from Eq. (3.21) will be the starting point for every downfoled model, which will be presented in this dissertation. It will be called the undistorted Hamiltonian since it provides the Kohn-Sham eigenvalues for the undistorted crystal structure. Distortions will be incorporated via phonons in Chapter 4 and the electron-phonon coupling in Chapter 5.

4

Phonons

In the previous chapter discussing electrons, DFT is shown to provide Born-Oppenheimer potential energy surfaces for arbitrary lattice configurations and thus enabling molecular dynamics simulations. However, the computational demands for large systems over extended time scales are prohibitively high. This dissertation introduces downfolded lattice models as an alternative, significantly reducing computational requirements by utilizing interatomic force constants that give access to the second-order Born-Oppenheimer potential energy surface. However, in the presence of phase transitions, the harmonic term (Sec. 4.1) alone yields a downward opened energy surface around the equilibrium positions and thus cannot stabilize atomic lattice positions. Consequently, solely calculating the second-order force constants is insufficient for molecular dynamics simulations as they cannot faithfully reproduce the full DFT potential energy surfaces. Therefore, it becomes necessary to compute anharmonic terms originating from the electronic part of the model Hamiltonian. To avoid double counting, the force constants must exclude virtual electronic processes within the electronic model subspace. This can be achieved by partial screening via methods like constrained density functional perturbation theory (Sec. 4.2.1) or unscreening (Sec. 4.2.2) with phonon self-energies.
This chapter is mainly inspired by the review article on density functional perturbation theory [79] (Sec. 4.2). Furthermore, Ref. [80] is used for the description of the constrained density functional perturbation theory. Lastly, Ref. [81] is insightful for a detailed description on different ways to obtain partially screened phonon quantities for downfolded models.

4.1. Harmonic approximation

The Born-Oppenheimer Hamiltonian defined in Eq. (2.3) yields a ground-state energy $E(\boldsymbol{R})$ of a system of interacting electrons moving in the field of fixed nuclei. The derivative of this ground-state energy with respect to the nuclei coordinates yields the force and can be evaluated using the Hellman-Feynmann theorem:

$$\boldsymbol{F}_I = -\frac{\partial E(\boldsymbol{R})}{\partial \boldsymbol{R}_I} = -\left\langle \Psi(\boldsymbol{R}) \middle| \frac{\partial H_{\mathrm{BO}}(\boldsymbol{R})}{\partial \boldsymbol{R}_I} \middle| \Psi(\boldsymbol{R}) \right\rangle = -\int n_{\boldsymbol{R}}(\boldsymbol{r}) \frac{\partial V_{\boldsymbol{R}}(\boldsymbol{r})}{\partial \boldsymbol{R}_I} d\boldsymbol{r} - \frac{\partial E_N(\boldsymbol{R})}{\partial \boldsymbol{R}_I}. \tag{4.1}$$

The Hellman-Feynman theorem is extremely useful as it allows one to calculate forces without having to obtain derivatives of the electron density $n_{\boldsymbol{R}}$ (wave function Ψ). In fact, it will be used for the downfolded models as well (cf. Appendix B of Ch. 13). Differentiating Eq. (4.1) again, yields the

interatomic force constants (cf. Eq. 10 of Ref. [79])

$$C_{IJ}(\boldsymbol{R}) = \frac{\partial^2 E(\boldsymbol{R})}{\partial \boldsymbol{R}_I \partial \boldsymbol{R}_J} = \int \frac{\partial n_{\boldsymbol{R}}}{\partial \boldsymbol{R}_J} \frac{\partial V_{\boldsymbol{R}}(\boldsymbol{r})}{\partial \boldsymbol{R}_I} d\boldsymbol{r} + \int n_{\boldsymbol{R}}(\boldsymbol{r}) \frac{\partial^2 V_{\boldsymbol{R}}(\boldsymbol{r})}{\partial \boldsymbol{R}_I \partial \boldsymbol{R}_J} d\boldsymbol{r} + \frac{\partial^2 E_N(\boldsymbol{R})}{\partial \boldsymbol{R}_I \partial \boldsymbol{R}_J}, \tag{4.2}$$

with the electron-nucleus interaction $V_{\boldsymbol{R}}(\boldsymbol{r}) = -\sum_{iI} Z_I / |\boldsymbol{r}_i - \boldsymbol{R}_I|$, the electrostatic interaction between different nuclei $E_N(\boldsymbol{R}) = 1/2 \sum_{I \neq J} Z_I Z_J / |\boldsymbol{R}_I - \boldsymbol{R}_J|$ and the ground-state electron charge density $n_{\boldsymbol{R}}(\boldsymbol{r})$. Thus, Eq. (4.2) is by construction part of the second-order term of the total (free) energy. An expansion around relaxed equilibrium lattice vectors $\boldsymbol{R}^0$ clarifies this relation:

$$E = E(\boldsymbol{R}^0) + \sum_I \left. \frac{\partial E(\boldsymbol{R})}{\partial \boldsymbol{R}_I} \right|_{\boldsymbol{R}^0} \boldsymbol{R}_I + \frac{1}{2} \sum_{IJ} \left. \frac{\partial^2 E(\boldsymbol{R})}{\partial \boldsymbol{R}_I \partial \boldsymbol{R}_J} \right|_{\boldsymbol{R}^0} \boldsymbol{R}_J \boldsymbol{R}_I + \dots . \tag{4.3}$$

Truncating the Taylor series to the second order is called the *harmonic approximation*. Consequently, all terms up to that point are referred to as harmonic terms, and all terms beyond that point are referred to as *anharmonic*.

With the help of a Fourier transform to the $\boldsymbol{q}$-space and dividing by the masses of the atoms, the dynamical matrix from Eq. (4.2) can be obtained,

$$D^{\alpha\alpha'}_{\kappa\kappa'}(\boldsymbol{q}) = \frac{1}{\sqrt{M_\kappa M_{\kappa'}}} C^{\alpha\alpha'}_{\kappa\kappa'}(\boldsymbol{q}), \tag{4.4}$$

where the index labeling has been changed to an index for the atoms κ in the unit cell and the direction of displacement $\alpha = \{x, y, z\}$. Diagonalizing the dynamical matrix

$$\sum_{\kappa'\alpha'} D^{\alpha\alpha'}_{\kappa\kappa'}(\boldsymbol{q}) e^{\alpha'}_{\kappa'}(\boldsymbol{q}) = \omega^2_{\boldsymbol{q}\nu} e^{\alpha}_{\kappa}(\boldsymbol{q}) \tag{4.5}$$

gives the phonon frequencies $\omega_{\boldsymbol{q}\nu}$ and the polarization vectors $e^{\alpha}_{\kappa}(\boldsymbol{q})$.

4.2. Density functional perturbation theory

The vibrational quantities defined in the previous section can be calculated with the density functional perturbation theory. As can be seen in Eq. (4.2), a direct evaluation of the force constants is hindered by the unknown response of the electronic density to lattice distortions $\Delta n(\boldsymbol{r})$. Hence, the linear response of the Kohn-Sham electronic density (Eq. 3.3) is needed and can be calculated with (cf. Eq. 69 of Ref. [79] or Eq. 5 of Ref. [80])

$$\Delta n(\boldsymbol{r}) = \sum_{n,m} \frac{\tilde{\theta}_{F,n} - \tilde{\theta}_{F,m}}{\varepsilon_n - \varepsilon_m} \psi^*_n(\boldsymbol{r}) \psi_m(\boldsymbol{r}) \langle \psi_m | \Delta V_{\mathrm{SCF}} | \psi_n \rangle \tag{4.6}$$

with composite indices for the band and the momentum n, m, the Kohn-Sham wave function ψ_n, and the Kohn-Sham eigenenergy ε_n. The $\tilde{\theta}(x)$ is a smoothed step function which fascilitates the treatments of metals in DFT calculations. It is related to the smearing function, $\tilde{\delta}(x)$, via $\tilde{\theta}(x) = \int_{-\infty}^{x} \tilde{\delta}(x')dx'$. In the case of Fermi-Dirac smearing, it can be replaced with the Fermi-Dirac distribution $\tilde{\theta}_{F,n} = f((\varepsilon_F - \varepsilon_n)/kT)$.

The change in the potential ΔV_{SCF} due to displacements of the nuclei is given by

$$\Delta V_{\mathrm{SCF}}(\boldsymbol{r}) = \Delta V_{\mathrm{ext}}(\boldsymbol{r}) + e^2 \int \frac{\Delta n(\boldsymbol{r'})}{|\boldsymbol{r} - \boldsymbol{r'}|} d\boldsymbol{r'} + \left.\frac{dv_{\mathrm{XC}}(n)}{dn}\right|_{n=n(\boldsymbol{r})} \Delta n(\boldsymbol{r}), \tag{4.7}$$

with the same contributions as defined in Eq. (3.7). Since the linear response of the density $\Delta n(\boldsymbol{r})$ is part of this equation, the determination has to be achieved in a self-consistent iteration together with Eq. (4.6).

The calculation of Eq. (4.6) would require extensive summations over conduction bands. Thus, in practice, this equation will be projected onto the occupied states only. This will be demonstrated for the example of a non-metal material with a gap between the conduction $|c\rangle$ and valence states $|v\rangle$. The linear response of the electronic density can be written in this case as

$$\begin{aligned} \Delta n(\boldsymbol{r}) &= 2 \sum_{c,v} \frac{1}{\varepsilon_v - \varepsilon_c} \langle c|\Delta V_{\mathrm{SCF}}|v\rangle \Psi_v^*(\boldsymbol{r}) \Psi_c(\boldsymbol{r}) \\ &= 2 \sum_{v} \Psi_v^* \Delta_v(\boldsymbol{r}), \end{aligned} \tag{4.8}$$

with the definition

$$|\Delta_v\rangle = \sum_c \frac{1}{\varepsilon_v - \varepsilon_c} |c\rangle\langle c|\Delta V_{\mathrm{SCF}}|v\rangle. \tag{4.9}$$

This leads to the so-called *Sternheimer equation*

$$\begin{aligned} (H - \varepsilon_v)|\Delta_v\rangle &= \sum_c \frac{H - \varepsilon_v}{\varepsilon_v - \varepsilon_c} |c\rangle\langle c|\Delta V_{\mathrm{SCF}}|v\rangle \\ &= \sum_c \frac{\varepsilon_c - \varepsilon_v}{\varepsilon_v - \varepsilon_c} |c\rangle\langle c|\Delta V_{\mathrm{SCF}}|v\rangle \\ &= -\sum_c |c\rangle\langle c|\Delta V_{\mathrm{SCF}}|v\rangle \\ &= -P_c \Delta V_{\mathrm{SCF}}|v\rangle \\ &= (P_v - 1)\Delta V_{\mathrm{SCF}}|v\rangle, \end{aligned}$$

where P_v and P_c are projectors onto the valence and conduction space. As can be seen, the final form contains quantities of the valence space only. This is a computational advantage as it circumvents the summation over the empty conduction space.

4.2.1. Constrained density functional perturbation theory

The constrained density functional perturbation theory is a downfolding technique for electron-lattice coupled systems. In particular, it can be used to obtain partially screened phonon frequencies and electron-phonon coupling matrix elements within the DFT-framework. In order to understand this theory, it is insightful to look at each part of the interatomic force constants from Eq. (4.2) individually.

The third term on the right-hand side is a purely ionic contribution. Physically, this term describes the total energy change upon displacing the bare nuclei in the crystal. Naively one might think this is the only contribution to the force constants when dealing with “lattice vibrations”. However,

lattice vibrations are influenced by the electronic density as well. Thus, there is the second term, which consists of an electronic contribution due to the ground-state electronic density and a quadratic electron-phonon coupling. Both terms taken together are defined as the *bare* force-constants

$$ {}^{\text{bare}}C^{\alpha\alpha'}_{\kappa\kappa'}(\boldsymbol{q}) = \frac{1}{N}\left[\frac{\partial^2 E_N}{\partial u^{*\alpha}_{\kappa}(\boldsymbol{q}) u^{\alpha'}_{\kappa'}(\boldsymbol{q})} + \int n(\boldsymbol{r}) \frac{\partial^2 V_{\text{ext}}(\boldsymbol{r})}{\partial u^{*\alpha}_{\kappa}(\boldsymbol{q}) u^{\alpha'}_{\kappa'}(\boldsymbol{q})} d\boldsymbol{r}\right], \tag{4.10} $$

and the contribution from the linear electron-phonon coupling is called the *renormalizing* term

$$ {}^{\text{ren.}}C^{\alpha\alpha'}_{\kappa\kappa'}(\boldsymbol{q}) = \frac{1}{N}\int \left(\frac{\partial n(\boldsymbol{r})}{\partial u^{\alpha}_{\kappa}(\boldsymbol{q})}\right)^{*} \frac{\partial V_{\text{ext}}(\boldsymbol{r})}{\partial u^{\alpha'}_{\kappa'}(\boldsymbol{q})} d\boldsymbol{r}. \tag{4.11} $$

By inserting the linear response of the electronic density from Eq. (4.6), it can be shown (see Sec. 2.4.2 of Ref. [82]) that this expression leads to

$$ {}^{\text{ren.}}C^{\alpha\alpha'}_{\kappa\kappa'}(\boldsymbol{q}) = \frac{2}{N}\sum_{\boldsymbol{k}mn} \frac{f(\varepsilon_{\boldsymbol{k}+\boldsymbol{q}m}) - f(\varepsilon_{\boldsymbol{k}n})}{\varepsilon_{\boldsymbol{k}+\boldsymbol{q}m} - \varepsilon_{\boldsymbol{k}n}} \langle \boldsymbol{k}n| \frac{\partial V_{\text{ext}}}{\partial u^{\alpha}_{\kappa}(-\boldsymbol{q})} |\boldsymbol{k}+\boldsymbol{q}m\rangle \langle \boldsymbol{k}+\boldsymbol{q}m| \frac{\partial V_{\text{SCF}}}{\partial u^{\alpha}_{\kappa}(\boldsymbol{q})} |\boldsymbol{k}n\rangle, \tag{4.12} $$

where the first term is the bare susceptibility χ^0 (also called total irreducible polarization) and the two last terms are the bare (screened) electron-phonon coupling matrix elements, which correspond to the potentials V_{ext} (V_{SCF}) respectively [83].

Equation 4.12 is essentially known as the static ($\omega = 0$) phonon renormalization within the random phase approximation (RPA – see Sec. 6.3) and is related to the phonon self-energy, defined by

$$ \Pi^{\text{b0}} := \frac{{}^{\text{ren.}}C}{2M\omega^{(b)}} = |g^{(b)}|^2 \chi_{\text{DFT}} = (g^{(b)})^{\dagger} \chi^0 g^{(f)}, \tag{4.13} $$

with $\chi_{\text{DFT}} = \chi^0(1 - \tilde{v}\chi^0)^{-1}\Delta V_{\text{ext}}$. Diagrammatically, the phonon self-energy can be expressed as (cf. Eq. 40 of Ref. [81])

$$ \Pi^{\text{b0}}(T) \equiv $$

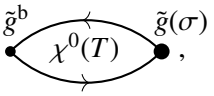

, (4.14)

where a different definition of electron-phonon coupling matrix elements $\tilde{g}$ has been used (see Appendix A.1). In this expression only the electronic temperature arguments σ and T are shown. Their meaning will be discussed in Sec. 4.2.2, since they are of relevance for the downfolded lattice models.

It is crucial to highlight that in the RPA, the frequency renormalization of a phonon mode is solely governed by the electron-lattice coupling and the electronic processes rendered by χ^0. This renormalization is not influenced by the presence or absence of other phonon modes. Consequently, the RPA neglects what is commonly known as mode-mode coupling [84].

The idea of the constrained theories, cDFPT and cRPA (see Sec. 6.3.1), is to divide this screening process into two steps. Meaning, the bare susceptibility will be separated as

$$ \chi^0_{\boldsymbol{q}\boldsymbol{k}mn}(T) = \chi^{0,\text{t}}_{\boldsymbol{q}\boldsymbol{k}mn}(T) + \chi^{0,\text{r}}_{\boldsymbol{q}\boldsymbol{k}mn}(T). \tag{4.15} $$

Thus, the bare quantities are renormalized due to the coupling between the phonons and the high-energy electrons, i.e. mediated by the "rest subspace" susceptibility $\chi^{0,\text{r}}$. This leads to *partially* screened quantities. The coupling between the phonons and the low-energy electrons is the second

renormalization. However, this step is considered when solving the low-energy model or by explicitely reconstructing the fully screened quantities with phonon self-energies. The first part is presented in Chapter 13 of this dissertation, while the latter will be demonstrated in the following.

The active-subspace phonon self-energy needed to reconstruct the fully screened phonons is given by:

$$\Pi^{\mathrm{p}0}(T) \equiv \tilde{g}^{\mathrm{p}}(\sigma)\ \chi^{0,\mathrm{t}}(T)\ \tilde{g}(\sigma) \,. \tag{4.16}$$

Thus, in the second step, the screened phonon Green's function $G(T)$ is recreated from the partially screened $G^{\mathrm{p}}(T)$,

$$G(T) = G^{\mathrm{p}}(T) + G^{\mathrm{p}}(T)\ \tilde{g}^{\mathrm{p}}(T)\ \chi^{0,\mathrm{t}}(T)\ \tilde{g}(T)\ G(T) \,, \tag{4.17}$$

which translates into a simple addition of dynamical matrix and phonon self-energy,

$$D_{\boldsymbol{q}}(T) = D^{\mathrm{p}}_{\boldsymbol{q}}(T) + \Pi^{\mathrm{t}}_{\boldsymbol{q}}(T). \tag{4.18}$$

This relationship is illustrated in Fig. 4.1. As can be seen, the partially screened phonons from cDFPT plus the aforementioned phonon self-energy $\Pi^{\mathrm{p}0}$ (dark gray dashed line) is identical to the fully screened phonons from DFPT (gray solid line). Furthermore, the partially screened phonons alone do not show any instability as opposed to the screened phonons. Meaning that the instability is induced by the low-energy electronic subspace. A situation like this gives rise to construct a low-energy lattice model within the defined active subspace. This was done in one of the publications of this dissertation (see Ch. 13). There, the downfolded model is called model I and the interatomic force constants for this model are taken from cDFPT.

In practical calculations, it is not necessary to implement susceptibilities into an exisiting DFPT code. Instead, as it is proposed in Ref. [80], in order to exclude target-target processes from Eq. (4.6), one should include yet another projector into the Stermheimer equation, like (cf. Eq. 22 of Ref. [80])

$$(H_{\mathrm{SCF}} + Q - \varepsilon_n)|\Delta\psi_n\rangle = -P_r(\tilde{\theta}_{F,n} - P_n)\Delta V_{\mathrm{SCF}}|\psi_n\rangle \tag{4.19}$$

with the initial projectors

$$Q = \sum_m \alpha_m |\psi_m\rangle\langle\psi_m|, \quad P_n = \sum_m \beta_{n,m}|\psi_m\rangle\langle\psi_m| \tag{4.20}$$

and the additional projector P_r that projects onto the r subspace only. The parameters α_m are chosen such that null eigenvalues are avoided [79, 80]. Equation 4.19 is a more sophisticated version of the Sternheimer equation shown in Eq. (4.10), since it is valid for metals with partially occupied bands as well.

Instead of implementing the P_r projector, it is equivalent to modify the coefficients of the P_n projector [80] in the following way:

$$\tilde{\beta}_{n,m} = \begin{cases} \tilde{\theta}_{F,n} & (n, m \in t - \text{subspace}) \\ \tilde{\theta}_{F,n}\tilde{\theta}_{n,m} + \tilde{\theta}_{F,m}\tilde{\theta}_{m,n} + \alpha_m \frac{\tilde{\theta}_{F,n} - \tilde{\theta}_{F,m}}{\varepsilon_n - \varepsilon_m}\tilde{\theta}_{m,n} & (\text{other cases}) \end{cases} \tag{4.21}$$

This modification can be conveniently applied to the existing DFPT code from Quantum ESPRESSO. For the results of this dissertation, the necessary cDFPT modification was applied with the `elphmod` code.

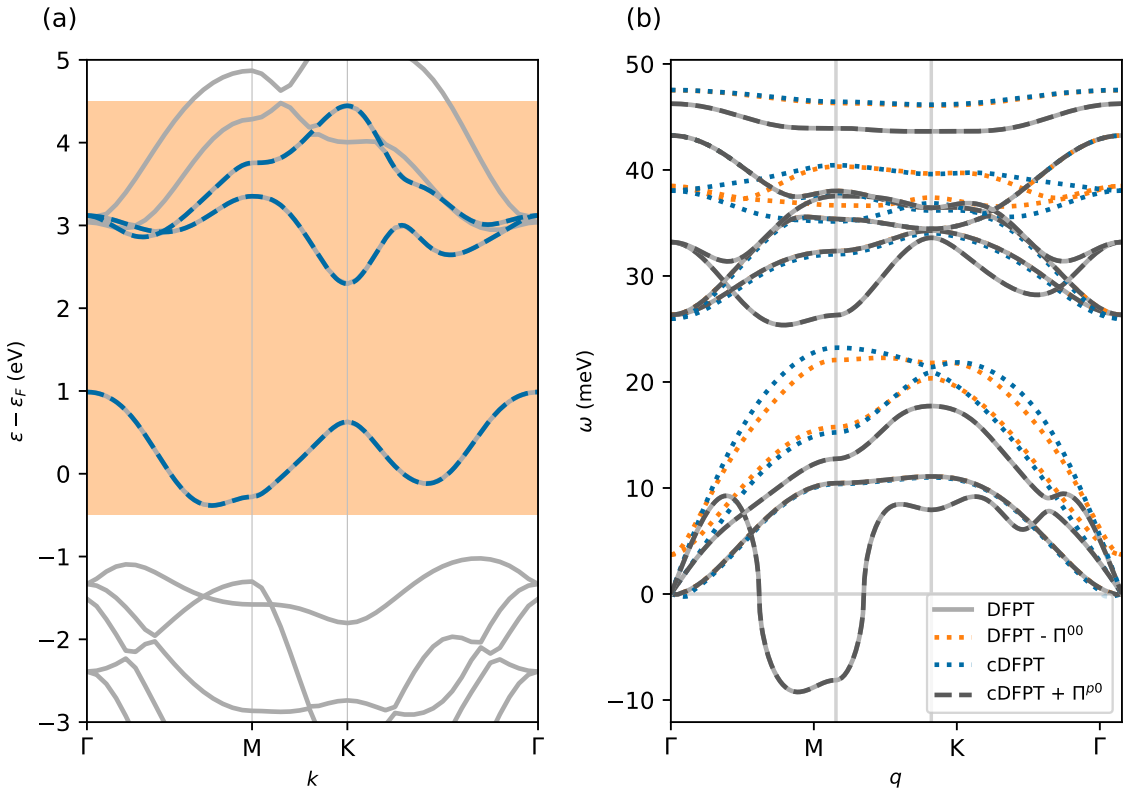

Figure 4.1: (a) Electronic band structure of monolayer TaS_2 from DFT (gray). The target subspace is highlighted in orange and the corresponding three Wannier bands as dashed blue lines. (b) Standard fully screened phonon dispersion from DFPT (light gray) with an instability of the longitudinal acoustic branch. Two types of partially screened phonons, where the instability has been lifted: unsreened phonons (orange dots) and cDFPT phonons (blue dots). A reconstruction of the fully screened phonons is recovered from the cDFPT phonons plus the phonon self-energy Π^{p0} (dashed gray). (Computational details concerning this Fig. can be found in App. A.3.2)

4.2.2. Theory of unscreening: Phonons

There is an alternative approach to obtain partially screened phonons and electron-phonon couplings. This approach follows the philosophy of *unscreening* fully screened quantities:

$$D^{\mathrm{u}}_{\boldsymbol{q}}(\sigma) \equiv D_{\boldsymbol{q}}(\sigma) - \Pi^{00}_{\boldsymbol{q}}(\sigma), \tag{4.22}$$

with the phonon self-energy,

$$\Pi^{00}(T) \equiv \tilde{g}(\sigma, 0) \quad \chi^{0,\mathrm{t}}(T) \quad \tilde{g}(\sigma) \,. \tag{4.23}$$

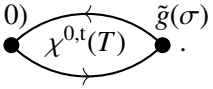

The phonon dispersion corresponding to Eq. (4.22) is shown in Fig. 4.1 as orange dots. Additionally, the partially screened phonons from cDFPT are shown as blue dots. Qualitatively both curves are very similar with the exception that the unscreened phonons do not fulfill the acoustic sum rule at Γ ($\boldsymbol{q} = 0$). This particular attribute of partially screened phonons is discussed in detail in Ref. [51].

Another interesting feature of the phonon renormalization is the temperature dependence. The temperatures enter through the occupation function $f(\varepsilon/k_B T)$ as shown in Eq. (4.12). The distinction between σ and T is useful since the electron-phonon coupling is obtained through *ab initio* calulations with a DFT smearing parameter σ, whereas the phonon renormalization can be carried out with a different electronic temperature T. In Ref. [81] it is shown how accurate different renormalization schemes can be when changing the electronic temperature T compared to the initial *ab initio* smearing σ. Additionally, in Fig. 6 of Chapter 13, the agreement of the harmonic contribution between approximative and exact approach is illustrated, which highlights that it is indeed possible to choose a different electronic temperature within the active model subspace.

This concludes the discussion on phonons, which had the role to introduce the various second-order terms in the downfolding models presented in Chapter 13. To elaborate further, cDFPT phonons were applied in model I, while unscreened phonons were employed for model III. Additionally, a different set of partially screened phonons was utilized for model II, with the unscreening process elaborated in Chapter 13.

5

Electron-phonon interaction

The electron-phonon coupling plays a central role in downfolded lattice models as it enables interactions between electronic and nuclear degrees of freedom. One might assume that introducing electron-phonon coupling automatically leads to a departure from the Born-Oppenheimer approximation. However, this is not the case. Within the Born-Oppenheimer approximation, atomic positions are treated as parameters in the electronic Schrödinger equation, directly influencing the electronic structure and, consequently, altering the free energy. Subsequently, by minimizing the free energy, new atomic positions are determined, which in turn affect the electronic equations once again. The electron-phonon coupling mediates between these two processes.

This chapter introduces the electron-phonon coupling as it is used within the downfolded lattice models. This entails the coupling Hamiltonian (Sec. 5.1) for the supercell approach and the representation with Wannier functions (Sec. 5.2). Inspiration for this chapter is drawn from Ref. [85].

5.1. Electron-phonon coupling Hamiltonian

The coupling between the electronic and nuclear degrees of freedom can be written in second quantization as

$$H_{\text{el-n}} = \sum_{\boldsymbol{q}\boldsymbol{k}mn} V_{\boldsymbol{q}\boldsymbol{k}mn}(\boldsymbol{u}_1, \ldots, \boldsymbol{u}_{N_\text{n}}) c^\dagger_{\boldsymbol{k}+\boldsymbol{q}m} c_{\boldsymbol{k}n}, \tag{5.1}$$

where V describes the coupling to displacements $\boldsymbol{u}$ in infinite order. From a technical perspective within an *ab initio* approach, only the first-order coupling can be efficiently calculated. The higher-order couplings are beyond the reach of nowadays *ab initio* software. In the following it will be described how to prepare the linear electron-phonon coupling term, which is obtained from DFPT, for the downfolded lattice models.

In the framework of the DFT Kohn-Sham formalism, the electron-phonon coupling Hamiltonian can be derived by expanding the Kohn-Sham effective potential with respect to the nuclear displacements $\Delta\boldsymbol{u}_{\kappa p}$ from their equilibrium positions $\boldsymbol{u}^0_{\kappa p}$. To first order in the displacements, the potential is given by

$$V_{\text{SCF}}(\{\boldsymbol{u}_{\kappa p}\}) = V_{\text{SCF}}(\{\boldsymbol{u}^0_{\kappa p}\}) + \sum_{\kappa x p} \frac{\partial V_{\text{SCF}}}{\partial u_{\kappa x p}} \Delta u_{\kappa x p}, \tag{5.2}$$

where $u_{\kappa x p}$ denotes the displacement of the nucleus κ, from the unit cell p in the Cartesian direction x.

With this expression, the coupling Hamiltonian can be rewritten as (cf. Eq. 36 of Ref. [85])

$$H_{\text{el-n}} = \sum_{\boldsymbol{k}n,\boldsymbol{k}'n'} \langle \psi_{\boldsymbol{k}n} | V_{\text{SCF}}(\{\boldsymbol{u}_{\kappa p}\}) - V_{\text{SCF}}(\{\boldsymbol{u}^0_{\kappa p}\}) | \psi_{\boldsymbol{k}'n'} \rangle \, c^\dagger_{\boldsymbol{k}'n'} c_{\boldsymbol{k}n} \tag{5.3}$$

$$= \sum_{\boldsymbol{k}m\boldsymbol{q}n\kappa x} \langle \psi_{\boldsymbol{k}+\boldsymbol{q}m} | \frac{\partial V_{\text{SCF}}}{\partial u_{\boldsymbol{q}\kappa x}} | \psi_{\boldsymbol{k}n} \rangle \, u_{\boldsymbol{q}\kappa x} \, c^\dagger_{\boldsymbol{k}+\boldsymbol{q}m} c_{\boldsymbol{k}n} \tag{5.4}$$

$$= \boldsymbol{u} \sum_{\boldsymbol{q}\boldsymbol{k}mn} \boldsymbol{d}_{\boldsymbol{q}\boldsymbol{k}mn} c^\dagger_{\boldsymbol{k}+\boldsymbol{q}m} c_{\boldsymbol{k}n}. \tag{5.5}$$

In the case of the downfolded lattice models, the electron-phonon coupling is mapped onto a supercell. For displacements with the supercell periodicity, one can set $\boldsymbol{q} = 0$ in Eq. (5.5), which brings the coupling term into the same form as the undistorted tight-binding Hamiltonian from Eq. (3.21). Adding both terms together yields

$$H_{\text{el}} + H_{\text{el-n}} = \sum_{\boldsymbol{k}mn} \left(t_{mn}(\boldsymbol{k}) + \boldsymbol{u}\boldsymbol{d}_{mn}(\boldsymbol{k}) \right) c^\dagger_{\boldsymbol{k}m} c_{\boldsymbol{k}n}, \tag{5.6}$$

where $\boldsymbol{u} \cdot \boldsymbol{d}_{mn}$ can be viewed as a displacement-induced deformation potential. Thus, similar to the SSH model (see Ch. 11), the atomic displacements couple linearly to the electronic degrees of freedom and directly induce changes in the electronic structure. Interestingly, even though the coupling is linear on the level of the Hamiltonian, the resulting electronic eigenvalues response non-linearly to atomic displacements. This non-linearity arises from the inherent nature of the eigenvalue problem, which is fundamentally non-linear. Consequently, the Born-Oppenheimer potential energy surfaces resulting from this non-interacting Hamiltonian can exhibit strong anharmonic behavior. This can be seen in the third publication of this dissertation (see Ch. 13), where the non-interacting model is referred to as model III.

In other approaches, e.g. the Peierls model (see Sec. 10.2), the coupling term is expressed with the help of normal phonon coordinates. The coordinates transform the real cartesian displacement of an atom into a collective displacement of a phonon wave. Consequently, there is an alternative formulation of the coupling term

$$H_{\text{el-n}} = N_p^{-1/2} \sum_{\boldsymbol{k},\boldsymbol{q}mn\nu} g_{\boldsymbol{q}\nu\boldsymbol{k}mn} \, c^\dagger_{\boldsymbol{k}+\boldsymbol{q}m} c_{\boldsymbol{k}n} (a_{\boldsymbol{q}\nu} + a^\dagger_{-\boldsymbol{q}\nu}) \tag{5.7}$$

with

$$g_{\boldsymbol{q}\nu\boldsymbol{k}mn} = \frac{1}{\sqrt{2\omega_{\boldsymbol{q}\nu}}} \sum_i e_{\boldsymbol{q}i\nu} \frac{1}{\sqrt{M_i}} \langle \psi_{\boldsymbol{k}+\boldsymbol{q}m} | \frac{\partial V_{\text{SCF}}}{\partial u_{\boldsymbol{q}i}} | \psi_{\boldsymbol{k}n} \rangle, \tag{5.8}$$

where the indices κ and x have been combined to the index $i = (x, \kappa)$[1].

5.2. Wannier representation

The use of the Wannier representation offers several advantages when studying electron-phonon interactions. Apart from its computational efficiency, the Wannier representation serves as an excellent analytical tool for investigating electron-phonon interactions using simplified tight-binding models (for electrons) and force-constant models (for phonons) [86].

[1]The combined index $i = (x, \kappa)$ labels the Cartesian direction x of the displacement and the atom in the unit cell κ.

The downfoled lattice models, developed in this dissertation, will be written in the localized Wannier basis and atomic displacements. Hence, the transform between the delocalized Bloch basis and the localized Wannier basis will be shown here,

$$d_{\boldsymbol{R}i\boldsymbol{R}'\alpha\beta} = \frac{1}{NN'} \sum_{\boldsymbol{q}\nu\boldsymbol{k}mn} e^*_{\boldsymbol{q}i\nu} U_{\boldsymbol{k}+\boldsymbol{q}\alpha m} d_{\boldsymbol{q}\nu\boldsymbol{k}mn} U^*_{\boldsymbol{k}\beta n} e^{-i(\boldsymbol{q}\boldsymbol{R}+\boldsymbol{k}\boldsymbol{R}')} \tag{5.9}$$

with the matrix elements,

$$d_{\boldsymbol{R}i\boldsymbol{R}'\alpha\beta} = \langle \alpha\boldsymbol{0} | \partial_{i,\boldsymbol{R}} V | \beta\boldsymbol{R}' \rangle. \tag{5.10}$$

These matrix elements are written in real space with localized Wannier orbitals. They are the electron-phonon equivalent to the tight-binding hopping matrix elements from Eq. (3.19). The physical interpretation of these objects is the following: They describe the *first order change* of the hopping process from the orbital α (located at the home cell $\boldsymbol{0}$) to the orbital β (located at the unit cell $\boldsymbol{R}'$) under the influence of the displacement i in the unit cell $\boldsymbol{R}$.

For completeness, the back-transform will be given

$$d_{\boldsymbol{q}\nu\boldsymbol{k}mn} = \sum_{\boldsymbol{R}i\boldsymbol{R}'\alpha\beta} e_{\boldsymbol{q}i\nu} U^*_{\boldsymbol{k}+\boldsymbol{q}\alpha m} d_{\boldsymbol{R}i\boldsymbol{R}'\alpha\beta} U_{\boldsymbol{k}\beta n} e^{i(\boldsymbol{q}\boldsymbol{R}+\boldsymbol{k}\boldsymbol{R}')}. \tag{5.11}$$

To give an insight into the technical aspects: both transforms (Eqs. 5.9 and 5.11) are part of the EPW software, which was used to generate the electron-phonon coupling matrix elements from first-principles. However, for the downfolded lattice models, only the first transform is carried out using EPW. The resultant matrix elements $d_{\boldsymbol{R}i\boldsymbol{R}'\alpha\beta}$ are extracted and subsequently mapped onto a supercell to build the tight-binding lattice model. The second part is carried out using the `elphmod` code.

6

Electron-electron interaction

The final ingredient of the downfolded lattice models are explicit electron-electron interactions happening within the low-energy model subspace. Implicitely, the Hartree and exchange-correlation interactions are taken into account by the undistorted eigenenergies, the force-constants and electron-phonon interactions from the high-energy electronic degrees of freedom. This is shown in the prior sections discussing downfolding techniques like cDFPT or unscreening, where virtual electronic excitations confined within the model subspace are deliberately excluded from the partially screened variables. Thus, the initial model is "bare" within the low-energy subspace. Nevertheless, it is imperative to incorporate these interactions since they carry the low-energy physics.

In an ideal scenario, one would seek to fully recover the *ab initio* solution from DFT — even when atoms are displaced away from their high-symmetry positions. Nonetheless, in the anharmonic terms, approximations come into play due to the perturbative approach with the *linear* electron-phonon coupling. Additionally, the treatment of the electron-electron interactions involves the *Hartree approximation* (Sec. 6.2), which is the simplest way of including the Coulomb interaction of the model subspace. Furthermore, the *ab intio* generated Coulomb matrix elements on the level of the *contrained random phase approximation* (Sec. 6.3.1) will be truncated to *density-density* type of interactions.

This chapter on explicit electron-electron interactions concerns the so-called models I and II of Chapter 13. Please note that the effectively non-interacting model III only involves the implicit Coulomb interactions carried by the fully screened electron-phonon coupling.

6.1. Wannier representation

This section is inspired by Chapter 2.3.3 of Ref. [87].

The general form of a Coulomb matrix element in reciprocal space is

$$U^{\boldsymbol{k}\boldsymbol{k}'\boldsymbol{q}}_{\alpha\beta\gamma\delta} = \int d^3\boldsymbol{r} \int d^3\boldsymbol{r}' \phi^*_{\alpha\boldsymbol{k}-\boldsymbol{q}}(\boldsymbol{r})\phi^*_{\beta\boldsymbol{k}'+\boldsymbol{q}}(\boldsymbol{r}')U(\boldsymbol{r},\boldsymbol{r}',\omega)\phi_{\gamma\boldsymbol{k}'}(\boldsymbol{r}')\phi_{\delta\boldsymbol{k}}(\boldsymbol{r}), \tag{6.1}$$

where the Bloch functions

$$\phi^*_{\alpha\boldsymbol{k}}(\boldsymbol{r}) = \sum_{\boldsymbol{R}} e^{i\boldsymbol{k}\boldsymbol{R}} w_{\alpha\boldsymbol{R}}(\boldsymbol{r}) \tag{6.2}$$

are defined using Wannier functions $w_{\alpha \boldsymbol{R}}(\boldsymbol{r})$ with the orbital character α located in the unit cell around $\boldsymbol{R}$. Inserting the Bloch functions into the Coulomb matrix elements from Eq. (6.1), yields

$$U^{\boldsymbol{k}\boldsymbol{k}'\boldsymbol{q}}_{\alpha\beta\gamma\delta} = \int d^3\boldsymbol{r} \int d^3\boldsymbol{r}' U(\boldsymbol{r},\boldsymbol{r}',\omega) \sum_{\boldsymbol{R}_1\boldsymbol{R}_4} w^*_{\alpha\boldsymbol{R}_1}(\boldsymbol{r}) w_{\delta\boldsymbol{R}_4}(\boldsymbol{r}) e^{i(\boldsymbol{R}_4-\boldsymbol{R}_1)\boldsymbol{k}} e^{i\boldsymbol{R}_1\boldsymbol{q}} \tag{6.3}$$

$$\sum_{\boldsymbol{R}_2\boldsymbol{R}_3} w^*_{\beta\boldsymbol{R}_2}(\boldsymbol{r}') w_{\gamma\boldsymbol{R}_3}(\boldsymbol{r}') e^{i(\boldsymbol{R}_3-\boldsymbol{R}_2)\boldsymbol{k}'} e^{-i\boldsymbol{R}_2\boldsymbol{q}}. \tag{6.4}$$

By assuming that the Wannier functions are *strongly localized*, the $\boldsymbol{k}$- and $\boldsymbol{k}'$-dependencies can be eliminated in

$$U^{\boldsymbol{q}}_{\alpha\beta\gamma\delta} = \sum_{\boldsymbol{R}} \int d^3\boldsymbol{r} \int d^3\boldsymbol{r}' U(\boldsymbol{r},\boldsymbol{r}',\omega) w^*_{\alpha\boldsymbol{0}}(\boldsymbol{r}) w_{\delta\boldsymbol{0}}(\boldsymbol{r}) w^*_{\beta\boldsymbol{R}}(\boldsymbol{r}') w_{\gamma\boldsymbol{R}}(\boldsymbol{r}') e^{i\boldsymbol{R}\boldsymbol{q}}. \tag{6.5}$$

Furthermore, the largest Coulomb matrix elements are assumed to be the so-called *density-density* matrix elements, where $\alpha = \delta$ and $\beta = \gamma$, which leads to

$$U^{\boldsymbol{q}}_{\alpha\beta\beta\alpha} = \sum_{\boldsymbol{R}} \int d^3\boldsymbol{r} \int d^3\boldsymbol{r}' U(\boldsymbol{r},\boldsymbol{r}',\omega) |w_{\alpha\boldsymbol{0}}(\boldsymbol{r})|^2 |w_{\beta\boldsymbol{R}}(\boldsymbol{r}')|^2 e^{i\boldsymbol{R}\boldsymbol{q}} \tag{6.6}$$

$$= \sum_{\boldsymbol{R}} U^{\boldsymbol{R}}_{\alpha\beta\beta\alpha} e^{i\boldsymbol{R}\boldsymbol{q}}. \tag{6.7}$$

6.1.1. Example: Coulomb matrix elements for two-dimensional monolayer TaS_2

For the downfolded models, $\boldsymbol{Q}$-dependent Coulomb matrix elements are needed, which live in the Brillouin zone of the $N \times N$ supercell. Given for this task are the Coulomb matrix elements on the unit cell, where $\boldsymbol{q}$ lives on the Brillouin zone of the unit cell.

At first, the Coulomb matrix elements in real space are obtained by a Fourier transform

$$U_{\alpha\beta}(\boldsymbol{R}) = \frac{V_{\mathrm{EZ}}}{(2\pi)^2} \int d^2\boldsymbol{q}\, U_{\alpha\beta}(\boldsymbol{q}) e^{-i\boldsymbol{q}\boldsymbol{R}} = \frac{1}{N_{\boldsymbol{q}}^2} \sum_{\boldsymbol{q}} U_{\alpha\beta}(\boldsymbol{q}) e^{-i\boldsymbol{q}\boldsymbol{R}}. \tag{6.8}$$

The $\boldsymbol{q}$ sum runs over a uniform two-dimensional grid of the size $N_q \times N_q \times 1$. Note that all $\boldsymbol{q}$ points must be in the first Brillouin zone of the primitive Bravais lattice. For instance, a grid of $N_q = 24$ $\boldsymbol{q}$-points per axis corresponds to $24 \times 24 \times 1$ primitive unit cells in real space. For the sake of clarity, the inverse Fourier-transform is given by Eq. (6.7).

However, a transformation back to the original matrix elements $U_{\alpha\beta}(\boldsymbol{q})$ is not desired. Instead, in the case of 1H-TaS_2, matrix elements for a 3×3 supercell shall be constructed. Since there are three orbitals per unit cell $\alpha, \beta \in \{d_{z^2}, d_{xy}, d_{x^2-y^2}\}$ and 9 unit cells, 27 matrix elements in total need to be determined. These matrix elements can be calculated as matrix blocks

$$\underline{\underline{U}}_{nm}(\boldsymbol{Q}) = \sum_{\tilde{\boldsymbol{R}}} \underline{\underline{U}}(\boldsymbol{r}_{nm} + \tilde{\boldsymbol{R}}) e^{-i\boldsymbol{Q}\tilde{\boldsymbol{R}}} \tag{6.9}$$

where $\underline{\underline{U}}(\boldsymbol{r}_{nm} + \tilde{\boldsymbol{R}})$ is a 3×3 matrix, which captures all the orbital dependencies. Note that $\tilde{\boldsymbol{R}}$ is now the Bravais lattice vector of the supercell. The result $\underline{\underline{U}}_{nm}(\boldsymbol{Q})$ still carries the indices n, m, which indicate the unit cells within the supercell (see Fig. 6.1). Finally, the full matrix reads

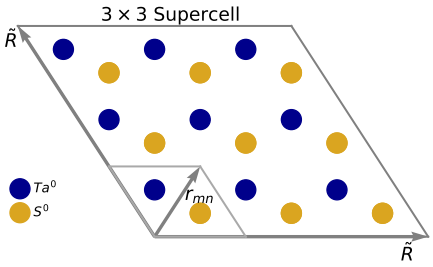

Figure 6.1: Sketch of the 3×3 supercell of 1H-TaS_2 to illustrate the internal lattice vector $\boldsymbol{r}_{mn}$

$$U(\boldsymbol{Q}) = \begin{pmatrix} \underline{\underline{U}}_{11}(\boldsymbol{Q}) & \dots & \underline{\underline{U}}_{19}(\boldsymbol{Q}) \\ \vdots & \ddots & \vdots \\ \underline{\underline{U}}_{91}(\boldsymbol{Q}) & \dots & \underline{\underline{U}}_{99}(\boldsymbol{Q}) \end{pmatrix}. \tag{6.10}$$

By inserting the Fourier transform from Eq. (6.8) directly into Eq. (6.9), it is found that

$$\underline{\underline{U}}_{nm}(\boldsymbol{Q}) = \sum_{\tilde{\boldsymbol{R}}} \Big[\frac{V_{\mathrm{EZ}}}{(2\pi)^2} \int d^2\boldsymbol{q}\, \underline{\underline{U}}(\boldsymbol{q}) e^{i\boldsymbol{q}(\boldsymbol{r}_{nm}+\tilde{\boldsymbol{R}})} \Big] e^{-i\boldsymbol{Q}\tilde{\boldsymbol{R}}} \tag{6.11}$$

$$= \int d^2\boldsymbol{q}\, \underline{\underline{U}}(\boldsymbol{q}) e^{i\boldsymbol{q}\boldsymbol{r}_{nm}} \Big[\frac{V_{\mathrm{EZ}}}{(2\pi)^2} \sum_{\tilde{\boldsymbol{R}}} e^{i(\boldsymbol{q}-\boldsymbol{Q})\tilde{\boldsymbol{R}}} \Big]. \tag{6.12}$$

The last term in the bracket would be simply a delta distribution $\delta(\boldsymbol{q}-\boldsymbol{Q})$, if $\tilde{\boldsymbol{R}}$ would be the original primitive lattice vectors. However, since the supercell lattice vectors are being used, a sum over delta distributions is obtained:

$$\underline{\underline{U}}_{nm}(\boldsymbol{Q}) = \int d^2\boldsymbol{q}\, \underline{\underline{U}}(\boldsymbol{q}) e^{i\boldsymbol{q}\boldsymbol{r}_{nm}} \Big[\sum_{\boldsymbol{G}} \delta(\boldsymbol{q}-\boldsymbol{Q}+\boldsymbol{G}) \frac{V_{\mathrm{EZ}}}{V_{\mathrm{SZ}}} \Big] \tag{6.13}$$

$$= \frac{V_{\mathrm{EZ}}}{V_{\mathrm{SZ}}} \sum_{\boldsymbol{G}} \underline{\underline{U}}(\boldsymbol{Q}-\boldsymbol{G}) e^{i(\boldsymbol{Q}-\boldsymbol{G})\boldsymbol{r}_{nm}}. \tag{6.14}$$

6.1.2. Elimination of the $Q = 0$ divergence

The Coulomb matrix on the supercell (Eq. 6.10) has the size 27×27, which leads to 27 eigenvalues. One of these eigenvalues diverges at $\boldsymbol{Q} = 0$, which corresponds to a homogenous charging of the whole system. This eigenvalue will be eliminated by setting it to zero in the spectral representation.

For the spectral representation, the Coulomb matrix at $\boldsymbol{Q} = 0$ needs to be diagonalized:

$$U(\boldsymbol{Q}=0)|e_n\rangle = \nu_n |e_n\rangle. \tag{6.15}$$

Thus, the spectral representation can be calculated as

$$\tilde{U}(\boldsymbol{Q}=0) = \sum_{n\neq 0} \nu_n |e_n\rangle\langle e_n|. \tag{6.16}$$

where the diverging eigenvalue with index $n = 0$ has been excluded from the sum.

6.2. Hartree-Fock approximation

This section is inspired by Ref. [88].

Introducing Coulomb interactions in the simplest form can be done by using the Hartree-Fock approximation. Here, a non-interacting Hamiltonian H_0 and an interaction V_{int} are defined:

$$H = H_0 + V_{\text{int}}, \tag{6.17a}$$

$$H_0 = \sum_{\nu} \varepsilon_\nu c_\nu^\dagger c_\nu, \tag{6.17b}$$

$$V_{\text{int}} = \frac{1}{2} \sum_{\nu\nu',\mu\mu'} V_{\nu\mu,\nu'\mu'} c_\nu^\dagger c_\mu^\dagger c_{\mu'} c_{\nu'}. \tag{6.17c}$$

By using Wick's theorem, the four-term product can be factorized

$$c_\nu^\dagger c_\mu^\dagger c_{\mu'} c_{\nu'} \approx c_\nu^\dagger c_{\nu'} \langle c_\mu^\dagger c_{\mu'} \rangle_{\text{MF}} + c_\mu^\dagger c_{\mu'} \langle c_\nu^\dagger c_{\nu'} \rangle_{\text{MF}} \tag{6.18}$$

$$\pm c_\nu^\dagger c_{\mu'} \langle c_\mu^\dagger c_{\nu'} \rangle_{\text{MF}} \pm c_\mu^\dagger c_{\nu'} \langle c_\nu^\dagger c_{\mu'} \rangle_{\text{MF}} \tag{6.19}$$

$$-\langle c_\nu^\dagger c_{\nu'} \rangle_{\text{MF}} \langle c_\mu^\dagger c_{\mu'} \rangle_{\text{MF}} \mp \langle c_\nu^\dagger c_{\mu'} \rangle_{\text{MF}} \langle c_\mu^\dagger c_{\nu'} \rangle_{\text{MF}}, \tag{6.20}$$

where the lower (upper) signs hold for fermions (bosons) respectively. Inserting this expression into Eq. (6.17c) yields in the fermionic case:

$$V_{\text{int}}^{\text{Hartree}} = \frac{1}{2} \sum_{\nu\nu',\mu\mu'} V_{\nu\mu,\nu'\mu'} \bar{n}_{\mu\mu'} c_\nu^\dagger c_{\nu'} + \frac{1}{2} \sum_{\nu\nu',\mu\mu'} V_{\nu\mu,\nu'\mu'} \bar{n}_{\nu\nu'} c_\mu^\dagger c_{\mu'} - \frac{1}{2} \sum_{\nu\nu',\mu\mu'} V_{\nu\mu,\nu'\mu'} \bar{n}_{\nu\nu'} \bar{n}_{\mu\mu'} \tag{6.21}$$

and

$$V_{\text{int}}^{\text{Fock}} = -\frac{1}{2} \sum_{\nu\nu',\mu\mu'} V_{\nu\mu,\nu'\mu'} \bar{n}_{\nu\mu'} c_\mu^\dagger c_{\nu'} - \frac{1}{2} \sum_{\nu\nu',\mu\mu'} V_{\nu\mu,\nu'\mu'} \bar{n}_{\mu\nu'} c_\nu^\dagger c_{\mu'} + \frac{1}{2} \sum_{\nu\nu',\mu\mu'} V_{\nu\mu,\nu'\mu'} \bar{n}_{\nu\mu'} \bar{n}_{\mu\nu'}. \tag{6.22}$$

Thus, the final mean-field Hamiltonian within Hartree-Fock approximation reads

$$H^{\text{HF}} = H_0 + V_{\text{int}}^{\text{Hartree}} + V_{\text{int}}^{\text{Fock}}. \tag{6.23}$$

6.2.1. Applying the Hartree-Fock approximation

The interaction term is defined as (cf. Eq. 1.136 of Ref. [89])

$$V_{\text{int}} = \frac{1}{2} \sum_{klmn} V_{klmn} c_k^\dagger c_m^\dagger c_n c_l \tag{6.24}$$

with the matrix elements

$$V_{klmn} = \int d^3\boldsymbol{r} \int d^3\boldsymbol{r}' \phi_k^*(\boldsymbol{r}) \phi_m^*(\boldsymbol{r}') V(\boldsymbol{r}, \boldsymbol{r}') \phi_l(\boldsymbol{r}) \phi_n(\boldsymbol{r}'). \tag{6.25}$$

This means that the full interaction term corresponding to the matrix element from Eq. (6.1), can be written as

$$V_{\text{int}} = \frac{1}{2} \sum_{\alpha\beta\gamma\delta} \sum_{\boldsymbol{k},\boldsymbol{k'q}} U_{\alpha\beta\gamma\delta}^{\boldsymbol{k},\boldsymbol{k'q}} c_{\alpha\boldsymbol{k}-\boldsymbol{q}}^\dagger c_{\beta\boldsymbol{k'}+\boldsymbol{q}}^\dagger c_{\gamma\boldsymbol{k'}} c_{\delta\boldsymbol{k}}. \tag{6.26}$$

and the interaction term corresponding only to density-density matrix elements from Eq. (6.6), reads

$$V_{\text{int}} = \frac{1}{2}\sum_{\alpha\beta}\sum_{\boldsymbol{k},\boldsymbol{k}'\boldsymbol{q}} U^{\boldsymbol{q}}_{\alpha\beta\beta\alpha} c^\dagger_{\alpha\boldsymbol{k}-\boldsymbol{q}} c^\dagger_{\beta\boldsymbol{k}'+\boldsymbol{q}} c_{\beta\boldsymbol{k}'} c_{\alpha\boldsymbol{k}}. \tag{6.27}$$

Mapping this interaction to a supercell, means that the former orbital index is replaced by a combined index $\alpha \to \tilde{\alpha} = (n, \alpha)$, where n indicates the unit cell within the supercell. Applying this substitution yields

$$V_{\text{int}} = \frac{1}{2}\sum_{\tilde{\alpha}\tilde{\beta}}\sum_{\boldsymbol{k},\boldsymbol{k}'\boldsymbol{q}} \tilde{U}^{\boldsymbol{q}}_{\tilde{\alpha}\tilde{\beta}} c^\dagger_{\tilde{\alpha}\boldsymbol{k}-\boldsymbol{q}} c^\dagger_{\tilde{\beta}\boldsymbol{k}'+\boldsymbol{q}} c_{\tilde{\beta}\boldsymbol{k}'} c_{\tilde{\alpha}\boldsymbol{k}}, \tag{6.28}$$

where the matrix element is taken from Eq. (6.16).
All preparations have been made to apply the Hartree-Fock decoupling to the interaction term. Again, Wick's theorem will be used:

$$c^\dagger_{\tilde{\alpha}\boldsymbol{k}-\boldsymbol{q}} c^\dagger_{\tilde{\beta}\boldsymbol{k}'+\boldsymbol{q}} c_{\tilde{\beta}\boldsymbol{k}'} c_{\tilde{\alpha}\boldsymbol{k}} \approx c^\dagger_{\tilde{\alpha}\boldsymbol{k}-\boldsymbol{q}} c_{\tilde{\alpha}\boldsymbol{k}} \langle c^\dagger_{\tilde{\beta}\boldsymbol{k}'+\boldsymbol{q}} c_{\tilde{\beta}\boldsymbol{k}'}\rangle_{\text{MF}} + c^\dagger_{\tilde{\beta}\boldsymbol{k}'+\boldsymbol{q}} c_{\tilde{\beta}\boldsymbol{k}'} \langle b^\dagger_{\tilde{\alpha}\boldsymbol{k}-\boldsymbol{q}} c_{\tilde{\alpha}\boldsymbol{k}}\rangle_{\text{MF}} \tag{6.29}$$

$$\pm c^\dagger_{\tilde{\alpha}\boldsymbol{k}-\boldsymbol{q}} c_{\tilde{\beta}\boldsymbol{k}'} \langle c^\dagger_{\tilde{\beta}\boldsymbol{k}'+\boldsymbol{q}} c_{\tilde{\alpha}\boldsymbol{k}}\rangle_{\text{MF}} \pm c^\dagger_{\tilde{\beta}\boldsymbol{k}'+\boldsymbol{q}} c_{\tilde{\alpha}\boldsymbol{k}} \langle c^\dagger_{\tilde{\alpha}\boldsymbol{k}-\boldsymbol{q}} c_{\tilde{\beta}\boldsymbol{k}'}\rangle_{\text{MF}} \tag{6.30}$$

$$-\langle c^\dagger_{\tilde{\alpha}\boldsymbol{k}-\boldsymbol{q}} c_{\tilde{\alpha}\boldsymbol{k}}\rangle_{\text{MF}} \langle c^\dagger_{\tilde{\beta}\boldsymbol{k}'+\boldsymbol{q}} c_{\tilde{\beta}\boldsymbol{k}'}\rangle_{\text{MF}} \mp \langle c^\dagger_{\tilde{\alpha}\boldsymbol{k}-\boldsymbol{q}} c_{\tilde{\beta}\boldsymbol{k}'}\rangle_{\text{MF}} \langle c^\dagger_{\tilde{\beta}\boldsymbol{k}'+\boldsymbol{q}} c_{\tilde{\alpha}\boldsymbol{k}}\rangle_{\text{MF}}. \tag{6.31}$$

Accordingly, the Hartree term will be

$$\begin{aligned} V^{\text{Hartree}}_{\text{int}} = \frac{1}{2}\sum_{\tilde{\alpha}\tilde{\beta}}\sum_{\boldsymbol{k},\boldsymbol{k}'\boldsymbol{q}} \tilde{U}^{\boldsymbol{q}}_{\tilde{\alpha}\tilde{\beta}} c^\dagger_{\tilde{\alpha}\boldsymbol{k}-\boldsymbol{q}} c_{\tilde{\alpha}\boldsymbol{k}} \langle c^\dagger_{\tilde{\beta}\boldsymbol{k}'+\boldsymbol{q}} c_{\tilde{\beta}\boldsymbol{k}'}\rangle_{\text{MF}} + \frac{1}{2}\sum_{\tilde{\alpha}\tilde{\beta}}\sum_{\boldsymbol{k},\boldsymbol{k}'\boldsymbol{q}} \tilde{U}^{\boldsymbol{q}}_{\tilde{\alpha}\tilde{\beta}} c^\dagger_{\tilde{\beta}\boldsymbol{k}'+\boldsymbol{q}} c_{\tilde{\beta}\boldsymbol{k}'} \langle c^\dagger_{\tilde{\alpha}\boldsymbol{k}-\boldsymbol{q}} c_{\tilde{\alpha}\boldsymbol{k}}\rangle_{\text{MF}} \\ - \frac{1}{2}\sum_{\tilde{\alpha}\tilde{\beta}}\sum_{\boldsymbol{k},\boldsymbol{k}'\boldsymbol{q}} \tilde{U}^{\boldsymbol{q}}_{\tilde{\alpha}\tilde{\beta}} \langle c^\dagger_{\tilde{\alpha}\boldsymbol{k}-\boldsymbol{q}} c_{\tilde{\alpha}\boldsymbol{k}}\rangle_{\text{MF}} \langle c^\dagger_{\tilde{\beta}\boldsymbol{k}'+\boldsymbol{q}} c_{\tilde{\beta}\boldsymbol{k}'}\rangle_{\text{MF}}. \end{aligned} \tag{6.32}$$

Note, that all expectation values in the Hartree term are of the form $\langle c^\dagger_{\alpha\boldsymbol{k}\pm\boldsymbol{q}} c_{\alpha\boldsymbol{k}}\rangle_{\text{MF}}$, which can be rewritten to

$$\langle c^\dagger_{\alpha\boldsymbol{k}\pm\boldsymbol{q}} c_{\alpha\boldsymbol{k}}\rangle_{\text{MF}} = \langle c^\dagger_{\alpha\boldsymbol{k}} c_{\alpha\boldsymbol{k}}\rangle_{\text{MF}} \delta_{\boldsymbol{q},0}. \tag{6.33}$$

This is due to the fact that the $|\alpha\boldsymbol{k}\rangle$ states are orthogonal to each other. Next, by observing that there is no mixture between $\boldsymbol{k}$ and $\boldsymbol{k}'$ momenta in the expectation values, one $\boldsymbol{k}$-sum in each term can be evalauted. This leads to

$$\sum_{\boldsymbol{k}} \langle c^\dagger_{\alpha\boldsymbol{k}} c_{\alpha\boldsymbol{k}}\rangle_{\text{MF}} = n_\alpha = \langle c^\dagger_\alpha c_\alpha\rangle_{\text{MF}}, \tag{6.34}$$

which is the occupation of the orbital α (see App. A.2). Using both Eq. (6.33) and Eq. (6.34) in Eq. (6.32), yields

$$V^{\text{Hartree}}_{\text{int}} = \frac{1}{2}\sum_{\tilde{\alpha}\tilde{\beta}}\sum_{\boldsymbol{k}} \tilde{U}^{\boldsymbol{q}=0}_{\tilde{\alpha}\tilde{\beta}} c^\dagger_{\tilde{\alpha}\boldsymbol{k}} c_{\tilde{\alpha}\boldsymbol{k}} n_{\tilde{\beta}} + \frac{1}{2}\sum_{\tilde{\alpha}\tilde{\beta}}\sum_{\boldsymbol{k}'} \tilde{U}^{\boldsymbol{q}=0}_{\tilde{\alpha}\tilde{\beta}} c^\dagger_{\tilde{\beta}\boldsymbol{k}'} c_{\tilde{\beta}\boldsymbol{k}'} n_{\tilde{\alpha}} - \frac{1}{2}\sum_{\tilde{\alpha}\tilde{\beta}} \tilde{U}^{\boldsymbol{q}=0}_{\tilde{\alpha}\tilde{\beta}} n_{\tilde{\alpha}} n_{\tilde{\beta}}. \tag{6.35}$$

By renaming $\tilde{\alpha}, \tilde{\beta}, \boldsymbol{k}'$ to $\tilde{\beta}, \tilde{\alpha}, \boldsymbol{k}$ in the second summand, the first and second summand can be added together, which will lead to the real part of the Coulomb matrix element $\Re(\tilde{U}^{\boldsymbol{q}=0}_{\tilde{\alpha}\tilde{\beta}})$:

$$V^{\text{Hartree}}_{\text{int}} = \frac{1}{2}\sum_{\tilde{\alpha}\tilde{\beta}}\sum_{\boldsymbol{k}} \tilde{U}^{\boldsymbol{q}=0}_{\tilde{\alpha}\tilde{\beta}} c^\dagger_{\tilde{\alpha}\boldsymbol{k}} c_{\tilde{\alpha}\boldsymbol{k}} n_{\tilde{\beta}} + \frac{1}{2}\sum_{\tilde{\alpha}\tilde{\beta}}\sum_{\boldsymbol{k}'} \tilde{U}^{\boldsymbol{q}=0}_{\tilde{\beta}\tilde{\alpha}} c^\dagger_{\tilde{\alpha}\boldsymbol{k}'} c_{\tilde{\alpha}\boldsymbol{k}'} n_{\tilde{\beta}} - \frac{1}{2}\sum_{\tilde{\alpha}\tilde{\beta}} \tilde{U}^{\boldsymbol{q}=0}_{\tilde{\alpha}\tilde{\beta}} n_{\tilde{\alpha}} n_{\tilde{\beta}} \tag{6.36}$$

$$= \sum_{\tilde{\alpha}\tilde{\beta}}\sum_{\boldsymbol{k}} \frac{1}{2}(\tilde{U}^{\boldsymbol{q}=0}_{\tilde{\alpha}\tilde{\beta}} + \tilde{U}^{\boldsymbol{q}=0}_{\tilde{\beta}\tilde{\alpha}}) c^\dagger_{\tilde{\alpha}\boldsymbol{k}} c_{\tilde{\alpha}\boldsymbol{k}} n_{\tilde{\beta}} - \frac{1}{2}\sum_{\tilde{\alpha}\tilde{\beta}} \tilde{U}^{\boldsymbol{q}=0}_{\tilde{\alpha}\tilde{\beta}} n_{\tilde{\alpha}} n_{\tilde{\beta}} \tag{6.37}$$

$$= \sum_{\tilde{\alpha}\tilde{\beta}}\sum_{\boldsymbol{k}} \Re(\tilde{U}^{\boldsymbol{q}=0}_{\tilde{\alpha}\tilde{\beta}}) c^\dagger_{\tilde{\alpha}\boldsymbol{k}} c_{\tilde{\alpha}\boldsymbol{k}} n_{\tilde{\beta}} - \frac{1}{2}\sum_{\tilde{\alpha}\tilde{\beta}} \tilde{U}^{\boldsymbol{q}=0}_{\tilde{\alpha}\tilde{\beta}} n_{\tilde{\alpha}} n_{\tilde{\beta}}. \tag{6.38}$$

Finally, the $\tilde{\beta}$ sum in the first term can be defined as $\sum_{\tilde{\beta}} \Re(\tilde{U}^{\boldsymbol{q}=0}_{\tilde{\alpha}\tilde{\beta}}) n_{\tilde{\beta}} =: \overline{U}_{\tilde{\alpha}}$:

$$V^{\text{Hartree}}_{\text{int}} = \sum_{\tilde{\alpha}}\sum_{\boldsymbol{k}} \overline{U}_{\tilde{\alpha}} c^\dagger_{\tilde{\alpha}\boldsymbol{k}} c_{\tilde{\alpha}\boldsymbol{k}} - \frac{1}{2}\sum_{\tilde{\alpha}\tilde{\beta}} \tilde{U}^{\boldsymbol{q}=0}_{\tilde{\alpha}\tilde{\beta}} n_{\tilde{\alpha}} n_{\tilde{\beta}} \tag{6.39}$$

$$= \sum_{\tilde{\alpha}\tilde{\beta}}\sum_{\boldsymbol{k}} \overline{U}_{\tilde{\alpha}} \delta_{\tilde{\alpha}\tilde{\beta}} c^\dagger_{\tilde{\alpha}\boldsymbol{k}} c_{\tilde{\beta}\boldsymbol{k}} - \frac{1}{2}\sum_{\tilde{\alpha}\tilde{\beta}} \tilde{U}^{\boldsymbol{q}=0}_{\tilde{\alpha}\tilde{\beta}} n_{\tilde{\alpha}} n_{\tilde{\beta}}. \tag{6.40}$$

The last equation shows that the Hartree term is diagonal in the orbital basis. In the matrix representation, this diagonal matrix is simply added to the previous non-interacting Hamiltonian.

6.3. Random phase approximation

The following (sub)sections on the (constrained) random-phase approximation are based on Refs. [40, 90, 91].

The random phase approximation (RPA) is a key concept in many-body physics, first developed to describe the properties in the jellium, where electrons interact in a background of uniform positive charge [92, 93]. The authors used a Hamiltonian formulation to separate the collective motion of electrons (plasma oscillations) from their individual motions, known as RPA. This formulation was later recognized as equivalent to an infinite summation of ring (or bubble) diagrams in diagrammatic many-body perturbation theory [94, 95]. In the DFT framework, RPA is considered a fifth-rung approximation to the exchange-correlation energy functional. This classification scheme, known as Jacob's ladder [67] of DFT, was already mentioned in Sec. 3.1.1. Lastly, it was recognized that RPA can be understood as the time-dependent Hartree approximation. The linear density response function calculated within RPA considers only the variation in the Hartree potential caused by a time-dependent perturbing field [96, 97].

For this dissertation, the summation of bubble diagrams, such as

$$\chi^0 = \tag{6.41}$$

is of particular interest. The polarization in RPA for a non-interacting system [98, 99], is given by

$$\chi^0(\boldsymbol{r}_1, \boldsymbol{r}_2) = \sum_{n}^{\text{occ}}\sum_{n'}^{\text{unocc}} \left[\frac{\psi_n(\boldsymbol{r_2})\psi^*_{n'}(\boldsymbol{r_2})\psi^*_n(\boldsymbol{r_1})\psi_{n'}(\boldsymbol{r_1})}{-(\varepsilon_{n'} - \varepsilon_n - i\delta)} - \frac{\psi_n(\boldsymbol{r_1})\psi^*_{n'}(\boldsymbol{r_1})\psi^*_n(\boldsymbol{r_2})\psi_{n'}(\boldsymbol{r_2})}{(\varepsilon_{n'} - \varepsilon_n - i\delta)} \right] \tag{6.42}$$

With the help of this polarization, the screened interaction W can be written in matrix form as (cf. Eq. 3.97 of Ref. [40])

$$W = v + v\chi^0 W \quad \text{or} \quad W = (1 - v\chi^0)^{-1} v, \tag{6.43}$$

where v is the bare Coulomb interaction. Similar to the renormalization of the force constants in Eq. (4.13), this equation describes the screening process from the bare to the fully screened quantity. In the next subsection, it will be shown how to divide this screening process into two steps.

6.3.1. Constrained random phase approximation

The purpose of the constrained random phase approximation is to obtain partially screened Coulomb interactions. These can be used to construct model Hamiltonians such as the downfolded lattice models discussed in this dissertation.

The idea is to divide the Hilbert space into a low-energy active subspace (also called target subspace or correlated subspace), in which the downfolded model is solved, and the rest subspace, which consists of high-energy states. Mathematically, this idea is realized by separating the summation in Eq. (6.42) in the following way:

$$\sum_{n}^{\text{occ}} \sum_{n'}^{\text{unocc}} \longrightarrow \underbrace{\sum_{t}^{\text{occ}} \sum_{t'}^{\text{unocc}}}_{t-\text{subspace}} + \underbrace{\sum_{r}^{\text{occ}} \sum_{r'}^{\text{unocc}} + \sum_{r}^{\text{occ}} \sum_{t'}^{\text{unocc}} + \sum_{t}^{\text{occ}} \sum_{r'}^{\text{unocc}}}_{r-\text{subspace}} \tag{6.44}$$

Thus, the virtual target-target excitations have been excluded from the polarization due to the imposed *constraint*. The resulting polarizations according to Eq. (6.44) are

$$\chi^0 = \chi^0_t + \chi^0_r. \tag{6.45}$$

Thus, according to the separation of the Hilbert space, the bare Coulomb interaction can be screened by the high-energy states (r subspace) only (cf. Eq. B1 and B2 of Ref. [80])

$$W^{(p)} = (1 - v\chi^0_r)^{-1} v, \tag{6.46}$$

which leads to the *partially* screened Coulomb interaction. For completeness, it is shown how to recover the fully screened Coulomb interaction:

$$W = (1 - W^{(p)}\chi^0_t)^{-1} W^{(p)} \tag{6.47}$$

Thus, in principle, one would have to screen the partially screened interaction within the active subpace. However, this renomalization effect is ideally imposed by solving the model within the correlated subspace.

7

Statistical mechanics

Density functional theory does not have access to the ensemble temperature of the *lattice* degrees of freedom, often earning it the colloquial label of a "T = 0" theory. Nevertheless, through the utilization of smearing functions and the inclusion of an entropy term, an *electronic* temperature can be incorporated into the framework. This extension is sometimes referred to as ensemble DFT as it makes simulations within the canonical ensemble possible [100]. In these simulations, the number of particles remains constant, although exceptions exist in chemical applications, where the grand canonical ensemble is applied [101].
In this chapter, the canonical ensemble (Sec. 7.1) is introduced and the significance of the free energy of non-interacting electrons (Sec. 7.2) is emphasized. This quantity holds a central role in this dissertation, as it is indispensable for the evaluation of Born-Oppenheimer potential energy surfaces in DFT and the associated downfolded models.

7.1. Canonical ensemble

The canonical ensemble is a statistical mechanics concept used to describe a system in thermal equilibrium with a heat reservoir at a fixed temperature, allowing for fluctuations in energy while maintaining constant temperature and number of particles. The partition function of this ensemble is given by

$$Z = \mathrm{Tr}\, e^{-\beta \hat{H}}, \tag{7.1}$$

where $\beta = 1/k_B T$.

Similar to the microcanonical ensemble, the partition function signifies the total count of accessible microscopic states. However, unlike the microcanonical ensemble, the canonical ensemble allows for energy exchange with the surroundings, and therefore, the Hamiltonian is not conserved. As a result of this energy exchange, the system follows the Boltzmann distribution, leading to variations in the number of accessible microscopic states [102].

In molecular dynamics simulations of the canonical ensemble, a heat reservoir is introduced to mimic the interaction between the system and its surroundings, allowing for energy exchange. The heat reservoir serves as an infinite heat bath, maintaining a constant temperature during the simulation.

7.2. Free energy of non-interacting fermions

For simplicity, the free energy of non-interacting fermions will be derived starting from the grand canonical partition function. In second quantization, the particle operator is given by $N = \sum_{n\boldsymbol{k}} c^\dagger_{n\boldsymbol{k}} c_{n\boldsymbol{k}}$ and the non-interacting Hamilton operator by $H = \sum_{n\boldsymbol{k}} \varepsilon_{n\boldsymbol{k}} c^\dagger_{n\boldsymbol{k}} c_{n\boldsymbol{k}}$. Thus, the grand canonical partition function becomes

$$Z_G = \operatorname{Tr} e^{\beta(H-\mu N)} = \prod_{n\boldsymbol{k}} \sum_{n_{n\boldsymbol{k}}} \left[e^{-\beta(\varepsilon_{n\boldsymbol{k}}-\mu) n_{n\boldsymbol{k}}} \right] = \prod_{n\boldsymbol{k}} \left[1 + e^{-\beta(\varepsilon_{n\boldsymbol{k}}-\mu)} \right], \tag{7.2}$$

where it was used that the occupation of a fermionic state can only be $n_{n\boldsymbol{k}} \in \{0, 1\}$. From the partition function, one can directly evaluate the grand canonical potential

$$\Omega(\mu, V, T) = -k_B T \ln Z_G = -k_B T \sum_{n\boldsymbol{k}} \ln \left[1 + e^{-\beta(\varepsilon_{n\boldsymbol{k}}-\mu)} \right]. \tag{7.3}$$

Important thermodynamic quantities can be obtained by derivations of the grand canonical potential and will be listed in the following. The particle number

$$\langle N \rangle = -\frac{\partial \Omega}{\partial \mu} = \sum_{n\boldsymbol{k}} f(\varepsilon_{n\boldsymbol{k}}) \tag{7.4}$$

and the internal energy

$$\langle E \rangle = \frac{\partial \Omega \beta}{\partial \beta} = \sum_{n\boldsymbol{k}} f(\varepsilon_{n\boldsymbol{k}}) \varepsilon_{n\boldsymbol{k}} \tag{7.5}$$

both depend on the Fermi-Dirac statistics

$$f(\varepsilon_{n\boldsymbol{k}}) = \frac{1}{e^{\beta(\varepsilon_{n\boldsymbol{k}}-\mu)} + 1}. \tag{7.6}$$

The entropy in the case of Fermi-Dirac smearing thus becomes (cf. Eq. 1.42 of Ref [100]):

$$S = -\frac{\partial \Omega}{\partial T} = -k_B \sum_{n\boldsymbol{k}} [f(\varepsilon_{n\boldsymbol{k}}) \ln f(\varepsilon_{n\boldsymbol{k}}) + (1 - f(\varepsilon_{n\boldsymbol{k}})) \ln(1 - f(\varepsilon_{n\boldsymbol{k}}))] \tag{7.7}$$

Finally, taken together Eqs. (7.3), (7.5) and (7.4), the *Helmholtz* free energy [103] is given by

$$F = \Omega + \mu N = E - TS. \tag{7.8}$$

All downfolded lattice models developed in this dissertation and DFT as well, are either non-interacting from the beginning or employ mean-field approximations. As such, the grand canonical potential for non-interacting fermions is applicable.

8

Molecular dynamics

Once the free energy and corresponding forces are available, obtained either through DFT or a downfolded lattice model, molecular dynamics (MD) simulations can be conducted. MD simulations open up a new realm of physics that was previously beyond the reach of static DFT calculations. Notably, MD simulations allow to utilize the ensemble temperature, granting access to thermodynamic properties like transition temperatures in phase transitions. Furthermore, dynamic properties, such as temperature-dependent phonon dispersions, can be extracted through MD simulations. Both categories of properties can be investigated either using classical physics or extended through path integral MD (PIMD - Sec. 8.2), which incorporates quantum mechanical effects.

In the third publication of this dissertation (see Ch. 13), classical and path integral replica exchange MD simulations are performed using downfolded lattice model III. This approach is now referred to as *downfolding-based molecular dynamics*. Consequently, this chapter will provide an introduction to the fundamentals of MD simulations.

8.1. Born-Oppenheimer molecular dynamics

The Born-Oppenheimer molecular dynamics (BOMD) scheme is a variant of molecular dynamics. It assumes, in accordance with Sec. 2.1, that the motion of atomic nuclei and electrons can be separated, allowing the nuclei to move on potential energy surfaces generated by fixed electron distributions. This approach enables efficient simulations of complex molecular systems by treating electrons as a static background during the simulation of nuclear dynamics.

The potential energy surfaces in the BOMD scheme are typically generated from DFT [104, 105] or tight-binding schemes, which provide representations of the electronic structure and interactions within the system.

Depending on the chosen scheme, the total energy E has to be minimized (iteratively) w.r.t. the electronic wave functions ψ_i in each time step of the simulation. This ensures that the electronic wave function ψ_i resides on the Born-Oppenheimer potential energy surface, which leads to the following equation of motion:

$$M_I \ddot{R}_I = -\nabla_I \min_{\{\psi_i\}} E\Big[\{\psi_i\}; \{\boldsymbol{R}_I\}\Big], \tag{8.1}$$

where the nuclear masses M_I and their coordinates $\boldsymbol{R}_I$ enter as parameters.

The minimization of the total energy reduces the computational speed. Typically, the self-consistency cycle in DFT requires around 10–100 interations. With a non-interacting approach,

the self-consistency loop can be circumvented, leading to a computational speedup (see Benchmark of model III in Ch. 13).

Moreover, there exists Car-Parrinello Molecular Dynamics (CPMD) [106], where the conventional minimization step is omitted and replaced by fictitious dynamics of electrons, leading to a considerable speedup in computation time. Consequently, in CPMD, the electrons are not inherently in the true ground state. However, the evolution becomes adiabatic, with electrons adapting to the instantaneous state of the nuclei, if the electron dynamics are significantly faster than the nuclear dynamics. Initiating from the Kohn-Sham ground state at time $t = 0$, the system evolves with the electrons consistently "wandering" around the instantaneous ground state under the condition of sufficiently fast electron dynamics.

A challenge arises when the electron frequency fails to meet the specified condition. If the dynamics of the electrons are not adequately fast, indicating that the fictitious mass is not sufficiently small, an electron drag on the dynamics of the nuclei perturbs the accurate Born-Oppenheimer dynamics. This dichotomy between CPMD vs. BOMD can be reconciled through a hybrid approach [107] that ensures the system remains consistently close to the electronic ground state.

Additional molecular dynamics methods, such as Ehrenfest Molecular Dynamics (Ehrenfest-MD), offer alternative approaches. Unlike traditional methods, Ehrenfest-MD does not rely on the Born-Oppenheimer approximation. Instead, it explicitly addresses the time-dependence of both electronic wave functions and nuclei simultaneously. In this method, the dynamic interplay between electrons and nuclei is considered in a more direct and explicit manner, departing from the conventional Born-Oppenheimer separation of electronic and nuclear motion.

Going beyond the Born-Oppenheimer approximation is beyond the scope of this dissertation. Although the explicit dynamics of the electronic wave function in connection with downfolding models should be explored in the future.

8.1.1. Integrating the equations of motion: Velocity-verlet algorithm

In this section, the Velocity Verlet algorithm [108] will be demonstrated, which is a widely-used numerical integration method in molecular dynamics simulations. Before going into details, it should be noted that equations of motion can be too complex or intractable, making numerical approaches like Velocity Verlet essential for approximating solutions. The algorithm belongs to the symplectic integrators, which means that the structure of the Hamiltonian is preserved.

It employs a Taylor series expansion alongside position and velocity updates for time advancement up to second order in Δt:

$$\boldsymbol{r}_i(t + \Delta t) \approx \boldsymbol{r}_i(t) + \Delta t \boldsymbol{v}_i(t) + \frac{\Delta t^2}{2m_i} \boldsymbol{F}_i(t), \tag{8.2}$$

$$\boldsymbol{v}_i(t + \Delta t) = \boldsymbol{v}_i(t) + \frac{\Delta t}{2m_i} [\boldsymbol{F}_i + \boldsymbol{F}_i(t + \Delta t)]. \tag{8.3}$$

8.2. Path integral molecular dynamics

This section is inspired by Ref. [102].

Path integral molecular dynamics (PIMD) is a powerful simulation technique to investigate quantum mechanical effects in solid state systems. By treating particles as quantum-mechanical objects rather

than classical particles, PIMD offers a more accurate description of nuclear quantum effects, such as zero-point energy, tunneling, and quantum statistics. This scheme becomes essential when studying systems with light atoms, low temperatures, and strong quantum behavior, where classical molecular dynamics fails to capture the intricacies of quantum effects [109].

The development of the path integral molecular dynamics equations can be viewed as a byproduct in the search for an expression of the amplitude A of detecting a particle, initially prepared in the eigenstate $|x\rangle$, after a time t at a point x'. The particle evolves under the action of the time evolution operator, which can be written as a matrix element in the position space

$$A \equiv U(x, x'; t) = \langle x'|e^{-i\hat{H}t/\hbar}|x\rangle. \tag{8.4}$$

Interestingly, by applying the Wick rotation [110], this expression is equivalent to evaluating the canonical density matrix at an imaginary time $t = -i\beta\hbar$

$$\rho(x, x'; \beta) = \langle x'|e^{-\beta\hat{H}}|x\rangle. \tag{8.5}$$

For a Hamiltonian $\hat{H} = \hat{T} + \hat{V}$, whose summands do not commute, it is a standard procedure to exploit the Trooter theorem [111], which states that

$$e^{-\beta(\hat{T}+\hat{V})} = \lim_{P\to\infty}\left[e^{-\beta\hat{V}/2P}e^{-\beta\hat{T}/P}e^{-\beta\hat{V}/2P}\right]^P. \tag{8.6}$$

Inserting Eq. (8.6) into Eq. (8.5) and additionally inserting $(P-1)$ identity operators $\hat{1} = \int dx|x\rangle\langle x|$ between the P products, yields the following terms

$$\langle x_{k+1}|e^{-\beta\hat{V}/2P}e^{-\beta\hat{T}/P}e^{-\beta\hat{V}/2P}|x_k\rangle \tag{8.7}$$

$$= e^{-\beta V(x_{k+1})/2P}\langle x_{k+1}|e^{-\beta\hat{T}/P}|x_k\rangle e^{-\beta V(x_k)/2P}. \tag{8.8}$$

Thus, the exponental terms of the potential could be pulled out of the matrix element, since the states $|x\rangle$ are eigenvectors of $\hat{V} = V(x)$. Similarly, for the kinetic operator, the identity operator expressed in momentum eigenvectors will be inserted, yielding

$$\langle x_{k+1}|e^{-\beta\hat{T}/P}|x_k\rangle = \int dp\langle x_{k+1}|e^{-\beta\hat{T}/P}|p\rangle\langle p|x_k\rangle = \int dp\langle x_{k+1}|p\rangle\langle p|x_k\rangle e^{-\beta p^2/2mP} \tag{8.9}$$

Using $\langle x|p\rangle = 1/\sqrt{2\pi\hbar}\, e^{ipx/\hbar}$ and evaluating the momentum integral, yields the density matrix in the coordinate basis

$$\rho(x, x'; \beta) = \lim_{P\to\infty}\left(\frac{mP}{2\pi\beta\hbar^2}\right)^{P/2}\int dx_2 ... dx_P \tag{8.10}$$

$$\times \exp\left\{-\frac{1}{\hbar}\sum_{k=1}^{P}\left[\frac{mP}{2\beta\hbar}(x_{k+1} - x_k)^2 + \frac{\beta\hbar}{2P}\Big(V(x_{k+1}) + V(x_k)\Big)\right]\right\} \tag{8.11}$$

Going from this expression to the canonical partition function requires only one addditional real space integral, since

$$Z = \mathrm{Tr}\, e^{\beta(H)} = \int dx\, \rho(x, x'; \beta). \tag{8.12}$$

Written in a compact form, with the definitions $\omega_P = \sqrt{P}/\beta\hbar$ and $x_{P+1} = x_1$, the canonical partition function becomes

$$Z = \lim_{P\to\infty} Z_P, \tag{8.13}$$

$$U_P(x_1...x_P) = \sum_{k=1}^{P} \frac{1}{2} m\omega_P^2 (x_{k+1} - x_k)^2 + V(x_k), \tag{8.14}$$

$$Z_P = \left(\frac{mP}{2\pi\beta\hbar^2}\right)^{P/2} \int dx_1...dx_P e^{-\beta_P U_P(x_1,...,x_P)}. \tag{8.15}$$

The main result of the (imaginary time) path integral formalism is the establishment of an isomorphism between the (discrete) quantum canonical partition function and the partition function of a ring polymer coupled by harmonic springs vibrating with the frequency ω_P. Effectively, the problem of determining equilibrium properties in a quantum system has been transformed into an equivalent problem of equilibrium properties in a classical system. This relationship is known as the "classical isomorphism" [112]. Notably, this approach bears some resemblance to the Feynman path integral formalism, where a particle traverses all conceivable trajectories simultaneously from one point to another.

8.2.1. Thermodynamics and expectation values from the path integral

The expectation value of an observable A, which depends on the position x only, can be calculated with the partition function

$$\langle A\rangle = \frac{1}{Z}\mathrm{Tr}\left[Ae^{-\beta H}\right] = \frac{1}{Z}\int A(x)\langle x|e^{-\beta H}|x\rangle dx \tag{8.16}$$

$$= \lim_{P\to\infty} \frac{1}{Z}\left(\frac{mP}{2\pi\beta\hbar^2}\right)^{P/2} \int dx_1...dx_P \left[\frac{1}{P}\sum_{k=1}^{P} A(x_k)\right] e^{-\beta_P U_P(x_1...x_P)}. \tag{8.17}$$

In path integral calculations, the equilibrium expectation values can be estimated by employing *estimator* functions that rely on the P coordinates, namely $x_1, ..., x_P$. Meaning, an appropriate estimator for $\langle A\rangle$ will be

$$A_P(x_1, ..., x_P) = \frac{1}{P}\sum_{k=1}^{P} A(x_k) \tag{8.18}$$

and the expectation value will be given by an average over the probability distribution function $f(x_1, ..., x_P)$

$$\langle A\rangle_P = \lim_{P\to\infty} \langle A_P(x_1, ..., x_P)\rangle_f, \tag{8.19}$$

$$\langle A\rangle = \lim_{P\to\infty} \langle A\rangle_P. \tag{8.20}$$

In pratical numerical calculations, only a finite number of beads can be included. This number is chosen based on a convergence criterion.

8.3. Replica Exchange

Standard MD simulations are limited by their inherent dependence on the initial states of the system, which can often lead to getting trapped in local energy minima and slow exploration of the phase space.

To overcome these limitations, a method called *replica-exchange molecular dynamics* (REMD) was introduced [113–116]. REMD, also known as Parallel Tempering, is an enhancement to conventional MD that aims to accelerate the sampling of conformational space and address the challenge of getting stuck in local minima. This is achieved by running multiple replicas, each at a different temperature, and allowing them to exchange conformations periodically during the simulation.

The exchange of conformations between replicas is performed stochastically with a certain exchange probability that depends on the temperatures and potential energies of the replicas involved in the swap. The exchange criterion is commonly based on the Metropolis-Hastings algorithm [117, 118], and the acceptance probability for exchanging configurations between replica i and replica j is given by (cf. Eq. 17 of Ref. [116]):

$$w(X \to X') \equiv w(x_m^{[i]} | x_n^{[j]}) = \begin{cases} 1 & \text{for } \Delta \leq 0 \\ \exp(-\Delta) & \text{for } \Delta > 0 \end{cases} \tag{8.21}$$

where

$$\Delta \equiv (\beta_n - \beta_m)[E(q^{[i]}) - E(q^{[j]})]. \tag{8.22}$$

9

Anharmonicity

In the chapter on phonons (see Ch. 4), the concept of lattice vibrations was explored, focusing primarily on obtaining a lattice model that effectively captures the second-order, i.e. the harmonic contributions within the Born-Oppenheimer potential energy surface. While this endeavor proved relatively straightforward, it is essential to recognize that the harmonic terms alone are insufficient in fully describing the behavior of lattice vibrations.

In fact, in the presence of phase transitions, it is the anharmonic terms within the potential energy surface that eventually stabilize the crystal structure and subsequently dictate the characteristics of said structural displacive phase transitions. Consequently, the objective within the scope of downfolded lattice models is to reproduce these anharmonic contributions observed in DFT calculations.

In this chapter, the concept of anharmonicity will be discussed based on the phenomenological Landau theory (Sec. 9.1) to provide insights into the nature of structural phase transitions. Subsequently, the concept of soft phonons (Sec. 9.2) will be explored, which serve as an indicator of structural phase transitions. Finally, temperature-dependent phonon dispersions [119] (Sec. 9.3) will be introduced, showcasing one particular anharmonic effect through the eyes of various methods with the downfolding-based molecular dynamics being one of them.

9.1. Landau theory

The Landau theory is a phenomenological theory for phase transitions in general and can be applied to the subclass of structural displacive phase transitions. It is part of the review article [120] and the following paragraph will follow it closely.

In the simplest form, a phase transition can be described by a free energy F expanded up to fourth order

$$F = F_0 + l\alpha + \frac{1}{2}r\alpha^2 + d\alpha^3 + u\alpha^4, \tag{9.1}$$

with a single order parameter α, where the coefficients may be temperature dependent. The assumption is that a phase is only stable if

$$\left.\frac{\partial F}{\partial \alpha}\right|_{\alpha_0} = 0 \quad \text{and} \quad \left.\frac{\partial^2 F}{\partial \alpha^2}\right|_{\alpha_0} > 0. \tag{9.2}$$

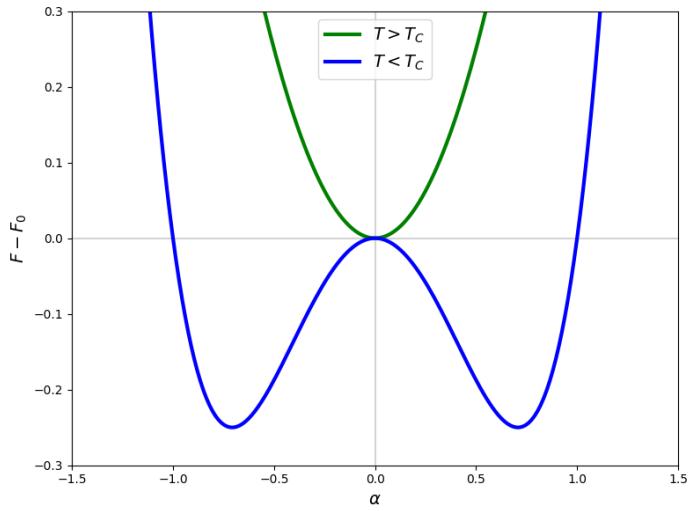

Figure 9.1: The free energy $F - F_0$ for the high-symmetry phase (green) and the distorted structure (blue)

Hence, the coefficient l needs to be zero and $r > 0$. Furthermore, according to Landau the coeffcient r switches its sign at a critical temperature T_C. A further assumption is that the coeffcient r follows a linear temperature dependence,

$$r = a(T - T_C), \tag{9.3}$$

which is the so-called soft phonon approach (see also Sec. 9.2). For a continuous phase transition the free energy shall increase with $|\alpha|$ at T_C. Hence, the cubic term in Eq. (9.1) must vanish. This leads to the free energy

$$F - F_0 = \frac{1}{2}a(T - T_C)\alpha^2 + u\alpha^4. \tag{9.4}$$

In Fig. 9.1, the free energy from Eq. (9.4) was plotted for $T > T_C$ and $T < T_C$. Since this is a discussion on structural phase transitions, the order parameter α corresponds to displacements of atomic coordinates. More specifically, $\alpha = 0$ represents the high-symmetry phase of a material and $\alpha \neq 0$ a distorted phase with lower symmetry. For $T > T_C$, the green line shows an energy increase with a displacement away from high-symmetry phase. Thus, the high-symmetry phase will be stable. However, for $T < T_C$ there are two lower minima, which are illustrated by the blue line. Since lower free energies will be prefered, the system will undergo a phase transition.

This simple model is a good introduction to understand the structural phase transitions that are associated with *soft phonon modes*.

9.2. Soft phonon modes

The following section will not only be based on the review articles Ref. [120, 121], but also on three articles that deal with anharmonicity and soft phonon modes [122–124].

In Ref. [120] it is claimed that "structural phase transitions occur only in crystals that are significantly anharmonic and for which the strictly harmonic frequencies, $\omega_j(\boldsymbol{q})$, may be imaginary". When a phonon mode has imaginary frequencies, one speaks of a *soft* phonon mode. Consider a mechanical spring as a classical counterpart to help illustrate the concept of a soft phonon mode. The term "soft phonon mode" is derived from this classical analogy, where a mechanical spring serves as a representative example. According to the harmonic oscillator, the relation between the force constant k, which describes the stiffness of the spring, and the frequency ω is given by

$$\omega = \sqrt{\frac{k}{m}}. \tag{9.5}$$

A reduced constant k will result in a reduced frequency ω, which is called a softening of the spring. However, the softening of a phonon mode can be so extreme that the phonon frequencies become imaginary below a certain temperature T_C, which indicates a lattice instability of the current lattice structure.

In the context of the soft mode approach, phase transitions are interpreted as the crystal becoming unstable with respect to a specific soft normal mode. The frequency of this mode approaches zero as the temperature reaches $T \approx T_C$. Within the phase of lower symmetry, the crystal undergoes distortions to support and stabilize this particular mode. These distortions are characterized by a fixed amplitude of the normal mode that becomes frozen-in. In the following, a few real-world examples from the literature will be presented for the interested reader.

In Ref. [123], soft phonon modes in Cs_2SnI_6 are identified at 44 K and 137 K via lattice-dynamics calculations. Similarly, in Ref. [124], imaginary phonon frequencies appear in SnSe's high-temperature phase (700 K to 800 K). Lastly, Ref. [122] observes temperature-dependent softening in iron's transverse (T1) mode.

The essence of this matter is that all three articles present a lattice instability, which is indicated by imaginary phonon frequencies. By displacing the lattice in the direction of this soft mode a new stable lattice structure is found. In the case of Cs_2SnI_6 there are phase transitions at temperatures of 44 K (monoclinic-tetragonal) and 137 K (tetragonal-cubic) [123]. For SnSe, it is the transition from the *Cmcm* phase to the *Pnma* phase [124] and lastly, for iron, it is the transition from a BCC to FCC lattice and from FCC to a BCC lattice again, which is a unique feature of iron [122].

These phase transitions are illustrated by double-well potentials in all three articles, which remind of the double-well free energy in Fig. 9.1. As order parameter α, the displacement in the direction of the eigenvector has been chosen.

To conclude, imaginary phonons can indicate structural phase transitions, which are naturally asscociated with double-well potentials and thus with anharmonicty. In this dissertation, a large focus is laid on charge density waves, which are a variant of structural phase transitions. An introduction of this phenomenon is given in Chapter 10.

9.3. Incorporating anharmonicity into phonon dispersions

Lattice vibrations of materials are often described using the harmonic approximation, which assumes that the vibrations are small and thus justifying the neglect of anharmonic terms in the Born-Oppenheimer potential energy surface (see Sec. 4.1). However, real-world systems rarely conform to this simple assumption. In fact, anharmonicity is omnipresent, gaining importance with larger displacements and ultimately contributing to the material's melting, as elucidated by the Lindemann

criterion [125]. Nevertheless, certain materials exhibit harmonic behavior across a substantial range of displacements. To name a few candidates: Semiconducting materials like silicon [126, 127] or tungsten disulfide (1H-WS_2) (see Fig. 6 of Ch. 13) are considered to be harmonic. Meanwhile the isostructural compound, tantalum disulfide (1H-TaS_2), shows strong anharmonic contributions illustrated by the double-well potential (see Fig. 6 of Ch. 13).

The figures depict the Born-Oppenheimer potential energy surface as obtained from static DFT or downfolded model calculations. Meaning that the free energy only depends on the *electronic temperature* via a smearing function and not on the overall *ensemble temperature*. As demonstrated later, the literature explicitly employs the concept of anharmonicity to introduce the ensemble temperature, which manifests in temperature-dependent lattice vibrations.

Hence, the consideration of anharmonicity is crucial for obtaining accurate dynamical properties such as temperature-dependent changes in vibrational frequencies [128–133] and thermodynamic properties such as heat capacities, entropies, and free energies.

This chapter introduces the concept of anharmonicity and its importance in understanding the behavior of materials, followed by an exploration of methods used to calculate anharmonic free energies. The method section should provide an overview that emphasises the complexity, popularity and importance of this branch in the literature. The chapter concludes with an introduction to a novel method for calculating anharmonic free energies, which offers significant advantages over existing approaches.

9.3.1. Quasi-harmonic approximation

The quasi-harmonic approximation (QHA) is the most straightforward framework for including anharmonic effects such as thermal expansion. This is achieved by introducing a direct dependence on the volume of phonon frequencies, while still preserving the harmonic expression for the Helmholtz free energy [126, 134, 135] (cf. Eq. 6 of Ref. [119]),

$$F = \sum_{\mu} \Big[\frac{1}{2}\hbar\omega_{\mu} - \frac{1}{\beta} \ln[1 + n_B(\omega_{\mu})] \Big], \tag{9.6}$$

where $n_B(\omega) = 1/(e^{\beta\hbar\omega} - 1)$ is the Bose-Einstein distribution, which introduces a temperature dependence, even though the phonon frequencies themselves are independent of temperature.

9.3.2. Self-consistent phonon theory

The self-consistent phonon (SCPH) theory is a broad term encompassing a variety of methods [136–139]. In these theories an effective harmonic potential is adjusted such that the nuclear density matrix resulting from the potential minimizes the free energy at a certain temperature. The challenge at hand is essentially to calculate the temperature-dependent interatomic force constants (cf. Eq. 7 of Ref. [139])

$$C_{p\kappa\alpha,p'\kappa'\alpha'}(T) = \left\langle \frac{\partial^2 U^{(\tau)}}{\partial\tau_{p\kappa\alpha}\partial\tau_{p'\kappa'\alpha'}} \right\rangle_T, \tag{9.7}$$

iteratively until self-consistency is achieved. The symbol $\langle . \rangle_T$ denotes the ensemble thermal average as the trace over the entire array of quantum harmonic oscillators. This average is weighted by the conventional Boltzmann factor at temperature T and is normalized by the canonical partition function [139].

The SCPH theory is also performed with a Green's function approach [140, 141]. In many-body perturbation theory, anharmonic effects are treated as self-energies [128–132]. These self-energies describe the intrinsic phonon–phonon scattering events. In Refs. [140, 141], a self-energy diagram of fourth order (the loop diagram) is employed and the Dyson equation is solved self-consistently. Furthermore, a third order bubble diagram is treated in a perturbative manner after solving the SCPH equation.

Another SCPH-based approach is the self-consistent harmonic approximation (SCHA) [142–146], originally developed in Ref. [136], which is a non-perturbative variational method. In order to simplify the computation of quartic force constants, these techniques utilize stochastic methods in real-space and displace atoms in the supercell to model anharmonic effects.

9.3.3. (Downfolding-based) *ab initio* molecular dynamics

Molecular dynamics simulations is a popular method for studying anharmonicity. It comes in several variations such as *ab initio* molecular dynamics (AIMD) (see Sec. 8.1), path-integral molecular dynamics (PIMD) (see Sec. 8.2) and the newly developed method in this dissertation called *downfolding-based molecular dynamics* (see Ch. 13).

AIMD employs Newtonian mechanics to simulate nuclear motion, with forces determined by on-the-fly DFT calculations. Anharmonic phonon frequency shifts and lifetimes can be derived from velocity or position autocorrelation functions using Fourier transforms [147, 148]. While AIMD's classical nature limits accuracy at very low temperatures, methods like path-integral molecular dynamics [149] incorporate quantum effects. However, PIMD comes with a greater computational cost which hinders the combination with DFT for large systems and long time scales.

Downfolding offers a way out of this problem (see Ch. 13). Restricting the electronic subspace to a minimal orbital model makes PIMD affordable for large systems while maintaining reasonable amount of accuracy. Futhermore, in contrast to the methods mentioned above, the downfolding-based MD does not rely on an effective second order Hamiltonian. Instead, the anharmonicity is treated explicitly to infinite order, albeit approximately through the assumptions of the downfolding strategy.

9.3.4. Conclusion

In conclusion, various methods for incorporating anharmonicities into thermodynamic and vibrational properties have been discussed. The QHA and SCPH theory, which includes the SCHA, have been introduced, revealing their common reliance on an *effective* second-order Hamiltonian to describe anharmonic behavior. These methods have provided valuable insights into the aspects of materials' vibrational spectra. In contrast, the (downfolding-based) *ab initio* molecular dynamics method stands out for its treatment of anharmonicity by *explicitly* considering higher-order terms beyond the harmonic regime. The relationship between the discussed methods and the downfolding-based MD is not clear. It is a complex task that requires analytical and numerical evaluations of Feynman diagrams and remains as an open question for future investigations.

10

Charge density waves

This dissertation focuses on developing downfolded lattice models, with charge density waves serving as the key example of application. This chapter aims to establish the fundamentals of this physical phenomenon. The foundation of this chapter draws inspiration from two review articles [1, 150], primarily centered on elucidating the origins of charge density waves. The interested reader might also find other review articles insightful [151–154].

10.1. Origin of charge density waves?

Charge density waves (CDWs) are fascinating electronic phenomena that occur in materials. They involve periodic modulations in the charge density of electrons within a crystal lattice. These modulations are accompanied by periodic lattice distortions, leading to a distinct periodic patterns such as the Star of David [155].

CDWs have been observed in various materials, especially in low-dimensional systems like one-dimensional chains of atoms [156] or two-dimensional layered structures [157]. But also three-dimensional materials are known to host CDWs [158].

They can arise due to different mechanisms, such as electron-phonon interactions, Fermi surface nesting, or electron-electron interactions as it is the case in the excitonic insulator instability [159]. Understanding the origin and behavior of CDWs is crucial for exploring their impact on material properties and potential applications, especially in fields like superconductivity [160] and electronic devices [161].

Hence, the origin of CDWs will be discussed based on two review articles [1, 150]. Both articles introduce the Peierls model (see Sec. 10.2) as a classical textbook example for comprehending the emergence of CDWs within metallic one-dimensional atomic chains. In the Peierls model, the non-interacting susceptibility is the dominant player, which diverges in the one-dimensional case. Consequently, CDWs in (quasi)-one-dimensional have been attributed to the Fermi surface nesting mechanism [162].

However, the Peierls instability is unlikely to happen in real-world materials beyond the quasi-one-dimensional case. This is due to the fact that the logarithmic divergence of the susceptibility is fragile as it is less pronounced i.e. broadened in higher dimensions [163]. Nevertheless, there are studies claiming that the observed CDW is driven by Fermi surface nesting in three-dimensional materials such as bulk 1T-VSe_2 [164–166]. From this, uncertainty arises regarding the true origin of the CDW, leading to controversial discussions on this topic in the literature for several decades.

Due to this prevailing uncertainty, a recent technique known as *fluctuation diagnostics* has been applied to monolayer 1H-TaS_2. This innovative approach effectively distinguishes between Fermi-surface nesting and electron-phonon matrix element effects [39]. It relies on the momentum-resolved decomposition of the phonon self-energy, allowing for the investigation of the origins of giant Kohn anomalies in phonon dispersions. These Kohn anomalies provide insights into the dynamic instability towards a CDW. This concept aligns with the fundamental principles of the Landau theory, where the second-order term in the free energy plays a pivotal role in determining whether a phase transition occurs in the vicinity of a high-symmetry phase.

While the harmonic term in the free energy holds significance, it cannot pinpoint the final atomic positions of the CDW or determine which CDW takes precedence when multiple anomalies exist in phonon dispersions. These intricate decisions are shaped by the anharmonic terms within the free energy. This situation is exemplified in the second publication of this dissertation (see Ch. 12). Hence, accurately describing anharmonicity within real-world materials is imperative, and this is precisely the objective pursued in this dissertation through the development of downfolded lattice models.

10.2. Peierls instability

Peierls has shown that by displacing the atoms of a linear chain periodically from their rest positions, the resulting periodic potential opens up a gap at the Fermi surface. Occupied states experience a reduction of their energy and empty states experience a raise of their energy. Effectively, this results in an gain in electronic energy, which can be large enough to compensate for the energy loss due to elastic energy. When this condition is fullfilled, a CDW formation occurs. This delicate balance between electronic and elastic energy within the one-dimensional atomic chain can be described using the Fröhlich Hamiltonian:

$$H_{\mathrm{PI}} = \sum_{\boldsymbol{k}} \varepsilon_{\boldsymbol{k}} c_{\boldsymbol{k}}^{\dagger} c_{\boldsymbol{k}} + \sum_{\boldsymbol{q}} \hbar\omega_{\boldsymbol{q}} b_{\boldsymbol{q}}^{\dagger} b_{\boldsymbol{q}} + \frac{1}{\sqrt{N}} \sum_{\boldsymbol{k},\boldsymbol{q}} g_{\boldsymbol{q}} c_{\boldsymbol{k}+\boldsymbol{q}}^{\dagger} c_{\boldsymbol{k}} (b_{\boldsymbol{q}}^{\dagger} + b_{\boldsymbol{q}}), \tag{10.1}$$

with the undistorted electronic dispersion $\varepsilon_{\boldsymbol{k}}$, the bare phonon frequency $\omega_{\boldsymbol{q}}$ and the bare electron-phonon coupling matrix element $g_{\boldsymbol{q}}$. The total band energy change can be calculated within second-order perturbation theory

$$\delta E_{\mathrm{band}} = -|v_{\boldsymbol{q}}|^2 \chi_0(\boldsymbol{q}), \quad \text{with the potential} \quad v_{\boldsymbol{q}} = g_{\boldsymbol{q}} u_{\boldsymbol{q}} \sqrt{\frac{2M\omega_{\boldsymbol{q}}}{\hbar}}, \tag{10.2}$$

and χ_0, the non-interacting electronic susceptibility

$$\chi_0(\boldsymbol{q}) = \frac{1}{L} \sum_{\boldsymbol{k}} \frac{f_{\boldsymbol{k}+\boldsymbol{q}} - f_{\boldsymbol{k}}}{\varepsilon_{\boldsymbol{k}} - \varepsilon_{\boldsymbol{k}+\boldsymbol{q}}}, \tag{10.3}$$

where L is the length of the atomic chain, $f_{\boldsymbol{k}}$ is the Fermi function. On the other hand, the lattice strain energy due to the deformation is given by

$$\delta E_{\mathrm{lattice}} = \frac{1}{2} M \omega_{\boldsymbol{q}}^2 u_{\boldsymbol{q}}^2, \tag{10.4}$$

where $u_{\boldsymbol{q}}$ is a static displacement of phonon mode $\boldsymbol{q}$.

According to this model, a CDW will only appear, if $\delta E_{\text{band}} + \delta E_{\text{lattice}} < 0$, which leads to a simple instability condition [167]

$$\frac{4g_{\boldsymbol{q}^2}}{\hbar\omega_{\boldsymbol{q}}} > \frac{1}{\chi_0(\boldsymbol{q})}. \tag{10.5}$$

The instability condition states that the formation of a CDW can be achieved in systems with strong electron-phonon interaction $g_{\boldsymbol{q}}$, a small lattice strain energy $\omega_{\boldsymbol{q}}$ or a large non-interacting susceptibility $\chi_0(\boldsymbol{q})$. This inequality was evaluated in Ref. [1] for 2H-$TaSe_2$ with the result that a CDW formation should appear, but "all estimates are based on crude models and strong approximations and the error bars of some of the involved microscopic parameters are rather large". Indeed, the CDW is observed in experiments [168]. Thus, the instability condition can serve a valuable trend, but should not be interpreted as a general law.

Another important aspect for the appearance of a CDW is the so-called *Kohn anomaly*. A Kohn anomaly is a renormalization of the phonon frequencies in a narrow wavevector range, where the non-interacting susceptibility $\chi_0(\boldsymbol{q})$ diverges

$$\tilde{\omega}_{\boldsymbol{q}}^2 = \omega_{\boldsymbol{q}}^2\Big(1 - \frac{4g_{\boldsymbol{q}}^2}{\hbar\omega_{\boldsymbol{q}}}\chi_0(\boldsymbol{q})\Big). \tag{10.6}$$

The bracket in Eq. (10.6) can lead to a reduction of the frequency, which results in a softening of the phonon mode (cf. Sec. 9.2). The softening can be so extreme, that $\tilde{\omega}_{\boldsymbol{q}}^2 \leq 0$, indicating that the lattice phonon freezes completely, which is referred to as a CDW.

The Kohn anomaly highlights, similar to the instability condition, the interplay between electron-phonon coupling and susceptibility. In the next section, this interplay will be decoded with the help of fluctuation diagnostics.

10.3. Fluctuation diagnostics of phonon self-energies

This section is inspired by Ref. [39].

As stated in the introduction of this chapter, there is uncertainty regarding the origin of CDWs. The method known as "fluctuation diagnostics" aims to uncover the mysteries behind this phenomenon by investigating the momentum-resolved phonon self-energies. Before delving into this method, it is worth examining the formula (cf. Eq. 10.6) for the Kohn anomaly in a simple one-dimensional metallic chain. The term responsible for reducing the phonon frequency and ultimately leading to imaginary phonon frequencies consists of the product of the squared electron-phonon matrix element and the non-interacting susceptibility. Essentially, this constitutes the phonon self-energy. It is evident that both components contribute to the emergence of the giant Kohn anomaly. However, it is unclear which one dominates and which electronic processes are most significant.

This sets the stage for fluctuation diagnostics, which will be discussed using the example of monolayer 1H-TaS_2. What makes this material interesting is that the low-energy electronic band is completely isolated from other bands, making it particularly suitable for downfolding techniques like cDFPT (as done in the third publication, Ch. 13, and Ref. [39]). By applying the cDFPT method to obtain partially screened phonon frequencies and electron-phonon coupling matrix elements, the distinct electronic subspace can be analyzed.

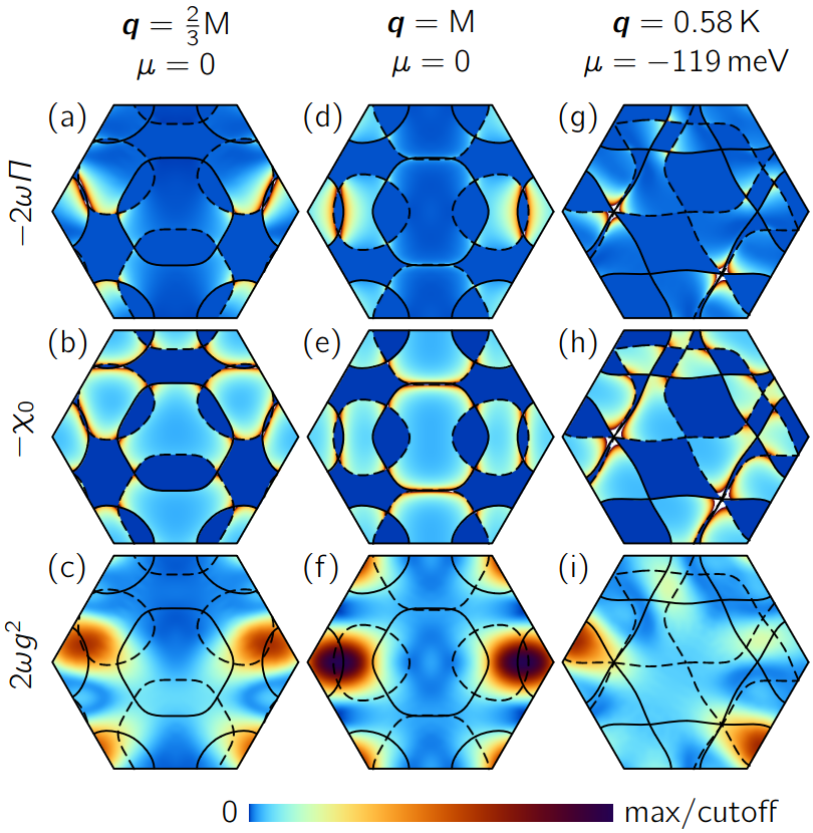

Figure 10.1: [*Reproduced with permission from Ref. [39]*] Momentum-resolved fluctuation diagnostics of LA-phonon-mode softening at $q = 2/3\mathrm{M}$ (left) and $q = \mathrm{M}$ (middle) in undoped 1H-TaS2 as well as at $\boldsymbol{q} = 0.58\mathrm{K}$ (right) at Van Hove filling (chemical potential $\mu = -119\mathrm{meV}$). The $\boldsymbol{k}$-dependent contributions to the phonon self-energy $2\omega\Pi$, the bare electronic susceptibility χ_0, and the coupling matrix elements $2\omega g^2$ are shown color-coded. Solid (dashed) lines indicate the Fermi surface (shifted by the respective $\boldsymbol{q}$ vectors).

At this point, revisiting the definition of phonon self-energy (cf. Eq. 4.16) and the corresponding renormalization of the phonon frequencies (cf. Eq. 4.18) is useful. As can be observed, similar to the simple Peierls model, the key players are the squared electron-phonon matrix element and the susceptibility. However, the dependence on $\boldsymbol{q}$ and $\boldsymbol{k}$ momentum complicates the situation. Therefore, it is insightful to plot each term of the momentum-resolved phonon self-energy, as shown in Fig. 10.1. The hexagonal Brillouin zones sample the electronic $\boldsymbol{k}$-values, where the solid lines represent the Fermi surface. Additionally, shifted Fermi surfaces due to phonon momentum wave vectors $\boldsymbol{q}$ can be plotted (in dashed lines), leading to immediate overlap of Fermi surfaces, so-called Fermi surface nesting.

In pristine 1H-TaS_2, which exhibits a 3×3 CDW at $\mu = 0$, the primary wave vector of interest is $\boldsymbol{q} = 2/3\mathrm{M}$. The analysis of phonon self-energy $2\omega\Pi$ reveals that the most significant contributions stem from specific regions in $\boldsymbol{k}$-space. These regions are where the original hole pocket around K nearly touches the pocket around K', shifted by $-\boldsymbol{q}$, resulting in two intervalley processes that strongly impact $2\omega\Pi$. However, these contributions do not affect the bare electronic susceptibility χ_0. The coupling matrix elements $2\omega g^2$ filter out intervalley coupling regions, and while one might initially consider nesting as an explanation for the remaining contributions from regions with touching K and K' pockets, the results refute this idea.

Additionally, at q = M, $2\omega\Pi$ exhibits a distinct extremum mainly due to slightly overlapping K and K' pockets, indicating the absence of nesting. Although nesting exists for the hole pocket around Γ, its impact on χ_0 is approximately logarithmic, and matrix-element effects in the phonon self-energy are the dominant factors in this scenario.

11

First publication: Downfolding the Su-Schrieffer-Heeger model

11.1. Statement of personal contribution

*This work has been published in SciPost Phys. **11**, 079 (2021), arXiv:2104.09207. It has been realized in collaboration with J. Berges, T. O. Wehling and E. G. C. P. van Loon. The Su-Schrieffer-Heeger (SSH) model is a typical textbook example. I have studied this model and carried out the calculations in Section 2 and 3, including Figs. 1 and 2. Furthermore, I have written substantial parts of the manuscript, which have been revised and edited by all authors of this work. The diagrammatic evaluation of this model was done by E. G. C. P. van Loon, who also designed and supervised this project.*

11.2. Positioning within the scientific landscape

The scientific field of downfolding is not a recent development. It has primarily found applications in electronic structure calculations of strongly correlated materials and has demonstrated considerable success in this regard [40]. Nevertheless, the integration of lattice degrees of freedom into downfolding approaches represents a relatively recent advancement. In this context, namely electron-phonon coupled systems, the pioneering work of the cDFPT method [80] stands out as it incorporates the cRPA ideas into DFPT. Subsequently, the cDFPT method has been employed in the study of various materials, including superconducting materials such as alkali-doped fullerides [169], light elements [170], monolayer 1H-TaS_2 [39] and molecules such as nitrogren and benzene [51].

However, due to the novelty of downfolding techniques involving lattice degrees of freedom, there exists uncertainty regarding their ability to faithfully recover Born-Oppenheimer potential energy surfaces and electronic structures. This fundamental question serves as the motivation behind the current study.

The SSH model [171] is an ideal candidate for applying downfolding techniques. This suitability arises from the model's distinctive characteristics, such as electronic bands that can be described using analytical formulas. In fact, the simplicity of the SSH model even facilitates the analytical derivation

of the potential energy landscape, which is completely out of reach for real-world materials. Notably, our investigations have revealed that the downfolded model is able to reconstruct the potential-energy landscape exactly. Furthermore, our findings confirm the accurate representation of band dispersions upon atomic displacement, with the downfolded model inherently focusing on spectral weight within the target space.

This work foreshadows the application of downfolding techniques, including lattice degrees of freedom, to describe Born-Oppenheimer potential energy surfaces of real-world systems. Please note that this achievement is discussed in the third publication of this dissertation (see. Ch. 13).

SciPost Phys. 11, 079 (2021)

Downfolding the Su-Schrieffer-Heeger model

Arne Schobert[1], Jan Berges[1], Tim Wehling[1] and Erik van Loon[1,2*]

1 Institut für Theoretische Physik, Bremen Center for Computational Materials Science, and MAPEX Center for Materials and Processes, Universität Bremen, Bremen, Germany
2 Department of Physics, Lund University, Lund, Sweden

⋆ erik.van_loon@teorfys.lu.se

Abstract

Charge-density waves are responsible for symmetry-breaking displacements of atoms and concomitant changes in the electronic structure. Linear response theories, in particular density-functional perturbation theory, provide a way to study the effect of displacements on both the total energy and the electronic structure based on a single *ab initio* calculation. In downfolding approaches, the electronic system is reduced to a smaller number of bands, allowing for the incorporation of additional correlation and environmental effects on these bands. However, the physical contents of this downfolded model and its potential limitations are not always obvious. Here, we study the potential-energy landscape and electronic structure of the Su-Schrieffer-Heeger (SSH) model, where all relevant quantities can be evaluated analytically. We compare the exact results at arbitrary displacement with diagrammatic perturbation theory both in the full model and in a downfolded effective single-band model, which gives an instructive insight into the properties of downfolding. An exact reconstruction of the potential-energy landscape is possible in a downfolded model, which requires a dynamical electron-biphonon interaction. The dispersion of the bands upon atomic displacement is also found correctly, where the downfolded model by construction only captures spectral weight in the target space. In the SSH model, the electron-phonon coupling mechanism involves exclusively hybridization between the low- and high-energy bands and this limits the computational efficiency gain of downfolded models.

Received 11-05-2021
Accepted 22-09-2021
Published 20-10-2021
doi:10.21468/SciPostPhys.11.4.079

Check for updates

Contents

SciPost SciPost Phys. 11, 079 (2021)

1 Introduction

The study of electron-phonon interactions (EPIs) goes back to the early days of solid-state theory. They are important for our understanding of basic material properties such as effective masses [1–4] and lattice constants [5,6]. Furthermore, this interaction is responsible for phase transitions, such as conventional superconductivity [7–18] and charge-density waves (CDWs) [19–30]. Even in unconventional superconductors, signatures of EPIs can be found [31–43]. However, the precise interplay responsible for these phenomena is not fully understood, which is one of the reasons that the fundamental interaction between electrons and phonons needs to be described accurately. Developments in this direction occur along two main paths: first-principles calculations and model Hamiltonians.

The standard *ab initio* method for calculating the EPI is the density-functional perturbation theory (DFPT) [44]. The most important ingredients of this theory are the adiabatic Born-Oppenheimer approximation [45], density-functional theory (DFT) [46], and linear-response theory. Briefly put, these state that it is possible to separate the dynamics of the electrons and ions, treat the electron in an effective one-body Schrödinger equation, and calculate the response of the electrons upon displacement of the nuclei within linear order, based only on the electronic density [47–49]. The resulting EPI simultaneously describes two sides of the same coin, namely how the electrons screen and renormalize the phonons and how the electronic structure will adjust to atomic displacements. For an overview of the historical development and the recent accomplishments of calculating the EPI from first principles, see Ref. [50].

Despite the unquestionable success of the current *ab initio* computational methods, another trend in the literature is to treat the important physical phenomena in correlated materials with *downfolding* approaches. The central idea is to reduce the number of degrees of freedom compared to the full system by keeping only the relevant states in a low-energy theory. The other states are integrated out and determine the parameters of the downfolded system. The overarching purpose of this procedure is the application of more advanced and expensive computational techniques only to the low-energy space where correlations take place.

For phonon-related properties, the *constrained* density-functional perturbation theory

SciPost Phys. 11, 079 (2021)

(cDFPT) was introduced [51] and successfully applied to superconducting materials such as alkali-doped fullerides [52] and light elements [53]. Additionally it was applied to monolayer 1H-TaS_2 [29], where it was shown that the CDW in this material is induced by coupling between the longitudinal-acoustic phonons and the electrons from an isolated low-energy metallic band. With the help of cDFPT it is possible to extract unscreened or partially screened parameters such as the phonon frequency and the electron-phonon vertex from an *ab initio* calculation and use these as the basis for an effective low-energy model Hamiltonian. The usefulness of partially screened parameters lies in the fact that they get rid of the coupling between phonons and the high-energy electrons.

As discussed, the description of real physical phenomena that are tightly linked to the EPIs is frequently based on *ab initio* theories (DFPT, cDFPT) that involve substantial numerical and computational effort. The structure of the theory is not always transparent, and also obscured by details of the numerical implementation. To avoid these complications, a second branch in the literature is focused on model Hamiltonians. The most popular models of the EPI are the Fröhlich model [54] for polaron formation, the Holstein model [55] for optical phonons, and the Su-Schrieffer-Heeger (SSH) model [56] for CDWs.

For understanding the interplay of electronic structure and atomic displacements, the SSH model is the most instructive since it explicitly describes how the electronic band structure is renormalized by the displacements of the atoms. Previous investigations using this model have studied properties such as the effective mass [57, 58] and the band structure [59, 60], but also phonon-related properties [61]. In the model, a periodic displacement of the atoms can open a band gap and thereby lower the total energy of the system [56], leading to a CDW transition. In other words, electronic screening makes the CDW phonon go soft. This textbook example of a CDW transition [62] is appealing for the investigation of downfolding since it is possible to perform all calculations exactly once the Born-Oppenheimer approximation has been applied.

The origin of this extraordinary simplicity lies in the observation that the Born-Oppenheimer approximation makes the phonons classical and the remaining electronic degrees of freedom in the SSH model are noninteracting. Thus, given any fixed displacement, the resulting electronic Hamiltonian is easily diagonalized. In some sense, this is similar to the method employed in Hirsch-Fye Quantum Monte Carlo [63], where a Hubbard-Stratonovich transformation is used to generate a system of noninteracting electrons coupled to classical fields and the subsequent analysis only involves varying the classical field and evaluating the noninteracting electron system. Unlike in Hirsch-Fye Quantum Monte Carlo, here the classical field is directly observable and has a clear physical meaning.

We choose to study the SSH model here for its simplicity, acting as a minimal model for electron-phonon coupling. At the same time, this means that there are many relevant aspects of electron-phonon coupling and CDWs that are not captured by the SSH model. In particular, the SSH model neglects Coulomb interactions between the electrons, and these are responsible for important effects such as screening and entirely electronic CDWs without lattice displacement. Furthermore, in higher dimensions, the shape of the Fermi surface can play an important role, in the form of nesting and Van Hove singularities. Given the complexity of electron-phonon systems, studying simple models is a useful way to identify relevant effects and mechanisms.

In this work, we compare the direct calculation of properties of the SSH model in the Born-Oppenheimer approximation at finite displacement with a perturbative diagrammatic expansion around the undistorted state à la DFPT. In this model, the diagrammatic expansion can be evaluated analytically order by order and we show that it correctly captures how the electron-phonon coupling renormalizes the phonon frequency and the electronic structure. Then, in the spirit of downfolding, we move to an effective single-band model for the dimerization transition in the SSH model. The diagrammatic structure in this effective model differs

SciPost Phys. 11, 079 (2021)

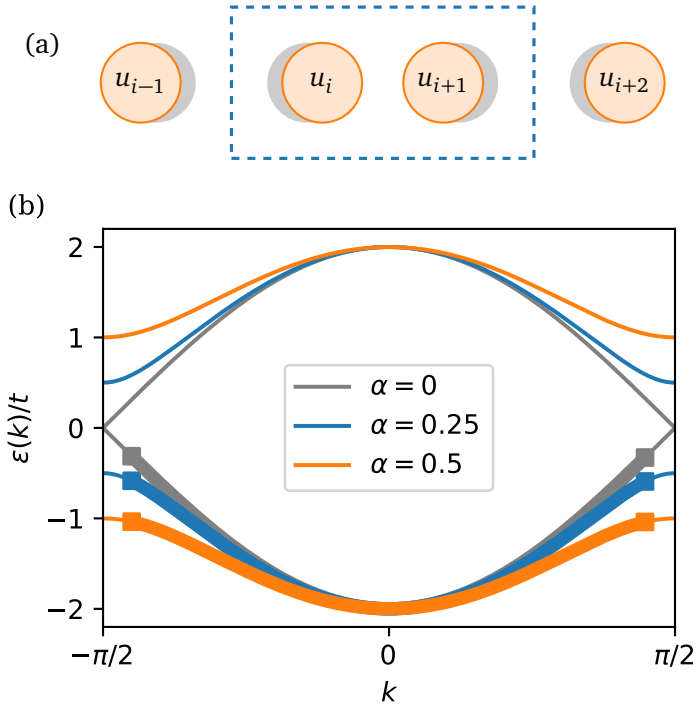

Figure 1: (a) Dimerization. (b) Band structure at various values of the atomic displacement α. The thick lines represent the occupied states when there are $\langle n \rangle = 0.9$ spinless electrons per dimer.

substantially from the original model: an interaction between an electron and two phonons appears and this interaction turns out to be dynamical with a frequency set by the high-energy electrons that were integrated out. We show that this downfolded model faithfully reproduces the energy landscape and the CDW. Furthermore, we discuss a cDFPT-like approach to downfolding, which correctly describes the screening of the phonon frequencies. In the SSH model, the displacement-induced orbital reconstruction between target and rest space is the central aspect of the downfolding and there is no remaining electron-phonon coupling in the cDFPT low-energy model.

2 Model

In this work, we consider the SSH model [56] in the classical Born-Oppenheimer limit [64], i.e., we ignore the kinetic energy of the atoms. We consider spinless fermions in a one-dimensional lattice with Hamiltonian

$$H = -t \sum_{i=0}^{N-1} (1 + u_i - u_{i+1})(c_i^\dagger c_{i+1} + c_{i+1}^\dagger c_i) + \frac{k_s}{2} \sum_{i=0}^{N-1} (u_{i+1} - u_i)^2. \tag{1}$$

Here, u_i is a (classical) variable describing the atomic displacements, with $0 \leq i < N$. We use the periodic boundary condition $u_N \equiv u_0$. The hopping $t > 0$ sets the electronic energy scale and the force constant $k_s > 0$ that of the phonons.

We consider dimerization, i.e., displacements of the form $u_i = (-1)^i \alpha/2$, and double the unit cell to include entire dimers. This is illustrated in Fig. 1a. Using the notation $a_i = c_{2i}$ and

SciPost SciPost Phys. 11, 079 (2021)

$b_i = c_{2i+1}$, we obtain

$$H = -t\sum_{i=0}^{N/2-1}(1+\alpha)(a_i^\dagger b_i + b_i^\dagger a_i) - t\sum_{i=0}^{N/2-1}(1-\alpha)(a_{i+1}^\dagger b_i + b_i^\dagger a_{i+1}) + \frac{1}{2}Nk_s\alpha^2. \tag{2}$$

Performing a Fourier transform to momentum space, the Hamiltonian in matrix form reads

$$H = \sum_k \begin{pmatrix} a_k^\dagger & b_k^\dagger \end{pmatrix} \hat{\varepsilon}(k) \begin{pmatrix} a_k \\ b_k \end{pmatrix} + \frac{1}{2}Nk_s\alpha^2, \tag{3}$$

$$\hat{\varepsilon}(k) = -t\begin{pmatrix} 0 & 1+\alpha+(1-\alpha)e^{2ik} \\ 1+\alpha+(1-\alpha)e^{-2ik} & 0 \end{pmatrix}, \tag{4}$$

with eigenvalues

$$\varepsilon_\pm(k) = \pm 2t\sqrt{1+(\alpha^2-1)\sin^2(k)} = \pm 2t\sqrt{\cos^2(k)+\alpha^2\sin^2(k)}. \tag{5}$$

These give the dispersion shown in Fig. 1b. Note that the Brillouin zone is $-\pi/2 \le k \le \pi/2$, where k is made dimensionless by setting the atomic distance to unity.

In the following, we assume that the electronic density $\langle n\rangle$ is smaller than 1 electron/dimer. Since the model is particle-hole symmetric, the case $\langle n\rangle > 1$ follows by symmetry. The situation $\langle n\rangle = 1$ (half-filling) is special and will be discussed in more detail below, see Sec. 7. At zero temperature, the electron density is proportional to the Fermi wave vector k_f and independent of α: $\langle n\rangle = 2k_f/\pi$. The total electronic energy per dimer, in the thermodynamic limit $N \to \infty$, is

$$E_{\rm el} = \frac{1}{\pi}\int_{-k_f}^{k_f} \varepsilon_-(k)dk, \tag{6}$$

and the total energy per dimer is

$$E = k_s\alpha^2 + E_{\rm el}. \tag{7}$$

Note that in this model, displacements do not change the Fermi surface and the electronic energy $E_{\rm el}$ depends on α only via Eq. (5), which will allow us to pull derivatives through the integral in Eq. (6).

In Fig. 2a, we show how the total energy depends on α for fixed k_s and $\langle n\rangle$. The total energy is obviously symmetric in α, and the undistorted lattice at $\alpha = 0$ is an extremum of the total energy. Without electrons, $E_{\rm bare} = k_s\alpha^2$ is a convex parabola with a minimum at $\alpha = 0$. However, the coupling to the electrons can lead to a Peierls CDW phase transition where $\alpha = 0$ turns into a local maximum and two global minima occur at $\alpha = \pm\alpha^*$. The finite α lowers the energy of the occupied states and thus the total electronic energy and this compensates for the gain in potential energy due to α.

SciPost Phys. 11, 079 (2021)

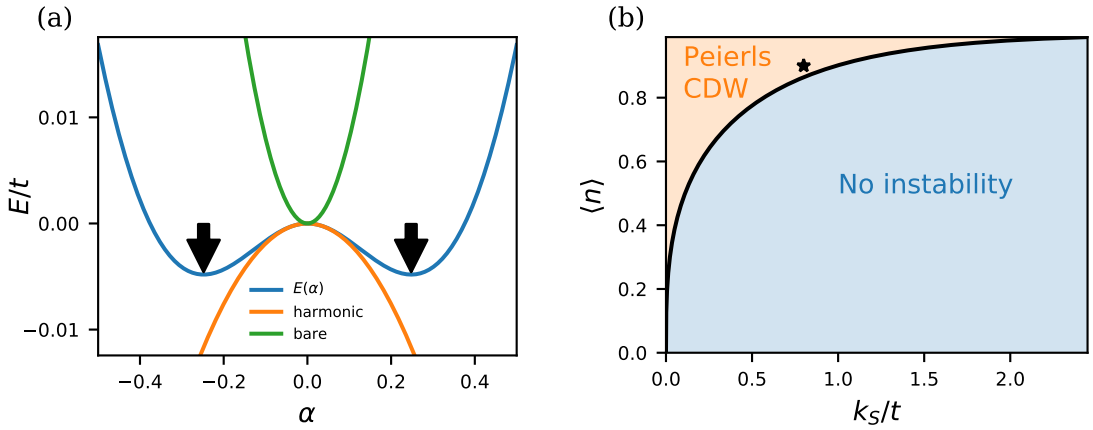

Figure 2: (a) Energy landscape at $k_s/t = 0.8$, $\langle n\rangle = 0.9$. The curves show the exact energy $E(\alpha)$, the harmonic approximation including electronic screening $E(0)+\frac{1}{2}\omega^2\alpha^2$, and the bare phonon energy $E(\alpha=0)+\frac{1}{2}\omega^2_{\text{bare}}\alpha^2$. The arrows indicate the minima at $\pm\alpha^*$. (b) Phase diagram of the SSH model for the density $\langle n\rangle$ and the force constant k_s. The black star marks the parameters of (a). We only consider the transition to the dimerized CDW.

3 Harmonic and anharmonic lattice potential

To analyze the phase transition, it is useful to perform a Taylor expansion of the lattice potential $E(\alpha)$ around $\alpha = 0$.

$$E(\alpha)-E(0) = \frac{1}{2}\left.\frac{d^2E(\alpha)}{d\alpha^2}\right|_{\alpha=0}\alpha^2 + \frac{1}{4!}\left.\frac{d^4E(\alpha)}{d\alpha^4}\right|_{\alpha=0}\alpha^4 + \ldots \tag{8}$$

$$\equiv \frac{1}{2}\omega^2\alpha^2 + h^{(4)}\alpha^4 + \ldots \tag{9}$$

$$\omega^2 = \omega^2_{\text{bare}} + \Delta\omega^2, \tag{10}$$

$$\omega^2_{\text{bare}} \equiv 2k_s, \tag{11}$$

$$\Delta\omega^2 \equiv \frac{1}{\pi}\int_{-k_f}^{k_f} dk \left.\frac{d^2\varepsilon_-(k)}{d\alpha^2}\right|_{\alpha=0} = -\frac{2t}{\pi}\int_{-k_f}^{k_f} dk \frac{\sin^2(k)}{\cos(k)}, \tag{12}$$

$$h^{(4)} = \frac{1}{\pi}\int_{-k_f}^{k_f} dk \frac{1}{4!}\left.\frac{d^4\varepsilon_-(k)}{d\alpha^4}\right|_{\alpha=0} = \frac{t}{4\pi}\int_{-k_f}^{k_f} dk \frac{\sin^4(k)}{\cos^3(k)}. \tag{13}$$

Here, we have introduced the bare phonon frequency ω_{bare} and the dressed phonon frequency ω. The difference $\Delta\omega^2$, the electronic screening of the phonon, originates in the change in electronic structure in response to the lattice distortion. Screening lowers the phonon frequency, and the Peierls transition occurs when the dressed phonon frequency is equal to zero, i.e., $\omega = 0$. In Fig. 2b, the Peierls transition is represented as the black line that separates the phases $\omega^2 < 0$ (Peierls instability) and $\omega^2 > 0$ (no instability). As we can see, a weak force constant k_s and a density $\langle n\rangle$ close to half-filling is preferred for a Peierls instability. Beyond the Peierls transition, $\alpha = 0$ is a local maximum of the potential and the higher-order terms, such as $h^{(4)}$, are responsible for ensuring that $E(\alpha)$ has a minimum at some finite α. In Appendix A, we show that there can be at most two minima, symmetrically located around $\alpha = 0$. Only even orders of α appear due to the symmetry of the system.

SciPost SciPost Phys. 11, 079 (2021)

4 Electron-phonon coupling: Two-band model

In the previous section, we used our knowledge of the exact dependence of the electronic structure $\hat{\varepsilon}$ on α to determine the potential-energy landscape. In *ab initio* calculations (e.g., DFPT), one will usually not have access to this. Instead, the only known quantities are the electronic structure of the undistorted structure $\hat{\varepsilon}_0$ and the electron-phonon coupling, the first derivative of the electronic structure with respect to the displacement. Access to the latter quantity is guaranteed by the $2n+1$ theorem [47–49]. Because of this, it is instructive to calculate the (approximate) potential-energy landscape of the SSH model—and in particular the screening of the phonon frequency—based just on these quantities in a perturbative expansion around $\alpha = 0$.

The Feynman rules can be read off from the Hamiltonian, Eq. (3), by writing it as

$$\hat{H} = \sum_k f_k^\dagger \hat{\varepsilon}_0(k) f_k + \alpha f_k^\dagger \underline{\hat{g}}(k) f_k + N\frac{1}{2}\omega_{\text{bare}}^2 \alpha^2. \tag{14}$$

Here, $f^\dagger$ is shorthand for the vector $(a^\dagger, b^\dagger)$. There is a single $q = 0$ phonon mode corresponding to dimerization, with frequency $\omega_{\text{bare}}^2 = 2k_s$. This mode is entirely classical, since we are interested only in a Born-Oppenheimer potential-energy landscape. The electron-phonon coupling is a matrix in electronic space and is obtained as $\underline{\hat{g}} = d\hat{\varepsilon}/d\alpha$ evaluated at $\alpha = 0$. In other words, it consists of the parts of $\hat{\varepsilon}$ that are proportional to α. Explicitly,

$$\underline{\hat{g}}(k) = -t\begin{pmatrix} 0 & 1-e^{2ik} \\ 1-e^{-2ik} & 0 \end{pmatrix} \text{ in the } (a^\dagger, b^\dagger) \text{ basis.} \tag{15}$$

Note that we are considering a single phonon mode at $q = 0$, so we do not need a q label on $\underline{\hat{g}}$. The lack of higher-order electron-phonon-coupling terms in Eq. (14) is a special property of the SSH model.

To evaluate the Feynman diagrams, it is most convenient to express the electronic part of the Hamiltonian in the eigenbasis of the unperturbed electronic system. This basis transformation can be seen in Appendix B. The transformed electron-phonon coupling is

$$\hat{g}(k) = 2t\begin{pmatrix} 0 & i\sin(k) \\ -i\sin(k) & 0 \end{pmatrix} \text{ in the band basis.} \tag{16}$$

We observe that g couples the two bands and has no intraband component. In other words, to linear order in α around $\alpha = 0$, distortions only change the orbital composition of the bands but not the dispersion of the bands.

The vanishing diagonal elements of g can also be understood as a symmetry selection rule. The inversion symmetry of the system implies that $\varepsilon(\alpha)$ and $\varepsilon(-\alpha)$ have the same eigenvalues and this implies both $\operatorname{Tr} g = \operatorname{Tr} \frac{d\hat{\varepsilon}}{d\alpha} = \frac{d}{d\alpha}\operatorname{Tr}\hat{\varepsilon} = 0$, which holds in any basis, and $\langle n|\,\hat{g}\,|n\rangle = 0$ for any $\alpha = 0$ eigenvector $|n\rangle$, since these $|n\rangle$ are eigenvectors of the inversion operator with eigenvalue ± 1.

4.1 Leading diagram

We are interested in establishing the effective potential felt by the atoms, including electronic screening. Diagrammatically, this means that the phonon mode only appears as external lines, whereas internally the diagram consists of electronic propagators and electron-phonon vertices. All diagrams with n external lines need to be summed to obtain the α^n coefficient in the potential $E(\alpha)$.[1]

[1] For the diagrammatic expansion of the free energy, see Ref. [65].

SciPost Phys. 11, 079 (2021)

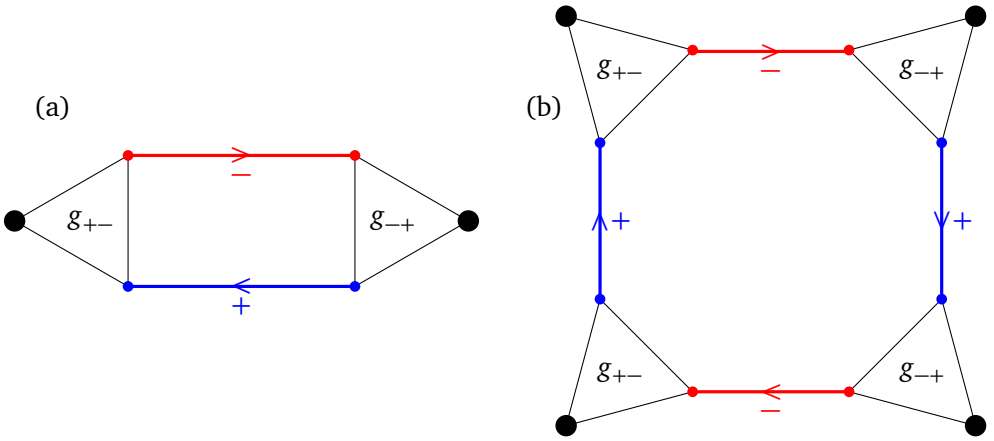

Figure 3: (a) Diagram for the renormalization of the phonon frequency. The black dots represent external phonon lines, the red and blue lines denote the electronic Green's functions $G_\pm$ in the band basis, and the triangles are the electron-phonon coupling. (b) Fourth order diagram.

For all upcoming diagrams, we will use the electronic Green's function

$$\hat{G}(E,k) = \frac{\hat{1}}{E\,\hat{1} - \hat{\varepsilon}_0(k) + i\hat{\eta}_k}, \tag{17}$$

where $\hat{1}$ is the identity matrix, the division denotes matrix inversion, and $\hat{\eta}_k$ denotes the usual small imaginary constant that is positive (negative) for empty (occupied) states, respectively.

For the phonon self-energy, i.e., with two external lines, there is only a single diagram, shown in Fig. 3a for one possible choice of the band indices, which corresponds to

$$\Delta\omega^2 = \sum_{m,n\in\{+,-\}} \int \frac{dk}{\pi}\, g_{m,n}(k)\Pi_{m,n}(k)g_{n,m}(k), \tag{18}$$

$$\Pi_{m,n}(k) = \frac{f_m(k) - f_n(k)}{\varepsilon_m(k) - \varepsilon_n(k)}, \tag{19}$$

$$f_m(k) = \begin{cases} 1 & \text{for } m = -1 \text{ and } |k| \le k_f, \\ 0 & \text{otherwise.} \end{cases} \tag{20}$$

This allows us to simplify the result to

$$\Delta\omega^2 = -\frac{2}{\pi}\int_{-k_f}^{k_f} dk\, \frac{|g_{+-}(k)|^2}{\varepsilon_+ - \varepsilon_-} = -\frac{2}{\pi}\int_{-k_f}^{k_f} dk\, \frac{4t^2\sin^2(k)}{4t\cos(k)} = -\frac{2t}{\pi}\int_{-k_f}^{k_f} \frac{\sin^2(k)}{\cos(k)}dk. \tag{21}$$

This is consistent with Eq. (12). This shows that the harmonic energy landscape can be calculated entirely from the undistorted structure at $\alpha = 0$, based on the electronic dispersion $\hat{\varepsilon}_0$ and the electron-phonon coupling $\hat{g}$.

4.2 Higher-order diagrams

It is also possible to calculate the energy landscape beyond the quadratic term. A special property of the SSH model is that the there are no higher-order electron-phonon vertices nor anharmonic bare phonon terms. Because of this, the entire perturbation theory is expressed in $\varepsilon_\pm$ and g. For example, the diagram for the fourth order contribution α^4 is shown in Fig. 3b.

SciPost SciPost Phys. 11, 079 (2021)

This is the only connected diagram at this order.[2] Note that all external phonons have $q = 0$, so all electronic lines have the same momentum k and energy E. The band index of the electronic lines is alternating, since the electron-phonon coupling is entirely off-diagonal. The expression corresponding to this diagram is of the form

$$h^{(4)} = \frac{1}{2}\int \frac{dk}{\pi}\int dE\; g_{+-}(k)g_{-+}(k)g_{+-}(k)g_{-+}(k)\; G_-(k,E)G_+(k,E)G_-(k,E)G_+(k,E), \quad (22)$$

which already includes a factor 2 accounting for the fact that there is a second way to assign the band indices.[3]

The product of Green's functions can be reduced by repeated application of the relation $AB = (B - A)/(A^{-1} - B^{-1})$ for $A \neq B$, which is helpful because $G_\pm^{-1}(k,E) = E \mp |\varepsilon_0(k)| + i\eta_k$ is very simple. Below, all G's have the same arguments k, E, which were dropped for notational convenience.

$$G_-G_+G_-G_+ = (G_+ - G_-)\frac{1}{2|\varepsilon_0|}(G_+ - G_-)\frac{1}{2|\varepsilon_0|} = \frac{G_-^2 + G_+^2}{4|\varepsilon_0|^2} - \frac{G_+ - G_-}{4|\varepsilon_0|^3}. \quad (23)$$

In the denominators we have already safely taken the limit $\eta \to 0$. Now, the integral over E can be performed using $\int dE G_\pm^2(E) = 0$ and $\int dE G_\pm(E) = n(\varepsilon_\pm(k))$. Here, $n(\varepsilon_\pm(k))$ is the occupation, which is unity for the $-$ branch and $|k| < k_f$ and zero otherwise. This gives the same result as Eq. (13),

$$h^{(4)} = \frac{1}{2}\int_{-k_f}^{k_f}\frac{dk}{\pi}(2t)^4\sin^4(k)\frac{1}{4(2t)^3\cos^3(k)} = \frac{t}{4\pi}\int_{-k_f}^{k_f} dk\frac{\sin^4(k)}{\cos^3(k)}. \quad (24)$$

Diagrams at higher order can be evaluated in the same way, by repeated simplification of products of Green's functions. An interesting aspect is that the entire potential-energy landscape $E(\alpha)$ can be calculated in this way (for $\langle n\rangle \neq 1$, see Sec. 7) without ever determining how the band dispersion changes.

4.3 Change in electronic structure

The change in the electronic structure is given by the self-energy $\Sigma(E,k)$ and can be obtained diagrammatically by considering the sum of all one-electron irreducible diagrams. Now, the electronic lines are amputated and the phononic ends of the vertices are connected to crosses representing α. This is similar to the way an external Zeeman magnetic field or scattering potential can be included in a diagrammatic theory. Note that due to the Born-Oppenheimer approximation, there is no true phonon propagator with two end points, which would represent the phonon dynamics.

In the present model, it turns out that there is only a single, trivial diagram for the self-energy,

$\Sigma_{+-} = g_{+-}\alpha =$ 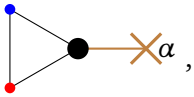 , (25)

with an equivalent diagram for Σ_{-+}. Together, they recover the exact electronic Green's function $\hat{\mathcal{G}}$ via the Dyson equation,

$$\hat{\mathcal{G}}^{-1} = \hat{G}^{-1} - \hat{\Sigma} = E - \hat{\varepsilon}_0 - \alpha\hat{g} + i\eta_k = E - \hat{\varepsilon} + i\eta_k. \quad (26)$$

[2] We remind the reader that we consider classical displacements, in the sense of the Born-Oppenheimer approximation. Thus, internal phonon propagators are not allowed in the diagrams.

[3] The $-$ line starting at the top left could also go to the bottom left instead of the top right. To keep the diagram connected, all other lines are then immediately fixed.

SciPost Phys. 11, 079 (2021)

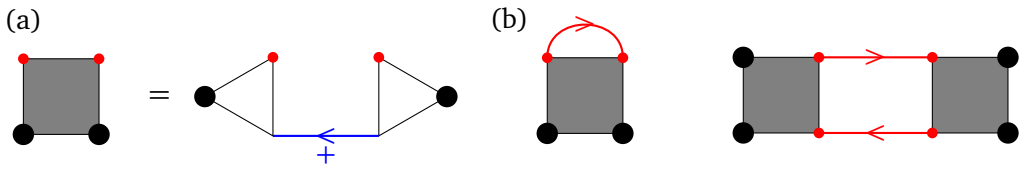

Figure 4: (a) The interaction vertex of the effective single-band theory (left-hand side) can be expressed in terms of the original vertices and the electronic band that is integrated out. (b) The diagrams responsible for the α^2 and α^4 contributions to the energy in the single-band model.

5 Single-band effective model

At $\langle n \rangle < 1$, there is only one partially filled band and this motivates us to investigate the possibility of describing the CDW via a single-band effective model. Here, we construct a model consisting of the partially filled electronic band, the bare phonon, and the coupling between the two. Formally, such a model is obtained by integrating out the unoccupied band of the two-band model. The effective action of the single-band model contains (partially) renormalized, dynamically screened interactions between these electrons and the phonons. In fact, the interaction vertices in this effective model can and do have an entirely different structure compared to those of the original two-band model. Generally, the vertices in the effective theory are obtained by collecting all connected diagrams consisting of rest space (here: ε_+) internal lines with a particular number of external phonon and target space (here: ε_-) lines, and an infinite set of vertices can appear in this way. The only general constraints are the conservation of the fermion number and momentum conservation. Thus, the low-energy Hamiltonian can contain interactions of the form $\alpha^m (c^\dagger c)^n$ for arbitrary m and n. However, additional symmetries of the system can provide further constraints on the effective action.

Here, the single-band model is energetically completely symmetric in $\alpha \longleftrightarrow -\alpha$ and this implies that only even powers of α can appear in the effective action. In other words, only interaction vertices with an even number of phonon lines are allowed.[4]

In fact, looking at the diagrammatic structure, it turns out that the single-band effective theory of the SSH model only contains one interaction vertex, shown in Fig 4a. This vertex has two phonon and two external electronic lines (one incoming, one outgoing) and takes the value

$$V(E,k) = |g_{+-}|^2 \, G(E,k) = 4t^2 \sin^2(k) \frac{1}{E - |\varepsilon_0(k)| + i\eta_k}. \tag{27}$$

Note that V depends explicitly on E; the screened interactions that enter the effective model are dynamical quantities. The effective model contains only a single fermion with dispersion ε_-, so no further electronic band label is necessary.

The downfolded SSH model has only a single effective interaction vertex. This happens because the electron-phonon coupling in the original SSH model only has a single external high-energy electron (blue line in Fig. 4a). On the other hand, if the original model had contained either electron-electron interactions in the high-energy band or electron-phonon coupling between different electronic states in the high-energy band, then the downfolding would be more involved, since more diagrammatic contributions would appear in the expression for the effective action.

[4] Note that in the two-band model, although the eigenvalues are symmetric in α, the eigenvectors are not and this leads to the finite value of $\hat{g}$, which is entirely off-diagonal in the electronic eigenbasis.

SciPost SciPost Phys. 11, 079 (2021)

For the energy $E(\alpha)$, the second-order contribution, shown in Fig. 4b, is

$$\frac{1}{2}\Delta\omega^2 = \int \frac{dk}{\pi} \int dE\, V(E,k)G(E,k), \tag{28}$$

which upon insertion of Eq. (27) is equal to the result we obtained in the two-band model. Similarly, the fourth-order contribution, also shown in Fig. 4b, is

$$\begin{aligned} h^{(4)} &= \frac{1}{2}\int \frac{dk}{\pi} \int dE\, V^2(E,k)G^2(E,k) \\ &= \frac{1}{2}\int \frac{dk}{\pi} \int dE \frac{16t^4\sin^4(k)}{(E-|\varepsilon_0(k)|+i\eta_k)^2}\frac{1}{(E+|\varepsilon_0(k)|+i\eta_k)^2}. \end{aligned} \tag{29}$$

The denominator can be simplified using the same techniques as above and this gives the same final result as the earlier expression for $h^{(4)}$.

5.1 Change in electronic structure in the single-band model

In the effective model, only the electronic target space is considered, corresponding to the lower band at zero displacement. The rest space has been integrated out. Σ is now a scalar quantity and it is once again given by a single diagram,

$$\Sigma(k,E) = \alpha^2 V(k,E) = 4\alpha^2 t^2 \frac{\sin^2(k)}{E-|\varepsilon_0(k)|+i\eta_k}. \tag{30}$$

In this case, $\Sigma(k,E)$ is an explicit function of E and it is not possible to interpret it purely as a change in the dispersion. Since the true change in the electronic structure involves a change in the orbital composition of the bands and thus coupling between the bands and changes in the wave functions, it is not possible to capture this entirely in a single-band model. However, if we restrict ourselves to the vicinity of the lower band in terms of energy, we find

$$\Sigma(k,-2t\cos k) = -t\frac{\sin^2(k)}{\cos(k)}\alpha^2, \tag{31}$$

which is equal to the exact second-order expansion of Eq. (5).

At the same time, the self-energy of Eq. (30) has a pole at $E=|\varepsilon_0|$, the energy of the upper band that has been integrated out. In the spectral function $A(E,k) = -\frac{1}{\pi}\operatorname{Im} G(E,k)$, this shows up as interaction-induced spectral-weight transfer, as shown in Fig. 5. The original spectral weight of the noninteracting, i.e., undistorted downfolded model (grey peak) is distributed to the positions of the lower and upper band of the interacting, i.e., distorted model (orange peaks). Thus, even though it cannot represent the matrix structure of the electronic Green's function, the downfolded model has spectral weight at the right locations. Note that there is no imaginary part in the self-energy and thus no additional broadening of these peaks in the downfolded model; all broadening comes from the constant $\eta = 0.05$ used for plotting the spectrum.

6 Constrained density-functional perturbation theory

The downfolding procedure employed above is based on an explicit resummation of the diagrammatic series and is able to reproduce the screening from bare to dressed lattice potential exactly. This approach can be applied here, since we have full knowledge of the entire electronic structure and the electron-phonon coupling. In *ab initio* calculations, the downfolding

SciPost Phys. 11, 079 (2021)

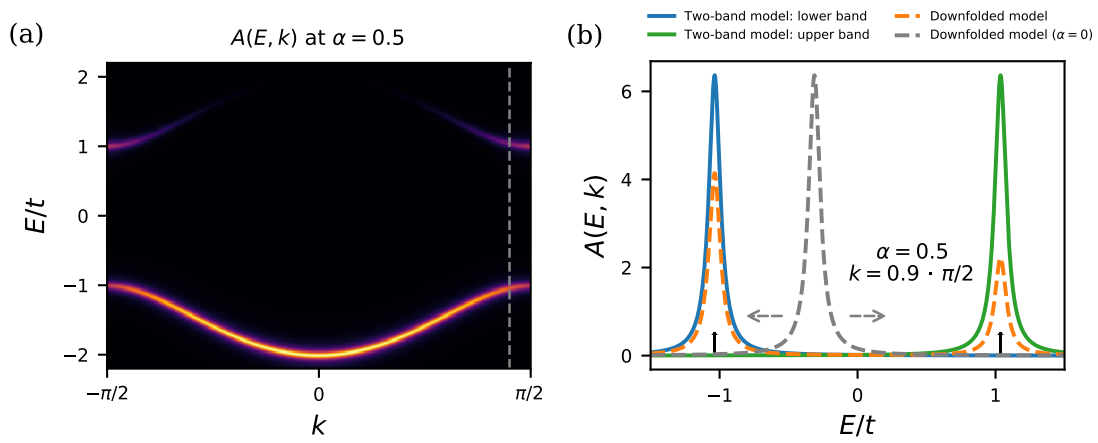

Figure 5: Spectral function of the downfolded single-band model for $\alpha = 0.5$. Here, a broadening $\eta = 0.05$ is used to improve visibility. (a) Spectral-weight transfer to the upper band occurs due to the self-energy. See Fig. 1b for the dispersion in the original two-band model. (b) Cross-section at $k = 0.9 \cdot \frac{\pi}{2}$, indicated by the grey dashed line in (a). The original model has two bands with spectral weight at $E = \pm|\varepsilon(k)|$, respectively (small vertical bars). In the single-band model at $\alpha > 0$, the self-energy leads to some spectral-weight transfer to the position of the upper band.

is usually done somewhat differently. Indeed, cDFPT is a tool commonly used for downfolding electron-phonon systems onto an electronic target space and calculating corresponding partially screened phonon frequencies. In general, it evaluates a Feynman diagram similar to Fig. 3a, with the restriction that at least one of the two electronic propagators shall not be part of the target space.

In the SSH model, if the lower band is chosen as the target space, cDFPT includes the only relevant screening process, with one + and one − electron, in its calculation of the partially screened phonon frequency. In other words,

$$\Pi^{\mathrm{cDFPT}}_{m,n} = \begin{cases} 0 & \text{for } m = n = -, \\ \Pi_{m,n}(k) & \text{otherwise.} \end{cases} \tag{32}$$

Here $\Pi_{m,n}(k)$ is defined and used as in Eq. (19). In the SSH model, Π_{--} anyway does not contribute to the phonon renormalization, and as a result the cDFPT phonon frequency is identical to the fully screened phonon frequency.

The cDFPT low-energy model then basically consists of the fully screened phonon, the lower electronic band, and *no* electron-phonon coupling, since $g_{--} = 0$. Because of this special property of the SSH model, there is no real distinction between the partially and fully screened phonon.

7 Breakdown of perturbation theory at half-filling

The series expansion of the potential $E(\alpha)$ around $\alpha = 0$, performed either diagrammatically or by directly taking derivatives of $\varepsilon(k, \alpha)$, shows a regular pattern. Only even powers of α are allowed. For a given power α^{2n}, the diagrammatic contribution will be of the form (modulo prefactor) $g^{2n} G_-^n G_+^n$. The $2n$ electron-phonon vertices g contribute $(2t)^{2n} \sin^{2n}(k)$, whereas the Green's functions can be reduced to $n(\varepsilon_-(k))/(2\varepsilon_0)^{2n-1} \propto n(\varepsilon_-(k))/\cos^{2n-1}(k)$. The only

SciPost SciPost Phys. 11, 079 (2021)

role of the density is to determine the integration range, via k_f. This becomes qualitatively important for $\langle n\rangle \to 1$, $k_f \to \pi/2$, since $\varepsilon_0(k_f) \to 0$. The denominator in the integral diverges and as a result the entire integral is no longer convergent. In other words, perturbation theory around $\alpha = 0$ is not possible since $E(\alpha)$ is not an analytical function anymore. Physically, the dimerization at half-filling is a Peierls transition caused by the perfect nesting of the Fermi surface points $\pm\pi/2$ with respect to the dimerization wave vector π (in the original Brillouin zone). Thus, at half-filling, dimerization will occur even at arbitrarily large force constant k_s.

8 Conclusion and discussion

A key question in the investigation of coupled electron-phonon systems is the evolution of the total energy and electronic structure as a function of atomic displacement. In *ab initio* studies, it is desirable to gain (perturbative) access to this energy landscape starting from the undistorted structure and a small set of relevant electronic bands. In the SSH model, it is actually possible to perform this perturbative, diagrammatic expansion analytically and to trace the performance of effective models. This both provides a unique insight into "exact downfolding" and highlights the successes and possible failures of effective models.

The bare phonons in the SSH model are entirely harmonic by definition. Thus, all anharmonic effects in the potential energy have to be created by the (linear) coupling to the electrons and the resulting electronic screening. Due to the simple structure of the model, the screening can be calculated to arbitrary order in the displacement. It reduces the energetic cost of displacements and eventually leads to a CDW transition, i.e., the appearance of a new global minimum in the energy landscape at a finite displacement. In this model, all relevant quantities can be reduced to integrals over the occupied part of the Brillouin zone.

It is also possible to downfold onto a single-band model with only half the electronic degrees of freedom of the original system. The diagrammatic structure changes due to the downfolding; the electron-phonon coupling is now dynamical and quadratic in the displacement field. Still, the analytical evaluation of the diagrams determining the energy landscape is possible and agrees with the exact result. Regarding the electronic structure, the effective single-band model only has the ability to describe spectral-weight transfer and by construction does not have the ability to describe the changes in the orbital composition of the bands as the atoms move. In the cDFPT approach, as well as in the cRPA approach to Coulomb interactions, these changes in the electronic structure are usually not considered at all.

This observation is potentially relevant for several two-dimensional transition-metal dichalcogenides. For example, monolayer 1H-TaS_2 has a single band crossing the Fermi level and this band consists of a combination of $d_{0,+2,-2}$ orbitals. It was already known that the electronic matrix structure is imprinted on the momentum structure of the electron-phonon coupling in *ab initio* downfolding [29] and that the resulting single-band electron-phonon model accurately describes the phonon frequencies (i.e., the energy landscape close to the undistorted structure). A similar situation, with a single composite band crossing the Fermi level, occurs in 1H-NbS_2 [66]. An open question is how these single-band effective models perform in the description of the true electronic structure of the distorted phase. If the distortions lead to hybridization between target and rest space, downfolded models can only capture the spectral-weight transfer. On the other hand, downfolded approaches can fully describe processes that occur entirely in the target space. Thus, fluctuation diagnostics of the electron-phonon coupling [29] can provide an answer to this question.

The SSH model in the Born-Oppenheimer approximation—as studied here—is very much a simplification of the complex reality of electron-phonon-coupling and charge-density-wave physics. We assume that the lattice is one-dimensional, that the electronic hopping amplitudes

SciPost Phys. 11, 079 (2021)

and the bare restoring forces are linear in the displacement, that there is no electron-electron interaction, that there is a single relevant phonon mode (dimerization), and that the system is in the $T = 0$ ground state. Still, some general conclusions are possible from our work. It is possible to generate anharmonic phonon terms entirely electronically, from an initial Hamiltonian that has purely harmonic phonons. Diagrammatic expressions can be constructed for the electronic screening at and beyond the harmonic level; in the general case these will be infinite series of diagrams, but here there is only a single diagram at any order in the displacement. In the presence of multiple relevant phonons, see Appendix C, the Born-Oppenheimer energy landscape will include mode-mode coupling as well. Downfolding of the electronic space generates a new perturbation series, in which effective higher-order vertices appear naturally. Unlike in the original Hamiltonian, the vertices of the downfolded system are also dynamical (frequency-dependent). As a result, the self-energy is dynamical as well, leading to spectral-weight transfer in the downfolded model. We note that this happens even though the electrons are noninteracting. The magnitude of the self-energy in the low-energy band is approximately given by the electron-phonon coupling (between the target and the rest space) squared times the displacement squared divided by the energy separation between the low-energy and the high-energy band. This supports the natural strategy of including bands in the low-energy model that are close in energy and those that are strongly coupled to the target space via the relevant phonon modes.

Funding information This work is supported by the Deutsche Forschungsgemeinschaft (DFG) through the Research Training Group Quantum Mechanical Materials Modelling (RTG 2247) and Germany's Excellence Strategy (University Allowance, EXC 2077) as well as by the Central Research Development Fund of the University of Bremen.

A Number of minima of $E(\alpha)$

The SSH model in the limit of large α is unlikely to be an accurate description of any real physics, but it is useful to establish some formal results. First of all, the triangle inequality provides us with bounds on the dispersion,

$$\max(\cos(k), \alpha\,|\sin(k)|) \leq \frac{|\varepsilon_{\pm}(k)|}{2t} \leq \cos(k) + \alpha\,|\sin(k)|\,. \tag{33}$$

Thus, in the limit of large α, $\varepsilon(k)$ is roughly proportional to $\alpha \sin(k)$. The total energy is then dominated by the purely lattice term proportional to $k_s\alpha^2$. We conclude that the energy landscape $E(\alpha)$ is bounded from below, as it should be.

Two types of energy landscape $E(\alpha)$ are discussed in the text, one with a single minimum at $\alpha = 0$ and one with two minima at $\alpha = \pm\alpha^*$. In fact, we can proof that these are the only two possibilities, no further local minima are allowed.

First, we define the auxiliary function $f(x) = -\sqrt{1+x^2}$, so that

$$\varepsilon_{-}(k,\alpha) = |\varepsilon_0(k)|\, f\left(\alpha \left|\frac{\sin(k)}{\cos(k)}\right|\right). \tag{34}$$

We observe that the second derivative of f, $f'' = -(1+x^2)^{-3/2}$, is monotonously increasing for $x \geq 0$. This implies that $d^2\varepsilon_{-}(k,\alpha)/d\alpha^2$ is also monotonously increasing as a function of α for $\alpha \geq 0$ and the same holds for $E(\alpha)$, which is just a k-integral over ε_{-}. Thus, there can be at most one $\alpha \geq 0$ where $d^2E(\alpha)/d\alpha^2 = 0$. In $E(\alpha)$, local minima ($d^2E/d\alpha^2 > 0$) and local maxima ($d^2E/d\alpha^2 < 0$) alternate, so by the intermediate value theorem $d^2E/d\alpha^2$ must cross zero between every local optimum of $E(\alpha)$. This can happen only once for $\alpha \geq 0$, so there are

SciPost Phys. 11, 079 (2021)

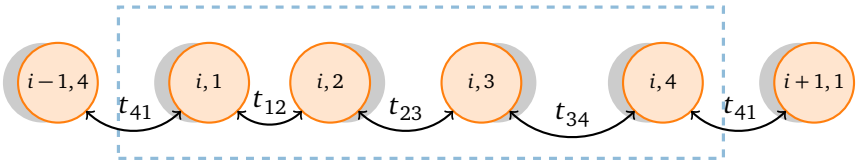

Figure 6: Length-4 unit cell with a periodic distortion (phonon eigenmode α_2). The double arrows indicate the four hopping parameters t_{ij}. The atoms are labeled by their unit-cell number and their position within the unit cell.

at most two optima at $\alpha \geq 0$ and one of them is at $\alpha = 0$ by symmetry. Since $E(\alpha) \to +\infty$ for $\alpha \to +\infty$, there is either a single global minimum at $\alpha = 0$ or a local maximum at $\alpha = 0$ and two global minima at $\pm\alpha^*$.

B Basis transformation of the electron-phonon coupling

The electronic part is most conveniently expressed in the band basis of $\hat{\varepsilon}_0$, which is $\hat{\varepsilon}$ evaluated at $\alpha = 0$. The two eigenvalues of $\hat{\varepsilon}_0$ are $\varepsilon_{\pm,0} = \pm 2t\cos(k)$ with corresponding eigenvectors

$$\vec{v}_\pm(k) = \frac{1}{\sqrt{2}}\begin{pmatrix} 1 \\ \mp e^{-ik} \end{pmatrix}. \tag{35}$$

With the eigenvectors, we can form the transformation matrix

$$\hat{U}(k) = \frac{1}{\sqrt{2}}\begin{pmatrix} 1 & 1 \\ -e^{-ik} & e^{-ik} \end{pmatrix}, \tag{36}$$

which diagonalizes $\hat{\varepsilon}_0$. This yields the electron-phonon coupling in the band basis,

$$\hat{g}(k) = \hat{U}^{-1}(k)\underline{\hat{g}}(k)\hat{U}(k) = 2t\begin{pmatrix} 0 & i\sin(k) \\ -i\sin(k) & 0 \end{pmatrix}. \tag{37}$$

C Beyond dimerization: 4-site unit cell

At half-filling, the dimerization is commensurate in the sense that $2k_f = q_{\text{dimerization}}$. We have already shown that dimerization can also be energetically favorable away from half-filling, but so far we have not considered CDWs with other periodicities. In this appendix, we consider periodicity 4, which allows for the study of additional phonon modes. Because this doubling of the unit cell increases both the number of phonons and the number of electronic bands, it is more difficult to derive compact formulas and our treatment remains relatively brief, highlighting some similarities and differences to the 2-site unit cell.

In this case, it is convenient to first consider the electronic dispersion as a function of the four hopping amplitudes t_{ij}, as shown in Fig. 6. In the SSH model, these hopping parameters will be linear functions of the atomic displacements.

The electronic Hamiltonian is

$$\hat{\varepsilon}(k) = \begin{pmatrix} 0 & t_{12} & 0 & t_{41}\exp(4ik) \\ t_{12} & 0 & t_{23} & 0 \\ 0 & t_{23} & 0 & t_{34} \\ t_{41}\exp(-4ik) & 0 & t_{34} & 0 \end{pmatrix}. \tag{38}$$

SciPost Phys. 11, 079 (2021)

With $t_{\mathrm{RMS}}^2 = (t_{12}^2 + t_{23}^2 + t_{34}^2 + t_{41}^2)/4$, its four eigenvalues ε_{++}, ε_{+-}, ε_{-+}, and ε_{--} read

$$\varepsilon_{\pm\pm}(k) = \pm\sqrt{2t_{\mathrm{RMS}}^2 \pm \sqrt{4t_{\mathrm{RMS}}^4 + 2t_{12}t_{23}t_{34}t_{41}\cos(4k) - t_{12}^2 t_{34}^2 - t_{23}^2 t_{41}^2}}. \tag{39}$$

Here, $-\pi/4 < k \leq \pi/4$ is the Brillouin zone corresponding to this unit cell. As for the dimerization transition, the total electronic energy is given by $\sum_m \int dk\, \varepsilon_m(k) n(\varepsilon_m(k))$.

Now, in the SSH model, the hopping parameters depend linearly on the atomic displacements. We consider three phonon modes α_1, α_2, and α_3 defined by

$$\begin{aligned} t_{12} &= t(1 + \alpha_1 + \alpha_2), \\ t_{23} &= t(1 - \alpha_1 + \alpha_3), \\ t_{34} &= t(1 + \alpha_1 - \alpha_2), \\ t_{41} &= t(1 - \alpha_1 - \alpha_3). \end{aligned} \tag{40}$$

α_1 is the dimerization mode studied in the main text, α_2 is sketched in Fig. 6, and α_3 is obtained from α_2 by translating the unit cell by one atom. They are eigenmodes at $q = 0$. Combining Eqs. (39) and (40), it is possible to calculate $\varepsilon(k; \alpha_1, \alpha_2, \alpha_3)$ and its derivatives with respect to α_i. Using computer algebra, it is possible to evaluate these derivatives straightforwardly, although the expressions quickly become unwieldy. Below, we will briefly discuss the nonzero terms at the lowest orders. Finally, integrating these derivatives of the dispersion over the filled part of the Brillouin zone (for each band) then gives the terms in the Taylor expansion of $E(\alpha_1, \alpha_2, \alpha_3)$, as in Sec. 3 of the main text. The first derivative vanishes as expected, $\partial_{\alpha_1}\varepsilon = \partial_{\alpha_2}\varepsilon = \partial_{\alpha_3}\varepsilon = 0$. The second derivative is diagonal in the phonon index, $\partial_{\alpha_1,\alpha_2}\varepsilon = \partial_{\alpha_1,\alpha_3}\varepsilon = \partial_{\alpha_2,\alpha_3}\varepsilon = 0$, so the only nonzero elements are $\partial_{\alpha_1,\alpha_1}\varepsilon$ and $\partial_{\alpha_2,\alpha_2}\varepsilon = \partial_{\alpha_3,\alpha_3}\varepsilon$. At the level of the third derivative, we find a finite term with mixed phonon labels, to be explicit:

$$\partial_{\alpha_1,\alpha_2,\alpha_2}\varepsilon = -\partial_{\alpha_1,\alpha_3,\alpha_3}\varepsilon = t\left(-\frac{\cos 2k}{\cos k}, \frac{\cos 2k}{\sin k}, -\frac{\cos 2k}{\sin k}, \frac{\cos 2k}{\cos k}\right). \tag{41}$$

Here, the four components in the vector correspond to the bands from lowest to highest energy, and we have assumed $k > 0$. At fourth order, we find nonzero expressions only for the terms where the derivatives appear in pairs, e.g., $\partial_{\alpha_1,\alpha_1,\alpha_2,\alpha_2}\varepsilon$. Symmetries and momentum conservation still ensure that many terms in the expansion vanish, but already at the third order we see that qualitatively new terms appear compared to energy landscape for the 2-site unit cell. In other words, the Feynman diagrams studied in the main text are all relevant in general, but diagrams that were "forbidden" in that simple system can play a role. It is difficult to make any statements about the sign and relative magnitude a priori; for a computational case study of nonlinear mode-mode coupling, see Ref. [67].

Similarly, the Hamiltonian can be written in terms of the bare dispersion and the electron-phonon couplings, now as 4×4 matrices. In analogy to the main text, the terms in the expansion of $E(\alpha_1, \alpha_2, \alpha_3)$ can then be obtained diagrammatically.

References

[1] E. Pytte, *Contribution of the electron-phonon interaction to the effective mass, superconducting transition temperature, and the resistivity in aluminium*, J. Phys. Chem. Solids **28**, 93 (1967), doi:10.1016/0022-3697(67)90201-6.

[2] P. Fulde, P. Horsch and A. Ramšak, *Effective mass decrease due to electron-phonon interaction in heavy fermion systems*, Z. Phys. B Condens. Matter **90**, 125 (1993), doi:10.1007/BF01321043.

[3] J. L. M. van Mechelen, D. van der Marel, C. Grimaldi, A. B. Kuzmenko, N. P. Armitage, N. Reyren, H. Hagemann and I. I. Mazin, *Electron-phonon interaction and charge carrier mass enhancement in $SrTiO_3$*, Phys. Rev. Lett. **100**, 226403 (2008), doi:10.1103/PhysRevLett.100.226403.

[4] W. A. Saidi and A. Kachmar, *Effects of electron–phonon coupling on electronic properties of methylammonium lead iodide perovskites*, J. Phys. Chem. Lett. **9**, 7090 (2018), doi:10.1021/acs.jpclett.8b03164.

[5] C. P. Koçer, K. Haule, G. Lucian Pascut and B. Monserrat, *Efficient lattice dynamics calculations for correlated materials with DFT+DMFT*, Phys. Rev. B **102**, 245104 (2020), doi:10.1103/PhysRevB.102.245104.

[6] W. H. Appelt, A. Östlin, I. Di Marco, I. Leonov, M. Sekania, D. Vollhardt and L. Chioncel, *Lattice dynamics of palladium in the presence of electronic correlations*, Phys. Rev. B **101**, 075120 (2020), doi:10.1103/PhysRevB.101.075120.

[7] J. Bardeen, L. N. Cooper and J. R. Schrieffer, *Theory of superconductivity*, Phys. Rev. **108**, 1175 (1957), doi:10.1103/PhysRev.108.1175.

[8] L. Y. L. Shen, *Evidence for the electron-phonon interaction in the superconductivity of a transition metal-tantalum*, Phys. Rev. Lett. **24**, 1104 (1970), doi:10.1103/PhysRevLett.24.1104.

[9] S. G. Louie and M. L. Cohen, *Superconducting transition temperatures for weak and strong electron-phonon coupling*, Solid State Commun. **22**, 1 (1977), doi:10.1016/0038-1098(77)90929-2.

[10] W. J. Carr, *Theory of superconductivity based on direct electron-phonon coupling. I*, Phys. Rev. B **33**, 1585 (1986), doi:10.1103/PhysRevB.33.1585.

[11] M. Shirai, N. Suzuki and K. Motizuki, *Electron-lattice interaction and superconductivity in $BaPb_{1-x}Bi_xO_3$ and $Ba_xK_{1-x}BiO_3$*, J. Phys.: Condens. Matter **2**, 3553 (1990), doi:10.1088/0953-8984/2/15/012.

[12] T. Oda, M. Shirai, N. Suzuki and K. Motizuki, *Electron-phonon interaction, lattice dynamics and superconductivity of an oxide spinel $LiTi_2O_4$*, J. Phys.: Condens. Matter **6**, 6997 (1994), doi:10.1088/0953-8984/6/35/009.

[13] T. Hakioğlu, V. A. Ivanov, A. S. Shumovsky and B. Tanatar, *Phonon squeezing via correlations in the superconducting electron-phonon interaction*, Phys. Rev. B **51**, 15363 (1995), doi:10.1103/PhysRevB.51.15363.

[14] I. I. Mazin and V. P. Antropov, *Electronic structure, electron–phonon coupling, and multiband effects in MgB_2*, Phys. C: Supercond. **385**, 49 (2003), doi:10.1016/S0921-4534(02)02299-2.

[15] A. Subedi and D. J. Singh, *Electron-phonon superconductivity in noncentrosymmetric $LaNiC_2$: First-principles calculations*, Phys. Rev. B **80**, 092506 (2009), doi:10.1103/PhysRevB.80.092506.

[16] G. Savini, A. C. Ferrari and F. Giustino, *First-principles prediction of doped graphane as a high-temperature electron-phonon superconductor*, Phys. Rev. Lett. **105**, 037002 (2010), doi:10.1103/PhysRevLett.105.037002.

[17] M. L. Cohen, *Electron–phonon induced pairing and its limits for superconducting systems*, Phys. E: Low-dimens. Syst. Nanostructures **43**, 657 (2011), doi:10.1016/j.physe.2010.07.023.

[18] R. Szczęśniak, A. M. Duda, E. A. Drzazga and M. A. Sowińska, *The Eliashberg study of the electron–phonon superconductivity in YSn_3 compound*, Phys. C: Supercond. Appl. **506**, 115 (2014), doi:10.1016/j.physc.2014.09.009.

[19] M. J. Rice, *Organic linear conductors as systems for the study of electron-phonon interactions in the organic solid state*, Phys. Rev. Lett. **37**, 36 (1976), doi:10.1103/PhysRevLett.37.36.

[20] S. N. Behera and S. G. Mishra, *Electron-phonon interaction in charge-density-wave superconductors*, Phys. Rev. B **31**, 2773 (1985), doi:10.1103/PhysRevB.31.2773.

[21] J. M. Carpinelli, H. H. Weitering, E. W. Plummer and R. Stumpf, *Direct observation of a surface charge density wave*, Nature **381**, 398 (1996), doi:10.1038/381398a0.

[22] S. Sharma, L. Nordström and B. Johansson, *Stabilization of charge-density waves in 1T-TaX_2(X=S,Se,Te): First-principles total energy calculations*, Phys. Rev. B **66**, 195101 (2002), doi:10.1103/PhysRevB.66.195101.

[23] C. Battaglia et al., *Fermi-surface-induced lattice distortion in $NbTe_2$*, Phys. Rev. B **72**, 195114 (2005), doi:10.1103/PhysRevB.72.195114.

[24] M. D. Johannes and I. I. Mazin, *Fermi surface nesting and the origin of charge density waves in metals*, Phys. Rev. B **77**, 165135 (2008), doi:10.1103/PhysRevB.77.165135.

[25] F. Weber et al., *Extended phonon collapse and the origin of the charge-density wave in 2H-$NbSe_2$*, Phys. Rev. Lett. **107**, 107403 (2011), doi:10.1103/PhysRevLett.107.107403.

[26] M. Calandra and F. Mauri, *Charge-density wave and superconducting dome in $TiSe_2$ from electron-phonon interaction*, Phys. Rev. Lett. **106**, 196406 (2011), doi:10.1103/PhysRevLett.106.196406.

[27] Y. Liu et al., *Nature of charge density waves and superconductivity in 1T-$TaSe_{2-x}Te_x$*, Phys. Rev. B **94**, 045131 (2016), doi:10.1103/PhysRevB.94.045131.

[28] Y. Y. Peng et al., *Enhanced electron-phonon coupling for charge-density-wave formation in $La_{1.8-x}Eu_{0.2}Sr_xCuO_{4+\delta}$*, Phys. Rev. Lett. **125**, 097002 (2020), doi:10.1103/PhysRevLett.125.097002.

[29] J. Berges, E. G. C. P. van Loon, A. Schobert, M. Rösner and T. O. Wehling, *Ab initio phonon self-energies and fluctuation diagnostics of phonon anomalies: Lattice instabilities from Dirac pseudospin physics in transition metal dichalcogenides*, Phys. Rev. B **101**, 155107 (2020), doi:10.1103/PhysRevB.101.155107.

[30] W. Wang, B. Wang, Z. Gao, G. Tang, W. Lei, X. Zheng, H. Li, X. Ming and C. Autieri, *Charge density wave instability and pressure-induced superconductivity in bulk 1T-NbS_2*, Phys. Rev. B **102**, 155115 (2020), doi:10.1103/PhysRevB.102.155115.

[31] J. Labbe, *Weak coupling electron-phonon for high T_c superconductors*, Phys. Scr. **T29**, 82 (1989), doi:10.1088/0031-8949/1989/T29/014.

[32] J. H. Kim and D. Ho Wu, *Unusual electron–phonon superconductivity in nickel borocarbides?*, Phys. C: Supercond. Appl. **364**, 24 (2001), doi:10.1016/S0921-4534(01)00718-3.

[33] A. Lanzara et al., *Evidence for ubiquitous strong electron–phonon coupling in high-temperature superconductors*, Nature **412**, 510 (2001), doi:10.1038/35087518.

[34] S. Ishihara and N. Nagaosa, *Interplay of electron-phonon interaction and electron correlation in high-temperature superconductivity*, Phys. Rev. B **69**, 144520 (2004), doi:10.1103/PhysRevB.69.144520.

[35] J. P. Hague, *d-wave superconductivity from electron-phonon interactions*, Phys. Rev. B **73**, 060503 (2006), doi:10.1103/PhysRevB.73.060503.

[36] V. Z. Kresin and S. A. Wolf, *Colloquium: Electron-lattice interaction and its impact on high T_c superconductivity*, Rev. Mod. Phys. **81**, 481 (2009), doi:10.1103/RevModPhys.81.481.

[37] J. Chang, I. Eremin and P. Thalmeier, *Cooper-pair formation by anharmonic rattling modes in the β-pyrochlore superconductor KOs_2O_6*, New J. Phys. **11**, 055068 (2009), doi:10.1088/1367-2630/11/5/055068.

[38] J. Bouvier and J. Bok, *Electron-phonon interaction in the high-T_c cuprates in the framework of the Van Hove scenario*, Adv. Condens. Matter Phys., 472636 (2010), doi:10.1155/2010/472636.

[39] V. Ashokan, B. D. Indu and A. K. Dimri, *Signature of electron-phonon interaction in high temperature superconductors*, AIP Adv. **1**, 032101 (2011), doi:10.1063/1.3610642.

[40] A. A. Kordyuk et al., *Angle-resolved photoemission spectroscopy of superconducting LiFeAs: Evidence for strong electron-phonon coupling*, Phys. Rev. B **83**, 134513 (2011), doi:10.1103/PhysRevB.83.134513.

[41] K. T. Chan, B. D. Malone and M. L. Cohen, *Electron-phonon coupling and superconductivity in arsenic under pressure*, Phys. Rev. B **86**, 094515 (2012), doi:10.1103/PhysRevB.86.094515.

[42] A.-M. Zhang and Q.-M. Zhang, *Electron—phonon coupling in cuprate and iron-based superconductors revealed by Raman scattering*, Chin. Phys. B **22**, 087103 (2013), doi:10.1088/1674-1056/22/8/087103.

[43] P. Zhang, H. Yuan and C. Cao, *Electron-phonon coupling and nontrivial band topology in noncentrosymmetric superconductors LaNiSi, LaPtSi, and LaPtGe*, Phys. Rev. B **101**, 245145 (2020), doi:10.1103/PhysRevB.101.245145.

[44] S. Baroni, S. de Gironcoli, A. Dal Corso and P. Giannozzi, *Phonons and related crystal properties from density-functional perturbation theory*, Rev. Mod. Phys. **73**, 515 (2001), doi:10.1103/RevModPhys.73.515.

[45] M. Born and R. Oppenheimer, *Zur Quantentheorie der Molekeln*, Ann. Phys. **389**, 457 (1927), doi:10.1002/andp.19273892002.

[46] P. Hohenberg and W. Kohn, *Inhomogeneous electron gas*, Phys. Rev. **136**, B864 (1964), doi:10.1103/PhysRev.136.B864.

[47] X. Gonze and J.-P. Vigneron, *Density-functional approach to nonlinear-response coefficients of solids*, Phys. Rev. B **39**, 13120 (1989), doi:10.1103/PhysRevB.39.13120.

[48] X. Gonze, *Perturbation expansion of variational principles at arbitrary order*, Phys. Rev. A **52**, 1086 (1995), doi:10.1103/PhysRevA.52.1086.

[49] X. Gonze, *Adiabatic density-functional perturbation theory*, Phys. Rev. A **52**, 1096 (1995), doi:10.1103/PhysRevA.52.1096.

[50] F. Giustino, *Electron-phonon interactions from first principles*, Rev. Mod. Phys. **89**, 015003 (2017), doi:10.1103/RevModPhys.89.015003.

[51] Y. Nomura and R. Arita, *Ab initio downfolding for electron-phonon-coupled systems: Constrained density-functional perturbation theory*, Phys. Rev. B **92**, 245108 (2015), doi:10.1103/PhysRevB.92.245108.

[52] Y. Nomura, S. Sakai, M. Capone and R. Arita, *Exotics-wave superconductivity in alkali-doped fullerides*, J. Phys.: Condens. Matter **28**, 153001 (2016), doi:10.1088/0953-8984/28/15/153001.

[53] R. Arita, T. Koretsune, S. Sakai, R. Akashi, Y. Nomura and W. Sano, *Nonempirical calculation of superconducting transition temperatures in light-element superconductors*, Adv. Mater. **29**, 1602421 (2017), doi:10.1002/adma.201602421.

[54] H. Fröhlich, *Electrons in lattice fields*, Adv. Phys. **3**, 325 (1954), doi:10.1080/00018735400101213.

[55] T. Holstein, *Studies of polaron motion*, Ann. Phys. **8**, 325 (1959), doi:10.1016/0003-4916(59)90002-8.

[56] W. P. Su, J. R. Schrieffer and A. J. Heeger, *Solitons in polyacetylene*, Phys. Rev. Lett. **42**, 1698 (1979), doi:10.1103/PhysRevLett.42.1698.

[57] M. Zoli, *Mass renormalization in the Su-Schrieffer-Heeger model*, Phys. Rev. B **66**, 012303 (2002), doi:10.1103/PhysRevB.66.012303.

[58] Z. Li, C. J. Chandler and F. Marsiglio, *Perturbation theory of the mass enhancement for a polaron coupled to acoustic phonons*, Phys. Rev. B **83**, 045104 (2011), doi:10.1103/PhysRevB.83.045104.

[59] E. Piegari, C. A. Perroni and V. Cataudella, *Signatures of polaron formation in systems with local and non-local electron-phonon couplings*, Eur. Phys. J. B **44**, 415 (2005), doi:10.1140/epjb/e2005-00140-5.

[60] D. J. J. Marchand, P. C. E. Stamp and M. Berciu, *Dual coupling effective band model for polarons*, Phys. Rev. B **95**, 035117 (2017), doi:10.1103/PhysRevB.95.035117.

[61] E. von Oelsen, A. Di Ciolo, J. Lorenzana, G. Seibold and M. Grilli, *Phonon renormalization from local and transitive electron-lattice couplings in strongly correlated systems*, Phys. Rev. B **81**, 155116 (2010), doi:10.1103/PhysRevB.81.155116.

[62] A. Altland and B. D. Simons, *Condensed matter field theory*, Cambridge University Press, Cambridge, ISBN 9780511789984 (2009), doi:10.1017/CBO9780511789984.

[63] J. E. Hirsch and R. M. Fye, *Monte Carlo method for magnetic impurities in metals*, Phys. Rev. Lett. **56**, 2521 (1986), doi:10.1103/PhysRevLett.56.2521.

[64] W. P. Su, J. R. Schrieffer and A. J. Heeger, *Soliton excitations in polyacetylene*, Phys. Rev. B **22**, 2099 (1980), doi:10.1103/PhysRevB.22.2099.

[65] T. Matsubara, *A new approach to quantum-statistical mechanics*, Prog. Theor. Phys. **14**, 351 (1955), doi:10.1143/PTP.14.351.

[66] E. G. C. P. van Loon, M. Rösner, G. Schönhoff, M. I. Katsnelson and T. O. Wehling, *Competing Coulomb and electron–phonon interactions in NbS_2*, npj Quantum Mater. **3**, 32 (2018), doi:10.1038/s41535-018-0105-4.

[67] C. van Efferen et al., *A full gap above the Fermi level: the charge density wave of monolayer VS_2*, arXiv:2101.01140.

12

Second publication: A full gap above the Fermi level: the charge density wave of monolayer VS_2

12.1. Statement of personal contribution

*This work has been published in Nat. Commun. **12**, 6837 (2021), arXiv:2101.01140. It has been realized in collaboration with C. van Efferen, J. Berges, J. Hall, E. G. C. P. van Loon, S. Kraus, T. Wekking, F. Huttmann, E. Plaar, N. Rothenbach, K. Ollefs, L. M. Arruda, N. Brookes, G. Schönhoff, K. Krummer, H. Wende, T. O. Wehling and T. Michely. My contribution to this work involved performing ab initio DFT and DFPT calculations. To this end, I relaxed large supercells to find CDW displacements. Afterwards, I calculated Born-Oppenheimer potential energy surfaces in the direction of these CDW displacements. Part of this work is the decomposition of CDW displacements into normal phonon modes. The idea was proposed by E. G. C. P. van Loon, where J. Berges and me constructed the necessary Python software to do this. With the help of this software I created Fig. 2b and 3 and wrote the corresponding parts of the manuscript, which have been revised and edited by all authors of this work. Furthermore, for the supplement, I created the data shown in Supplementary Figs. 5, 6a and the Table 1.*

12.2. Positioning within the scientific landscape

As previously discussed in Chapter 10 of this dissertation, the most straightforward depiction of a CDW is the Peierls model. According to this model, the displacements of atoms results in a complete gap in the electronic structure, yielding an electronic energy gain that counterbalances the energy loss from lattice distortion. Within the CDW literature, ongoing discussions have questioned whether these simple nesting scenarios adequately account for CDWs in diverse materials [172].

Conversely, it is often hypothesized that a strong and wavevector-dependent electron–phonon coupling serves as the principal driving force behind the transition [1]. In the case of such CDWs, spectral reconstructions are not confined to a narrow energy range around the Fermi energy but can manifest across the entire electronic structure. This opens the possibility for innovative spectral signatures of the CDW, including the potential for a complete gap situated away from the Fermi energy.

Despite this theoretical framework, there has been no experimental confirmation of a distinct CDW gap away from the Fermi energy for well-explored, strong-coupling transition metal dichalcogenides.

In our study, we identify a full gap in the density of states above the Fermi level of 1T-VS_2, using scanning tunneling spectroscopy (STM). Utilizing density functional theory and density functional perturbation theory, we confirm that, despite an initially unstable transverse phonon mode, the final CDW exhibits a significant combination of longitudinal modes. Our calculations align exceptionally well with experimental results, capturing the electronic structure of the CDW phase and the observed spatial charge distribution on the 1T-VS_2 islands.

After the publication of our work, another study emerged investigating CDWs in monolayer 1T-VS_2 [173]. In the following, their findings will be discussed and the differences between their work and ours will be highlighted. Their research combines experimental and theoretical approaches, much like our own study.

To set the stage for the contrasting results, let's first clarify the differences in the experimental setups. While our study used Gr/Ir(111) as the substrate, the authors of the contrasting paper grew 1T-VTe_2 on bilayer graphene/SiC(0001) and subsequently replaced Te atoms with S atoms. It should be noted that subtrates can have an influence on the formation of CDWs [174].

After growing the sample, the authors performed STM experiments. The resulting STM image reveals superlattice structures in the shape of a parallelogramm with a $\sqrt{2}1\mathrm{R}10.9^\circ \times \sqrt{3}\mathrm{R}30^\circ$ periodicity. This stands in contrast to our experimental findings, where the STM image depicts rectangular shaped $7 \times \sqrt{3}\mathrm{R}30^\circ$ and $9 \times \sqrt{3}\mathrm{R}30^\circ$ supercells. Both measurements are compelling and as such it seems that different CDWs are possible in monolayer VS_2.

The authors suggest higher-order Fermi-surface nesting as the proposed mechanism for the origin of the CDW. "Higher-order" refers to the doubling of the nesting vector $2\boldsymbol{q}$ instead of the conventional $\boldsymbol{q}$ nesting vector. This deviation from our findings warrants further investigation.

After proposing this mechanism, the authors continue to discuss the differences in the CDWs between VS_2 and VTe_2. In both materials, the wavevector $\boldsymbol{q} = 1/2\,\overline{\Gamma\mathrm{M}}$, which is commensurate with a 4×4 supercell, fulfills the nesting condition and additionally yields imaginary phonon frequencies. In Supplementary Fig. 7, the authors present the electronic susceptibility χ_0, with the largest peak residing at $\boldsymbol{q} = 1/2\,\overline{\Gamma\mathrm{M}}$. Based on these results one might be tempted to identify the 4×4 as the preferred CDW in both materials. However, this is clearly not the case for VS_2.

As written in our work, the clarification of the origin of the CDW based on nesting scenarios or more sophisticated fluctuations diagnostics, only concerns the harmonic term. Ultimately, the anharmonic terms are responsible for the stabilization. Consequently, the authors decision to conduct DFT calculations is noteworthy. These calculations allow for an assessment of the overall energy gain associated with different CDW configurations. For the $\sqrt{2}1\mathrm{R}10.9^\circ \times \sqrt{3}\mathrm{R}30^\circ$, the authors report an energy gain of 18 meV per unit cell. This value is slightly lower than the ~23 meV we reported, suggesting that the $7 \times \sqrt{3}\mathrm{R}30^\circ$ and $9 \times \sqrt{3}\mathrm{R}30^\circ$ are more stable based on DFT calculations.

Meanwhile, the 4×4 only comes with an energy gain of 4 meV per unit cell as can be seen in Fig. 2b of our work. Interestingly, in VTe_2, the 4×4 is preferred as seen in experiments [175, 176] and also at the DFT level. In the Supplementary Table 1, we report an energy gain of about 34 meV for the 4×4. Thus, DFT calculations are in these cases reliable in determining the energy gain of different CDWs, which align with the findings of experiments.

Lastly, I would like to propose the hypothesis that both identified CDWs ($\sqrt{2}1\mathrm{R}10.9^\circ \times \sqrt{3}\mathrm{R}30^\circ$ and $9 \times \sqrt{3}\mathrm{R}30^\circ$) are not very dissimilar. A direct comparison between Fig. 4d of Ref. [173] and Fig. 2c in our paper suggests that the atomic displacements are nearly identical. It is assumed that the apparent difference lies in the choice of the supercell geometry. In addition to the atomic positions,

the electronic structures in the distorted phases are similar as well (cf. Fig. 4e of Ref. [173] and Fig. 5a in our paper). The electronic band at Gamma seems to touch and slightly overlap the Fermi level, indicating that the gap opens above the Fermi level. This hypothesis should be further clarified in the future through an exchange of theoretically and experimentally derived data among the authors.

In summary, as highlighted in this section, the research field of CDWs is rich in complexity and occasionally marked by debates. Embracing the diversity of CDWs within a single material is the fascinating reality we must navigate. The competition between these different phases is what needs to be understood in the future.

nature COMMUNICATIONS

ARTICLE

https://doi.org/10.1038/s41467-021-27094-x OPEN

A full gap above the Fermi level: the charge density wave of monolayer VS_2

Camiel van Efferen[1✉], Jan Berges[2], Joshua Hall[1], Erik van Loon[2], Stefan Kraus[1], Arne Schobert[2], Tobias Wekking[1], Felix Huttmann[1], Eline Plaar[1], Nico Rothenbach[3], Katharina Ollefs[3], Lucas Machado Arruda[4], Nick Brookes[5], Gunnar Schönhoff[2], Kurt Kummer[5], Heiko Wende[3], Tim Wehling[2,6] & Thomas Michely[1]

In the standard model of charge density wave (CDW) transitions, the displacement along a single phonon mode lowers the total electronic energy by creating a gap at the Fermi level, making the CDW a metal–insulator transition. Here, using scanning tunneling microscopy and spectroscopy and ab initio calculations, we show that VS_2 realizes a CDW which stands out of this standard model. There is a full CDW gap residing in the unoccupied states of monolayer VS_2. At the Fermi level, the CDW induces a topological metal-metal (Lifshitz) transition. Non-linear coupling of transverse and longitudinal phonons is essential for the formation of the CDW and the full gap above the Fermi level. Additionally, x-ray magnetic circular dichroism reveals the absence of net magnetization in this phase, pointing to coexisting charge and spin density waves in the ground state.

[1] II. Physikalisches Institut, Universität zu Köln, Zülpicher Straße 77, 50937 Köln, Germany. [2] Institut für Theoretische Physik, Bremen Center for Computational Materials Science, and MAPEX Center for Materials and Processes, Universität Bremen, Otto-Hahn-Allee 1, 28359 Bremen, Germany. [3] Fakultät für Physik und Center für Nanointegration Duisburg-Essen (CENIDE), Universität Duisburg-Essen, Carl-Benz-Straße, 47057 Duisburg, Germany. [4] Institut für Experimentalphysik, Freie Universität Berlin, Arnimallee 14, 14195 Berlin, Germany. [5] European Synchrotron Research Facility (ESRF), Avenue des Martyrs 71, CS 40220, 38043 Grenoble Cedex 9, France. [6] Institute of Theoretical Physics, Universität Hamburg, Notkestraße 9-11, 22607 Hamburg, Germany. ✉email: efferen@ph2.uni-koeln.de

The many-body ground states of two-dimensional (2D) materials, wherein the reduced dimensionality leads to the enhancement of correlation effects, have been extensively researched in recent years. Of particular interest are the coexistence or competition between charge density waves (CDWs), as found in many 2D transition metal dichalcogenides (TMDCs), with superconducting and magnetic phases[1,2]. Since these phases can be strongly dependent on the substrate[3,4] or the defect density[5,6], the intrinsic properties of 2D materials are difficult to determine experimentally. In addition, CDWs themselves are the subject of an ongoing controversy regarding the driving force behind the CDW transition and the exact structure of the electronic system in the CDW phase of 2D materials[7,8].

Peierls' explanation for the CDW in a one-dimensional chain of atoms states that periodic lattice distortions open an electronic gap at the nesting wavevector. This gap at the Fermi level lowers the energy of the occupied states and thus the total energy, while increasing the energy of the unoccupied states that do not contribute to the total energy. Thus, this gapping mechanism requires the gap to be at the Fermi level. However, in many (quasi-)2D cases, CDWs form in the complete or partial absence of Fermi-surface nesting, suggesting that the driving mechanism behind their formation lies beyond a simple electronic disturbance[9], and it has been questioned whether the concept of nesting is essential for understanding CDW formation[10–12]. Instead, a strong and wavevector-dependent electron–phonon coupling is often predicted to be the driving force behind the transition[7]. For these CDWs, spectral reconstructions are not limited to a small energy window around the Fermi energy, but can occur throughout the entire electronic structure, opening the door to novel spectral fingerprints of the CDW. A full gap could occur away from the Fermi energy. However, even for the well-studied strong-coupling TMDCs 2H-$NbSe_2$[9,13,14] and 1T-TaS_2[7,15–17], no experimental verification of a clear CDW gap located away from the Fermi energy has been provided to date. Furthermore, at the Fermi energy, the undistorted phase and the CDW can have different Fermi-surface topologies, with the implication that the transition is a metal–metal Lifshitz transition[18].

Metallic 1T-VS_2 is not only a promising electrode material in lithium-ion batteries[19,20], but also a prototypical d^1 system, expected to host strongly correlated physics[21]. It is stated to be a CDW material[22,23] and a candidate for 2D magnetism[24,25] with layer-dependent properties[26], making it a model system for investigating complex ground states. Although difficult to synthesize, bulk 1T-VS_2 has been well studied, with many authors finding a CDW transition at around 305 K when it was prepared via the de-intercalation of Li[22,23,27–29]. However, recent powder samples prepared under high pressure show no CDW transition[30]. Based on their finding of a phonon instability at $2/3\ \overline{\Gamma K}$ corresponding to the experimental CDW wavevector of Li de-intercalated bulk samples[23], Gauzzi et al. point out that bulk "VS_2 is at the verge of CDW transition"[30] but not a CDW material. Due to a similar difficulty in synthesis, the properties of monolayer 1T-VS_2 have proven equally elusive[31]. Theoretical calculations had predicted ferromagnetism and a CDW with a wavevector of $2/3\ \overline{\Gamma K}$[21,25]. When it was first synthesized however, scanning tunneling microscope (STM) measurements did not reveal a CDW[31], presumably due to strong hybridization with the Au(111) substrate, similar to the case of 2H-TaS_2 on Au(111)[4,32,33].

Here we report the growth of VS_2 monolayers on the inert substrate graphene (Gr) on Ir(111) via a two-step molecular beam epitaxy (MBE) synthesis developed for sulfur-based TMDCs[34]. Using a combination of STM, scanning tunneling spectroscopy (STS), and ab initio density functional theory (DFT) calculations, we determine the spatial and electronic structure of monolayer VS_2. We observe a $\mathbf{q} \approx 2/3\ \overline{\Gamma K}$ CDW as the electronic ground state at 7 K, which remains stable up to room temperature. A full gap in the density of states (DOS), residing completely in the unoccupied states, is measured via STS. From DFT and density functional perturbation theory (DFPT), we find that, although a transverse phonon mode initially becomes unstable in the harmonic approximation, the final CDW has a substantial admixture of longitudinal modes. The calculations are in excellent agreement with experiment, regarding both the electronic structure of the CDW phase and the spatial charge distribution observed on the VS_2 islands.

X-ray magnetic circular dichroism (XMCD) measurements at 7 K and 9 T robustly show vanishing total net magnetization. The coupling of the CDW to a spin density wave (SDW), energetically favored in DFT calculations, could explain this observation, providing interesting prospects for future research on the interplay of CDWs and magnetism.

Results

CDW in monolayer VS_2. The typical morphology of the MBE-grown monolayer VS_2 islands on Gr/Ir(111) is shown in the large-scale STM image in Fig. 1a. The islands were grown by room-temperature deposition of vanadium in a sulfur background pressure of $P_S^g = 1 \times 10^{-8}$ mbar and subsequently annealed at 600 K in the same sulfur pressure. Annealing to temperatures of 800 K and above leads to the formation of a variety of sulfur-depleted phases, which are not under concern here. Similar observations were made by Arnold et al.[31], who established monolayer stoichiometric 1T-VS_2 on Au(111) by annealing in a sulfiding gas at 670–700 K, while sulfur-depleted monolayer phases form when annealed to the same or higher temperature in the absence of sulfiding species. We also note that depending on growth temperature and sulfur pressure bilayer samples without any monolayer islands evolve.

The monolayer islands are fully covered by a striped superstructure which is present regardless of island size or defect density and occurs in domains, typically separated by grain boundaries. In the topograph of Fig. 1b, taken at 7 K, the VS_2 lattice is resolved, exhibiting the hexagonal arrangement of top layer sulfur atoms as protrusions. We find that monolayer VS_2 has a lattice constant of $a_{VS_2} = (3.21 \pm 0.02)$ Å, in good agreement with the bulk lattice constant of 3.22 Å of 1T-VS_2[27,35]. The similarity of the lattice constants indicates also the absence of epitaxial strain, consistent with the random orientation of the VS_2 with respect to the Gr.

The stripes of the superstructure have an average periodicity of $(2.28 \pm 0.02)a_{VS_2}$. Close analogues to this structure have previously been observed in stoichiometric monolayer VSe_2. There, a superstructure of identical symmetry is attributed to a CDW[3,36–38] [compare Supplementary Fig. 1]. The superstructure is found to persist up to room temperature, as can be concluded from the STM topograph in Fig. 1c, taken at 300 K. At this temperature, the superstructure appears spontaneously only on larger islands, suggesting that the transition temperature between the superstructure and the undistorted phase is not far above room temperature. Indeed, on smaller islands the STM tip can be used to reversibly switch between the undistorted (1×1) structure and the superstructure, shown in Supplementary Fig. 2. This directly excludes the possibility that the superstructure is due to a sulfur-depleted phase. We conclude that the superstructure is most likely a CDW in a stoichiometric monolayer of 1T-VS_2.

For the DFT calculations below, the experimental wave pattern must be approximated by a commensurate structure. A close approximation with periodicity $2.25a_{VS_2}$ is overlaid on the atomic resolution image in Fig. 1b. It locally matches the

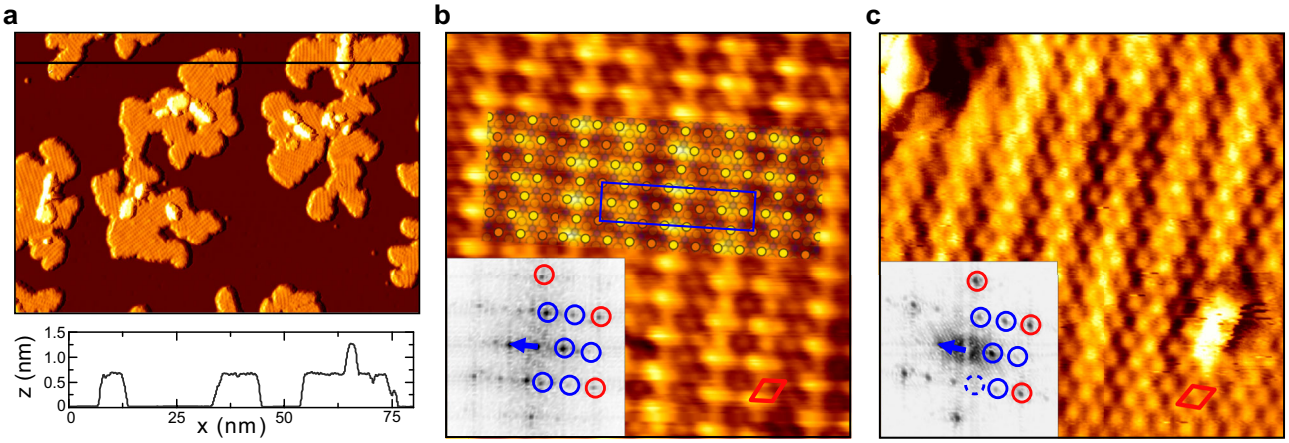

Fig. 1 Structure of VS_2 on Gr/Ir(111) at 7 and 300 K. a Large-scale 7 K STM topograph of monolayer VS_2 islands with small bilayers present. A height profile along the horizontal black line is shown below the image. **b**, **c** Atomically resolved STM images of monolayer VS_2 at 7 K (**b**) and 300 K (**c**). The Fourier transform of each image is shown as an inset, with the 1×1 VS_2 structure in red and the superstructure spots indicated in blue. In **b**, an atomic model for the $9\times\sqrt{3}$R30° superstructure is included as an overlay. The model depicts the top sulfur atoms, with their apparent height in STM coded in orange (low) and yellow (high). Measurement parameters: **a** 80×50 nm^2, $I_t = 0.8$ nA, $V_t = -800$ meV, **b** 6×6 nm^2, $I_t = 0.6$ nA, $V_t = 400$ meV, **c** 6×6 nm^2, $I_t = 1.0$ nA, $V_t = -1000$ meV.

incommensurate CDW quite well. The blue box indicates the corresponding $9\times\sqrt{3}$R30° unit cell. The Fourier transform of the topograph is shown as inset in Fig. 1b, with the wavevector of the CDW indicated (blue arrow). The same is done for the 300 K topograph in Fig. 1c. Within the margin of error, the wavevector is found to be temperature independent, with $\mathbf{q}_{\mathrm{CDW(7K)}} = (0.656\pm0.006)\ \overline{\Gamma\mathrm{K}}$ and $\mathbf{q}_{\mathrm{CDW(300K)}} = (0.65\pm0.03)\ \overline{\Gamma\mathrm{K}}$. Since the wavevector of the $9\times\sqrt{3}$R30° unit cell, $\mathbf{q}_{9\times\sqrt{3}\mathrm{R30°}} = 2/3\ \overline{\Gamma\mathrm{K}} \approx 0.667\ \overline{\Gamma\mathrm{K}}$, is slightly larger than the experimental value, we will in the following also consider another unit cell of size $7\times\sqrt{3}$R30°, with a slightly smaller wavevector $\mathbf{q}_{7\times\sqrt{3}\mathrm{R30°}} = 9/14\ \overline{\Gamma\mathrm{K}} \approx 0.643\ \overline{\Gamma\mathrm{K}}$. With the experimental wavevector lying in between $\mathbf{q}_{7\times\sqrt{3}\mathrm{R30°}}$ and $\mathbf{q}_{9\times\sqrt{3}\mathrm{R30°}}$, calculations with these two unit cells should capture the essential features of the incommensurate structure and provide a check on any artefacts or errors arising from using them for computational purposes (cf. Supplementary Fig. 3).

Energetics of lattice instabilities. Ab initio DFPT calculations of the acoustic phonon dispersion of undistorted monolayer 1T-VS_2 confirm that a structural instability and corresponding tendencies toward CDW formation exist for the experimental wavevector. Figure 2a shows that the longitudinal–acoustic and transverse–acoustic modes feature imaginary frequencies in several parts of the Brillouin zone. In other words, the Born–Oppenheimer energy surface is a downwards-opening parabola for small atomic displacements in the direction of these modes, as seen in Fig. 2b (triangle marks). At the experimental wavevector between $\mathbf{q} = 2/3\ \overline{\Gamma\mathrm{K}}$ and $\mathbf{q} = 9/14\ \overline{\Gamma\mathrm{K}}$, we find an instability of the transverse–acoustic branch. However, the dominant instability within the harmonic approximation (i.e., DFPT), is located at $\mathbf{q} = 1/2\ \overline{\Gamma\mathrm{M}}$ in the longitudinal–acoustic branch.

To go beyond the harmonic approximation, we have performed structural relaxations on appropriate unit cells. The resulting atomic positions are shown in Fig. 2c–e. On the aforementioned $9\times\sqrt{3}$R30° and $7\times\sqrt{3}$R30° unit cells, which can approximately host an integer multiple of the observed wavelength, the vanadium atoms are displaced from their symmetric positions by up to 8% of the lattice constant, while the positions of the sulfur atoms remain almost unchanged, see Fig. 2c, d. The associated energy gains amount to about 23 meV per VS_2 formula unit (cf. ref. [21]). The magnitude of these distortions and energy gains is similar to other octahedral TMDCs but exceeds by far what is found in trigonal–prismatic TMDCs[7,39]. For instance, on the DFT level, the maximum displacement in the $\sqrt{13}\times\sqrt{13}$ CDW of 1T-$NbSe_2$ is 8.8% of the lattice constant with an energy gain of 57 meV per formula unit[40], while in the 3×3 CDW of 2H-$NbSe_2$ distortions and energy gain amount to only 2.3% of the lattice constant and 3.7 meV per formula unit[41].

The vanadium displacement has components in both the transverse and longitudinal direction (vertical and horizontal in Fig. 2c, d), even though the instability of the phonons at $\mathbf{q} = 2/3\ \overline{\Gamma\mathrm{K}}$ and $\mathbf{q} = 9/14\ \overline{\Gamma\mathrm{K}}$ is of transverse character (white arrows in Fig. 2c, d). As a consequence, all longitudinal displacement components must stem from non-linear mode–mode coupling beyond the harmonic approximation. The admixture of longitudinal displacement components stems mainly from wavevectors $\mathbf{q} = 4/3\ \overline{\Gamma\mathrm{K}}$ and $\mathbf{q} = 9/7\ \overline{\Gamma\mathrm{K}}$, which are also commensurate with the $9\times\sqrt{3}$R30° and the $7\times\sqrt{3}$R30° unit cells, respectively. The admixed longitudinal modes at $\mathbf{q} = 4/3\ \overline{\Gamma\mathrm{K}}$ and $\mathbf{q} = 9/7\ \overline{\Gamma\mathrm{K}}$ are stable in the harmonic approximation and the non-linear admixture is not related to any nesting or Peierls physics (cf. Supplementary Fig. 4e, f).

We also find a distorted ground state on a 4×4 unit cell, see Fig. 2e. This structure is commensurate to the six wavevectors $\mathbf{q} = 1/2\ \overline{\Gamma\mathrm{M}}$, where we have instabilities in the longitudinal–acoustic branch arising from near perfect Fermi-surface nesting, see Supplementary Fig. 4a. However, here the displacements amount to only 4% of the lattice constant with a corresponding energy gain below 4 meV per 1T-VS_2 formula unit —much less than what is found for the $7\times\sqrt{3}$R30° or $9\times\sqrt{3}$R30° CDW structures. Thus, the DFT total energies of the fully relaxed structures are in line with the experimentally observed CDW patterns.

To illustrate the significance of the non-linear mode–mode coupling, in Fig. 2b, we also show the Born–Oppenheimer energy surfaces for displacements toward the relaxed structures (circle marks). The energy curve of the 4×4 structure is steeper in the vicinity of the origin. In other words, the 4×4 structure wins for

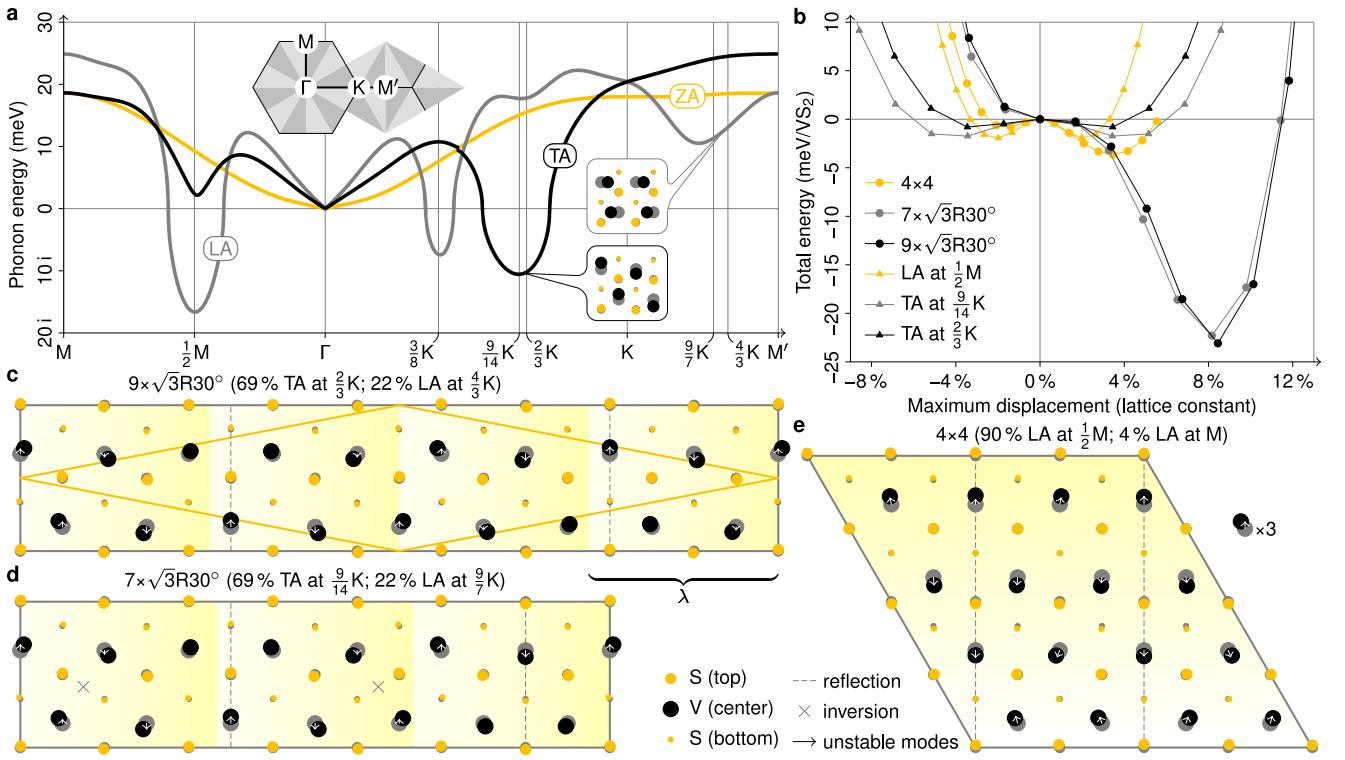

Fig. 2 Lattice instabilities in monolayer 1T-VS_2 from first principles. a Acoustic phonon dispersion from DFPT. LA, TA, and ZA stand for dominant longitudinal, transverse, and out-of-plane atomic displacements. The insets show selected displacement patterns corresponding to indicated modes. **b** Total energy from DFT as a function of the displacement amplitude for atomic displacements toward relaxed crystal structures and their projections onto soft phonon modes. **c**–**e** Relaxed crystal structures on $9\times\sqrt{3}$R30°, $7\times\sqrt{3}$R30°, and 4×4 unit cells from DFT. Vanadium and sulfur atoms are represented by black and yellow dots, their undistorted positions by gray shadows. Arrows represent the projections of the atomic displacements onto soft phonon modes. (Only arrows longer than 2% of the lattice constant are shown.) The contributions of different phonon modes are quantified in the figure titles. The displacements in **c**, **d** are drawn to scale, those in **e** have been magnified by a factor of three for better visibility. The primitive cell of the structure in **c**, which is in agreement with the results of ref. [21], is outlined in yellow. Dashed lines and crosses mark reflection planes and inversion centers.

small displacements. However, for larger displacements, the structures corresponding to the experimental wavevector reach by far the lowest values. These large energy gains at large displacements are inaccessible without non-linear mode–mode coupling, i.e., without the contribution of stable phonon modes (triangle marks). In the next section, we will address the non-linear regime of the distortions in a quantitative manner.

Non-linear mode–mode coupling. We decompose the entirety of atomic displacements of the relaxed $7\times\sqrt{3}$R30° structure as $\mathbf{u}+\mathbf{v}$, where $\mathbf{u}$ points in the direction of the unstable transverse–acoustic phonon modes at $\mathbf{q}=\pm9/14\ \overline{\Gamma\mathrm{K}}$ and the orthogonal complement $\mathbf{v}\perp\mathbf{u}$ combines contributions from all other phonon modes. The unstable modes account for $|\mathbf{u}|^2/|\mathbf{u}+\mathbf{v}|^2\approx69\%$ of the total displacement only. In Fig. 2b, we have already seen one-dimensional cross sections of the Born–Oppenheimer energy surface, $E(\alpha\mathbf{u})$ and $E(\beta(\mathbf{u}+\mathbf{v}))$, where α and β are dimensionless scaling factors. Now, we will consider the full 2D Born–Oppenheimer surface spanned by $\mathbf{u}$ and $\mathbf{v}$. Figure 3 shows $E(x\mathbf{u}+y\mathbf{v})$, where the minimum at $x=y=1$ corresponds to the $7\times\sqrt{3}$R30° structure and $x=y=0$ is the undistorted structure. A fourth-order polynomial fit,

$$\frac{E(x\mathbf{u}+y\mathbf{v})}{\mathrm{meV/VS_2}}\approx-25x^2+29y^2+34x^3-99x^2y-20xy^2-12y^3+0.1x^4+44x^3y+13x^2y^2+4.8xy^3+7.2y^4, \quad (1)$$

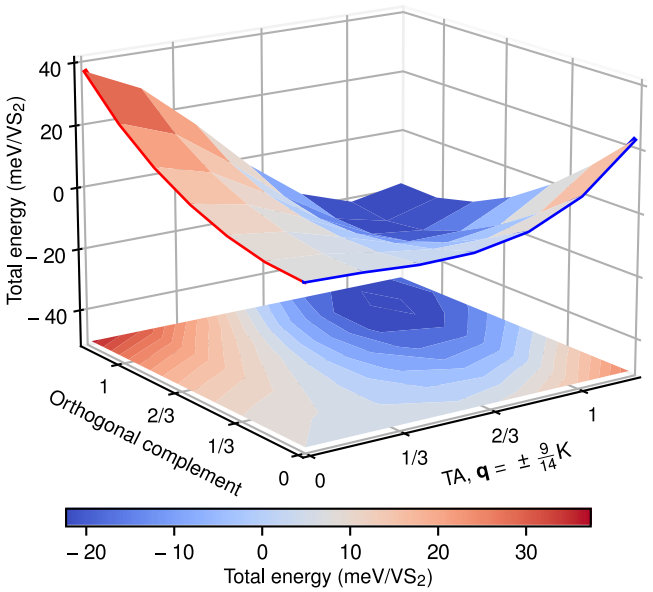

Fig. 3 Born–Oppenheimer energy surface for the $7\times\sqrt{3}$R30° structure of 1T-VS_2. The axes represent the projection of the full CDW displacement onto the transverse-acoustic (TA) phonon modes at $\mathbf{q}=\pm9/14\ \overline{\Gamma\mathrm{K}}$ and the orthogonal complement, which combines all other contributing modes. The full CDW displacement is located at the point (1, 1). The forces resulting from this energy surface are predominantly non-linear and coupled in both directions.

accurately describes the DFT Born Oppenheimer surface. Here, the first and second line give rise to linear and non-linear forces $\mathbf{F} = -\nabla\mathbf{E}$, respectively. It turns out that the non-linear part of the forces is dominated by mode–mode coupled terms[42–44] (dependent on both x and y). The energy reduction stems largely from the x^2y and xy^2 terms above, which correspond to a shift of the minimum of the potential-energy surface toward finite positive y upon finite displacement in x direction and a softening of the effective spring constant in y direction for finite positive x, respectively. Note that within the harmonic approximation the x^2 (y^2) term lowers (raises) the energy.

The decisive role of mode–mode coupling terms x^2y and xy^2 distinguishes 1T-VS_2 from systems like 2H-$NbSe_2$ or 2H-TaS_2, where a single mode can be employed to describe anharmonicities, and distortions along a single effective coordinate suffice to explain the relaxation pattern of the full CDW and associated energy gains (cf. Supplementary Fig. 5).

The non-linear mode–mode coupling also manifests in monolayer 1T-VTe_2, which is isoelectronic to monolayer 1T-VS_2. Monolayer 1T-VTe_2 in experiment realizes a 4×4 CDW[45] in contrast to monolayer 1T-VS_2. In line with experiment, the comparison of DFT total energies in the fully relaxed supercells (Supplementary Table 1) reveals a clear preference of the 4×4 structure in 1T-VTe_2. At the harmonic level, this is likely related to a shift of the lattice instabilities, especially in the transverse-acoustic branch, toward smaller wavevectors in 1T-VTe_2 as compared to 1T-VS_2 (cf. Fig. 2a and Supplementary Fig. 6a), which can be traced back to differences in the Fermi surface (cf. Supplementary Figs. 4 and 6b–g). At the harmonic level, a CDW with $7\times\sqrt{3}R30^\circ$ structure of monolayer 1T-VS_2 is not expected, as Supplementary Fig. 6a shows. The small energy gain and still appreciable distortions obtained from the relaxation of a $7\times\sqrt{3}R30^\circ$ structure of monolayer 1T-VS_2 (Supplementary Table 1) despite the stability on the harmonic level suggest that non-linear mode–mode coupling is also effective, here.

Full CDW gap in the unoccupied states. To better understand this CDW phase, we determined the electronic structure of monolayer VS_2 by a combination of STS experiments and simulated dI/dV maps based on the ab initio calculations using the $7\times\sqrt{3}R30^\circ$ and $9\times\sqrt{3}R30^\circ$ unit cells. STS spectra were used to locally probe the DOS of monolayer VS_2 at 7 K (black line) and 78.5 K (purple line), shown in Fig. 4a. Both spectra were taken with a clean Au tip in the middle of VS_2 islands. The most prominent feature is the gap located at about 0.175 eV, which is absent in calculations of undistorted monolayer VS_2[21]. At 7 K, the dI/dV signal vanishes completely, corresponding to a full gap in the DOS. At 78.5 K, this gap is not fully open, appearing as a wide depression with a finite value at its minimum. In most other characteristic features the spectra agree qualitatively.

While the lack of energy resolution at 78.5 K certainly smears out the spectra and the gap, the reason for its absence is not immediately evident. When discussing the band structure below,

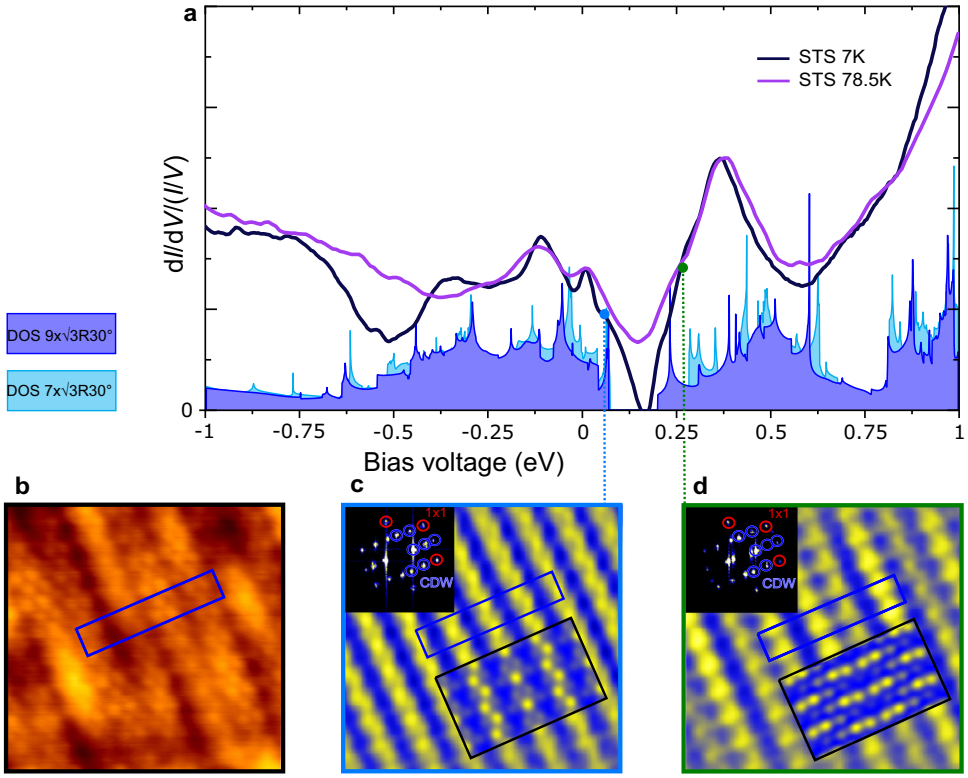

Fig. 4 Spatially and electronically resolved CDW phase in monolayer VS_2. a Scanning tunneling spectroscopy (STS) dI/dV spectra taken with a Au tip on monolayer VS_2 at 78.5 K (purple) and 7 K (black). The spectra are plotted along with the DFT-calculated density of states (DOS) for the $7\times\sqrt{3}R30^\circ$ (cyan) and $9\times\sqrt{3}R30^\circ$ (indigo) CDW phases of monolayer 1T-VS_2. **b** Atomically resolved STM topograph of monolayer VS_2 taken at $V_t = 175$ meV. **c**, **d** Fourier-filtered dI/dV conductance maps of the same region as in **b**, taken at $V_t = 75$ meV (**c**) and $V_t = 275$ meV (**d**). A linear yellow (maximum) to blue (minimum) color scale is used to depict the dI/dV intensity. The blue box indicates the same location in **b**–**d** and corresponds to a single $9\times\sqrt{3}R30^\circ$ unit cell of the CDW. In the same color scale, DFT-simulated dI/dV maps below (**c**) and above (**d**) the gap of the charge density wave (CDW) are overlaid as insets. The maps show the integrated DOS from 0 to 137 meV (**c**) and from 137 to 275 meV (**d**). Additionally, the Fourier transforms of the conductance maps are shown in the upper-left corners with the 1×1 (red) and CDW peaks (blue) highlighted by circles. Measurement parameters: $f = 777.7$ Hz, **a** $T = 78.5$ K, $I_t = 0.3$ nA, $V_{r.m.s.} = 6$ meV and $T = 7$ K, $I_t = 0.45$ nA, $V_{r.m.s.} = 4$ meV, **b**–**d** $T = 7$ K, 5.5×5.5 nm^2, $I_t = 0.3$ nA, $V_{r.m.s.} = 10$ meV.

it will be seen that the width and existence of the full gap depend on the magnitude of the lattice distortions, which may already be diminished at 78.5 K.

In the same figure, ab initio calculations for the DOS of VS_2, structurally relaxed in the $7\times\sqrt{3}R30^\circ$ (cyan) or $9\times\sqrt{3}R30^\circ$ (indigo) unit cell, are shown. Both unit cells feature quite similar structures, as expected for close-lying **q** vectors. Most striking, for both cases a full gap in the unoccupied states is predicted. They only differ in size: 0.13 eV and 0.21 eV for the $9\times\sqrt{3}R30^\circ$ and $7\times\sqrt{3}R30^\circ$ unit cell, respectively. The location of the gap matches the STS data. That the width of the gap in the spectrum is smaller than in DFT might stem from the ground-state calculation assumed in DFT, overestimating the vanadium atom displacement at realistic temperatures. Note also that while many of the characteristic features of calculated and measured DOS (peaks, minima) seem to agree, the experimental spectra appear to be compressed with respect to the DFT calculated DOS. This quasiparticle renormalization is indicative of strong electron–electron correlations beyond the approximations of DFT (compare Supplementary Fig. 7).

With theory and experiment largely agreeing on the electronic structure, we turn to the relation between the gap and the CDW measured on the VS_2 islands. For that purpose, dI/dV conductance maps were taken on either side of the gap (both in the unoccupied states), in the location shown in Fig. 4b. The maps help to distinguish structural from electronic contributions, providing a close approximation of the spatial distribution of the DOS at the selected energies. As shown in Fig. 4c, d, we find two different DOS distributions on either side of the gap (see Supplementary Fig. 8 for the in-gap DOS). Both distributions are locked into the distorted lattice periodicity. They are out-of-phase, as seen in the blue unit cell drawn in the same location in Fig. 4b–d: The DOS maxima below the gap correspond to DOS minima above the gap and vice versa. This behavior is perfectly analogous to that for a CDW with a symmetric gap around the Fermi level[4]. Simulated dI/dV maps derived from the DFT DOS for a $9\times\sqrt{3}R30^\circ$ CDW are shown as an overlay in Fig. 4c, d. In Fig. 4c, the simulation reproduces both the alternating rows of single and zigzag atoms and the DOS minima between the rows. Its counterpart in Fig. 4d shows higher DOS contrast than experiment, but presents the same qualitative features. With the simulated maps based on the displacement patterns of Fig. 2c, the close agreement with experiment emphasizes the need to look beyond the harmonic approximation to understand this type of CDW.

Band structure and Fermi-surface topology. To deepen our understanding of the system, we calculated the spin-degenerate band structure, density of states, and Fermi surface of monolayer 1T-VS_2 with DFT. The results are shown in Fig. 5 and the Supplementary Movies. In the undistorted case, we find a single electronic band at the Fermi level, which strongly disperses between M and K and features a Van Hove singularity in the unoccupied states, as shown in Fig. 5a. The Fermi surface, depicted in Fig. 5b, consists of cigar-shaped electron pockets around the M points. For small distortions, partial gaps open at the Fermi level (e.g., between M and K). With increasing amplitude of the distortion, the gaps become larger and the bands are heavily reconstructed also for high energies. Only then, a full gap as observed in STS at 7 K emerges (cf. Supplementary Movie 1).

The presence of the CDW is therefore in the first place correlated with the gap between M and K, which opens already for small displacements and results in a partial gapping of the

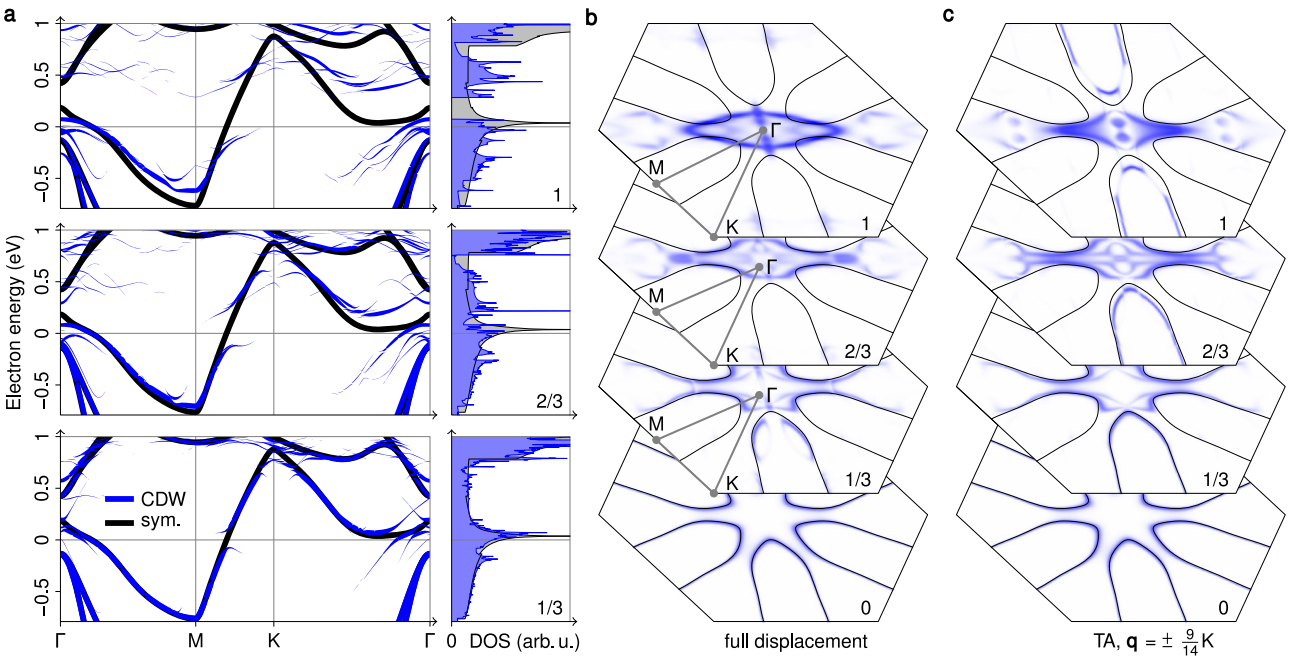

Fig. 5 Electronic structure of monolayer 1T-VS_2 from DFT. Data for the undistorted structure and the $7\times\sqrt{3}R30^\circ$ CDW is shown in black and blue, respectively. The CDW data has been unfolded to the Brillouin zone of the undistorted structure. Here, the linewidth/saturation corresponds to the overlap of CDW and undistorted wave functions for the same **k** point. Analogous results for 1T-VSe_2 and the $9\times\sqrt{3}R30^\circ$ CDW are shown in Supplementary Fig. 3. **a** Electronic band structure and density of states (DOS) for 0 %, 1/3, 2/3, and 100 % of the displacements of the relaxed CDW structure. Please note that since the CDW breaks the C_3 symmetry, the chosen path, indicated in **b**, does not represent the full Brillouin zone. The bands along an extended path are shown in Supplementary Fig. 9. **b**, **c** Lifshitz transition. The Fermi surface is shown for displacements toward the relaxed CDW structure (**b**) and its projection onto unstable transverse-acoustic (TA) phonon modes (**c**). The Supplementary Movies 1 and 2 show animations of the transitions in **b** and **c**, respectively (including bands, DOS, and structures).

total DOS. Presumably it is the associated gain in electronic energy that initially drives the CDW transition. Since the full gap only starts to open at 70% of the final displacements, the experimental observation of a full gap above the Fermi level is an indication that the displacements in the experiments do not fall much below the calculated ones.

At the Fermi level, there is no complete gap even at large distortion, since the downwards-dispersing bands along Γ–M are only slightly shifted downwards and remain above the Fermi level near Γ. On the other hand, the originally flat portion of the band structure between Γ and K now disperses downwards and crosses the Fermi level. The preservation of states near Γ that mask the partial gap at the Fermi level can be understood in terms of band characters and degeneracies, as shown in Supplementary Fig. 10. Altogether, the Fermi surface is reconstructed and not completely destroyed by the lattice distortion. The CDW transition is thus a metal–metal Lifshitz transition with a change in Fermi-surface topology, instead of the usual metal–insulator Peierls transition.

As shown in Fig. 5c, we cannot understand this Fermi-surface reconstruction based on a single unstable mode: The displacements expected from the harmonic approximation (**u** in Eq. (1)) only induce gaps in two-third of the cigar-shaped electron pockets (cf. Supplementary Movie 2). The other component **v** couples to segments of the Fermi surface that are not affected by **u**, i.e., the remaining third of the electron pockets (cf. Supplementary Movie 3). Together, they transform the Fermi surface from multiple cigar-shaped electron pockets around the M points to the single elliptical hole pocket around Γ visible in Fig. 5b. The decomposition of the CDW contains modes at more than one wavevector **q**, so several approximate Fermi-surface nesting conditions and electron–phonon coupling matrix elements play a role (Supplementary Fig. 4b, c, e, f), enabling the CDW to affect distinct parts of the Fermi surface.

Magnetic properties of monolayer VS_2. Prompted by the prediction of ferromagnetism for monolayer 1T-VS_2 in its $\mathbf{q} = 2/3\ \overline{\Gamma K}$ CDW phase[21], we also examined the magnetic properties of VS_2, by means of X-ray magnetic circular dichroism (XMCD). The monolayer VS_2 samples were grown in situ and investigated with STM beforehand to make sure that the same phase and decent coverage were obtained. A STM topograph of the sample investigated by XMCD is shown in Supplementary Fig. 11. The blue curve in Fig. 6a represents the X-ray absorption spectrum averaged over both helicities and external field directions. The overall line shape is very similar to previous bulk crystal measurements[23] and clearly fits to a $3d^1$ configuration[46]. The red signal in Fig. 6a is the XMCD magnified by a factor of 10, where no signal above the noise level is visible. This implies that the total magnetization vanishes. Sum rule analysis would yield an upper bound of $0.02\mu_B$ per vanadium atom. Since it cannot be strictly applied to the case of the $V_{2,3}$ edges[47], this analysis yields only a zero-order estimate of the upper bound, but we can safely conclude that neither ferromagnetic nor paramagnetic behavior is present in this system.

We investigated magnetic order in monolayer VS_2 using spin-polarized DFT. We were able to stabilize both ferromagnetic and SDW structures within the $7\times\sqrt{3}$R30° unit cell. In fact, magnetically ordered CDW phases are preferred over nonmagnetic CDW phases by energies of the order of 1 meV per VS_2 unit. Figure 6b shows the most favorable SDW pattern in the $7\times\sqrt{3}$R30° CDW phase. The magnetic moments on vanadium reach $\pm0.18\mu_B$, those on sulfur only $\pm0.01\mu_B$ and are thus not shown. While the CDW alone reduces the total energy to −22.7 meV per VS_2 unit with respect to the symmetric structure, the SDW lowers this value by another 1.5 to −24.2 meV. Interestingly, without the CDW, a similar SDW with larger local moments of up to $\pm0.51\mu_B$ (shown in Fig. 6c) leads to an energy reduction of 7.1 meV. As already suggested by previous calculations of ferromagnetism in the $9\times\sqrt{3}$R30° structure of 1T-VS_2[21], there is a competition between the lattice distortion and the formation of local moments. Although a full account of magnetism needs to go beyond the DFT level, in view of the good agreement between our ab initio results and the experimental STS and XMCD data, the formation of coupled CDW–SDW state in 1T-VS_2 is plausible. This presumption is further supported by comparison of the calculated DOS in the CDW–SDW state to the STS shown in Supplementary Fig. 12: the SDW formation on top of the CDW leads to a reduction of the gap size and the DOS of the coupled CDW–SDW is even in better agreement with the experiment than the non-spin-polarized CDW DOS.

Discussion

Both the electronic and magnetic results for VS_2 shed some light on the properties of the isoelectronic compound VSe_2, which displays a CDW of the same periodicity[3,38,48]. Our calculations strongly suggest that also for this system non-linear effects are relevant and that a full gap opens in the unoccupied states (compare Supplementary Fig. 3). A full gap at the Fermi level, as proposed for 1T-VSe_2[6,38,48,49], would be unlikely to intrinsically occur for a CDW with the observed wavevector. The strong similarity between our calculations and experimental data, especially for those VSe_2 systems where only the $7\times\sqrt{3}$R30° CDW is observed[36,37], lends credence to our analysis (compare Supplementary Fig. 13). It is possible that the simultaneous occurrence of a 4×1 CDW[3,6], perhaps due to substrate-induced strain[50], causes an additional gap opening near the Fermi level as a result of the interplay between the CDWs. In any case, similar to VS_2, the presence of a SDW coupled to the $7\times\sqrt{3}$R30° CDW

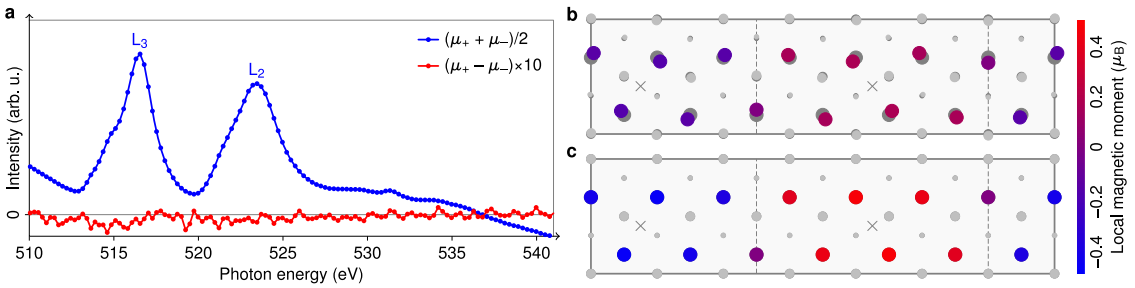

Fig. 6 Magnetic properties of monolayer 1T-VS_2. a Plotted in blue is the X-ray absorption signal averaged over both helicities and directions of the *B* field. The corresponding XMCD is shown in red. All measurements have been conducted in *B* fields of ±9 T and at a temperature of 7 K. **b**, **c** Possible SDW pattern with (**b**) and without CDW (**c**).

could explain the absence of net magnetization in XMCD experiments[37,38,48]. Spin-polarized STM or XMLD might be able to detect the magnetic ground state for both VS_2 and VSe_2.

In conclusion, VS_2 defies the common phenomenology of CDW formation, as the complete CDW gap occurs above the Fermi level, there is giant non-linear longitudinal–transverse mode–mode coupling, and the CDW formation is accompanied by a change of the Fermi-surface topology. The unconventional CDW appears to host further electronic correlations as signalled by the quasiparticle renormalization and magnetic-moment formation. In this respect, it is reminiscent of correlated phases in superlattice structures such as Star of David phases[7], moiré superlattices[51], and doped cuprate superconductors[52]. In the latter class, lattice anharmonicities are central to boosting superconductivity under THz optical driving[44]. The case of VS_2 presents new terrain: A metal–metal Lifshitz transition from non-linear electron–lattice effects in the strong-coupling regime is intertwined with electronic correlations. We note that the full gap in the DOS, situated within 0.2 eV from the Fermi level, opens up the possibility of inducing a metal–insulator transition upon mild gating or doping (e.g., with Li). Finally, we are convinced that the excellent agreement of experiment and theory for the unconventional CDW of monolayer VS_2 with the full gap in the unoccupied states provides a paradigmatic case study of strong-coupling CDWs in general.

Methods

The Ir(111) crystal is cleaned by grazing incidence 1.5 keV Ar^+ ion exposure and flash annealing to 1500 K. A closed monolayer of single-crystalline Gr on Ir(111) is grown by room temperature exposure of Ir(111) to ethylene until saturation, subsequent annealing to 1300 K, followed by exposure to 200 L ethylene at 1300 K[53].

The synthesis of vanadium sulfides on Gr/Ir(111) is based on a two-step MBE approach introduced in detail in ref. [34] for MoS_2. In the first step, the sample is held at room temperature and vanadium is evaporated at a rate of $F_V = 2.5 \times 10^{16}$ atoms/(m^2s) into a sulfur background pressure of $P_S^g = 1 \times 10^{-8}$ mbar built up by thermal decomposition of pyrite inside a Knudsen cell. This results in dendritic TMDC islands of poor epitaxy. To make the islands larger and more compact, the sample is flashed in a sulfur background to 600 K.

The VS_2 layers were analyzed by STM, STS, and low-energy electron diffraction (LEED) inside a variable temperature (30–700 K) ultrahigh vacuum apparatus and a low-temperature STM operating at 7 and 78.5 K. The software WSXM[54] was used for STM data processing. XMCD measurements have been conducted at the beamline ID32 of the European Synchrotron Radiation Facility (ESRF) in Grenoble, France. The VS_2 samples were grown in situ inside the preparation chamber and checked with LEED and STM before X-ray absorption spectroscopy measurements. To be surface sensitive, the measurements were conducted in the total-electron-yield mode under normal incidence. The measurement temperature was 7 K and fields of 9 T were used. The spectra were recorded at the $L_{3,2}$ edges, i.e., using the dipole allowed transition from 2*p* states into the 3*d* shell potentially generating magnetism.

All DFT and DFPT calculations were performed using Quantum ESPRESSO[55,56]. We apply the PBE functional[57,58] and norm-conserving pseudopotentials from the PseudoDojo table[59,60]. In the undistorted case, uniform meshes (including Γ) of 12×12 **q** and 24×24 **k** points are combined with a Fermi–Dirac smearing of 300 K. For a fixed unit-cell height of 15 Å, minimizing forces and in-plane pressure to below 1×10^{-5} Ry/Bohr and 0.1 kbar yields a lattice constant of 3.18 Å and a layer height (vertical sulfur–sulfur distance) of 2.93 Å. For the superstructure calculations, appropriate **k**-point meshes of similar density are chosen, except for the precise total energies quoted in the section about magnetism and in Supplementary Table 1, which required four times as dense meshes. The average lattice constant of superstructures is kept fixed at the value of the symmetric structure. Fourier interpolation to higher **k** resolutions (1000×1000 for calculations of the DOS) and the unfolding of electronic states is based on localized representations generated with Wannier90[61]. For the visualization of the unfolded Fermi surfaces, a Fermi–Dirac broadening of 10 meV is used.

Data availability

All the data and methods are present in the main text and the supplementary materials. Any other relevant data are available from the authors upon reasonable request.

Code availability

Codes used in this work are available from the authors upon reasonable request.

Received: 18 December 2020; Accepted: 4 November 2021;
Published online: 25 November 2021

References

1. Ugeda, M. M. et al. Characterization of collective ground states in single-layer $NbSe_2$. *Nat. Phys.* **12**, 92 (2016).
2. Zheng, B.-X. et al. Stripe order in the underdoped region of the two-dimensional Hubbard model. *Science* **358**, 1155 (2017).
3. Duvjir, G. et al. Emergence of a metal–insulator transition and high-temperature charge-density waves in VSe_2 at the monolayer limit. *Nano Lett.* **18**, 5432 (2018).
4. Hall, J. et al. Environmental control of charge density wave order in monolayer 2H-TaS_2. *ACS Nano* **13**, 10210 (2019).
5. Yu, W. et al. Chemically exfoliated VSe_2 monolayers with room-temperature ferromagnetism. *Adv. Mater.* **31**, 1903779 (2019).
6. Chua, R. et al. Can reconstructed Se-deficient line defects in monolayer VSe_2 induce magnetism? *Adv. Mater.* **32**, 2000693 (2020).
7. Rossnagel, K. On the origin of charge-density waves in select layered transition-metal dichalcogenides. *J. Phys. Condens. Matter* **23**, 213001 (2011).
8. Li, Y. W. et al. Folded superstructure and degeneracy-enhanced band gap in the weak-coupling charge density wave system 2H-$TaSe_2$. *Phys. Rev. B* **97**, 115118 (2018).
9. Zhu, X., Guo, J., Zhang, J. & Plummer, E. W. Misconceptions associated with the origin of charge density waves. *Adv. Phys. X* **2**, 622 (2017).
10. Johannes, M. D. & Mazin, I. I. Fermi surface nesting and the origin of charge density waves in metals. *Phys. Rev. B* **77**, 165135 (2008).
11. Inosov, D. S. et al. Fermi surface nesting in several transition metal dichalcogenides. *New J. Phys.* **10**, 125027 (2008).
12. Berges, J., van Loon, E. G. C. P., Schobert, A., Rösner, M. & Wehling, T. O. Ab initio phonon self-energies and fluctuation diagnostics of phonon anomalies: Lattice instabilities from Dirac pseudospin physics in transition metal dichalcogenides. *Phys. Rev. B* **101**, 155107 (2020).
13. Borisenko, S. V. et al. Two energy gaps and Fermi-surface "arcs" in $NbSe_2$. *Phys. Rev. Lett.* **102**, 166402 (2009).
14. Weber, F. et al. Extended phonon collapse and the origin of the charge-density wave in 2H-$NbSe_2$. *Phys. Rev. Lett.* **107**, 107403 (2011).
15. Dardel, B. et al. Temperature-dependent pseudogap and electron localization in 1T-TaS_2. *Phys. Rev. B* **45**, 1462 (1992).
16. Dardel, B. et al. Spectroscopic signatures of phase transitions in a charge-density-wave system: 1T-TaS_2. *Phys. Rev. B* **46**, 7407 (1992).
17. Zwick, F. et al. Spectral consequences of broken phase coherence in 1T-TaS_2. *Phys. Rev. Lett.* **81**, 1058 (1998).
18. Lifshitz, I. M. Anomalies of electron characteristics of a metal in the high pressure region. *Zh. Eksp. Teor. Fiz.* **38**, 1569 (1960).
19. Ji, Q. et al. Metallic vanadium disulfide nanosheets as a platform material for multifunctional electrode applications. *Nano Lett.* **17**, 4908 (2017).
20. Li, Q., Zhou, Q., Shi, L., Chen, Q. & Wang, J. Recent advances in oxidation and degradation mechanisms of ultrathin 2D materials under ambient conditions and their passivation strategies. *J. Mater. Chem. A* **7**, 4291 (2019).
21. Isaacs, E. B. & Marianetti, C. A. Electronic correlations in monolayer VS_2. *Phys. Rev. B* **94**, 035120 (2016).
22. Tsuda, T., Yasuoka, H., Kitaoka, Y. & Di Salvo, F. J. ^{51}V NMR study of the phase transition in 1T-VS_2. *J. Magn. Magn. Mater.* **31-34**, 1101 (1983).
23. Mulazzi, M. et al. Absence of nesting in the charge-density-wave system 1T-VS_2 as seen by photoelectron spectroscopy. *Phys. Rev. B* **82**, 075130 (2010).
24. Ma, Y. et al. Evidence of the existence of magnetism in pristine VX_2 monolayers (X = S, Se) and their strain-induced tunable magnetic properties. *ACS Nano* **6**, 1695 (2012).
25. Zhuang, H. L. & Hennig, R. G. Stability and magnetism of strongly correlated single-layer VS_2. *Phys. Rev. B* **93**, 054429 (2016).
26. Zhang, H., Liu, L.-M. & Lau, W.-M. Dimension-dependent phase transition and magnetic properties of VS_2. *J. Mater. Chem. A* **1**, 10821 (2013).
27. Murphy, D. W., Cros, C., Di Salvo, F. J. & Waszczak, J. V. Preparation and properties of Li_xVS_2 ($0 \le x \le 1$). *Inorg. Chem.* **16**, 3027 (1977).
28. Magonov, S., Contow, H.-J., Hillebrecht, H., Drechlser, M. & Rotter, W. Atomic structure and superstructure of vanadium disulfide by scanning tunneling microscopy. *Optik* **83**, 60 (1989).
29. Sun, X. et al. In situ unravelling structural modulation across the charge-density-wave transition in vanadium disulfide. *Phys. Chem. Chem. Phys.* **17**, 13333 (2015).
30. Gauzzi, A. et al. Possible phase separation and weak localization in the absence of a charge-density wave in single-phase 1T-VS_2. *Phys. Rev. B* **89**, 235125 (2014).
31. Arnold, F. et al. Novel single-layer vanadium sulphide phases. *2D Mater.* **5**, 045009 (2018).
32. Sanders, C. E. et al. Crystalline and electronic structure of single-layer TaS_2. *Phys. Rev. B* **94**, 081404(R) (2016).

33. Lefcochilos-Fogelquist, H. M., Albertini, O. R. & Liu, A. Y. Substrate-induced suppression of charge density wave phase in monolayer 1H-TaS_2 on Au(111). *Phys. Rev. B* **99**, 174113 (2019).
34. Hall, J. et al. Molecular beam epitaxy of quasi-freestanding transition metal disulphide monolayers on van der Waals substrates: a growth study. *2D Mater.* **5**, 025005 (2018).
35. Feng, J. et al. Metallic few-layered VS_2 ultrathin nanosheets: high two-dimensional conductivity for in-plane supercapacitors. *J. Am. Chem. Soc.* **133**, 17832 (2011).
36. Chen, P. et al. Unique gap structure and symmetry of the charge density wave in single-layer VSe_2. *Phys. Rev. Lett.* **121**, 196402 (2018).
37. Coelho, P. M. et al. Charge density wave state suppresses ferromagnetic ordering in VSe_2 monolayers. *J. Phys. Chem. C* **123**, 14089 (2019).
38. Wong, P. K. J. et al. Evidence of spin frustration in a vanadium diselenide monolayer magnet. *Adv. Mater.* **31**, 1901185 (2019).
39. Miller, D. C., Mahanti, S. D. & Duxbury, P. M. Charge density wave states in tantalum dichalcogenides. *Phys. Rev. B* **97**, 045133 (2018).
40. Calandra, M. Phonon-assisted magnetic Mott-insulating state in the charge density wave phase of single-layer 1T-$NbSe_2$. *Phys. Rev. Lett.* **121**, 026401 (2018).
41. Lian, C.-S., Si, C. & Duan, W. Unveiling charge-density wave, superconductivity, and their competitive nature in two-dimensional $NbSe_2$. *Nano Lett.* **18**, 2924 (2018).
42. Först, M. et al. Nonlinear phononics as an ultrafast route to lattice control. *Nat. Phys.* **7**, 854 (2011).
43. Truitt, P. A., Hertzberg, J. B., Altunkaya, E. & Schwab, K. C. Linear and nonlinear coupling between transverse modes of a nanomechanical resonator. *J. Appl. Phys.* **114**, 114307 (2013).
44. Mankowsky, R. et al. Nonlinear lattice dynamics as a basis for enhanced superconductivity in $YBa_2Cu_3O_{6.5}$. *Nature* **516**, 71 (2014).
45. Wang, Y. et al. Evidence of charge density wave with anisotropic gap in a monolayer VTe_2 film. *Phys. Rev. B* **100**, 241404 (2019).
46. Brik, M. G., Ogasawara, K., Ikeno, H. & Tanaka, I. Fully relativistic calculations of the $L_{2,3}$-edge XANES spectra for vanadium oxides. *Eur. Phys. J. B* **51**, 345 (2006).
47. Scherz, A. et al. Relation between $L_{2,3}$ XMCD and the magnetic ground-state properties for the early 3d element V. *Phys. Rev. B* **66**, 184401 (2002).
48. Feng, J. et al. Electronic structure and enhanced charge-density wave order of monolayer VSe_2. *Nano Lett.* **18**, 4493 (2018).
49. Bonilla, M. et al. Strong room-temperature ferromagnetism in VSe_2 monolayers on van der Waals substrates. *Nat. Nanotechnol.* **13**, 289 (2018).
50. Si, J. G. et al. Origin of the multiple charge density wave order in 1T-VSe_2. *Phys. Rev. B* **101**, 235405 (2020).
51. Cao, Y. et al. Correlated insulator behaviour at half-filling in magic-angle graphene superlattices. *Nature* **556**, 80 (2018).
52. Tranquada, J. M., Sternlieb, B. J., Axe, J. D., Nakamura, Y. & Uchida, S. Evidence for stripe correlations of spins and holes in copper oxide superconductors. *Nature* **375**, 561 (1995).
53. van Gastel, R. et al. Selecting a single orientation for millimeter sized graphene sheets. *Appl. Phys. Lett.* **95**, 121901 (2009).
54. Horcas, I. et al. WSXM: a software for scanning probe microscopy and a tool for nanotechnology. *Rev. Sci. Instrum.* **78**, 013705 (2007).
55. Giannozzi, P. et al. QUANTUM ESPRESSO: a modular and open-source software project for quantum simulations of materials. *J. Phys. Condens. Matter* **21**, 395502 (2009).
56. Giannozzi, P. et al. Advanced capabilities for materials modelling with QUANTUM ESPRESSO. *J. Phys. Condens. Matter* **29**, 465901 (2017).
57. Perdew, J. P., Burke, K. & Ernzerhof, M. Generalized gradient approximation made simple. *Phys. Rev. Lett.* **77**, 3865 (1996).
58. Perdew, J. P., Burke, K. & Ernzerhof, M. Generalized gradient approximation made simple. *Phys. Rev. Lett.* **78**, 1396(E) (1997).
59. Hamann, D. R. Optimized norm-conserving Vanderbilt pseudopotentials. *Phys. Rev. B* **88**, 085117 (2013).
60. van Setten, M. J. et al. The PSEUDODOJO: Training and grading a 85 element optimized norm-conserving pseudopotential table. *Comput. Phys. Commun.* **226**, 39 (2018).
61. Mostofi, A. A. et al. An updated version of wannier90: a tool for obtaining maximally-localised Wannier functions. *Comput. Phys. Commun.* **185**, 2309 (2014).

Acknowledgements

This work was funded by the Deutsche Forschungsgemeinschaft (DFG, German Research foundation) through CRC 1238 (project no. 277146847, subprojects A01 and B06). J.B., A.S., and T.Weh. acknowledge financial support by the DFG through EXC 2077, GRK 2247, and SPP 2244. T.Weh. acknowledges support via the European Graphene Flagship Core3 Project (grant agreement 881603). J.B., A.S., and T.Weh. acknowledge computational resources of the North-German Supercomputing Alliance (HLRN). E.v.L. is supported by the Central Research Development Fund of the University of Bremen. L.M.A. acknowledges financial support from CAPES (project no. 9469/13-3).

Author contributions

T.Weh. and T.M. conceived this work and designed the research strategy. J.H. and discovered the CDW and developed, with the assistance of T.Wek., the growth method. C.v.E. and E.P. conducted and analyzed the STS experiments. J.B., A.S., and G.S., with support from E.v.L. and T.Weh., performed ab initio calculations. F.H. and S.K., with support from N.R., K.O., L.A., N.B., K.K., and H.W., performed and analyzed the XMCD experiment. The results were discussed by all authors. C.v.E., J.B., J.H., E.v.L., S.K., T.Weh., and T.M. wrote the manuscript with input from all authors. The first three authors have comparable contributions to this work.

Funding

Open Access funding enabled and organized by Projekt DEAL.

Competing interests

The authors declare no competing interests.

Additional information

Supplementary information The online version contains supplementary material available at https://doi.org/10.1038/s41467-021-27094-x.

Correspondence and requests for materials should be addressed to Camielvan Efferen.

Peer review information *Nature Communications* thanks Matteo Calandra and the other, anonymous, reviewer(s) for their contribution to the peer review of this work. Peer reviewer reports are available.

Reprints and permission information is available at http://www.nature.com/reprints

Publisher's note Springer Nature remains neutral with regard to jurisdictional claims in published maps and institutional affiliations.

Supplementary Information of "A full gap above the Fermi level: the charge density wave of monolayer VS_2"

Camiel van Efferen[1]*, Jan Berges[2], Joshua Hall[1], Erik van Loon[2], Stefan Kraus[1], Arne Schobert[2], Tobias Wekking[1], Felix Huttmann[1], Eline Plaar[1], Nico Rothenbach[3], Katharina Ollefs[3], Lucas Machado Arruda[4], Nick Brookes[5], Gunnar Schönhoff[2], Kurt Kummer[5], Heiko Wende[3], Tim Wehling[2], Thomas Michely[1]

[1]*II. Physikalisches Institut, Universität zu Köln, Zülpicher Straße 77, 50937 Köln, Germany*
[2]*Institut für Theoretische Physik, Bremen Center for Computational Materials Science, and MAPEX Center for Materials and Processes, Otto-Hahn-Allee 1, Universität Bremen, 28359 Bremen, Germany*
[3]*Fakultät für Physik und Center für Nanointegration Duisburg-Essen (CENIDE), Universität Duisburg-Essen, Carl-Benz-Straße, 47057 Duisburg, Germany*
[4]*Institut für Experimentalphysik, Freie Universität Berlin, Arnimallee 14, 14195 Berlin, Germany*
[5]*European Synchrotron Research Facility (ESRF), Avenue des Martyrs 71, CS 40220, 38043 Grenoble Cedex 9, France*

Supplementary Note 1: Unit cells

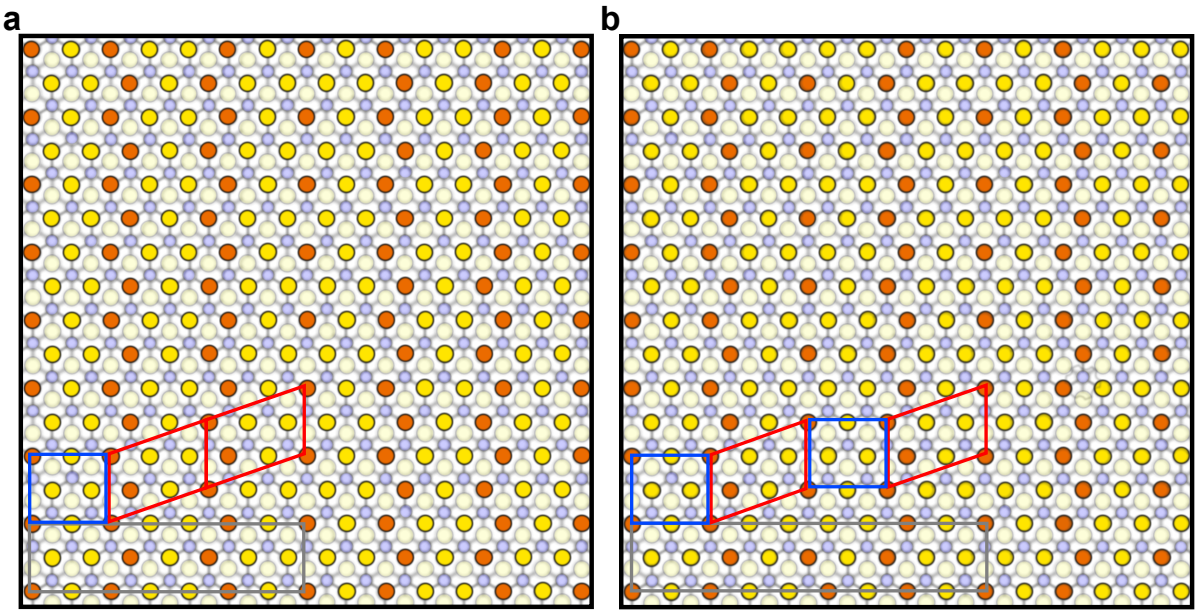

Supplementary Figure 1: Correspondence between unit cells in monolayer VSe_2 literature and the unit cells used in this paper. In **a** and **b**, models of the 1T-VS_2 atomic lattice are depicted with V atoms in blue and bottom-S atoms in faint yellow. $7 \times \sqrt{3}\mathrm{R}30°$ (**a**) and $9 \times \sqrt{3}\mathrm{R}30°$ (**b**) superstructures are visible in the top-S atoms, which are drawn in two colors to mimic the experimental apparent height in yellow (bright) and orange (dark). The dark gray rectangles indicate the $7 \times \sqrt{3}\mathrm{R}30°$ (**a**) and $9 \times \sqrt{3}\mathrm{R}30°$ (**b**) unit cells. The blue rectangle is a $2 \times \sqrt{3}\mathrm{R}30°$ unit, the red rhombus a $\sqrt{7}\mathrm{R}19.1° \times \sqrt{3}\mathrm{R}30°$.

In the isotypic material VSe_2, a superstructure of same symmetry as in VS_2, has been identified and attributed to a charge density wave (CDW)[1–4]. In these studies, the superstructure was described by a combination of $2 \times \sqrt{3}\mathrm{R}30°$ and $\sqrt{7}\mathrm{R}19.1° \times \sqrt{3}\mathrm{R}30°$ units, which we mark in our model in Supplementary Figure 1a, b in blue and red, respectively. By the combination of a single $2 \times \sqrt{3}\mathrm{R}30°$ and two $\sqrt{7}\mathrm{R}19.1° \times \sqrt{3}\mathrm{R}30°$ units, the $7 \times \sqrt{3}\mathrm{R}30°$ CDW lattice can be described; two $2 \times \sqrt{3}\mathrm{R}30°$ units and two $\sqrt{7}\mathrm{R}19.1° \times \sqrt{3}\mathrm{R}30°$ units make up the $9 \times \sqrt{3}\mathrm{R}30°$ lattice.

Supplementary Note 2: Tip-induced switching between distorted and undistorted phase

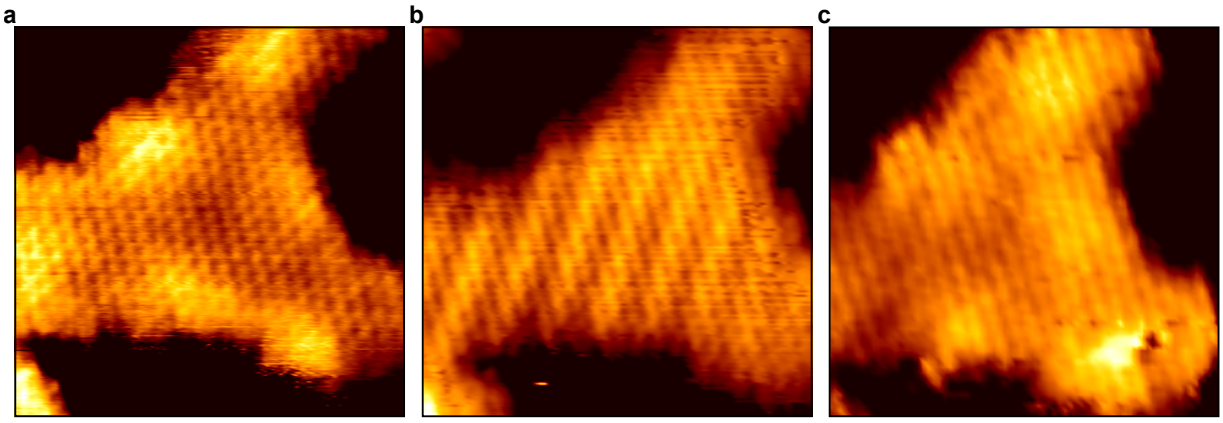

Supplementary Figure 2: Influence of STM tip on monolayer VS_2: the two consecutive STM scans in panel **a** and **b** document the STM-tip-induced switch from the undistorted to the superstructure CDW phase. Scan **c** is taken 15 minutes later and shows no more signs of the superstructure. Images taken at $300\,\mathrm{K}$. Measurement parameters: **a–c** $7 \times 7\,\mathrm{nm}^2$, $I_\mathrm{t} = 0.5\,\mathrm{nA}$, $V_\mathrm{t} = -90\,\mathrm{meV}$.

The presence of the superstructure at room temperature can also be influenced by the scanning tunneling microscope (STM) tip. Supplementary Figure 2a, b shows two consecutive STM scans, taken at the same position, tunnelling current, and bias. In Supplementary Figure 2a, the STM reveals only hexagonal atomic ordering inside the small VS_2 structure. In the successive STM scan in Supplementary Figure 2b, the wave superstructure is observed in the same region, with the phase transition apparently triggered by the interaction with the STM tip. A subsequent STM scan taken about 15 minutes later, displayed in Supplementary Figure 2c, again shows the absence of the superstructure.

Supplementary Note 3: 1T-VSe_2 vs 1T-VS_2 and $9 \times \sqrt{3}\mathrm{R}30°$ vs $7 \times \sqrt{3}\mathrm{R}30°$

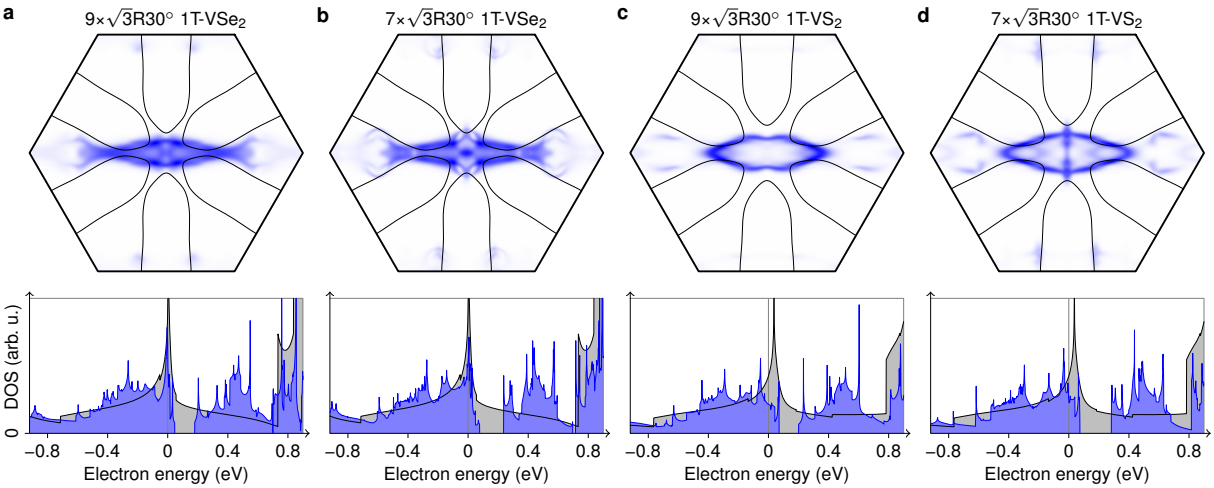

Supplementary Figure 3: Fermi surface and density of states (DOS) of monolayer **a, b** 1T-VSe_2 and **c, d** 1T-VS_2 in the undistorted phase as well as for the **a, c** $9 \times \sqrt{3}\mathrm{R}30°$ and **b, d** $7 \times \sqrt{3}\mathrm{R}30°$ CDW as obtained from DFT. The CDW data has been unfolded to the Brillouin zone of the undistorted structure. Here, the color saturation corresponds to the overlap of CDW and undistorted wave functions for the same **k** point.

In Supplementary Figure 3a, b, we show the Fermi surface and density of states (DOS) of monolayer 1T-VSe_2 in the undistorted as well as $9 \times \sqrt{3}\mathrm{R}30°$ and $7 \times \sqrt{3}\mathrm{R}30°$ CDW phases from density functional theory (DFT). In VSe_2 a similar CDW as the one found in VS_2 has been reported repeatedly[1,2,4–6]. As points of reference, corresponding results for monolayer 1T-VS_2 are displayed in Supplementary Figure 3c, d. The results for the $9 \times \sqrt{3}\mathrm{R}30°$ and $7 \times \sqrt{3}\mathrm{R}30°$ cells agree qualitatively. Furthermore, our calculations suggest that 1T-VSe_2 and 1T-VS_2 are very similar in their electronic structure. In the distorted phase, 1T-VSe_2 will also have a full gap in the unoccupied states; at the Fermi energy, only a partial gap is expected. Though this has been observed in experiment[2,3], most studies on monolayer VSe_2 agree on a full gap located at the Fermi level[1,4,6,7]. To our understanding, such a gap would require a filling of the downwards-dispersing bands near Γ, which are not gapped in the CDW configuration. According to our DFT calculations for both 1T-VS_2 and 1T-VSe_2 on a $9 \times \sqrt{3}\mathrm{R}30°$ ($7 \times \sqrt{3}\mathrm{R}30°$) supercell, $1/9 \approx 0.11$ ($1/7 \approx 0.14$) additional electrons would shift the gap to the Fermi energy (compare Supplementary Figure 10a, b). This charge could be provided by, e.g., the substrate or defects.

Supplementary Note 4: Nesting conditions and electron–phonon coupling

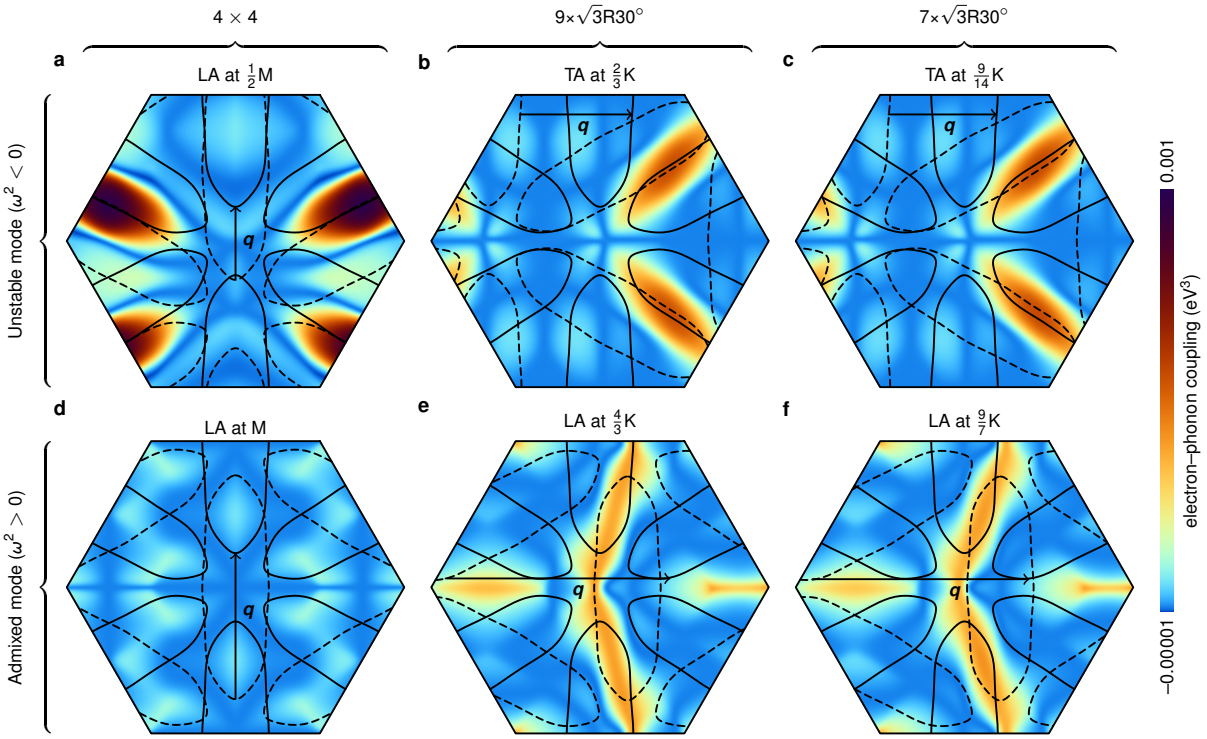

Supplementary Figure 4: Nesting conditions for different longitudinal– and transverse–acoustic (LA and TA) phonon wavevectors $\mathbf{q}$. We show the relevant electron–phonon coupling $2\omega_{\mathbf{q}} g_{\mathbf{k}+\mathbf{q},\mathbf{k}} \widetilde{g}_{\mathbf{k},\mathbf{k}+\mathbf{q}}$ as a function of the electron wavevector $\mathbf{k}$ (color scale) together with the original Fermi surface (solid lines) and the Fermi surface shifted by $-\mathbf{q}$ (dashed lines). Nesting parts of the Fermi surface can only have a strong effect on the phonons if they occur in $\mathbf{k}$-space regions with significant electron–phonon coupling (dark/brown spots). While the $\widetilde{g}$ from DFPT is fully screened, the partially screened g from constrained DFPT (cDFPT)[8] excludes low-energy electronic screening (precisely, from within the isolated band at the Fermi level). Together with the bare electronic susceptibility χ_0, they determine the phonon self-energy $\Pi = g^* \chi_0 \widetilde{g}$ responsible for the instabilities in the phonon dispersion. This analysis is equivalent to the fluctuation diagnostics in Ref. 9. The electron–phonon coupling has been obtained via the EPW code[10,11].

In Supplementary Figure 2a of the manuscript, we can observe two main instabilities in the acoustic phonon dispersion of monolayer 1T-$VS_2$from density functional perturbation theory (DFPT): one in the longitudinal branch at $\mathbf{q} \approx 1/2\,\overline{\Gamma\mathrm{M}}$ and one in the transverse branch at $\mathbf{q} \approx 2/3\,\overline{\Gamma\mathrm{K}}$. A mode with momentum $\mathbf{q}$ will be favoured if there is a large electron–phonon coupling matrix element connecting momenta $\mathbf{k}$ and $\mathbf{k}+\mathbf{q}$ close to the Fermi surface. These nesting conditions are investigated in Supplementary Figure 4. In the longitudinal case, shown in Supplementary Figure 4a, we have almost perfect Fermi-surface nesting together with a strong electron–phonon coupling (cf. Fig. 5c, d of Ref. 12 for the case of 1T-VSe_2). This $\mathbf{q}$ point is compatible with the formation

of a 4×4 CDW, as found, e.g., in bulk VSe_2[13]. Interestingly, despite these favorable conditions, this is not the preferred ground state of monolayer VS_2. Instead, a CDW with a wavevector near $\mathbf{q} = 2/3\,\overline{\Gamma\mathrm{K}}$ and $\mathbf{q} = 9/14\,\overline{\Gamma\mathrm{K}}$ develops, which features only approximate nesting and a slightly reduced coupling strength, as seen in Supplementary Figure 4b, c. As discussed in the main text, the formation of the CDW can only be understood considering non-linear mode–mode coupling. Phonon modes that appear stable in the harmonic approximation contribute significantly to the final atomic displacements, especially the longitudinal–acoustic modes for twice the momenta of the unstable modes, i.e., $\mathbf{q} = \mathrm{M}$, $\mathbf{q} = 9/7\,\overline{\Gamma\mathrm{K}}$, and $\mathbf{q} = 4/3\,\overline{\Gamma\mathrm{K}}$, see Supplementary Figure 4d–f. For both the harmonic (Supplementary Figure 4b, c) and the higher-order contributions (Supplementary Figure 4e, f) to the experimentally observed CDW, we find a similar situation of partially overlapping Fermi pockets in $\mathbf{k}$-space regions of considerable coupling, except that different pairs of pockets are involved.

Supplementary Note 5: Born–Oppenheimer energy surface in TaS_2

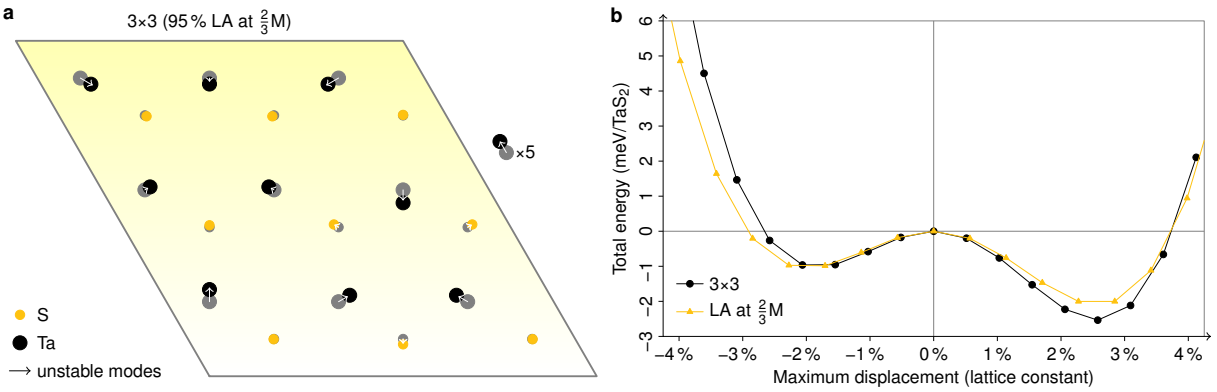

Supplementary Figure 5: a CDW distortion in monolayer 2H-TaS_2 and **b** corresponding Born–Oppenheimer energy surface. Full circles indicate atomic positions and energies for displacements in the direction of the relaxed structure, arrows and triangle marks those for the projection onto the unstable longitudinal–acoustic (LA) phonon modes at the six wavevectors $\mathbf{q} = 2/3\,\overline{\Gamma\mathrm{M}}$. The relaxed atomic displacements have been amplified by a factor of five for better visibility.

While the experimentally observed CDW in VS_2 can only be explained by the nonlinear coupling between soft and stable phonon modes, the 3×3 CDW in the trigonal–prismatic TMDCs is an example of a lattice instability that is determined essentially by a single unstable phonon mode. Analogous to Supplementary Figure 2b–e, Supplementary Figure 5 shows the 3×3 CDW structure and the corresponding Born–Oppenheimer energy surface of monolayer 2H-TaS_2 from DFT: Here, the distortion along the leading unstable phonon normal-mode coordinate largely captures the energy gain associated with the full CDW relaxation. We used the same computational parameters as in Ref. 9.

Supplementary Note 6: Phonon dispersion, nesting conditions, and electron–phonon coupling in 1T-VTe_2

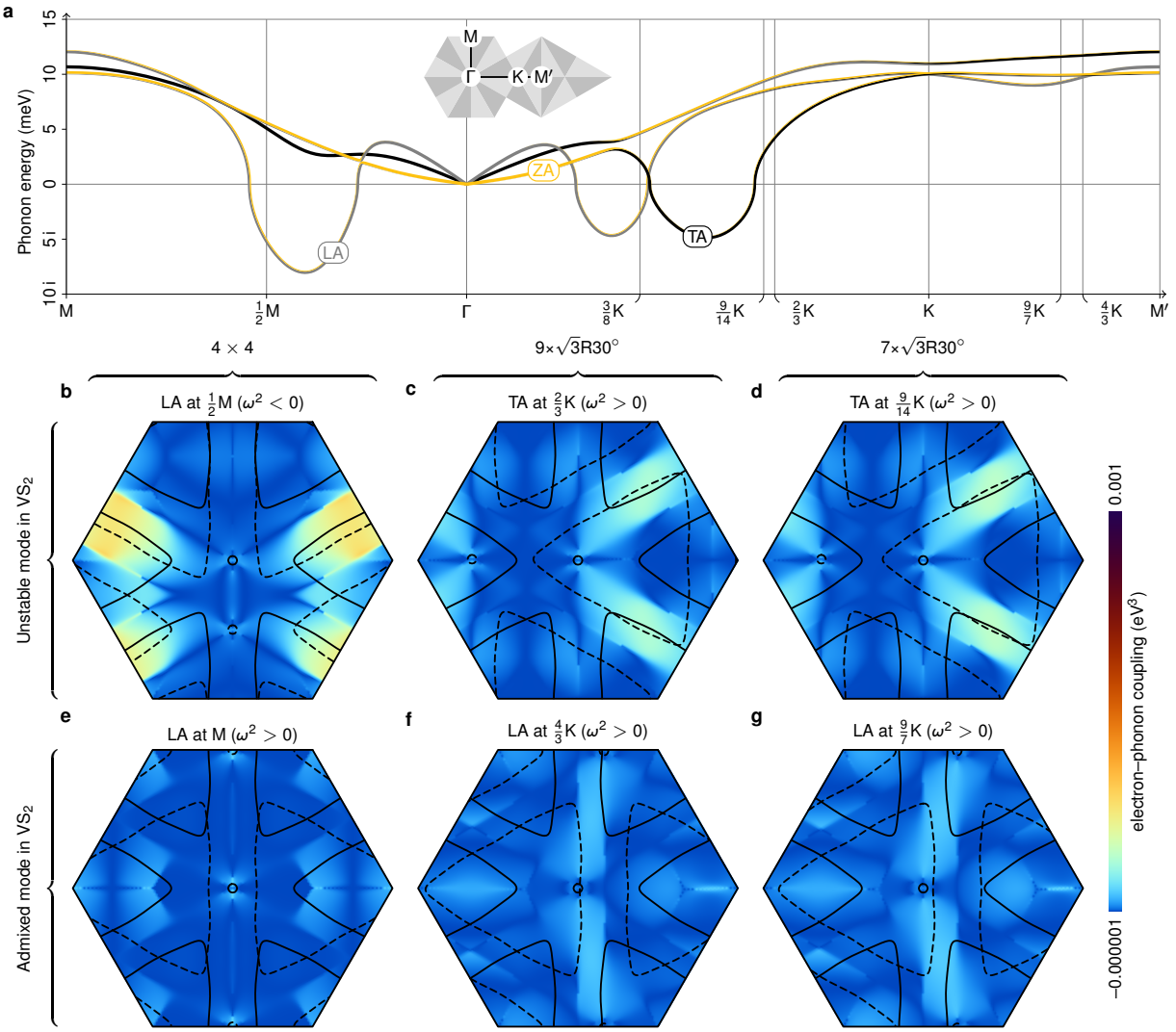

Supplementary Figure 6: a Longitudinal–, transverse– and z–acoustic (LA, TA and ZA) phonon dispersion of monolayer 1T-VTe_2. **b–g** Corresponding electron–phonon coupling $2\omega_{\mathbf{q}} g_{\mathbf{k}+\mathbf{q},\mathbf{k}} \widetilde{g}_{\mathbf{k},\mathbf{k}+\mathbf{q}}$ together with the $\mathbf{k}$ and $\mathbf{k}+\mathbf{q}$ Fermi surfaces (cf. Supplementary Figure 4).

The phonon dispersion of monolayer 1T-VTe_2 obtained from DFPT is shown in Supplementary Figure 6a. We find similar lattice instabilities as in the case of 1T-VS_2 (cf. Supplementary Figure 2a of the main text), albeit shifted to smaller $|\mathbf{q}|$. This shift, which is more pronounced for the transverse–acoustic instability in the $\overline{\Gamma\mathrm{K}}$ direction than for the longitudinal–acoustic instability in the $\overline{\Gamma\mathrm{M}}$ direction, can be traced back to differences in the Fermi surface (topology) rather than in the electron–phonon coupling, see Supplementary Figure 6b–g: Instead of the cigar-shaped electron pockets around the M points in 1T-VS_2 (cf. Supplementary Figure 4), we find triangular

hole pockets around the K points (as well as a small hole pocket at Γ) in 1T-VTe_2. In the latter case, the approximately parallel segments of the Fermi surface are closer together.

Supplementary Note 7: CDW energy gains in VS_2 vs VTe_2

Supplementary Table 1: Comparison of maximum atomic displacements and energy gains upon CDW formation for different materials and periodicities from DFT (PBE). All energies refer to a single VX_2 unit; the reference for the displacements is the lattice constant.

	1T-VS_2		1T-VTe_2	
4×4	$4\,\%$	$3.4\,\mathrm{meV}$	$13\,\%$	$34.2\,\mathrm{meV}$
$7 \times \sqrt{3}\mathrm{R}30°$	$8\,\%$	$22.7\,\mathrm{meV}$	$6\,\%$	$2.5\,\mathrm{meV}$

To compare the energy gains associated with CDW formation in 1T-VS_2 and in 1T-VTe_2 for the different periodicities, we performed structural relaxations on corresponding supercells in the framework of DFT (PBE). The energy gains reported in Table 1 show that in 1T-VS_2 the $7 \times \sqrt{3}\mathrm{R}30°$ CDW is favored over the 4×4 CDW; in 1T-VTe_2 vice versa. The DFT prediction is thus in line with experimental observation for both materials.

Supplementary Note 8: Compression of electronic spectrum

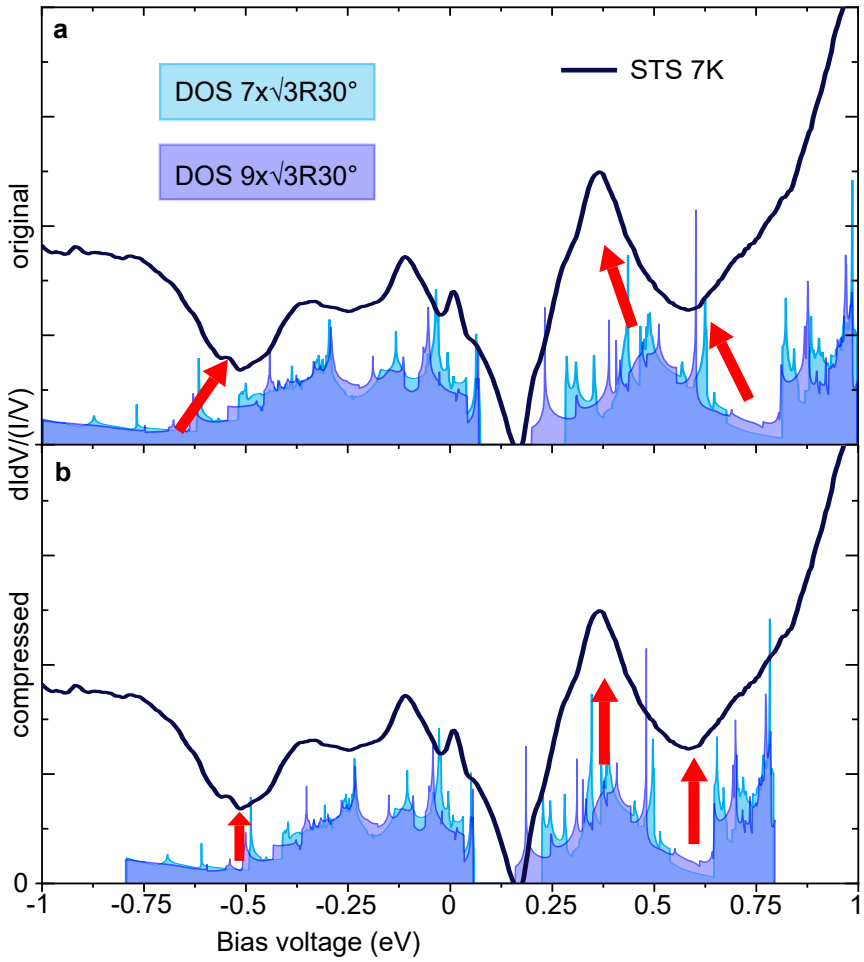

Supplementary Figure 7: Compression of experimental scanning tunneling spectroscopy (STS) data relative to density-functional theory (DFT)-calculated density of states (DOS). In **a**, the $7\,\mathrm{K}$ spectrum from the main manuscript is compared to the calculated DOS for the $7 \times \sqrt{3}\mathrm{R}30°$ and $9 \times \sqrt{3}\mathrm{R}30°$ unit cells. In **b**, the calculated DOS is compressed to about $80\,\%$ of its original width. The red arrows in **a, b** indicate three major features in the spectrum and DOS that can be harmonized between them when the DOS is compressed.

In Supplementary Figure 4a of the main text, the DOS from DFT appears to be wider than the experimental spectrum. Dynamic electronic correlation effects beyond DFT are a possible source of this discrepancy, since they can lead to band renormalization[14]. More precisely, they effect a mass enhancement of the electrons, i.e., the quasi-particle dispersions become flatter than what is expected from theories like DFT. In the case of purely local correlations[15], this effect is described by a single renormalization factor Z or the corresponding mass enhancement factor $1/Z$. Supplementary Figure 7 shows that we obtain a good match between experimental and theoretical spectra by setting $Z = 0.8$. This is indicative of moderate electronic correlations. For comparison, examples range

from diverging mass enhancement at Mott–Hubbard transitions, via mass enhancement factors of about 10 to 1000 in Kondo or heavy fermion systems, to enhancement factors between 1 and 10 in transition-metal compounds like metallic chromium or iron-based superconductors. The mass enhancement factor of $1/Z \approx 1.25$ puts VS_2 at similar electronic correlation strengths as, e.g., metallic chromium[16].

The rise in the normalized $\mathrm{d}I/\mathrm{d}V$ beyond $-0.5\,\mathrm{eV}$ can be attributed to contributions from the graphene/Ir(111) substrate, which can come to dominate the signal for large V when the VS_2 has a small DOS. In this case, the graphene spectrum (not shown) diverges beyond the Ir(111) surface state at $-190\,\mathrm{meV}$.

Supplementary Note 9: Suppression of CDW Fourier intensity within the gap

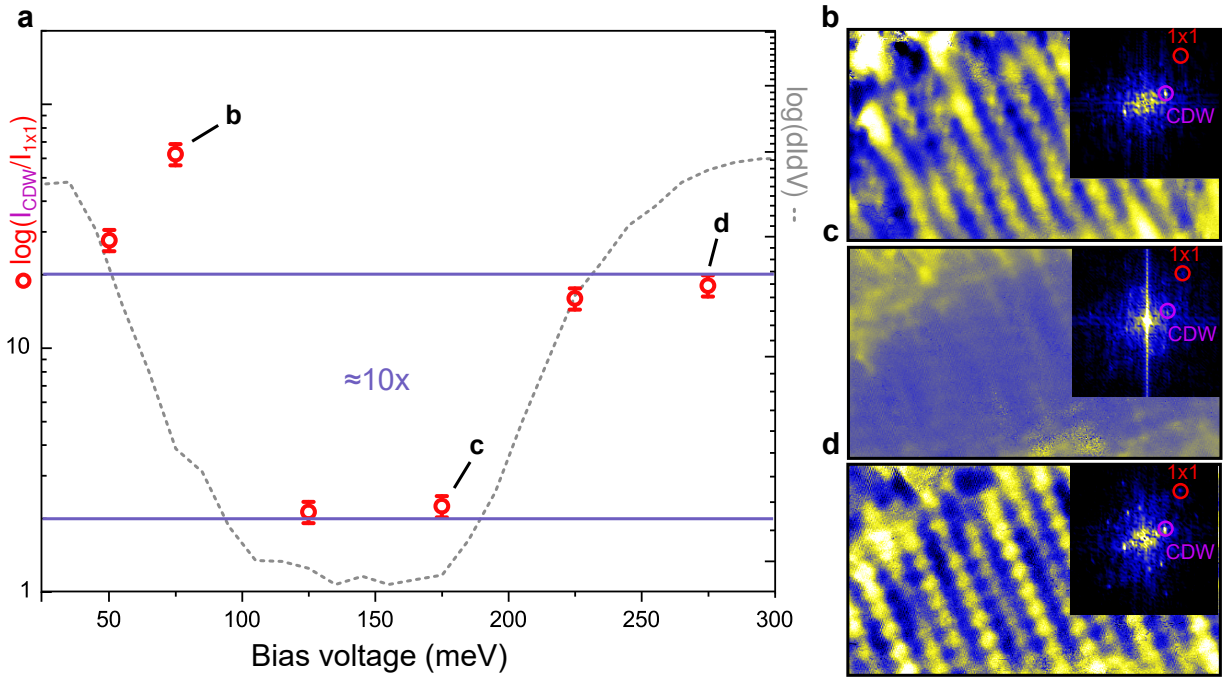

Supplementary Figure 8: Suppression of charge density wave (CDW) within the gap. **a** Logarithmic plot of the CDW intensity in the Fourier transform of $\mathrm{d}I/\mathrm{d}V$ conductance maps, normalized to the 1×1 lattice intensity. Additionally, a $\mathrm{d}I/\mathrm{d}V$ spectrum is plotted in order to indicate the location and width of the gap. **b–d** $\mathrm{d}I/\mathrm{d}V$ conductance maps taken at the voltages indicated in **a**. Measurement settings: (maps) $9.5 \times 5.5\,\mathrm{nm}^2$, $I_\mathrm{t} = 0.3\,\mathrm{nA}$, except for the map at $50\,\mathrm{meV}$, which is taken at $I_\mathrm{t} = 0.6\,\mathrm{nA}$; ($\mathrm{d}I/\mathrm{d}V$ spectrum) $f = 777.7\,\mathrm{Hz}$, $I_\mathrm{t} = 0.4\,\mathrm{nA}$, $V_\mathrm{r.m.s.} = 6\,\mathrm{meV}$. All data taken at $T = 7\,\mathrm{K}$.

Apart from the different charge distributions on either side of the gap discussed in the main manuscript, $\mathrm{d}I/\mathrm{d}V$ maps taken within the gap show a clear suppression of the CDW. For a quantitative analysis, we have Fourier analyzed the $\mathrm{d}I/\mathrm{d}V$ maps and normalized the CDW peak in the Fourier spectrum with respect to the 1×1 lattice peak intensity. The resulting value $R = I_\mathrm{CDW}/I_{1\times1}$ is observed to fall by an order of magnitude within the gap. Since a gap of other than CDW origin would have the same value of R in- and outside of the gap region[17], this is another clear indication of the relation between gap and CDW.

Supplementary Note 10: Bands along extended Brillouin-zone path

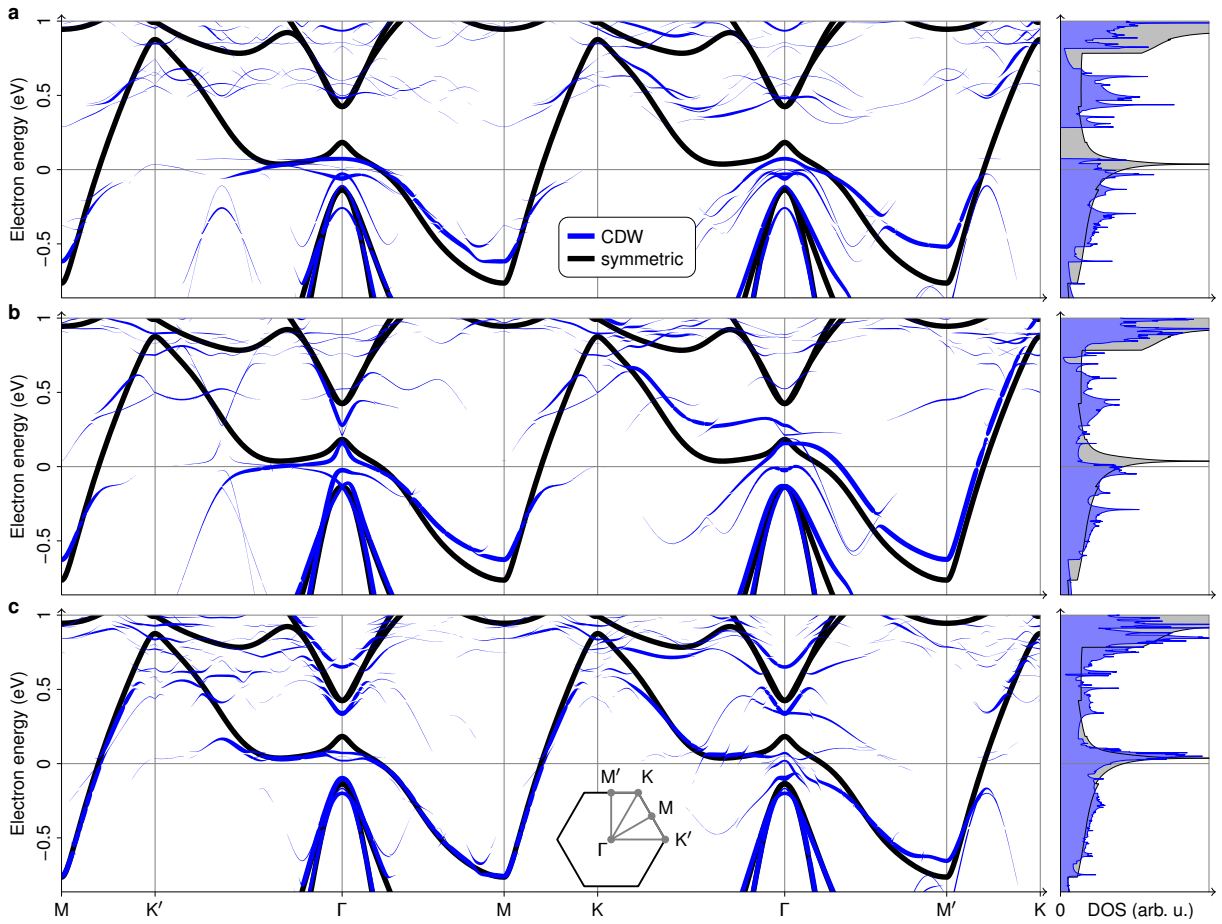

Supplementary Figure 9: Electronic band structure along an extended Brillouin-zone path and density of states (DOS) of monolayer 1T-VS_2 for **a** the full $7 \times \sqrt{3}\mathrm{R}30°$ charge density wave (CDW) displacements, **b** their projection onto unstable phonon modes, and **c** the orthogonal complement.

In Supplementary Figure 5a of the manuscript, we show the electronic band structure of monolayer 1T-VS_2 in the $7 \times \sqrt{3}\mathrm{R}30°$ phase along a selected high-symmetry path Γ–M–K–Γ of the undistorted phase only. Once the distortion breaks the C_3 symmetry, this path is not representative of the full Brillouin zone anymore. For completeness, in Supplementary Figure 9a, we thus reproduce the respective data along an extended path, again supplemented with the DOS. In Supplementary Figure 9b, c, we show the analogous results for the projection of the displacement onto the soft transverse–acoustic phonon modes at $\mathbf{q} = \pm 9/14\,\overline{\Gamma\mathrm{K}}$ and the orthogonal complement. There are some salient differences between the electrons for the full and partial CDW displacement. In Supplementary Figure 9b, the gap between M′ and K is missing; in turn, in Supplementary Figure 9c, there is no gap between M and K′ as well as M and K. The combination of both displacement components is needed to open a full gap.

Supplementary Note 11: Preservation of states at the Fermi level

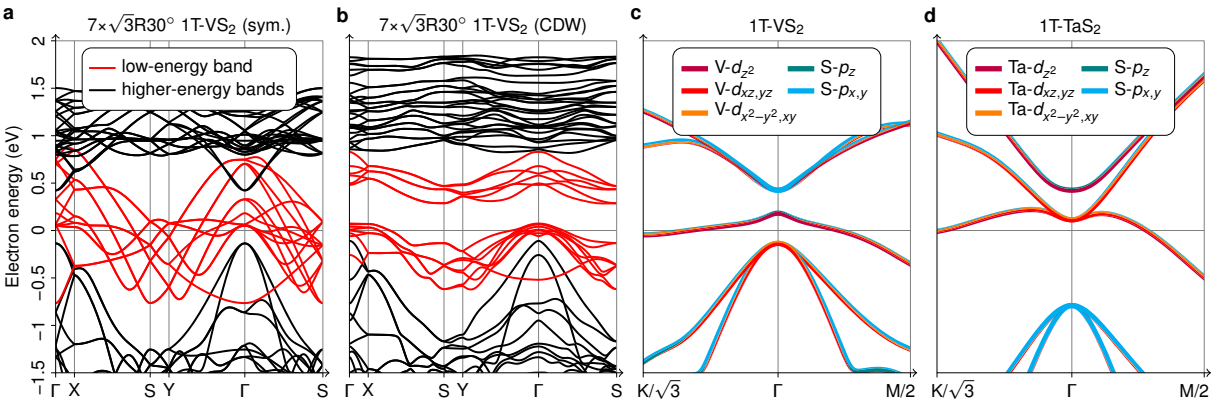

Supplementary Figure 10: a, b Band structure of symmetric and distorted 1T-VS_2 along path through Brillouin zone corresponding to $7 \times \sqrt{3}\mathrm{R}30°$ cell. The low-energy band is half-filled and splits into seven four-fold (including spin) bands between X and S. Thus, there must be 1/7 unoccupied states per V atom below the gap. **c, d** Orbital-resolved low-energy electron dispersion of 1T-TaS_2 and 1T-VS_2 near Γ. In the case of 1T-VS_2 there is an avoided crossing between V-d and S-$p_{x,y}$ bands.

The CDW does not create a complete gap at the Fermi level. For the commensurate structures used to approximate the incommensurate CDW, it is the combination of the electron count and the symmetry of the unit cell that guarantees a partially filled band, i.e., a metallic DOS. A complete gap at the Fermi level in the CDW would require the splitting of bands that must be degenerate by symmetry of the CDW structures (Supplementary Figure 10a, b), i.e., further symmetry breaking.

The particular form of the remaining spectral weight at the Fermi level resembling a downwards dispersing parabola around Γ in the CDW state (cf. Supplementary Figure 5) can be understood in terms of orbital band characters: In 1T-VS_2, we find an avoided crossing of V-d and S-$p_{x,y}$ bands in the relevant region and thus a signification hybridization between these states (Supplementary Figure 10c). This is opposed to, e.g., the case of 1T-TaS_2, where the S-$p_{x,y}$ states are much lower in energy (Supplementary Figure 10d). Now, while the d-type bands are heavily reconstructed due to the CDW, the p orbitals are less affected and can contribute to a new Fermi surface in the case of 1T-VS_2 in contrast to 1T-TaS_2.

Supplementary Note 12: XMCD sample morphology

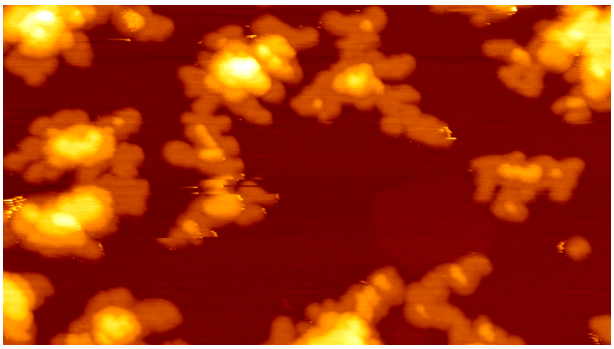

Supplementary Figure 11: Magnetic properties of VS_2: STM topograph illustrating the sample morphology of the XMCD measured sample. Image size: $100 \times 50\,\mathrm{nm}^2$.

In the main manuscript, we describe the magnetic properties of VS_2 as measured by x-ray absorption spectroscopy (XAS) and x-ray magnetic circular dichroism (XMCD). Supplementary Figure 11 displays the sample morphology of the investigated sample. Like the samples shown in the main text, the island shape is dendritic. By comparison to substrate step edges, the monolayer height is measured to be $7\,\text{Å}$. The sample has a monolayer coverage of about $40\,\%$. Distinct height levels indicate up to three layers, with multilayer VS_2 making up approximately $25\,\%$ of the total amount of VS_2 present on the surface.

Supplementary Note 13: DOS for SDW

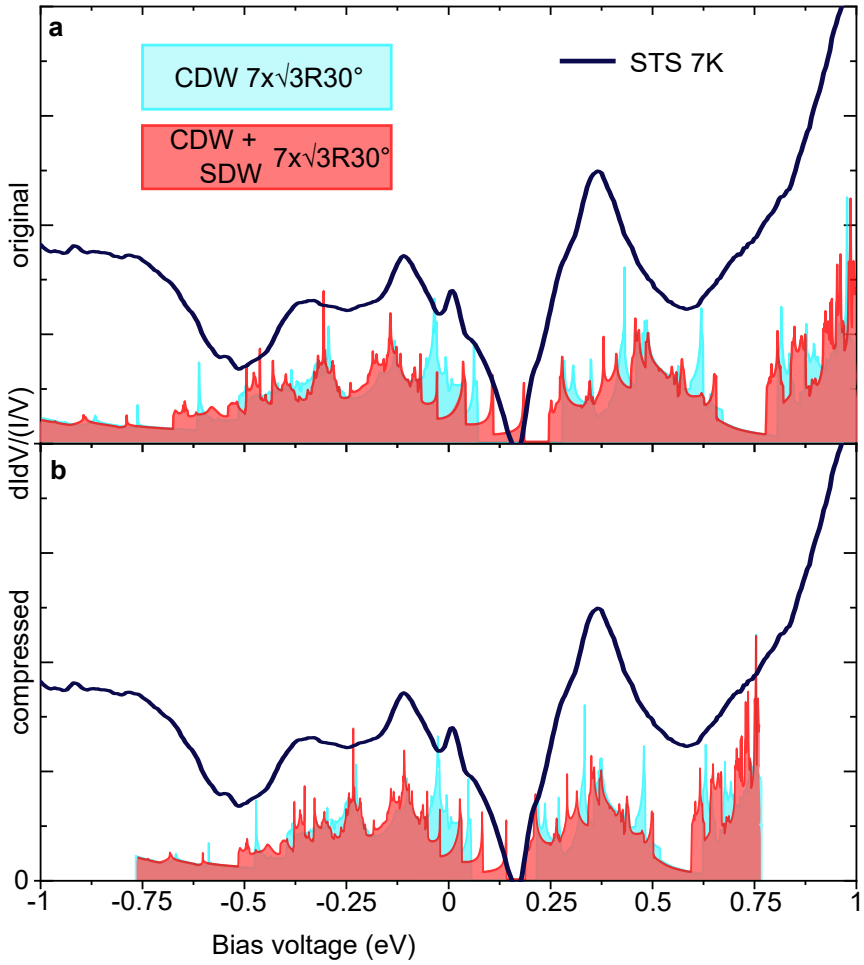

Supplementary Figure 12: **a** Scanning tunneling spectroscopy (STS) data taken with a Au tip on monolayer VS_2 at $7\,\mathrm{K}$ along with density-functional theory (DFT) calculated charge density wave (CDW) density of states (DOS) with (red) and without (cyan) SDW. **b** The same data after compressing calculated DOS to 80% of original size.

In Supplementary Figure 12a, we show the DOS of the CDW structure with and without spin density wave (SDW), along with the experimental $\mathrm{d}I/\mathrm{d}V$ spectra. The most prominent difference in the DOS is the reduction of the gap size. For the $7 \times \sqrt{3}\mathrm{R}30°$ structure, the gap shrinks from $0.21\,\mathrm{eV}$ to $0.06\,\mathrm{eV}$ when the CDW is coupled to a SDW. Since the CDW gap is indeed much larger in DFT than the experimental gap, this can be considered as an additional argument for the simultaneous presence of a SDW. Taking into account the compression of the experimental data, discussed under Supplementary Figure 7, the DOS of the coupled CDW–SDW is in even better agreement with the experimental spectra, as seen in Supplementary Figure 12b.

Supplementary Note 14: Comparison of DFT results with literature data for VSe2

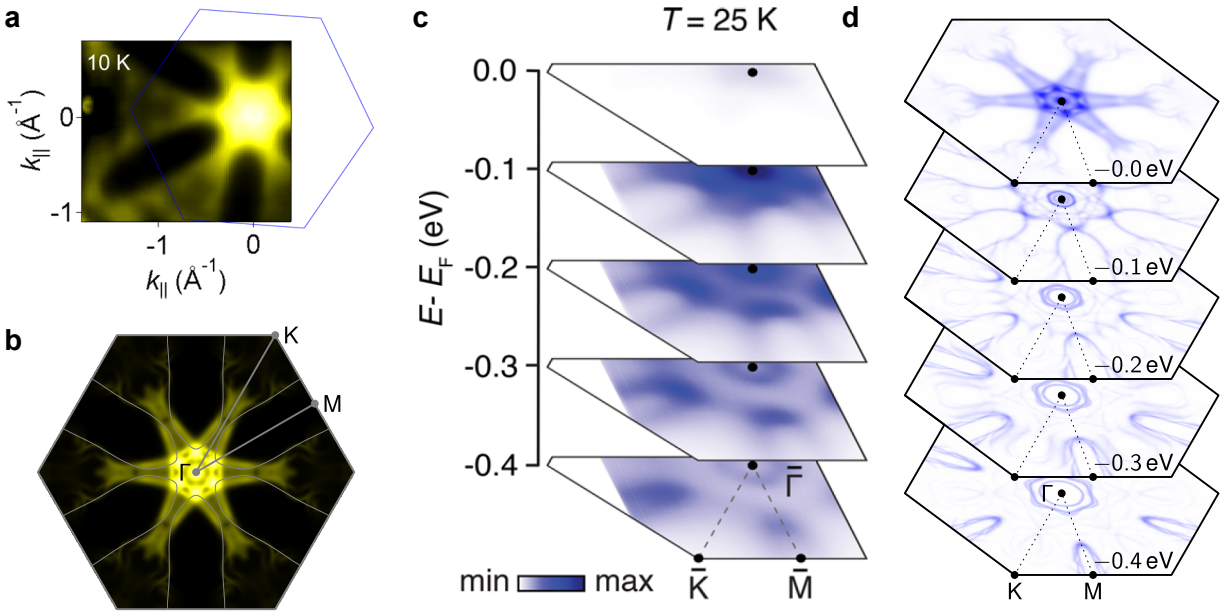

Supplementary Figure 13: Fermi surface of $7 \times \sqrt{3}\mathrm{R}30°$ CDW of monolayer 1T-VSe_2 averaged over regions of different CDW orientations and comparison to experiment. **a** Fermi surface reprinted with permission from Ref. 2 © 2018 American Physical Society. **b** Symmetrized Fermi surface calculated in this work. **c** Energy isolines reprinted with permission from Ref. 7 © 2018 American Chemical Society. **d** Symmetrized energy isolines calculated in this work.

In order to compare our DFT results for monolayer VSe_2 to existing ARPES studies, we have averaged our calculated Fermi surface of VSe_2 in the $7 \times \sqrt{3}\mathrm{R}30°$ CDW phase over all domains of the CDW with respect to the lattice. In this way, many of the familiar ARPES characteristics of VSe_2 are uncovered. If we compare to VSe_2 systems where only the $7 \times \sqrt{3}\mathrm{R}30°$ CDW was observed[2,3], we see that the experimental data in Supplementary Figure 13a, taken from Ref. 2, shows excellent agreement with our calculated Fermi surface in Supplementary Figure 13b. In particular, we observe the formation of gaps between M and K, while the rest of the Fermi surface remains intact. The apparent persistence of the six cigar-shaped electron pockets and the appearance of the hole pocket around Γ are visible in both theory and experiment. That the ARPES measurements show such small changes during the transition to the CDW phase can therefore be understood as stemming mostly from the fact that it is an averaging technique. More subtle changes to the band structure around Γ and the elliptic electron pockets cannot easily be compared by eye. All in all, our theoretical studies match very well to experimental ARPES reports of VSe_2 in the $7 \times \sqrt{3}\mathrm{R}30°$ phase[2,3].

It must however be noted that most publications on VSe_2 find, in contrast to our prediction, a full gap at the Fermi level[1,4,6,7]. Monolayer VSe_2, especially in the light of recent works[12,18,19], seems to have a strong substrate-dependence. It is therefore likely that our calculation, which is based on freestanding VSe_2, does not capture the intricacies of all experimental systems. At the Fermi surface, an (additional) 4×1 CDW found on some substrates[1,6,12,19], might induce

an insulating state. A possible cause for the presence of different and competing CDW orders might be substrate-induced strain[20], which is not included in our DFT calculations. Supplementary Figure 13c shows the Fermi surface and constant-energy contours at higher binding energies of a VSe_2 system where the Fermi surface is fully gapped at $25\,\mathrm{K}$, taken from Ref. 7. In this case, though our calculation in Supplementary Figure 13d does not predict the fully gapped surface, we see that it captures the features of the band structure away from the Fermi level quite well. The dissimilarities between VSe_2 systems with different CDW orders might therefore pertain mostly to the Fermi surface and the unoccupied states.

References

1. Duvjir, G. *et al.* Emergence of a metal–insulator transition and high-temperature charge-density waves in VSe_2 at the monolayer limit. *Nano Lett.* **18**, 5432 (2018). URL https://doi.org/10.1021/acs.nanolett.8b01764.

2. Chen, P. *et al.* Unique gap structure and symmetry of the charge density wave in single-layer VSe_2. *Phys. Rev. Lett.* **121**, 196402 (2018). URL https://doi.org/10.1103/PhysRevLett.121.196402.

3. Coelho, P. M. *et al.* Charge density wave state suppresses ferromagnetic ordering in VSe_2 monolayers. *J. Phys. Chem. C* **123**, 14089 (2019). URL https://doi.org/10.1021/acs.jpcc.9b04281.

4. Wong, P. K. J. *et al.* Evidence of spin frustration in a vanadium diselenide monolayer magnet. *Adv. Mater.* **31**, 1901185 (2019). URL https://doi.org/10.1002/adma.201901185.

5. Bonilla, M. *et al.* Strong room-temperature ferromagnetism in VSe_2 monolayers on van der Waals substrates. *Nat. Nanotechnol.* **13**, 289 (2018). URL https://doi.org/10.1038/s41565-018-0063-9.

6. Chua, R. *et al.* Can reconstructed Se-deficient line defects in monolayer VSe_2 induce magnetism? *Adv. Mater.* **32**, 2000693 (2020). URL https://doi.org/10.1002/adma.202000693.

7. Feng, J. *et al.* Electronic structure and enhanced charge-density wave order of monolayer VSe_2. *Nano Lett.* **18**, 4493 (2018). URL https://doi.org/10.1021/acs.nanolett.8b01649.

8. Nomura, Y. & Arita, R. Ab initio downfolding for electron-phonon-coupled systems: Constrained density-functional perturbation theory. *Phys. Rev. B* **92**, 245108 (2015). URL https://doi.org/10.1103/PhysRevB.92.245108.

9. Berges, J., van Loon, E. G. C. P., Schobert, A., Rösner, M. & Wehling, T. O. Ab initio phonon self-energies and fluctuation diagnostics of phonon anomalies: Lattice instabilities from Dirac pseudospin physics in transition metal dichalcogenides. *Phys. Rev. B* **101**, 155107 (2020). URL https://doi.org/10.1103/PhysRevB.101.155107.

10. Giustino, F., Cohen, M. L. & Louie, S. G. Electron-phonon interaction using Wannier functions. *Phys. Rev. B* **76**, 165108 (2007). URL https://doi.org/10.1103/PhysRevB.76.165108.

11. Poncé, S., Margine, E., Verdi, C. & Giustino, F. EPW: Electron–phonon coupling, transport and superconducting properties using maximally localized Wannier functions. *Comput. Phys. Commun.* **209**, 116 (2016). URL https://doi.org/10.1016/j.cpc.2016.07.028.

12. Chua, R. *et al.* Coexisting charge-ordered states with distinct driving mechanisms in monolayer VSe_2 (2021). URL https://arxiv.org/abs/2104.12420.

13. Williams, P. M. Phase transitions and charge density waves in the layered transition metal dichalcogenides. In Lévy, F. (ed.) *Crystallography and Crystal Chemistry of Materials with Layered Structures* (Reidel, Dordrecht, 1976). URL https://doi.org/10.1007/978-94-010-1433-5_2.

14. Giuliani, G. & Vignale, G. *Quantum Theory of the Electron Liquid* (Cambridge University Press, Cambridge, 2005). URL https://doi.org/10.1017/CBO9780511619915.

15. Georges, A., Kotliar, G., Krauth, W. & Rozenberg, M. J. Dynamical mean-field theory of strongly correlated fermion systems and the limit of infinite dimensions. *Rev. Mod. Phys.* **68**, 13 (1996). URL https://doi.org/10.1103/RevModPhys.68.13.

16. Qazilbash, M. M. *et al.* Electronic correlations in the iron pnictides. *Nat. Phys.* **5**, 647 (2009). URL https://doi.org/10.1038/nphys1343.

17. Ugeda, M. M. *et al.* Characterization of collective ground states in single-layer $NbSe_2$. *Nat. Phys.* **12**, 92 (2016). URL https://doi.org/10.1038/nphys3527.

18. Zong, J. *et al.* Observation of multiple charge density wave phases in epitaxial monolayer 1T-VSe_2 film. *Research Square* (2021). URL https://doi.org/10.21203/rs.3.rs-498840/v1.

19. Duvjir, G. *et al.* Multiple charge density wave phases of monolayer VSe_2 manifested by graphene substrates. *Nanotechnology* **32**, 364002 (2021). URL https://doi.org/10.1088/1361-6528/ac06f3.

20. Si, J. G. *et al.* Origin of the multiple charge density wave order in 1T-VSe_2. *Phys. Rev. B* **101**, 235405 (2020). URL https://doi.org/10.1103/PhysRevB.101.235405.

13

Third publication: *Ab initio* electron-lattice downfolding: potential energy landscapes, anharmonicity, and molecular dynamics in charge density wave materials

13.1. Statement of personal contribution

This work has been published as a preprint in arXiv:2303.07261 and is submitted to SciPost Phys. It has been realized in collaboration with J. Berges, E. G. C. P. van Loon, M. A. Sentef, S. Brener, M. Rossi and T. O. Wehling. The development of the downfolded lattice models was lead by T. O. Wehling. For the diagrammatic theory, J. Berges, E. G. C. P. van Loon and S. Brener have been consulted. The molecular dynamics simulations have been supervised and initiated by M. Rossi with the i-PI code, where J. Berges created the interface between the downfolded models and the i-PI code. The benchmark has been performed by J. Berges, who created Fig. 7 consequently. The introductory Fig. 1 was created by J. Berges as well. Apart from that, all calculations have been performed by me. To be more specific, setting up the downfolded models for all materials, benchmarking the potential energy surfaces, and lastly, performing and analyzing the MD simulations. In the course of this I created Figs. 2, 3, 4, 5, 6, 8 and 9. Furthermore, I have written substantial parts of the manuscript, which have been revised and edited by all authors of this work.

13.2. Positioning within the scientific landscape

The primary focus of this work revolves around the development of downfolded models, which explicitly consider both electronic and lattice degrees of freedom. These models have been utilized to explore CDW materials through MD simulations.

In the realm of scientific literature, only one article has reported molecular dynamics simulations for an H-phase transition metal dichalcogenide, specifically NbS_2 [177]. In this case, the authors conducted full *ab initio* MD simulations on 3×3 supercells. They determined free energies and forces using DFT calculations with the VASP software package [178–180]. As detailed in the computational section,

they utilized AIMD (PIMD) simulations for twelve (six) picoseconds, highlighting the substantial computational costs associated with full *ab initio* simulations.

In contrast, the newly developed method presented in this work demonstrates a computational speedup of more than *five* orders of magnitude compared to full *ab initio* methods. This advancement allows for simulations of an 18×18 supercell for 500 picoseconds. This breakthrough not only eliminates finite-size effects [181] but also has the potential to approach the thermodynamic limit.

From a technical perspective, the approach developed here is considered an *ab initio* method rather than a post-processing technique. This is because all components of the downfolded Hamiltonian can be directly derived from first principles without requiring alterations. This stands in contrast to machine learning or (density functional) tight-binding potentials, which often rely on parameter training or fitting to specific datasets.

Although not demonstrated in this work, it is possible to utilize this method for the computation of temperature-dependent vibrational quantities such as phonon frequencies and lifetimes [147, 148]. In principle, the combination of PIMD simulations with computationally efficient downfolded models offers an extension beyond conventional methods like the quasi-harmonic approximation and self-consistent phonon theory, including the stochastic self-consistent harmonic approximation. This extension is attributed to the explicit treatment of anharmonicity, as opposed to the effective harmonic framework traditionally employed in these methods.

The downfolded lattice models developed in this work are applicable to materials under two conditions. First, the material exhibits a distorted ground state in which the original atomic positions are still meaningful. Complete reconstructions, including scenarios of bond breaking, are not compatible with the chosen perturbative approach in these models. And second, the low-energy subspace significantly influences the physical phenomena of interest, as it is the case for CDWs. In the model ansatz, the low-energy electrons couple linearly to the nuclear degrees of freedom, which leads to anharmonic Born-Oppenheimer potential energy surfaces that can describe CDW physics. To study polarons, Refs. [182, 183] employ an approach based on the linear electron-phonon coupling as well. Thus, it is anticipated that the downfolding methodology can be applied to explore polaron physics also.

SciPost Physics Submission

Arne Schobert [1,2,3], Jan Berges [4,2], Erik van Loon [5], Michael Sentef [6,7], Sergey Brener [3], Mariana Rossi [7], Tim Wehling [3,8*]

1 Institut für Theoretische Physik, Universität Bremen, D-28359 Bremen, Germany
2 Bremen Center for Computational Materials Science and MAPEX Center for Materials and Processes, Universität Bremen, D-28359 Bremen, Germany
3 I. Institute of Theoretical Physics, Universität Hamburg, D-22607 Hamburg, Germany
4 U Bremen Excellence Chair, Universität Bremen, D-28359 Bremen, Germany
5 Division of Mathematical Physics, Department of Physics, Lund University, SE-22100 Lund, Sweden
7 Max Planck Institute for the Structure and Dynamics of Matter, Center for Free Electron Laser Science (CFEL), D-22761 Hamburg, Germany
6 H H Wills Physics Laboratory, University of Bristol, Bristol BS8 1TL, United Kingdom
8 The Hamburg Centre for Ultrafast Imaging, Luruper Chaussee 149, D-22761 Hamburg, Germany
* tim.wehling@uni-hamburg.de

Ab initio electron-lattice downfolding: potential energy landscapes, anharmonicity, and molecular dynamics in charge density wave materials

August 8, 2023

Abstract

The interplay of electronic and nuclear degrees of freedom presents an outstanding problem in condensed matter physics and chemistry. Computational challenges arise especially for large systems, long time scales, in nonequilibrium, or in systems with strong correlations. In this work, we show how downfolding approaches facilitate complexity reduction on the electronic side and thereby boost the simulation of electronic properties and nuclear motion—in particular molecular dynamics (MD) simulations. Three different downfolding strategies based on constraining, unscreening, and combinations thereof are benchmarked against full density functional calculations for selected charge density wave (CDW) systems, namely 1H-TaS_2, 1T-$TiSe_2$, 1H-NbS_2, and a one-dimensional carbon chain. We find that the downfolded models can reproduce potential energy surfaces on supercells accurately and facilitate computational speedup in MD simulations by about five orders of magnitude in comparison to purely *ab initio* calculations. For monolayer 1H-TaS_2 we report classical and path integral replica exchange MD simulations, revealing the impact of thermal and quantum fluctuations on the CDW transition.

Contents

1 Introduction

The coupling of electronic and nuclear degrees of freedom is an extremely complex problem of relevance to multiple branches of the natural sciences, ranging from quantum materials in and out of thermal equilibrium [1–6] to chemical reaction dynamics [7,8]. Long-standing problems include the simulation of coupled electronic and nuclear degrees of freedom for large systems and large time scales, in excited states of matter or systems with strong electronic correlations. A central contributor to these challenges is the complexity of first-principles treatments of the electronic subsystem usually required to address real materials.

Charge density wave (CDW) materials exemplify these challenges. The bidirectional coupling between electrons and nuclei results in a phase transition, where the atoms of the CDW material acquire a periodic displacement from a high-temperature symmetric structure [1, 3, 9]. Understanding the characteristics of the CDW phase transitions, the emergence of collective CDW excitations, the control of CDW states, and excitation induced dynamics of CDW systems [10–19] requires typically simulations on supercells involving several hundred or thousand atoms, where eV-scale electronic processes intertwine with collective mode dynamics at the meV scale. CDW systems thus define a formidable spatio-temporal multiscale problem. Solutions to this problem can be attempted with variational techniques [20–24], which neglect certain anharmonic effects like the anharmonic phonon decay, or by trying to circumvent the multi-scale problem by scale-separation [25, 26].

Corresponding complexity reduction strategies have been developed in distinct fields: multi-scale coarse-grained models, machine-learning models [27–31], or (density functional) tight binding potentials [32–53] have been put forward. In these methods, models

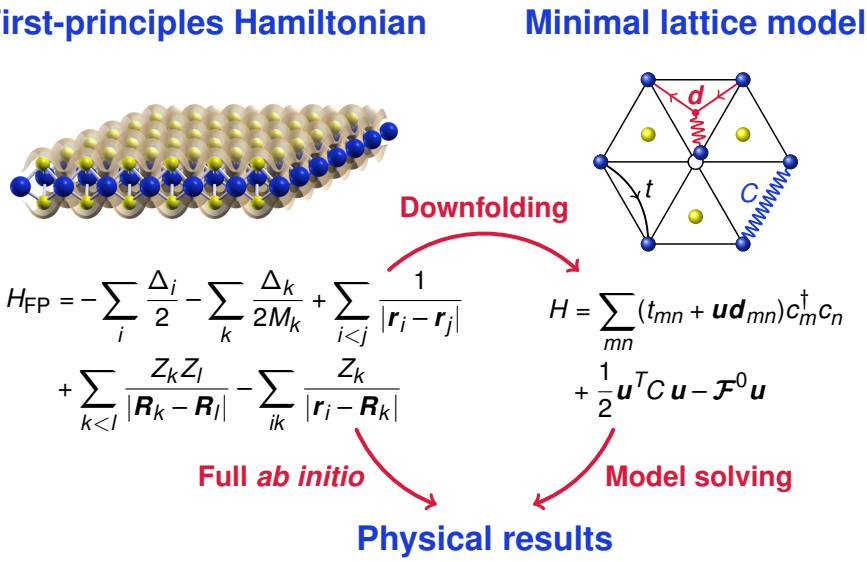

Figure 1: *Ab initio* versus *ab initio* based downfolding approaches to coupled electron-nuclear dynamics.

are defined by fitting semiempirical or "machine learned" (neural networks, Gaussian processes, others) based parameter functions to reference data often taken from density-functional theory (DFT) [54] calculations.

In the field of strongly correlated electrons, one also deals with minimal models, which typically focus on low-energy degrees of freedom: The electronic system is divided into high- and low-energy sectors. Then, the high-energy states are integrated out via field theoretical or perturbative means, leaving an effective low-energy model [55]. Methods for the derivation of model parameters include the constrained random phase approximation (cRPA) [56–62], constrained density functional perturbation theory (cDFPT) [63–67], and the constrained functional renormalization group [68–70]. The field theoretical integrating out of certain electronic states is often called "downfolding".

In this work, we demonstrate how downfolding approaches for complexity reduction on the electronic side boost the simulation of coupled electronic and nuclear degrees of freedom—in particular molecular dynamics (MD) simulations. The idea is to map the first-principles solid-state Hamiltonian onto minimal quantum lattice models, where "minimal" refers to the dimension of the single-particle Hilbert space. Three different downfolding strategies based on constraining, unscreening, and combinations thereof, are compared and demonstrated along example cases from the domain of CDW materials.

We start by introducing the first-principles electron-nuclear Hamiltonian and the minimal quantum lattice models together with the three downfolding schemes in Section 2. Potential energy surfaces resulting from the downfolded models are benchmarked against DFT for exemplary CDW systems in Section 3. MD simulations based on a downfolded model are presented in Section 4, where the CDW transition of 1H-TaS_2 is studied as a function of temperature, and the computational performance gain from downfolding is analyzed.

2 From first-principles to minimal lattice models

The general Hamiltonian of interacting electrons and nuclei in the position representation and atomic units, where in particular $m_\mathrm{e} = e = 1$, reads

$$H_\mathrm{FP} = -\sum_i \frac{\Delta_i}{2} - \sum_k \frac{\Delta_k}{2M_k} + \sum_{i<j} \frac{1}{|\boldsymbol{r}_i - \boldsymbol{r}_j|} + \sum_{k<l} \frac{Z_k Z_l}{|\boldsymbol{R}_k - \boldsymbol{R}_l|} - \sum_{ik} \frac{Z_k}{|\boldsymbol{r}_i - \boldsymbol{R}_k|}, \tag{1}$$

where $\boldsymbol{r}_i$ and $\boldsymbol{R}_k$ are electronic and nuclear positions, Δ_i and Δ_k are the corresponding Laplace operators, and Z_k and M_k are atomic numbers and nuclear masses. This Hamiltonian is also called "first-principles (FP) Hamiltonian", since only fundamental laws (i.e., the Schrödinger equation, Coulomb potential, etc.) and fundamental constants (elementary charges etc.) enter. It accounts for full atomic scale and chemical details. Numerical treatments leading directly from this Hamiltonian to physical results are called "ab initio", cf. Fig. 1 (left).

In principle, DFT provides us with a tool to calculate the total (free) energy and forces given fixed atomic positions $\boldsymbol{R}_k$ as needed for MD simulations in the Born-Oppenheimer approximation [71]. However, since DFT calculations with large supercells are prohibitively expensive, it is desirable to obtain these energies and forces in a cheaper way, while remaining close to the quantum mechanical accuracy of *ab initio* simulations.

Here, our goal is to use a reduced low-energy electronic Hilbert space for this purpose, with only a few orbitals per unit cell, cf. Fig. 1 (right).

We thus aim to work with a lattice model

$$H = H_\mathrm{el} + H_\mathrm{n} + H_\mathrm{el\text{-}n}, \tag{2}$$

which consists of the low-energy electronic subsystem

$$H_\mathrm{el} = H^0_\mathrm{el} + H^1_\mathrm{el} + H_\mathrm{DC} \tag{3}$$

with one-body

$$H^0_\mathrm{el} = \sum_{\boldsymbol{k}n} \varepsilon^0_{\boldsymbol{k}n} c^\dagger_{\boldsymbol{k}n} c_{\boldsymbol{k}n}, \tag{4}$$

Coulomb interaction

$$H^1_\mathrm{el} = \frac{1}{2N} \sum U_{\boldsymbol{q}\boldsymbol{k}mn\boldsymbol{k}'m'n'} c^\dagger_{\boldsymbol{k}+\boldsymbol{q}m} c^\dagger_{\boldsymbol{k}'n'} c_{\boldsymbol{k}'+\boldsymbol{q}m'} c_{\boldsymbol{k}n}, \tag{5}$$

and double counting (H_DC) parts, the nuclear subsystem

$$H_\mathrm{n} = -\sum_k \frac{\Delta_k}{2M_k} + V^0(\boldsymbol{u}_1, \ldots, \boldsymbol{u}_{N_\mathrm{n}}), \tag{6}$$

and a coupling between the electronic and nuclear degrees of freedom

$$H_\mathrm{el\text{-}n} = \sum_{\boldsymbol{q}\boldsymbol{k}mn} V_{\boldsymbol{q}\boldsymbol{k}mn}(\boldsymbol{u}_1, \ldots, \boldsymbol{u}_{N_\mathrm{n}}) c^\dagger_{\boldsymbol{k}+\boldsymbol{q}m} c_{\boldsymbol{k}n}. \tag{7}$$

The electronic subspace is spanned by a set of low-energy single particle states $|\boldsymbol{k}n\rangle$, with $\boldsymbol{k}$ the crystal momentum, and n summarizing further quantum numbers (band index, spin). $c^\dagger_{\boldsymbol{k}n}$ ($c_{\boldsymbol{k}n}$) are the corresponding electronic creation (annihilation) operators. N is the number of $\boldsymbol{k}$ points summed over. The nuclear degrees of freedom are expressed in terms of displacements $(\boldsymbol{u}_1, \ldots, \boldsymbol{u}_{N_\mathrm{n}}) \equiv \boldsymbol{u} = \boldsymbol{R} - \boldsymbol{R}_0$ from a relaxed reference structure $\boldsymbol{R}_0$.

H_{el} describes the low-energy electronic subsystem in the non-distorted configuration ($\boldsymbol{u} = 0$) with the effective electronic dispersion $\varepsilon^0_{\boldsymbol{k}n}$ and an effective Coulomb interaction U. In this work, $\varepsilon^0_{\boldsymbol{k}n}$ is always taken from the DFT Kohn-Sham eigenvalues of the undistorted reference system. Whenever $U \neq 0$, a term H_{DC} has to be added to avoid double counting (DC) of the Coulomb interaction already contained in the Kohn-Sham eigenvalues (see Appendix A).

V^0 plays the role of an effective interaction between the nuclei, or equivalently a partially screened deformation energy, which accounts for the Coulomb interaction between the nuclei and the interaction between the nuclei and the high-energy electrons not accounted for in H_{el}. In this work, we expand V^0 to second order in the atomic displacements $\boldsymbol{u}$,

$$H_{\mathrm{def}} = V^0 = -\sum_i \mathcal{F}^0_i u_i + \frac{1}{2}\sum_{ij} u_i C_{ij} u_j, \tag{8}$$

where $\boldsymbol{\mathcal{F}}^0$ is a force vector and C a force constant matrix. The coupling between the displacements and the low-energy electronic system from Eq. (7) is expanded to first order in the displacements $\boldsymbol{u}$:

$$H_{\text{el-n}} = \boldsymbol{u}\sum_{\boldsymbol{q}\boldsymbol{k}mn} \boldsymbol{d}_{\boldsymbol{q}\boldsymbol{k}mn} c^\dagger_{\boldsymbol{k}+\boldsymbol{q}m} c_{\boldsymbol{k}n}. \tag{9}$$

Here, $\boldsymbol{d}_{\boldsymbol{q}\boldsymbol{k}mn} = \boldsymbol{\nabla}_{\boldsymbol{u}} V_{\boldsymbol{q}\boldsymbol{k}mn}(\boldsymbol{u})$, and $\boldsymbol{u}\cdot\boldsymbol{d}_{\boldsymbol{q}\boldsymbol{k}mn}$ plays the role of a displacement-induced potential acting on the low-energy electrons.

MD simulations are a major motivation for constructing the low-energy electronic model. These simulations are here performed at various temperatures, using an electronic model that is established based on a single DFT and density functional perturbation theory (DFPT) calculation. The effective free energy of the system at given nuclear coordinates $\boldsymbol{R} = \boldsymbol{R}_0 + \boldsymbol{u}$ is

$$F(\boldsymbol{u}) = -kT \log Z(\boldsymbol{u}). \tag{10}$$

Here, the partition function $Z(\boldsymbol{u}) = \mathrm{Tr}_{\mathrm{el}} \exp(-\beta H)$ traces out the electronic degrees of freedom but not the nuclei. Thus, $F(\boldsymbol{u})$ plays the role of a potential energy surface, which governs the dynamics of the nuclei in Born-Oppenheimer approximation. Forces acting on the nuclei are then $\boldsymbol{\mathcal{F}} = -\boldsymbol{\nabla}_{\boldsymbol{u}} F(\boldsymbol{u})$ and can be conveniently obtained using the Hellman-Feynman theorem (see Appendix B):

$$\boldsymbol{\mathcal{F}} = -\sum_{\boldsymbol{q}\boldsymbol{k}mn} \boldsymbol{d}_{\boldsymbol{q}\boldsymbol{k}mn} \langle c^\dagger_{\boldsymbol{k}+\boldsymbol{q}m} c_{\boldsymbol{k}n}\rangle. \tag{11}$$

C, U, and $\boldsymbol{d}$ entering the model Hamiltonian H are not bare but (partially) screened quantities. The (partial) screening has to account for electronic processes not contained explicitly in H. Here, we consider three different schemes to determine C, U, and $\boldsymbol{d}$:

Model I strictly follows the idea of the constrained theories [57,64]. In these theories, the high-energy electronic degrees of freedom are integrated out to derive the low-energy model. The parameters entering the low-energy Hamiltonian are therefore "partially screened" by the high-energy electrons. In particular, we use cRPA for the Coulomb interaction U and cDFPT for the displacement-induced potential $\boldsymbol{d}$ and for the force constant matrix C.

Model II again applies U from cRPA. Now, however, $\boldsymbol{d}$ and C are based on the *unscreening* of the respective DFPT quantities using U inspired by Ref. [72].

Model III considers a non-interacting low-energy system, $U = 0$. $\boldsymbol{d}$ is taken from DFPT. C is obtained from unscreening DFPT. This approach is inspired by Ref. [73].

In all models, the force vector $\boldsymbol{\mathcal{F}}^0$ entering H_{def} in Eq. (8) is chosen to guarantee that $\mathrm{d}F/\mathrm{d}u_i|_{\boldsymbol{u}=0} = 0$, i.e., vanishing forces also in the models for the reference structure $\boldsymbol{R}_0$. The term $-\boldsymbol{\mathcal{F}}^0\boldsymbol{u}$, thus, plays the role of a "force double counting correction" similar to Refs. [63, 64].

Since the downfolding is done on the primitive unit cell for $\boldsymbol{u} = 0$, and we are interested in the potential energy surface for displacements on supercells, we have to map the model parameters ε^0, C, U, and $\boldsymbol{d}$ from the unit cell to the supercell. For displacements with the supercell periodicity, we can set $\boldsymbol{q} = 0$ in Eq. (9) and—within the random phase approximation (RPA)—also in Eq. (5) and drop the corresponding subscripts.

We have implemented this mapping for arbitrary commensurate supercells defined by their primitive lattice vectors $\boldsymbol{A}_i = \sum_j N_{ij}\boldsymbol{a}_j$ with integer N_{ij} [74]. It relies on localized representations in the basis of Wannier functions and atomic displacements [75], for which the mapping is essentially a relabeling of basis and lattice vectors.

2.1 Unscreening in models II and III

The central idea of models II and III is to choose C entering H_{def} such that $\mathrm{d}^2F/\mathrm{d}u_i\mathrm{d}u_j|_{\boldsymbol{u}=0} = C_{ij}^{\mathrm{DFT}}$, where the latter are the DFT force constants, accessible via DFPT. In model II we additionally require that the screened deformation-induced potential and accordingly the screened electron-phonon vertex at the level of the static RPA matches the corresponding DFPT quantity.

The unscreening procedure is represented diagrammatically: The Green's function resulting from the undistorted Kohn-Sham dispersion $\varepsilon^0_{\boldsymbol{k}n}$ is shown as a black arrow line, $G \to$ ⟶. We use a wavy line to denote the Coulomb interaction $U \to$ ∿ obtained from cRPA. The deformation-induced potential obtained from DFPT, which is by definition fully screened, is represented as a black dot, $\boldsymbol{d}^{\mathrm{DFT}} = \boldsymbol{d}^{\mathrm{III}} \to$ ●.

2.1.1 Model II

We define the unscreened deformation-induced potential $\boldsymbol{d}^{\mathrm{II}} \to$ ● (red dot) entering model II via Eq. (9) as

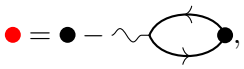

(12)

which can be written in shorthand notation as $d^{\mathrm{II}} = d - U\Pi d$, or explicitly as

$$\boldsymbol{d}^{\mathrm{II}}_{\boldsymbol{k}mn} = \boldsymbol{d}_{\boldsymbol{k}mn} - \frac{1}{N}\sum_{\boldsymbol{k}'m'n'\alpha\beta} \varphi^*_{\boldsymbol{k}\alpha m}\varphi_{\boldsymbol{k}\beta n}U_{\alpha\beta}\varphi_{\boldsymbol{k}'\alpha m'}\varphi^*_{\boldsymbol{k}'\beta n'}\frac{f(\varepsilon_{\boldsymbol{k}'m'}) - f(\varepsilon_{\boldsymbol{k}'n'})}{\varepsilon_{\boldsymbol{k}'m'} - \varepsilon_{\boldsymbol{k}'n'}}\boldsymbol{d}_{\boldsymbol{k}'m'n'}. \quad (13)$$

Here, $\varepsilon_{\boldsymbol{k}n}, \varphi_{\boldsymbol{k}\beta n}$ are the eigenvalue and -vector of band n from the undistorted Wannier Hamiltonian, and $U_{\alpha\beta}$ is the cRPA Coulomb interaction in the orbital basis.

The definition in Eq. (12) implies that the static RPA screening of the deformation-induced potential in model II indeed matches the DFPT input, since

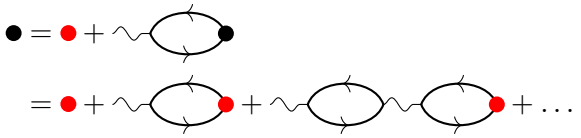

(14)

Table 1: Comparison of downfolding models

	Model I	**Model II**	**Model III**
Coulomb interaction [Eq. (5)]	cRPA	cRPA	—
Electron-phonon coupling[1] [Eq. (9)]	cDFPT	DFPT $(\star)^*$ ●	DFPT ●
Force constants [Eq. (8)]	cDFPT	DFPT $(\star)^*$	DFPT $(\star)^*$

[1] as in displacement-induced potential
[*] $(\star)$ refers to *unscreened* quantities.

The force constant matrix $C = C^{\mathrm{DFT}} - \Delta C^{\mathrm{RPA}}$ entering model II is obtained by unscreening the DFPT fully screened force constants C^{DFT} on the RPA level, i.e., we subtract the second-order response in RPA of the electronic system to the atomic displacements, as given by the bubble diagram

$$\Delta C^{\mathrm{RPA}} = \quad . \tag{15}$$

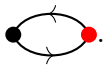

2.1.2 Model III

Again, we construct the total free energy to be exact in second order. As in model II, we have to subtract the unwanted second order, $C = C^{\mathrm{DFT}} - \Delta C^{\mathrm{III}}$. The change in the interatomic force constants for this non-interacting model is given by the bubble diagram (cf. Appendix B)

$$\Delta C^{\mathrm{III}} = \quad . \tag{16}$$

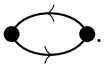

The unscreening is exact when the DFT force constants, the bubble diagram, and the free energy are evaluated at the same electronic temperature T_{DFT}. This electronic temperature facilitates the treatment of metals within DFT calculations. However, on the model side we have the freedom to evaluate the free energy at a different electronic temperature T_M. Interestingly, the resulting second order is still a very good approximation to the DFT force constants at temperature T_M [73, 76], as it will be demonstrated in this work.

This completes the definitions of models I, II, and III, which are also summarized in Table 1. In the following, we will explain and demonstrate the downfolding according to models I–III along the case example of monolayer 1H-TaS_2.

3 CDW potential energy landscapes in 1H-TaS_2: DFT vs downfolding

Monolayer 1H-TaS_2 exhibits a 3×3 CDW [77–79], where atoms are displaced from their symmetric positions as illustrated in Fig. 2a. Coupling between electrons within the low-energy subspace (highlighted in Fig. 2b) and the lattice distortions $\boldsymbol{u}$ is responsible for the 3×3 CDW instability [66]. Hence, we choose these three bands to span the low-energy subspace of electrons in the Hamiltonian H.

We present practical calculations using downfolding models I–III and benchmark the resulting potential energy landscapes against full DFT calculations. Details of the DFT calculations are presented in Appendix C. The energy landscapes will be illustrated along the displacement direction of the CDW distortion: $\boldsymbol{u} = \alpha(\boldsymbol{R}_{\mathrm{CDW}} - \boldsymbol{R}_0)$. Here, $\boldsymbol{R}_0$ is the symmetric relaxed structure, and $\boldsymbol{R}_{\mathrm{CDW}}$ is the CDW structure as obtained by DFT. α plays the role of a scalar coordinate, where by construction $\alpha = 0$ yields the symmetric

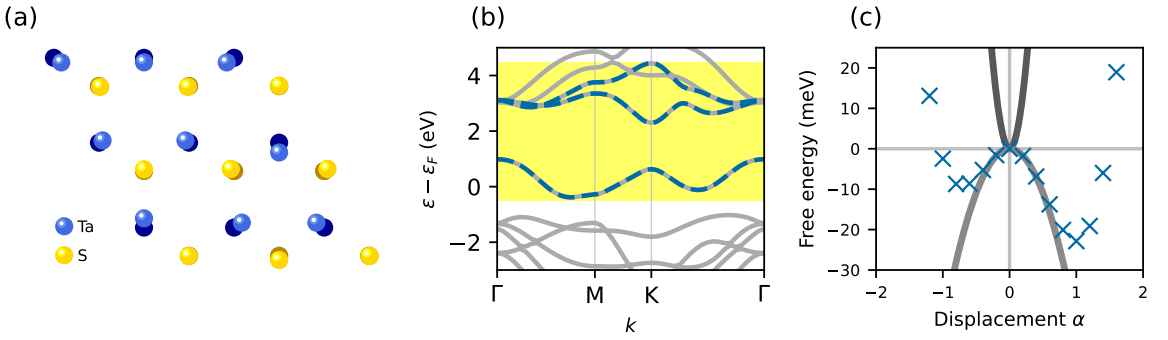

Figure 2: (a) Crystal structure of the 3×3 CDW in 1H-TaS_2 (displacements are increased by a factor of 5 for visibility). (b) Electronic bands of 1H-TaS_2 from DFT (gray) and Wannier bands (blue dashed), which span the cDFPT active subspace highlighted in yellow. (c) Born-Oppenheimer potential energy surface from DFT for the 3×3 CDW in 1H-TaS_2 (blue crosses). Its negative curvature matches the DFPT parabola (gray curve). The cDFPT parabola, which is not screened by the active subspace electrons, is opened upward (dark gray curve).

state and $\alpha = 1$ the CDW displacement pattern. Note, however, that the models readily yield the full energy landscape for arbitrary displacements.

Model I starts with partially screened force constants C from cDFPT in H_{def}, which exclude screening processes taking place within the low-energy electronic target space highlighted in Fig. 2b. The "bare" harmonic potential energy versus displacement curves resulting from H_{def} (dark gray cDFPT parabola) is compared to full DFT total energy calculations (crosses) in Fig. 2c. The upward opened cDFPT parabola shows that the CDW lattice instability is induced by the electrons of the target subspace, in accordance with Ref. [66].

We account for density-density type Coulomb matrix elements in H_{el}, which we obtain from cRPA, and solve the resulting model Hamiltonian H for the potential energy landscape $F(\boldsymbol{u})$ in Hartree approximation. See Appendix A for a detailed description of the Hartree calculations. The resulting total (free) energy versus displacement curve is compared to DFT in Fig. 3a. Model I generates an anharmonic double-well potential and thus features a CDW instability like DFT, which is qualitatively reproduced. Nevertheless, there is some deviation of model I from DFT, which originates mainly from the harmonic term. In comparison to DFT, model I and its subsequent Hartree solution involve two additional approximations, which could be responsible for the deviations to second order: neglecting non density-density type Coulomb terms, and neglecting exchange-correlation effects.

Model II suppresses deviations from the DFT potential energy landscape to second order in $\boldsymbol{u}$ by construction: Since the fully screened deformation energy from DFPT agrees with the DFT energy versus displacement curve (see Fig. 2b), as it must be, also the solution of the downfolded model II matches DFT to second order in the displacement (Fig. 3b). The overall match between the downfolded model II and DFT is clearly much better than for model I and indeed almost quantitative also at displacements $|\alpha| > 1$, where anharmonic terms are substantial.

Also **model III**, which involves non-interacting electrons coupled to lattice deformations via fully screened DFPT displacement-induced potentials, recovers the DFT potential

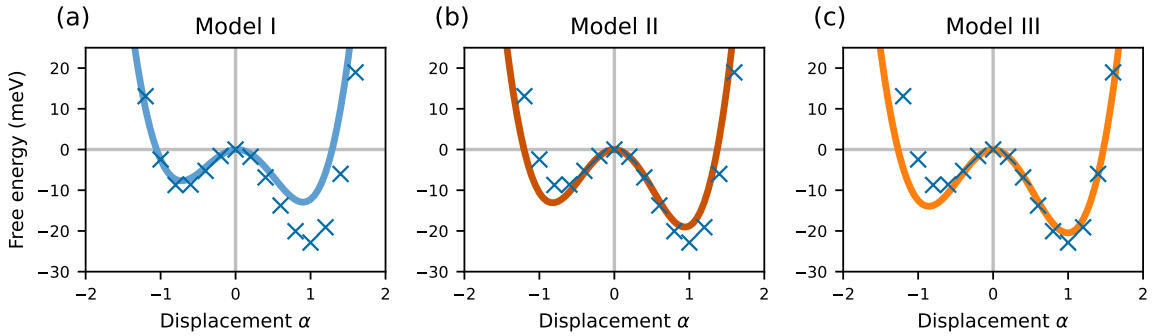

Figure 3: Free energies of the 3×3 CDW mode in 1H-TaS_2 from DFT (blue crosses) and downfolded models. (a) Interacting model with partially screened quantities from constrained theories cRPA and cDFPT (start from cDFPT parabola). (b) Interacting model with partially screened quantities from unscreening (start from DFPT parabola). (c) Non-interacting model with fully screened quantities (start from DFPT parabola).

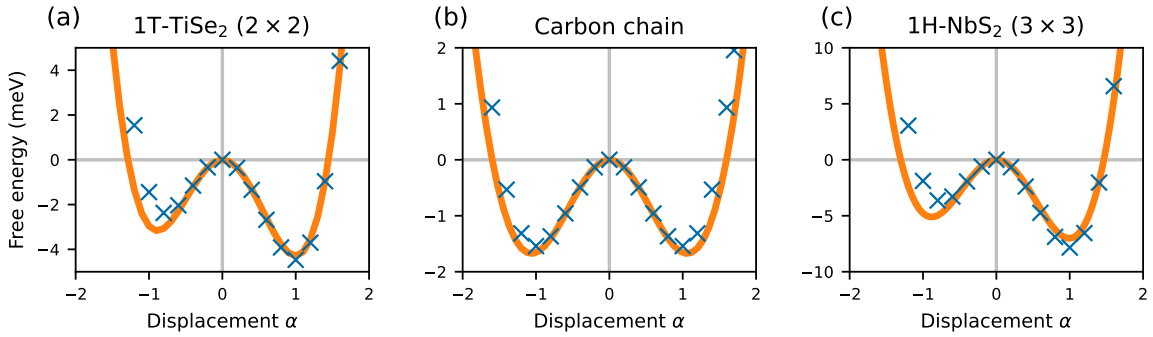

Figure 4: Free energies of (a) the 2×2 CDW in 1T-$TiSe_2$, (b) the CDW in the carbon chain, and (c) the 3×3 CDW in 1H-NbS_2. The blue crosses are data points from DFT and the orange curves are the model III results.

energy vs displacement curve for the 3×3 CDW distortion in 1H-TaS_2 almost quantitatively (Fig. 3c) and even slightly better than model II.

We also applied downfolding model III to monolayer 1T-$TiSe_2$, a one-dimensional carbon chain, and monolayer 1H-NbS_2 as examples of further CDW materials. The resulting potential energy landscapes in Fig. 4 show the agreement between DFT and the downfolded model. Hence, model III captures the most important anharmonicities in these cases. CDWs are especially, but not exclusively, found in low-dimensional systems. As a consequence, we focussed on low-dimensional materials for this benchmark. However, the downfolding formalism is independent of dimensionality.

3.1 Influence of Wannier orbitals and electronic Hilbert space dimension

Since the electronic Hamiltonian [Eq. (3)] is represented via Wannier functions, we have a certain freedom of choice. From a computational standpoint, we are aiming for a maximal reduction of the dimension of the single-particle Hilbert space, while maintaining a reasonable level of accuracy. Thus, the natural question arises: How many and which Wannier orbitals to choose to create the single-particle Hilbert space?

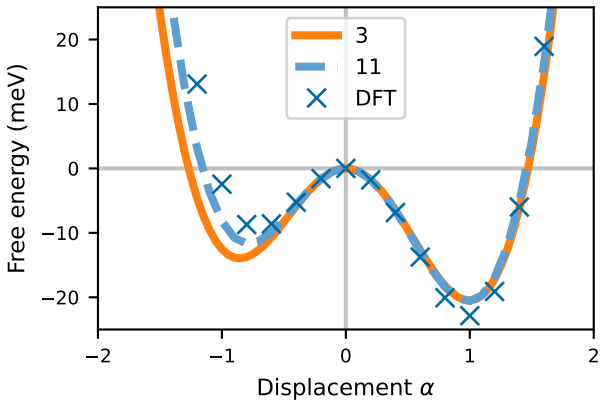

Figure 5: Free energies of the 3×3 CDW in 1H-TaS_2. We show DFT data points (blue crosses), model III results for three Wannier orbitals (orange solid curve), and model III results for eleven Wannier orbitals (blue dashed curve).

For 1H-TaS_2, we compare a "minimal" and a "maximal" model involving, respectively, three and eleven Wannier orbitals per unit cell: In the case of three orbitals, there are three d-type orbitals on the Ta atom $(d_{z^2}, d_{x^2-y^2}, d_{xy})$, and in the case of eleven orbitals, there are five d-type orbitals on the Ta atom $(d_{z^2}, d_{xz}, d_{yz}, d_{x^2-y^2}, d_{xy})$ and three p-type orbitals on both S atoms (p_x, p_y, p_z). Note, that these are the Hilbert space dimensions on the primitive unit cell. On the 3×3 supercell calculations, the dimensions are 27 and 99 respectively.

We compare the energy-displacement curves resulting from model III for both Hilbert space sizes to DFT in Fig. 5. While the results are similar in both cases, the eleven orbital model is slightly closer to full DFT than the three orbital model. In the eleven-orbital model, the displacement potentials directly induce changes in the d-p hybridization. We speculate that anharmonicities associated with these rehybridization terms are responsible for the slightly improved accuracy of the eleven band model.

3.2 Electronically generated anharmonicities

Models I, II, and III are based on the electronic structure at the symmetric equilibrium positions of the atoms, as well as the linear response to displacements that is accessible in DFPT. By construction, models II and III guarantee agreement with the full DFT calculation at small displacements $\boldsymbol{u}$, up to order $\boldsymbol{u}^2$ in the energy and up to order $\boldsymbol{u}$ in the electronic structure. One might wonder if these models, based on linear response, can ever be useful for the description of the distorted phase, which is necessarily stabilized by anharmonicity and terms of order $\boldsymbol{u}^3$, $\boldsymbol{u}^4$, and beyond.

The close match between the significantly anharmonic DFT potential energy landscapes and models II and III in Figs. 3, 4, and 5 at $|\alpha| > 1$ might thus come as a surprise. The reason behind the good match even in the anharmonically dominated region can be understood in the following sense: linear changes in the electronic potential lead to non-linear changes in eigenvalues of the electronic Hamiltonian and therefore in the total energy. Thus, if the low-energy electrons are responsible for the anharmonicity that stabilizes the CDW, then a low-energy electronic model based on DFPT quantities has the possibility to describe this.

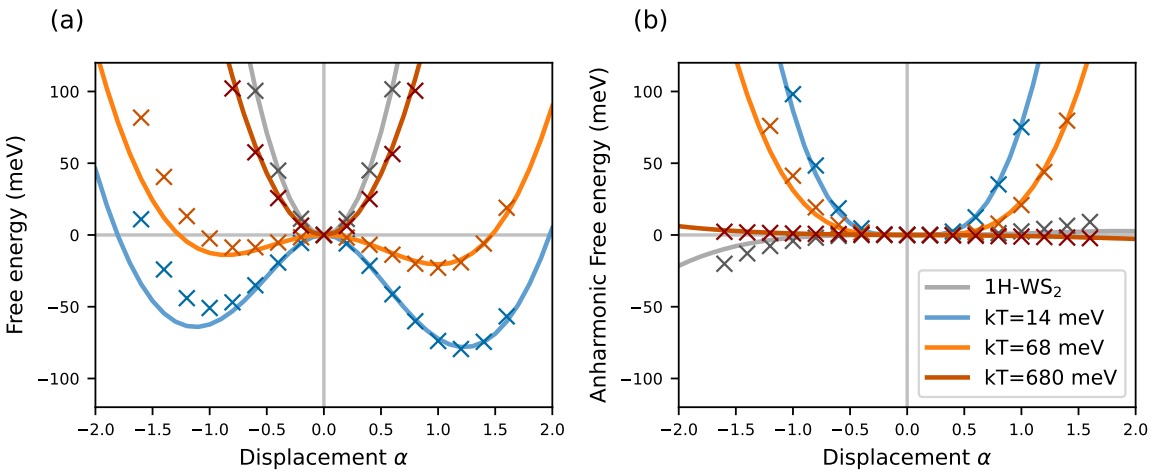

Figure 6: (a) Free energy and (b) anharmonic part of the free energy for 1H-TaS_2 at electronic smearings $kT = 14$ meV (blue), 68 meV (orange), 680 meV (dark red) and for 1H-WS_2 at smearing $kT = 68$ meV. Solid lines originate from model III and crosses from DFT. Even though the inputs for model III (see Table 1) were generated at the electronic temperature $T_{\mathrm{DFT}} = 68$ meV, we can still evaluate the free energy at higher or lower model temperatures T_{M} and get a good agreement with DFT.

The emergence of electronically driven anharmonicities can be illustrated with an electronic two-level system, $H^0_{\mathrm{el}} = \Delta\sigma_z$, coupled linearly to a nuclear displacement u through $H_{\text{el-n}} = u \cdot d\sigma_x$ [following Eq. (9)]. Here, σ_i denote Pauli matrices, 2Δ is the level-splitting and d encodes the strength of the coupling of electrons to nuclear displacements as in Eq. (9). The ground state eigenvalue of $H^0_{\mathrm{el}} + H_{\text{el-n}}$ reads $E_0 = -\sqrt{\Delta^2 + (du)^2} \approx -\Delta(1 + \frac{1}{2}\left(\frac{du}{\Delta}\right)^2 - \frac{1}{8}\left(\frac{du}{\Delta}\right)^4 + \dots)$. Thus, electronically generated anharmonicities appear at displacements on the order $u \approx \Delta/d$. Taking the level splitting Δ as a proxy for the electronic bandwidth $W \sim \Delta$ or for the inverse of the density of states at the Fermi level $\rho \sim 1/\Delta$, we have electronically generated anharmonicities appearing at displacements on the order $u \approx W/d \approx 1/(\rho d)$. In other words, systems with strong electron-lattice coupling and high density of states at the Fermi level are expected to be domains where the linearized electron-lattice coupling preferably works. In addition, the approximation of a linearized electron-lattice coupling as in Eq. (9) has also been successfully applied to describe polaronic lattice distortions [80, 81].

This hypothesis is further corroborated by the comparison of energy-displacement curves for 1H-TaS_2 at different electronic smearings to those of the related system 1H-WS_2, in Fig. 6.

The electronic band structure of WS_2 [82] is very similar to the one of TaS_2 (see Fig. 2b) with the key difference that it has one additional valence electron per unit cell. Hence, the half-filled conduction band of TaS_2 becomes completely filled in the WS_2 case, which renders WS_2 semiconducting and quenches the response of the low energy electronic system. Similarly, an increased electronic smearing/temperature quenches the response of the low-energy electronic system. Both WS_2 and TaS_2 at high smearing, are dynamically stable, which is indicated by the positive second order of the free energy in Fig. 6a. This tells us that at least the harmonic term is significantly affected by the occupation of the low-energy subspace. Furthermore, in Fig. 6b, we show the corresponding anharmonic part of the free energies. The flat shape of the high smearing (dark red) and the WS_2 (gray)

curves show that the anharmonicity is strongly reduced compared to the low smearing cases. These observations suggest that the anharmonicities associated with the CDW formation in 1H-TaS_2 indeed originate to a large extent from non-linearities in the response of the low-energy electronic system to the external displacement-induced potentials.

Anharmonicities associated with the non-linear low-energy electronic response comprise single-particle and Coulomb contributions. We analyze these contributions diagrammatically in the following for the grand canonical potential Ω:

Model III has the Coulomb contributions accounted for indirectly via the fully screened DFPT deformation-induced potential and the diagrams contributing to anharmonicities in Ω are of the following types:

$\Omega^{\mathrm{III}}_{\mathrm{anh}} =$ 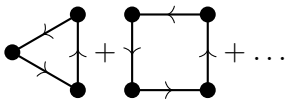 $+ \ldots$ (17)

Model II has explicit Coulomb interaction entering and the diagrammatic content is determined by the approximation used to treat the Coulomb interaction in model II. When solving model II in self-consistent Hartree approximation, we generate terms screening the deformation-induced potential according to Eq. (14). Thus, the anharmonic contributions to the grand potential in model II, $\Omega^{\mathrm{II}}_{\mathrm{anh}}$, contain those diagrams also present in model III but also further ones. For example, at order $\boldsymbol{u}^4$, model II contains a diagram of the form

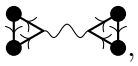 , (18)

which is not present in model III.

Both the Green's function (not shown here) and total energy or grand canonical potential in models II and III agree at small displacements (by construction) and disagree at higher orders in $\boldsymbol{u}$, and their difference scales with the strength of the Coulomb interaction. Fundamentally, the Green's function of the exact DFT solution contains interaction-mediated anharmonic response to displacements, just like model II does. At the same time, in our current implementation model II only contains Hartree-like diagrams of this kind and lacks other diagram topologies present in the exact DFT solution. These additional diagrams can lead to substantial error cancellation. Thus, it is hard to make general arguments about which model to prefer beyond order $\boldsymbol{u}^2$, given the opaqueness of the underlying DFT exchange-correlation functional. We speculate that cancellations similar to those occurring in second order [73, 76] in $\boldsymbol{u}$ could be also effective in higher orders. In our numerical studies, we find that the total energy curves of model II and III are relatively close for the systems studied here.

4 Downfolding-based molecular dynamics

So far we have seen that the downfolded models can reproduce total free energies from DFT. In the following Section 4.1, we assess the computational speed of these models, which ultimately paves the way to enhanced sampling simulations based on MD. As a demonstration of this enhancement, we perform the downfolding-based MD for the case example of monolayer 1H-TaS_2 in Section 4.2.

4.1 Benchmark of model III against DFT: force and free energy calculations

To demonstrate the performance gain of model III, we benchmark the calculation of forces and free energies against DFT. For this benchmark, we perform structural relaxations of 1H-TaS_2 starting from random displacements $|u_i| < 0.01$ Bohr—to mimic the conditions of a MD simulation step—on different supercells. Durations are averaged over five steps, excluding the first step starting from the initial guess for the density in the DFT case. Calculations are performed on identical machines, using equivalent computational parameters (cf. Appendix C). The results are shown in Fig. 7.

More precisely, we benchmark two implementations of model III: Calculations on finite $\boldsymbol{k}$ meshes, as shown in the previous Section 3, currently require a lot of memory to store the deformation-induced potential in the real-space ($\boldsymbol{d}_{\boldsymbol{R},\boldsymbol{R}'}$) and reciprocal-space ($\boldsymbol{d}_{\boldsymbol{q}=0,\boldsymbol{k}}$) representations, which limits the system to similar sizes as achievable in DFT (Fig. 7a). Thus, in this section, we instead use a sparse representation, which uses significantly less memory (Fig. 7b), reaching linear scaling with the system size (cf. Ref. [46]), but is currently restricted to $\boldsymbol{k} = 0$, appropriate for large supercells. It also increases the time needed to initialize the program (Fig. 7c, d), which however does not influence the MD simulations. Comparing to the same DFT program we use to obtain the parameters for the downfolded model, i.e., the plane-wave code Quantum ESPRESSO [83, 84], we find a speedup of about five orders of magnitude in the downfolding approach for the relevant systems (Fig. 7e, f). Note that our implementation is based on NumPy and SciPy [85, 86] and that optimizations both on the *ab initio* and on the model side are possible.

The computational advantage from the non-interacting model III over DFT is easily explained: While DFT relies on the self-consistent solution of the Kohn-Sham system, model III only needs a single matrix diagonalization to solve the Schrödinger equation. Most importantly, through downfolding, the matrix in model III only covers the low-energy subspace of the electronic structure, as opposed to DFT, whose matrix accounts for low- and high energy bands. In fact, most of the time is spent on setting up the Hamiltonian matrix and evaluating the forces [Eq. (11)]. To guarantee that the former is Hermitian and to make the use of sparse matrices more efficient, we have symmetrized $\boldsymbol{d}_{\boldsymbol{R},\boldsymbol{R}'\alpha\beta} = \boldsymbol{d}^*_{\boldsymbol{R}-\boldsymbol{R}',-\boldsymbol{R}'\beta\alpha}$ and neglected matrix elements smaller than 1 % of the maximum, the effect of which on the free-energy landscape is negligible.

4.2 Enhanced sampling simulations based on downfolded model III

We now perform enhanced sampling simulations based on MD with the downfolding scheme defined by model III. To this end, we implemented a Python-based tight-binding solver [74], which delivers displacement field dependent forces and total free energies to the i-PI (path integral) MD engine [87].

As stated in the previous section, we find a speedup of about five orders of magnitude in the downfolding approach. Thus, the downfolding approaches make larger system sizes and longer time scales well accessible. While for instance Ref. [88] simulates the dynamics of 3×3 supercells of 1H-NbS_2 with AIMD for time scales of about 6 to 12 ps, the downfolding-based MD allows us to address much larger 18×18 supercells for time scales of about 500 ps using a similar amount of CPU core hours.

For monolayer 1H-TaS_2, we performed classical (and path integral) replica exchange MD simulations (see Appendix D) on the 18×18 supercells using 26 replicas (and 10 beads) spanning a temperature range from 50 to 200 K in the canonical (NVT) ensemble. In each MD step ν we record the position vectors of all nuclei $\boldsymbol{R}_l(\nu, T)$ for all temperatures

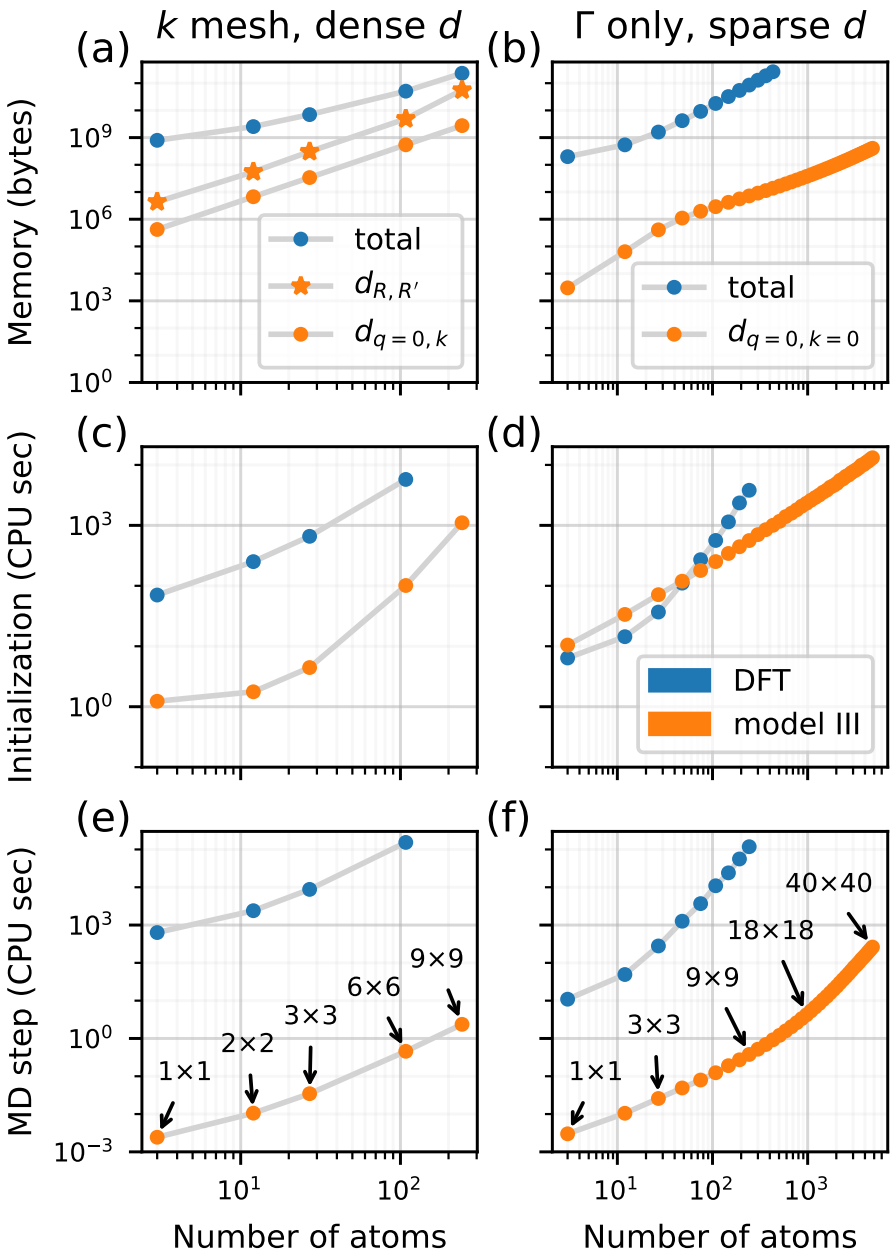

Figure 7: Comparison of (a, b) memory requirements, (c, d) initialization times, and (e, f) durations of energy and forces calculations using QUANTUM ESPRESSO (blue) and our PYTHON implementations of model III (orange) (cf. Appendix C). We consider (a, c, e) $\boldsymbol{k}$ meshes of constant density and (b, d, f) the Γ-only case, for which model III has been implemented using arrays of sparse matrices for the electron-phonon coupling $d_{i\alpha\beta}$. The DFT calculations have been parallelized over plane waves and real-space grids (`-nk 1 -nd 1`) using 40 CPUs; the model calculations have been run serially. In both cases, Intel Skylake 6148 processors have been used.

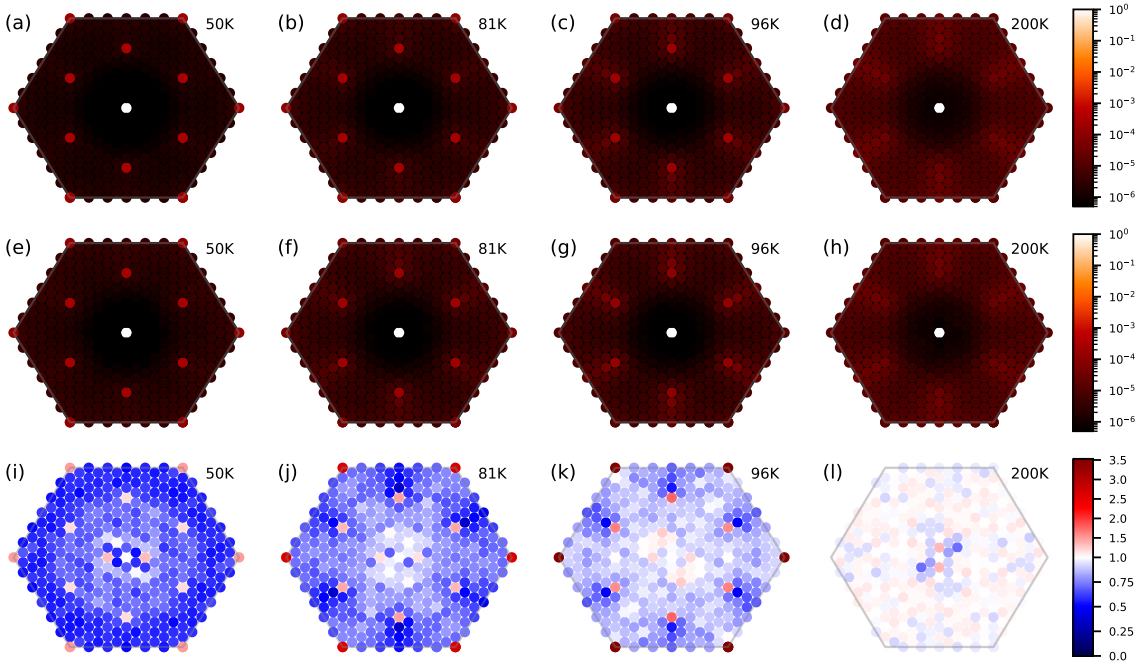

Figure 8: Structure factors $\langle S(\boldsymbol{q}, T)\rangle$ [Eq. 19] for 1H-TaS_2 on the 18×18 supercell. (a–d) Structure factor S_{CL} from classical MD. (e–h) Structure factor S_{PI} from PIMD. The peaks at $\boldsymbol{q} = 2/3\,\Gamma\mathrm{M}$ and $\boldsymbol{q} = \mathrm{K}$ for $T = 50$ K are characteristic for the 3×3 CDW. At higher temperatures, the peaks are broadened and reduced in intensity. (i–l) Ratio of structure factors $S_{\mathrm{CL}}/S_{\mathrm{PI}}$ from classical and path integral MD. A value close to 1 (indicated in white) corresponds to minimal differences between classical and quantum simulations.

T. Defining the structure factor

$$S(\boldsymbol{q}) = \frac{1}{N}\left|\sum_{l=1}^{N} e^{-i\boldsymbol{q}\cdot\boldsymbol{R}_l}\right|^2 \tag{19}$$

for a given atomic configuration $\boldsymbol{R}_l$, we obtain the temperature-dependent MD ensemble averaged structure factors $\langle S(\boldsymbol{q})\rangle_T$. We confine the summation to the positions of the tantalum atoms and normalize the structure factor such that $S(\boldsymbol{q} = 0) = 1$.

The resultant structure factor maps on the first Brillouin zone of 1H-TaS_2 are shown in Fig. 8 for temperatures $T = 50, 81, 96, 200$ K [1]. The upper row corresponds to classical MD simulations. At 50 K, we find peaks in the structure factor at $\boldsymbol{q} = 2/3\,\Gamma\mathrm{M}$, which are characteristic of the 3×3 CDW. These peaks broaden and become reduced in intensity upon increasing temperature. Fig. 9 shows the temperature dependence of $\langle S(\boldsymbol{q} = 2/3\,\Gamma\mathrm{M})\rangle_T$ in more detail. We see the aforementioned temperature-induced reduction in $\langle S(\boldsymbol{q} = 2/3\,\Gamma\mathrm{M})\rangle_T$ with an inflection point around $T_{\mathrm{CL}} \approx 96$ K. We take this inflection point as the finite system size approximation to the phase transition temperature that would be expected for an infinitely large simulation cell.

While a 3×3 CDW has been observed in monolayer 1H-TaS_2 [89], the exact transition temperature is not known in this system. For the three-dimensional bulk of 2H-TaS_2 CDW, transition temperatures on the order of $T_{\mathrm{exp}} \approx 75$ K have been reported [90–95].

[1] We show those $\boldsymbol{q}$-vectors compatible with the periodic boundary conditions on the 18×18 unit cell.

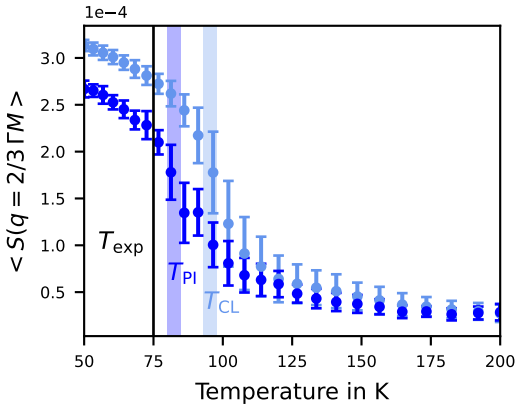

Figure 9: Structure factor $\langle S(\boldsymbol{q} = 2/3\,\Gamma\mathrm{M}, T)\rangle$ at the characteristic CDW wavevector $\boldsymbol{q} = 2/3\,\Gamma\mathrm{M}$ for the classical MD (light blue) and path integral MD (blue). The effective shift of the PIMD curve toward the experimental value can be attributed to nuclear quantum effects.

Our classical finite system size estimate exceeds these temperatures by about 25 %. One possible origin of this deviation can be quantum fluctuations in nuclear degrees of freedom.

Therefore, we performed path integral MD (PIMD) replica exchange simulations to assess the influence of nuclear quantum effects on the CDW formation. The PIMD structure factor maps in the middle row of Fig. 8 behave qualitatively similar to the classical counterpart. Their ratio is quantitatively illustrated in the lowest row. The overall area of the Brillouin zone turns from blue to white by heating up the system. Thus, as expected, the classical and quantum simulations agree at high temperatures. However, the CDW fingerprints ($\boldsymbol{q} = 2/3\,\Gamma\mathrm{M}$ and $\boldsymbol{q} = \mathrm{K}$) clearly increase in intensity and survive at higher temperatures in the classical case. Note that while there is no phonon instability at $\boldsymbol{q} = \mathrm{K}$, the corresponding displacements are commensurate with a 3×3 superstructure and couple anharmonically to the soft modes at $\boldsymbol{q} = 2/3\,\Gamma\mathrm{M}$. This explains the high ratios at the Brillouin-zone corners in Fig. 8 (i–k), especially in the vicinity of the transition temperature.

This difference between classical and quantum simulations can be inspected in more detail in Fig. 9. While the qualitative shape of the PIMD curve (dark blue) is similar to the classical MD (light blue) simulation, we find an effective shift of the curve and an inflection point at $T_{\mathrm{PI}} \approx 82$ K. Thus, quantum effects can significantly reduce the estimated CDW transition temperature as compared to the classical estimate and lead to a closer match with experiment.

From these demonstrator calculations it becomes clear that the downfolding-based MD developed in this work opens the gate for precise computational studies of CDW (thermo)dynamics, which were inaccessible in the domain of *ab initio* MD hitherto.

5 Conclusions

We presented three downfolding schemes to describe low-energy physics of electron-lattice coupled systems—in particular CDWs—on a similar level of accuracy as full *ab initio* DFT: model I is based on constrained theories and models II and III are based on unscreening, where model II features explicit Coulomb interactions and model III is effectively non-

interacting. The central goal of these downfolding schemes is to reduce the complexity of first-principles electronic structure calculations. This is achieved by mapping the general solid-state Hamiltonian onto minimal quantum lattice models with only a few localized Wannier orbitals per unit cell. The solution of these models is significantly faster than DFT. For model III, we found a speedup of about five orders for the example case of monolayer 1H-TaS_2. Despite this enormous speedup and an complexity reduction, we demonstrated a quantitative recovery of DFT potential energy surfaces in downfolded models II and III.

As a demonstration, we performed classical and path integral MD simulations using model III of the 1H-TaS_2 CDW systems. The downfolding-based speedup opens the gate for enhanced sampling techniques and path integral simulations of nuclear quantum effects on the CDW transition. This makes downfolding models the method of choice for precise computational studies of dynamics and thermodynamics in CDW systems, which were hitherto largely inaccessible to *ab initio* MD.

While we focussed, here, on Born-Oppenheimer MD, the Hamiltonians resulting from downfolding models I–III are generic and likely applicable also when dealing with non-adiabatic phenomena, electron-lattice coupled dynamics in excited electronic states, and situations where strong electron-electron correlations are at play. Due to the explicit account of Coulomb interactions in models I and II, these schemes offer themselves for treatments of situations where electronic interaction effects beyond semilocal DFT are to be included in studies of coupled electron-nuclear dynamics.

Future applications of the downfolding schemes developed here might reach to the physics of (nonequilibrium) phase transitions involving CDW order [10–18] or the interplay of correlations and (dis)ordering [19, 96] as well as driven quantum systems [4–6].

Acknowledgments

The authors would like to thank Jean-Baptiste Morée for discussions of the RESPACK software package and Bálint Aradi for technical advice.

Funding information We gratefully acknowledge support from the Deutsche Forschungsgemeinschaft (DFG, German Research Foundation) through RTG 2247 (QM^3, Project No. 286518848) (AS, TW), FOR 5249 (QUAST, Project No. 449872909) (TW), EXC 2056 (Cluster of Excellence "CUI: Advanced Imaging of Matter", Project No. 390715994) (TW, SB), EXC 2077 (University Allowance, University of Bremen, Project No. 390741603) (JB), SFB 951 (Project No. 182087777) (MR), and SE 2558/2 (Emmy Noether program) (MAS). JB gratefully acknowledges the support received from the "U Bremen Excellence Chair Program" and from all those involved in the project, especially Lucio Colombi Ciacchi and Nicola Marzari. EvL acknowledges support from the Swedish Research Council (VR) under grant 2022-03090 and from the Crafoord Foundation. We also acknowledge the computing time granted by the Resource Allocation Board and provided on the supercomputer Lise and Emmy at NHR@ZIB and NHR@Göttingen as part of the NHR infrastructure.

A Free energy calculations of the downfolded models in Hartree approximation

The Coulomb interaction in models I and II renders the electronic Hamiltonian interacting and requires approximate treatments. Here, we solve the interacting Hamiltonian

in Hartree approximation, which is the simplest mean-field approximation and as such requires a self-consistency loop.

For the Coulomb interaction, we assume here a density-density type interaction

$$H^1_{\text{el}} = \frac{1}{2N} \sum_{\boldsymbol{q}\boldsymbol{k}\boldsymbol{k}'\alpha\beta} U^{\boldsymbol{q}}_{\alpha\beta} c^\dagger_{\boldsymbol{k}+\boldsymbol{q}\alpha} c^\dagger_{\boldsymbol{k}'\beta} c_{\boldsymbol{k}'+\boldsymbol{q}\beta} c_{\boldsymbol{k}\alpha} \tag{20}$$

with $U^{\boldsymbol{q}}_{\alpha\beta}$ being cRPA density-density matrix elements evaluated at momentum transfer $\boldsymbol{q}$.

The Hartree decoupling of Eq. (20) reads

$$H^1_{\text{el}} = \frac{1}{N} \sum_{\boldsymbol{k}\boldsymbol{k}'\alpha\beta} U^{\boldsymbol{q}=\boldsymbol{0}}_{\alpha\beta} \left(c^\dagger_{\boldsymbol{k}\alpha} c_{\boldsymbol{k}\alpha} \left\langle c^\dagger_{\boldsymbol{k}'\beta} c_{\boldsymbol{k}'\beta} \right\rangle - \frac{1}{2} \left\langle c^\dagger_{\boldsymbol{k}\alpha} c_{\boldsymbol{k}\alpha} \right\rangle \left\langle c^\dagger_{\boldsymbol{k}'\beta} c_{\boldsymbol{k}'\beta} \right\rangle \right). \tag{21}$$

Since the DFT input parameters of models I and II already contain Coulomb contributions, we have to avoid double counting. The hopping terms $t^0_{\boldsymbol{k}\alpha\beta}$ stem from the Kohn-Sham eigenvalues of the undistorted structure, which contain (among others) a Hartree term. Here, we choose H_{DC} to compensate for the Hartree term of the undistorted structure:

$$H_{\text{DC}} = -\frac{1}{N} \sum_{\boldsymbol{k}\boldsymbol{k}'\alpha\beta} U^{\boldsymbol{q}=\boldsymbol{0}}_{\alpha\beta} \left(c^\dagger_{\boldsymbol{k}\alpha} c_{\boldsymbol{k}\alpha} \left\langle c^\dagger_{\boldsymbol{k}'\beta} c_{\boldsymbol{k}'\beta} \right\rangle_0 - \frac{1}{2} \left\langle c^\dagger_{\boldsymbol{k}\alpha} c_{\boldsymbol{k}\alpha} \right\rangle_0 \left\langle c^\dagger_{\boldsymbol{k}'\beta} c_{\boldsymbol{k}'\beta} \right\rangle_0 \right), \tag{22}$$

where $\langle \dots \rangle_0$ denotes expectation values obtained for the undistorted structure.

We introduce the Hartree potentials $\overline{U}_\alpha$ and $\overline{U}^0_\alpha$ for the distorted and undistorted structures, respectively,

$$\overline{U}_\alpha = \sum_\beta U^{\boldsymbol{q}=0}_{\alpha\beta} n_\beta \quad \text{and} \quad \overline{U}^0_\alpha = \sum_\beta U^{\boldsymbol{q}=0}_{\alpha\beta} n^0_\beta, \tag{23}$$

where $n^{(0)}_\beta = \frac{1}{N} \sum_{\boldsymbol{k}'\beta} \langle c^\dagger_{\boldsymbol{k}'\beta} c_{\boldsymbol{k}'\beta} \rangle_{(0)}$ denotes local orbital occupations. Then, the electronic mean-field Hamiltonian written in the Wannier orbital basis of the supercell reads

$$H_{\text{el}} + H_{\text{el-n}} = \sum_{\boldsymbol{k}\alpha\beta} \left(t^0_{\boldsymbol{k}\alpha\beta} + \boldsymbol{u}\boldsymbol{d}_{\boldsymbol{k}\alpha\boldsymbol{k}\beta} + (\overline{U}_\alpha - \overline{U}^0_\alpha)\delta_{\alpha\beta} \right) c^\dagger_{\boldsymbol{k}\alpha} c_{\boldsymbol{k}\beta} - \frac{1}{2} \sum_{\alpha\beta} U^{\boldsymbol{q}=0}_{\alpha\beta} (n_\alpha n_\beta - n^0_\alpha n^0_\beta). \tag{24}$$

This Hamiltonian is solved self-consistently. The converged electronic dispersion $\varepsilon_{\boldsymbol{k}n}$ and occupations n_α are used to determine the free energy:

$$F_{\text{el}} = \frac{2}{N_k} k_B T \sum_{n\boldsymbol{k}} \ln\Big(f\big[-(\varepsilon_{\boldsymbol{k}n} - \mu)/kT\big] \Big) + \mu N_{\text{el}} - \frac{1}{2} \sum_{\alpha\beta} U^{\boldsymbol{q}=0}_{\alpha\beta} (n_\alpha n_\beta - n^0_\alpha n^0_\beta). \tag{25}$$

The Coulomb matrix $U^{\boldsymbol{q}}_{\alpha\beta}$ contains one divergent eigenvalue for $\boldsymbol{q} \to 0$, which is associated with the homogeneous charging of the system. Since we are working at fixed system charge, we exclude the divergent contribution of $U^{\boldsymbol{q}}_{\alpha\beta}$. In practice we perform the eigenvector decomposition of Eq. (15) from Ref. [97] and exclude the contribution from the leading eigenvector.

B Perturbation expansion of grand potential and free energy

Changes of the grand potential of non-interacting electrons due to atomic displacements can be straightforwardly evaluated using diagrammatic perturbation theory [98]:

$$\Omega = \Omega\big|_0 + \sum_i \Omega_i^{(1)}\big|_0 u_i + \frac{1}{2}\sum_{ij} \Omega_{ij}^{(2)}\big|_0 u_i u_j + \dots \tag{26}$$

$$\equiv \Omega\big|_0 + \quad + \quad + \dots, \tag{27}$$

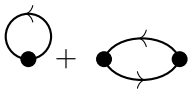

Without loss of generality, we consider $\boldsymbol{q} = 0$ in Eq. (9) and drop the corresponding subscript.

In first order, we then have

$$\boldsymbol{\Omega}^{(1)} = \frac{kT}{N}\sum_{\boldsymbol{k}n\nu} \boldsymbol{d}_{\boldsymbol{k}nn}\frac{1}{\mathrm{i}\omega_\nu - \varepsilon_{\boldsymbol{k}n} + \mu} = \frac{1}{N}\sum_{\boldsymbol{k}n} \boldsymbol{d}_{\boldsymbol{k}nn} f(\varepsilon_{\boldsymbol{k}n} - \mu), \tag{28}$$

with the Matsubara frequency $\omega_\nu = (2\nu + 1)\pi kT$.

In second order, we have

$$\Omega^{(2)} = \frac{kT}{N}\sum_{\boldsymbol{k}mn\nu} \boldsymbol{d}_{\boldsymbol{k}mn}\frac{1}{\mathrm{i}\omega_\nu - \varepsilon_{\boldsymbol{k}m} + \mu}\frac{1}{\mathrm{i}\omega_\nu - \varepsilon_{\boldsymbol{k}n} + \mu}\boldsymbol{d}^T_{\boldsymbol{k}nm} \tag{29}$$

$$= \frac{1}{N}\sum_{\boldsymbol{k}mn} \boldsymbol{d}_{\boldsymbol{k}mn}\frac{f(\varepsilon_{\boldsymbol{k}m} - \mu) - f(\varepsilon_{\boldsymbol{k}n} - \mu)}{\varepsilon_{\boldsymbol{k}m} - \varepsilon_{\boldsymbol{k}n}}\boldsymbol{d}^T_{\boldsymbol{k}nm}. \tag{30}$$

We deliberately have omitted the superscript zero from $\varepsilon_{\boldsymbol{k}n}$ [cf. Eq. (3)] as in our models with linear electron-phonon coupling these formulas also hold for $\boldsymbol{u} \neq 0$ as long as $\boldsymbol{d}$ is represented in the electronic eigenbasis.

The number of electrons N_el is typically conserved in DFT and MD calculations, so we are instead interested in the canonical ensemble and the free energy

$$F(N_\mathrm{el}) = \Omega(\mu(N_\mathrm{el})) + \mu(N_\mathrm{el})N_\mathrm{el}. \tag{31}$$

Its first derivative with respect to displacements is

$$F_i^{(1)} = \frac{\mathrm{d}F}{\mathrm{d}u_i} = \frac{\partial\Omega}{\partial u_i} + \Big[\frac{\partial\Omega}{\partial\mu} + N_\mathrm{el}\Big]\frac{\mathrm{d}\mu}{\mathrm{d}u_i} = \Omega_i^{(1)}, \tag{32}$$

since $\partial\Omega/\partial\mu = -N_\mathrm{el}$. In other words, the expression for the forces [cf. Eq. (11)] is the same in the canonical and the grand-canonical ensemble.

For the unscreening of the force constants (cf. Section 2.1), we also need access to the second derivative of the free energy at constant electron density,

$$F_{ij}^{(2)} = \frac{\mathrm{d}F_i^{(1)}}{\mathrm{d}u_j} = \frac{\partial\Omega_i^{(1)}}{\partial u_j} + \frac{\partial\Omega_i^{(1)}}{\partial\mu}\frac{\mathrm{d}\mu}{\mathrm{d}u_j}. \tag{33}$$

Expectedly, the first term on the right is $\Omega_{ij}^{(2)}$ from Eq. (30). Here, the second term does not vanish, at least not for monochromatic perturbations with $\boldsymbol{q} = 0$ [99]. The change of the chemical potential upon atomic displacements follows from the electron conservation,

$$0 \overset{!}{=} \frac{\mathrm{d}N_\mathrm{el}}{\mathrm{d}\boldsymbol{u}} = \frac{1}{N}\frac{\mathrm{d}}{\mathrm{d}\boldsymbol{u}}\sum_{\boldsymbol{k}n} f(\varepsilon_{\boldsymbol{k}n} - \mu) = -\frac{1}{N}\sum_{\boldsymbol{k}n}\Big[\boldsymbol{d}_{\boldsymbol{k}nn} - \frac{\mathrm{d}\mu}{\mathrm{d}\boldsymbol{u}}\Big]\delta(\varepsilon_{\boldsymbol{k}n} - \mu), \tag{34}$$

with $\delta(\varepsilon) = -\mathrm{d}f(\varepsilon)/\mathrm{d}\varepsilon$. We have used the Hellmann-Feynman theorem,

$$\frac{\mathrm{d}\varepsilon_{\boldsymbol{k}n}}{\mathrm{d}\boldsymbol{u}} = \frac{\mathrm{d}}{\mathrm{d}\boldsymbol{u}}\langle \boldsymbol{k}n|H^0_{\mathrm{el}} + H_{\text{el-n}}|\boldsymbol{k}n\rangle = \langle \boldsymbol{k}n|\frac{\mathrm{d}}{\mathrm{d}\boldsymbol{u}}(H^0_{\mathrm{el}} + H_{\text{el-n}})|\boldsymbol{k}n\rangle \equiv \boldsymbol{d}_{\boldsymbol{k}nn}. \tag{35}$$

Note that here the matrix element of the deformation-induced potential $\boldsymbol{d}_{\boldsymbol{k}nn}$ is represented in the basis of eigenstates $|\boldsymbol{k}n\rangle$ of the *perturbed* Hamiltonian. Rearranging Eq. (34) shows that the change of the chemical potential is nothing but the Fermi surface (FS) average of the intraband deformation-induced potential,

$$\frac{\mathrm{d}\mu}{\mathrm{d}\boldsymbol{u}} = \frac{\sum_{\boldsymbol{k}n}\boldsymbol{d}_{\boldsymbol{k}nn}\delta(\varepsilon_{\boldsymbol{k}n}-\mu)}{\sum_{\boldsymbol{k}n}\delta(\varepsilon_{\boldsymbol{k}n}-\mu)} \equiv \langle \boldsymbol{d}_{\boldsymbol{k}nn}\rangle_{\mathrm{FS}}. \tag{36}$$

From Eq. (28), we can also readily evaluate

$$\frac{\partial \boldsymbol{\Omega}^{(1)}}{\partial\mu} = \frac{1}{N}\sum_{\boldsymbol{k}n}\boldsymbol{d}_{\boldsymbol{k}nn}\delta(\varepsilon_{\boldsymbol{k}n}-\mu) \equiv \rho(\mu)\langle \boldsymbol{d}_{\boldsymbol{k}nn}\rangle_{\mathrm{FS}}, \tag{37}$$

where ρ is the electronic density of states per unit cell. Combining Eqs. (34), (36) and (37) yields

$$\Delta C^{\mathrm{III}}_{ij} = \Omega^{(2)}_{ij} + \rho(\mu)\langle d_{i\boldsymbol{k}nn}\rangle_{\mathrm{FS}}\langle d_{j\boldsymbol{k}nn}\rangle_{\mathrm{FS}}. \tag{38}$$

The first term are the force constants in the grand canonical ensemble, i.e., at constant chemical potential. The second term is the correction for going from the grand canonical to the canonical ensemble.

C Computational parameters DFT

All DFT and DFPT calculations are carried out using Quantum ESPRESSO [83, 84]. The modification that is required for cDFPT is described in detail in Ref. [64]. For the transformation of the electronic energies and electron-phonon couplings to the Wannier basis, we use Wannier90 [100] and the EPW code [101, 102]. The cRPA Coulomb interaction was calculated using RESPACK [103]. In the following, we will list the specific DFT and DFPT parameters for each material individually:

1H-TaS_2 Hartwigsen-Goedecker-Hutter (HGH) pseudopotentials [104, 105]; $18\times18\times1$ $\boldsymbol{k}$ mesh and $6\times6\times1$ $\boldsymbol{q}$ mesh for unit cell; Fermi-Dirac smearing of 5 mRy (Gaussian smearing of 0.1 Ry for Fig. 7b, d, f); energy convergence threshold of 10^{-15} Ry (10^{-8} Ry per unit cell for Fig. 7); lattice constant of 3.39 Å. The cRPA Coulomb interaction has been calculated on a $32\times32\times1$ $\boldsymbol{q}$ mesh taking 80 electronic bands into account.

1H-NbS_2 HGH pseudopotentials [104, 105]; $18\times18\times1$ $\boldsymbol{k}$ mesh and $6\times6\times1$ $\boldsymbol{q}$ mesh for unit cell; Fermi-Dirac smearing of 3 mRy; lattice constant of 3.34 Å.

1H-WS_2 HGH pseudopotentials [104, 105]; $18\times18\times1$ $\boldsymbol{k}$ mesh and $6\times6\times1$ $\boldsymbol{q}$ mesh for unit cell; Fermi-Dirac smearing of 5 mRy; lattice constant of 3.23 Å.

1T-$TiSe_2$ Ultrasoft pseudopotential [106] from the SSSP library [107, 108]; $18\times18\times1$ $\boldsymbol{k}$ mesh and $6\times6\times1$ $\boldsymbol{q}$ mesh for unit cell; Fermi-Dirac smearing of 5 mRy; lattice constant of 3.54 Å.

Carbon chain Optimized norm-conserving Vanderbilt pseudopotential (ONCVPSP) [109] from the PseudoDojo library [110]; $200 \times 1 \times 1$ $\boldsymbol{k}$ mesh and $20 \times 1 \times 1$ $\boldsymbol{q}$ mesh for unit cell; Fermi-Dirac smearing of 5 mRy; lattice constant of 1.30 Å.

In all cases, we have applied the Perdew-Burke-Ernzerhof (PBE) functional [111], set the plane-wave cutoff to 100 Ry, and minimized forces and pressure in the periodic directions to below 1 µRy/Bohr and 0.1 kbar. We have used a unit-cell dimension of 15 Å to separate images in the non-periodic directions.

D Replica Exchange

In order to characterize the CDW phase-transition, we employed replica exchange molecular dynamics (REMD) and replica exchange path integral molecular dynamics [87] (PI-REMD), as implemented in the i-PI code. For the 18×18 1H-TaS_2 supercell, we ran NVT simulations of 26 replicas in parallel that differed in the ensemble temperature. We covered a temperature range between 50 and 200 K. In the PI-REMD simulations, each temperature replica was represented by ten imaginary-time replicas (commonly called "beads" in the ring-polymer representation). This amount of beads proved to be converged within 1 meV/atom for the potential and quantum kinetic energy at the lowest temperature of 50 K. We note that due to the high dimensionality of the system, enhanced by the use of many imaginary-time replicas, the PI-REMD simulations with 26 temperature replicas in this range was not efficient in terms of the frequency of replica swaps, while the REMD simulations were.

References

[1] J. Wilson and A. Yoffe, *The transition metal dichalcogenides: Discussion and interpretation of the observed optical, electrical and structural properties*, Adv. Phys. **18**, 193 (1969), doi:10.1080/00018736900101307.

[2] M. Imada, A. Fujimori and Y. Tokura, *Metal-insulator transitions*, Rev. Mod. Phys. **70**, 1039 (1998), doi:10.1103/RevModPhys.70.1039.

[3] K. Rossnagel, *On the origin of charge-density waves in select layered transition-metal dichalcogenides*, J. Phys. Condens. Matter **23**, 213001 (2011), doi:10.1088/0953-8984/23/21/213001.

[4] D. N. Basov, R. D. Averitt and D. Hsieh, *Towards properties on demand in quantum materials*, Nat. Mater. **16**, 1077 (2017), doi:10.1038/nmat5017.

[5] A. Cavalleri, *Photo-induced superconductivity*, Contemp. Phys. **59**, 31 (2018), doi:10.1080/00107514.2017.1406623.

[6] A. de la Torre, D. M. Kennes, M. Claassen, S. Gerber, J. W. McIver and M. A. Sentef, *Colloquium: Nonthermal pathways to ultrafast control in quantum materials*, Rev. Mod. Phys. **93**, 041002 (2021), doi:10.1103/RevModPhys.93.041002, 2103.14888.

[7] D. J. Auerbach, J. C. Tully and A. M. Wodtke, *Chemical dynamics from the gas-phase to surfaces*, Nat. Sci. **1**, e10005 (2021), doi:10.1002/ntls.10005.

[8] B. Slater and A. Michaelides, *Surface premelting of water ice*, Nat. Rev. Chem. **3**, 172 (2019), doi:10.1038/s41570-019-0080-8.

[9] G. Grüner, *Density Waves In Solids*, CRC Press, Boca Raton, doi:10.1201/9780429501012 (2019).

[10] L. Perfetti, P. A. Loukakos, M. Lisowski, U. Bovensiepen, H. Berger, S. Biermann, P. S. Cornaglia, A. Georges and M. Wolf, *Time evolution of the electronic structure of 1T-TaS_2 through the insulator-metal transition*, Phys. Rev. Lett. **97**, 067402 (2006), doi:10.1103/PhysRevLett.97.067402.

[11] S. Hellmann, M. Beye, C. Sohrt, T. Rohwer, F. Sorgenfrei, H. Redlin, M. Kalläne, M. Marczynski-Bühlow, F. Hennies, M. Bauer, A. Föhlisch, L. Kipp *et al.*, *Ultrafast melting of a charge-density wave in the Mott insulator 1T-TaS_2*, Phys. Rev. Lett. **105**, 187401 (2010), doi:10.1103/PhysRevLett.105.187401, 1004.4790.

[12] M. Eichberger, H. Schäfer, M. Krumova, M. Beyer, J. Demsar, H. Berger, G. Moriena, G. Sciaini and R. J. D. Miller, *Snapshots of cooperative atomic motions in the optical suppression of charge density waves*, Nature **468**, 799 (2010), doi:10.1038/nature09539.

[13] F. Weber, S. Rosenkranz, J.-P. Castellan, R. Osborn, R. Hott, R. Heid, K.-P. Bohnen, T. Egami, A. H. Said and D. Reznik, *Extended phonon collapse and the origin of the charge-density wave in 2H-$NbSe_2$*, Phys. Rev. Lett. **107**, 107403 (2011), doi:10.1103/PhysRevLett.107.107403, 1103.5755.

[14] E. Möhr-Vorobeva, S. L. Johnson, P. Beaud, U. Staub, R. De Souza, C. Milne, G. Ingold, J. Demsar, H. Schaefer and A. Titov, *Nonthermal melting of a charge density wave in $TiSe_2$*, Phys. Rev. Lett. **107**, 036403 (2011), doi:10.1103/PhysRevLett.107.036403.

[15] L. Stojchevska, I. Vaskivskyi, T. Mertelj, P. Kusar, D. Svetin, S. Brazovskii and D. Mihailovic, *Ultrafast switching to a stable hidden quantum state in an electronic crystal*, Science **344**, 177 (2014), doi:10.1126/science.1241591, 1401.6786.

[16] S. Vogelgesang, G. Storeck, J. G. Horstmann, T. Diekmann, M. Sivis, S. Schramm, K. Rossnagel, S. Schäfer and C. Ropers, *Phase ordering of charge density waves traced by ultrafast low-energy electron diffraction*, Nat. Phys. **14**, 184 (2018), doi:10.1038/nphys4309, 1703.10589.

[17] A. Zong *et al.*, *Evidence for topological defects in a photoinduced phase transition*, Nat. Phys. **15**, 27 (2019), doi:10.1038/s41567-018-0311-9, 1806.02766.

[18] T. Danz, T. Domröse and C. Ropers, *Ultrafast nanoimaging of the order parameter in a structural phase transition*, Science **371**, 371 (2021), doi:10.1126/science.abd2774, 2007.07574.

[19] T. Neupert, M. M. Denner, J.-X. Yin, R. Thomale and M. Z. Hasan, *Charge order and superconductivity in kagome materials*, Nat. Phys. **18**, 137 (2022), doi:10.1038/s41567-021-01404-y.

[20] D. J. Hooton, *LI. A new treatment of anharmonicity in lattice thermodynamics: I*, Lond. Edinb. Dubl. Phil. Mag. **46**, 422 (1955), doi:10.1080/14786440408520575.

[21] J. M. Bowman, *Self-consistent field energies and wavefunctions for coupled oscillators*, J. Chem. Phys. **68**, 608 (1978), doi:10.1063/1.435782.

[22] P. Souvatzis, O. Eriksson, M. I. Katsnelson and S. P. Rudin, *Entropy driven stabilization of energetically unstable crystal structures explained from first principles theory*, Phys. Rev. Lett. **100**, 095901 (2008), doi:10.1103/PhysRevLett.100.095901, 0803.1325.

[23] I. Errea, M. Calandra and F. Mauri, *Anharmonic free energies and phonon dispersions from the stochastic self-consistent harmonic approximation: Application to platinum and palladium hydrides*, Phys. Rev. B **89**, 064302 (2014), doi:10.1103/PhysRevB.89.064302, 1311.3083.

[24] R. Bianco, L. Monacelli, M. Calandra, F. Mauri and I. Errea, *Weak dimensionality dependence and dominant role of ionic fluctuations in the charge-density-wave transition of $NbSe_2$*, Phys. Rev. Lett. **125**, 106101 (2020), doi:10.1103/PhysRevLett.125.106101, 2004.08147.

[25] C. Falter and M. Selmke, *Renormalization of the dielectric response with applications to effective ion interactions and phonons*, Phys. Rev. B **24**, 586 (1981), doi:10.1103/PhysRevB.24.586.

[26] C. Falter, *A unifying approach to lattice dynamical and electronic properties of solids*, Phys. Rep. **164**, 1 (1988), doi:10.1016/0370-1573(88)90058-0.

[27] A. P. Bartók, M. C. Payne, R. Kondor and G. Csányi, *Gaussian approximation potentials: The accuracy of quantum mechanics, without the electrons*, Phys. Rev. Lett. **104**, 136403 (2010), doi:10.1103/PhysRevLett.104.136403, 0910.1019.

[28] J. Finkelstein, J. S. Smith, S. M. Mniszewski, K. Barros, C. F. A. Negre, E. H. Rubensson and A. M. N. Niklasson, *Quantum-based molecular dynamics simulations using tensor cores*, J. Chem. Theory Comput. **17**, 6180 (2021), doi:10.1021/acs.jctc.1c00726, 2107.02737.

[29] V. L. Deringer, A. P. Bartók, N. Bernstein, D. M. Wilkins, M. Ceriotti and G. Csányi, *Gaussian process regression for materials and molecules*, Chem. Rev. **121**, 10073 (2021), doi:10.1021/acs.chemrev.1c00022.

[30] Z. Wang, J. Dong, J. Qiu and L. Wang, *All-atom nonadiabatic dynamics simulation of hybrid graphene nanoribbons based on Wannier analysis and machine learning*, ACS Appl. Mater. Interfaces **14**, 22929 (2022), doi:10.1021/acsami.1c22181.

[31] C. Cheng, S. Zhang and G.-W. Chern, *Machine learning for phase ordering dynamics of charge density waves* (2023), 2303.03493.

[32] M. W. Finnis, A. T. Paxton, D. G. Pettifor, A. P. Sutton and Y. Ohta, *Interatomic forces in transition metals*, Philos. Mag. A **58**, 143 (1988), doi:10.1080/01418618808205180.

[33] C. L. Brooks, *Computer simulation of liquids*, J. Solution Chem. **18**, 99 (1989), doi:10.1007/BF00646086.

[34] C. Z. Wang, C. T. Chan and K. M. Ho, *Empirical tight-binding force model for molecular-dynamics simulation of Si*, Phys. Rev. B **39**, 8586 (1989), doi:10.1103/PhysRevB.39.8586.

[35] L. Goodwin, A. J. Skinner and D. G. Pettifor, *Generating transferable tight-binding parameters: Application to silicon*, EPL **9**, 701 (1989), doi:10.1209/0295-5075/9/7/015.

[36] W. M. C. Foulkes and R. Haydock, *Tight-binding models and density-functional theory*, Phys. Rev. B **39**, 12520 (1989), doi:10.1103/PhysRevB.39.12520.

[37] O. F. Sankey and D. J. Niklewski, *Ab initio multicenter tight-binding model for molecular-dynamics simulations and other applications in covalent systems*, Phys. Rev. B **40**, 3979 (1989), doi:10.1103/PhysRevB.40.3979.

[38] K. Laasonen and R. M. Nieminen, *Molecular dynamics using the tight-binding approximation*, J. Phys. Condens. Matter **2**, 1509 (1990), doi:10.1088/0953-8984/2/6/010.

[39] R. Virkkunen, K. Laasonen and R. M. Nieminen, *Molecular dynamics using the tight-binding approximation: Application to liquid silicon*, J. Phys. Condens. Matter **3**, 7455 (1991), doi:10.1088/0953-8984/3/38/017.

[40] C. Z. Wang, C. T. Chan and K. M. Ho, *Tight-binding molecular-dynamics study of liquid Si*, Phys. Rev. B **45**, 12227 (1992), doi:10.1103/PhysRevB.45.12227.

[41] C. Molteni, L. Colombo and L. Miglio, *Structural properties of liquid and amorphous GaAs by tight-binding molecular dynamics*, EPL **24**, 659 (1993), doi:10.1209/0295-5075/24/8/007.

[42] D. Porezag, T. Frauenheim, T. Köhler, G. Seifert and R. Kaschner, *Construction of tight-binding-like potentials on the basis of density-functional theory: Application to carbon*, Phys. Rev. B **51**, 12947 (1995), doi:10.1103/PhysRevB.51.12947.

[43] Y. P. Feng, C. K. Ong, H. C. Poon and D. Tománek, *Tight-binding molecular dynamics simulations of semiconductor alloys: Clusters, surfaces, and defects*, J. Phys. Condens. Matter **9**, 4345 (1997), doi:10.1088/0953-8984/9/21/003.

[44] M. Elstner, D. Porezag, G. Jungnickel, J. Elsner, M. Haugk, T. Frauenheim, S. Suhai and G. Seifert, *Self-consistent-charge density-functional tight-binding method for simulations of complex materials properties*, Phys. Rev. B **58**, 7260 (1998), doi:10.1103/PhysRevB.58.7260.

[45] C.-C. Fu and M. Weissmann, *Tight-binding molecular-dynamics study of amorphous carbon deposits over silicon surfaces*, Phys. Rev. B **60**, 2762 (1999), doi:10.1103/PhysRevB.60.2762.

[46] B. Aradi, B. Hourahine and T. Frauenheim, *DFTB+, a sparse matrix-based implementation of the DFTB method*, J. Phys. Chem. A **111**, 5678 (2007), doi:10.1021/jp070186p.

[47] J. P. Lewis, P. Jelínek, J. Ortega, A. A. Demkov, D. G. Trabada, B. Haycock, H. Wang, G. Adams, J. K. Tomfohr, E. Abad, H. Wang and D. A. Drabold, *Advances and applications in the FIREBALL ab initio tight-binding molecular-dynamics formalism*, Phys. Status Solidi B **248**, 1989 (2011), doi:10.1002/pssb.201147259.

[48] P. García-Fernández, J. C. Wojdeł, J. Íñiguez and J. Junquera, *Second-principles method for materials simulations including electron and lattice degrees of freedom*, Phys. Rev. B **93**, 195137 (2016), doi:10.1103/PhysRevB.93.195137, 1511.07675.

[49] Z. H. He, X. B. Ye and B. C. Pan, *Linear scaling algorithm for tight-binding molecular dynamics simulations*, J. Chem. Phys. **150**, 114107 (2019), doi:10.1063/1.5088918.

[50] Y. Nishimura and H. Nakai, *Dcdftbmd: Divide-and-conquer density functional tight-binding program for huge-system quantum mechanical molecular dynamics simulations*, J. Comput. Chem. **40**, 1538 (2019), doi:10.1002/jcc.25804.

[51] B. Hourahine *et al.*, *DFTB+, a software package for efficient approximate density functional theory based atomistic simulations*, J. Chem. Phys. **152**, 124101 (2020), doi:10.1063/1.5143190.

[52] A. M. N. Niklasson, *Density-matrix based extended lagrangian Born–Oppenheimer molecular dynamics*, J. Chem. Theory Comput. **16**, 3628 (2020), doi:10.1021/acs.jctc.0c00264, 2003.09050.

[53] L. Zhang, B. Onat, G. Dusson, A. McSloy, G. Anand, R. J. Maurer, C. Ortner and J. R. Kermode, *Equivariant analytical mapping of first principles Hamiltonians to accurate and transferable materials models*, npj Comput. Mater. **8**, 1 (2022), doi:10.1038/s41524-022-00843-2, 2111.13736.

[54] P. Hohenberg and W. Kohn, *Inhomogeneous electron gas*, Phys. Rev. **136**, B864 (1964), doi:10.1103/PhysRev.136.B864.

[55] F. Aryasetiawan and F. Nilsson, *Downfolding Methods in Many-Electron Theory*, AIP Publishing LLC (2022).

[56] T. Fujiwara, S. Yamamoto and Y. Ishii, *Generalization of the iterative perturbation theory and metal–insulator transition in multi-orbital Hubbard bands*, J. Phys. Soc. Jpn. **72**, 777 (2003), doi:10.1143/JPSJ.72.777, cond-mat/0211159.

[57] F. Aryasetiawan, M. Imada, A. Georges, G. Kotliar, S. Biermann and A. I. Lichtenstein, *Frequency-dependent local interactions and low-energy effective models from electronic structure calculations*, Phys. Rev. B **70**, 195104 (2004), doi:10.1103/PhysRevB.70.195104, cond-mat/0401620.

[58] F. Aryasetiawan, K. Karlsson, O. Jepsen and U. Schönberger, *Calculations of Hubbard U from first-principles*, Phys. Rev. B **74**, 125106 (2006), doi:10.1103/PhysRevB.74.125106, cond-mat/0603138.

[59] K. Nakamura, R. Arita and M. Imada, *Ab initio derivation of low-energy model for iron-based superconductors LaFeAsO and LaFePO*, J. Phys. Soc. Jpn. **77**, 093711 (2008), doi:10.1143/JPSJ.77.093711, 0806.4750.

[60] Y. Nohara, S. Yamamoto and T. Fujiwara, *Electronic structure of perovskite-type transition metal oxides $LaMO_3$ (M=Ti∼Cu) by U+GW approximation*, Phys. Rev. B **79**, 195110 (2009), doi:10.1103/PhysRevB.79.195110.

[61] K. Nakamura, Y. Yoshimoto, T. Kosugi, R. Arita and M. Imada, *Ab initio derivation of low-energy model for κ-ET type organic conductors*, J. Phys. Soc. Jpn. **78**, 083710 (2009), doi:10.1143/JPSJ.78.083710, 0903.5409.

[62] K. Nakamura, Y. Nohara, Y. Yosimoto and Y. Nomura, *Ab initio GW plus cumulant calculation for isolated band systems: Application to organic conductor $TMTSF_2PF_6$ and transition-metal oxide $SrVO_3$*, Phys. Rev. B **93**, 085124 (2016), doi:10.1103/PhysRevB.93.085124, 1511.00218.

[63] G. Giovannetti, M. Casula, P. Werner, F. Mauri and M. Capone, *Downfolding electron-phonon Hamiltonians from ab initio calculations: Application to K_3 picene*, Phys. Rev. B **90**, 115435 (2014), doi:10.1103/PhysRevB.90.115435, 1406.4108.

[64] Y. Nomura and R. Arita, *Ab initio downfolding for electron-phonon-coupled systems: Constrained density-functional perturbation theory*, Phys. Rev. B **92**, 245108 (2015), doi:10.1103/PhysRevB.92.245108, 1509.01138.

[65] Y. Nomura, S. Sakai, M. Capone and R. Arita, *Exotics-wave superconductivity in alkali-doped fullerides*, J. Phys. Condens. Matter **28**, 153001 (2016), doi:10.1088/0953-8984/28/15/153001, 1512.05755.

[66] J. Berges, E. G. C. P. van Loon, A. Schobert, M. Rösner and T. O. Wehling, *Ab initio phonon self-energies and fluctuation diagnostics of phonon anomalies: Lattice instabilities from Dirac pseudospin physics in transition metal dichalcogenides*, Phys. Rev. B **101**, 155107 (2020), doi:10.1103/PhysRevB.101.155107, 1911.02450.

[67] E. G. C. P. van Loon, J. Berges and T. O. Wehling, *Downfolding approaches to electron-ion coupling: Constrained density-functional perturbation theory for molecules*, Phys. Rev. B **103**, 205103 (2021), doi:10.1103/PhysRevB.103.205103, 2102.10072.

[68] M. Kinza and C. Honerkamp, *Low-energy effective interactions beyond the constrained random-phase approximation by the functional renormalization group*, Phys. Rev. B **92**, 045113 (2015), doi:10.1103/PhysRevB.92.045113, 1504.00232.

[69] C. Honerkamp, *Efficient vertex parametrization for the constrained functional renormalization group for effective low-energy interactions in multiband systems*, Phys. Rev. B **98**, 155132 (2018), doi:10.1103/PhysRevB.98.155132, 1805.01669.

[70] X.-J. Han, P. Werner and C. Honerkamp, *Investigation of the effective interactions for the emery model by the constrained random-phase approximation and constrained functional renormalization group*, Phys. Rev. B **103**, 125130 (2021), doi:10.1103/PhysRevB.103.125130.

[71] M. Born and R. Oppenheimer, *Zur Quantentheorie der Molekeln*, Ann. Phys. **389**, 457 (1927), doi:10.1002/andp.19273892002.

[72] Y. Nomura, M. Kaltak, K. Nakamura, C. Taranto, S. Sakai, A. Toschi, R. Arita, K. Held, G. Kresse and M. Imada, *Effective on-site interaction for dynamical mean-field theory*, Phys. Rev. B **86**, 085117 (2012), doi:10.1103/PhysRevB.86.085117, 1205.2836.

[73] M. Calandra, G. Profeta and F. Mauri, *Adiabatic and nonadiabatic phonon dispersion in a Wannier function approach*, Phys. Rev. B **82**, 165111 (2010), doi:10.1103/PhysRevB.82.165111, 1007.2098.

[74] J. Berges, A. Schobert, E. G. C. P. van Loon, M. Rösner and T. O. Wehling, *elphmod: Python modules for electron–phonon models*, doi.org/10.5281/zenodo.5919992, doi:10.5281/zenodo.5919992 (2017).

[75] F. Giustino, M. L. Cohen and S. G. Louie, *Electron-phonon interaction using Wannier functions*, Phys. Rev. B **76**, 165108 (2007), doi:10.1103/PhysRevB.76.165108.

[76] J. Berges, N. Girotto, T. Wehling, N. Marzari and S. Poncé, *Phonon self-energy corrections: To screen, or not to screen* (2022), 2212.11806.

[77] O. R. Albertini, A. Y. Liu and M. Calandra, *Effect of electron doping on lattice instabilities in single-layer 1H-TaS_2*, Phys. Rev. B **95**, 235121 (2017), doi:10.1103/PhysRevB.95.235121, 1702.08588.

[78] D. C. Miller, S. D. Mahanti and P. M. Duxbury, *Charge density wave states in tantalum dichalcogenides*, Phys. Rev. B **97**, 045133 (2018), doi:10.1103/PhysRevB.97.045133.

[79] H. M. Lefcochilos-Fogelquist, O. R. Albertini and A. Y. Liu, *Substrate-induced suppression of charge density wave phase in monolayer 1H-TaS_2 on Au(111)*, Phys. Rev. B **99**, 174113 (2019), doi:10.1103/PhysRevB.99.174113, 1903.05177.

[80] W. H. Sio, C. Verdi, S. Poncé and F. Giustino, *Ab initio theory of polarons: Formalism and applications*, Phys. Rev. B **99**, 235139 (2019), doi:10.1103/PhysRevB.99.235139.

[81] W. H. Sio, C. Verdi, S. Poncé and F. Giustino, *Polarons from first principles, without supercells*, Phys. Rev. Lett. **122**, 246403 (2019), doi:10.1103/PhysRevLett.122.246403.

[82] A. Klein, S. Tiefenbacher, V. Eyert, C. Pettenkofer and W. Jaegermann, *Electronic band structure of single-crystal and single-layer WS_2: Influence of interlayer van der Waals interactions*, Phys. Rev. B **64**, 205416 (2001), doi:10.1103/PhysRevB.64.205416.

[83] P. Giannozzi *et al.*, QUANTUM ESPRESSO*: A modular and open-source software project for quantum simulations of materials*, J. Phys. Condens. Matter **21**, 395502 (2009), doi:10.1088/0953-8984/21/39/395502, 0906.2569.

[84] P. Giannozzi *et al.*, *Advanced capabilities for materials modelling with* QUANTUM ESPRESSO, J. Phys. Condens. Matter **29**, 465901 (2017), doi:10.1088/1361-648X/aa8f79, 1709.10010.

[85] C. R. Harris *et al.*, *Array programming with NumPy*, Nature **585**, 357 (2020), doi:10.1038/s41586-020-2649-2, 2006.10256.

[86] P. Virtanen *et al.*, *SciPy 1.0: Fundamental algorithms for scientific computing in Python*, Nat. Methods **17**, 261 (2020), doi:10.1038/s41592-019-0686-2, 1907.10121.

[87] V. Kapil *et al.*, *i-PI 2.0: A universal force engine for advanced molecular simulations*, Comput. Phys. Commun. **236**, 214 (2019), doi:10.1016/j.cpc.2018.09.020, 1808.03824.

[88] Y. Zheng, X. Jiang, X.-X. Xue, X. Yao, J. Zeng, K.-Q. Chen, E. Wang and Y. Feng, *Nuclear quantum effects on the charge-density wave transition in NbX_2 (X = S, Se)*, Nano Lett. **22**, 1858 (2022), doi:10.1021/acs.nanolett.1c04015.

[89] J. Hall *et al.*, *Environmental control of charge density wave order in monolayer 2H-TaS_2*, ACS Nano **13**, 10210 (2019), doi:10.1021/acsnano.9b03419.

[90] J. P. Tidman, O. Singh, A. E. Curzon and R. F. Frindt, *The phase transition in 2H-TaS_2 at 75 K*, Philos. Mag. **30**, 1191 (1974), doi:10.1080/14786437408207274.

[91] G. A. Scholz, O. Singh, R. F. Frindt and A. E. Curzon, *Charge density wave commensurability in 2H-TaS_2 and Ag_xTaS_2*, Solid State Commun. **44**, 1455 (1982), doi:10.1016/0038-1098(82)90030-8.

[92] S. Sugai, *Lattice vibrations in the charge-density-wave states of layered transition metal dichalcogenides*, Phys. Status Solidi B **129**, 13 (1985), doi:10.1002/pssb.2221290103.

[93] D. Lin, S. Li, J. Wen, H. Berger, L. Forró, H. Zhou, S. Jia, T. Taniguchi, K. Watanabe, X. Xi and M. S. Bahramy, *Patterns and driving forces of dimensionality-dependent charge density waves in 2H-type transition metal dichalcogenides*, Nat. Commun. **11**, 2406 (2020), doi:10.1038/s41467-020-15715-w, 2002.03386.

[94] X.-M. Zhao, K. Zhang, Z.-Y. Cao, Z.-W. Zhao, V. V. Struzhkin, A. F. Goncharov, H.-K. Wang, A. G. Gavriliuk, H.-K. Mao and X.-J. Chen, *Pressure tuning of the charge density wave and superconductivity in 2H-TaS_2*, Phys. Rev. B **101**, 134506 (2020), doi:10.1103/PhysRevB.101.134506.

[95] M. Lee, M. Šiškins, S. Mañas Valero, E. Coronado, P. G. Steeneken and H. S. J. van der Zant, *Study of charge density waves in suspended 2H-TaS_2 and 2H-$TaSe_2$ by nanomechanical resonance*, Appl. Phys. Lett. **118**, 193105 (2021), doi:10.1063/5.0051112, 2105.01214.

[96] S. Wall, S. Yang, L. Vidas, M. Chollet, J. M. Glownia, M. Kozina, T. Katayama, T. Henighan, M. Jiang, T. A. Miller, D. A. Reis, L. A. Boatner *et al.*, *Ultrafast disordering of vanadium dimers in photoexcited VO_2*, Science **362**, 572 (2018), doi:10.1126/science.aau3873.

[97] M. Rösner, E. Şaşıoğlu, C. Friedrich, S. Blügel and T. O. Wehling, *Wannier function approach to realistic Coulomb interactions in layered materials and heterostructures*, Phys. Rev. B **92**, 085102 (2015), doi:10.1103/PhysRevB.92.085102, 1504.05230.

[98] T. Matsubara, *A new approach to quantum-statistical mechanics*, Prog. Theor. Phys. **14**, 351 (1955), doi:10.1143/PTP.14.351.

[99] S. Baroni, S. de Gironcoli, A. Dal Corso and P. Giannozzi, *Phonons and related crystal properties from density-functional perturbation theory*, Rev. Mod. Phys. **73**, 515 (2001), doi:10.1103/RevModPhys.73.515, cond-mat/0012092.

[100] A. A. Mostofi, J. R. Yates, G. Pizzi, Y.-S. Lee, I. Souza, D. Vanderbilt and N. Marzari, *An updated version of wannier90: A tool for obtaining maximally-localised Wannier functions*, Comput. Phys. Commun. **185**, 2309 (2014), doi:10.1016/j.cpc.2014.05.003.

[101] J. Noffsinger, F. Giustino, B. D. Malone, C.-H. Park, S. G. Louie and M. L. Cohen, *EPW: A program for calculating the electron–phonon coupling using maximally localized Wannier functions*, Comput. Phys. Commun. **181**, 2140 (2010), doi:10.1016/j.cpc.2010.08.027, 1005.4418.

[102] S. Poncé, E. Margine, C. Verdi and F. Giustino, *EPW: Electron–phonon coupling, transport and superconducting properties using maximally localized Wannier functions*, Comput. Phys. Commun. **209**, 116 (2016), doi:10.1016/j.cpc.2016.07.028, 1604.03525.

[103] K. Nakamura, Y. Yoshimoto, Y. Nomura, T. Tadano, M. Kawamura, T. Kosugi, K. Yoshimi, T. Misawa and Y. Motoyama, *RESPACK: An ab initio tool for derivation of effective low-energy model of material*, Comput. Phys. Commun. **261**, 107781 (2021), doi:10.1016/j.cpc.2020.107781, 2001.02351.

[104] S. Goedecker, M. Teter and J. Hutter, *Separable dual-space Gaussian pseudopotentials*, Phys. Rev. B **54**, 1703 (1996), doi:10.1103/PhysRevB.54.1703, mtrl-th/9512004.

[105] C. Hartwigsen, S. Goedecker and J. Hutter, *Relativistic separable dual-space Gaussian pseudopotentials from H to Rn*, Phys. Rev. B **58**, 3641 (1998), doi:10.1103/PhysRevB.58.3641, cond-mat/9803286.

[106] D. Vanderbilt, *Soft self-consistent pseudopotentials in a generalized eigenvalue formalism*, Phys. Rev. B **41**, 7892 (1990), doi:10.1103/PhysRevB.41.7892.

[107] G. Prandini, A. Marrazzo, I. E. Castelli, N. Mounet and N. Marzari, *Precision and efficiency in solid-state pseudopotential calculations*, npj Comput. Mater. **4**, 1 (2018), doi:10.1038/s41524-018-0127-2, 1806.05609.

[108] G. Prandini, A. Marrazzo, I. E. Castelli, N. Mounet, E. Passaro and N. Marzari, *A standard solid state pseudopotentials (SSSP) library optimized for precision and efficiency*, Materials Cloud Archive **2021.76** (2021), doi:10.24435/materialscloud:rz-77.

[109] D. R. Hamann, *Optimized norm-conserving Vanderbilt pseudopotentials*, Phys. Rev. B **88**, 085117 (2013), doi:10.1103/PhysRevB.88.085117, 1306.4707.

[110] M. J. van Setten, M. Giantomassi, E. Bousquet, M. J. Verstraete, D. R. Hamann, X. Gonze and G. M. Rignanese, *The PseudoDojo: Training and grading a 85 element optimized norm-conserving pseudopotential table*, Comput. Phys. Commun. **226**, 39 (2018), doi:10.1016/j.cpc.2018.01.012, 1710.10138.

[111] J. P. Perdew, K. Burke and M. Ernzerhof, *Generalized gradient approximation made simple*, Phys. Rev. Lett. **77**, 3865 (1996), doi:10.1103/PhysRevLett.77.3865.

14

Fourth publication: Unconventional charge-density-wave gap in monolayer NbS_2

14.1. Statement of personal contribution

This work has been published as a preprint in arXiv:2307.13791 and is accepted for publication in Nano Letters. It has been realized in collaboration with T. Knispel, J. Berges, E. G. C. P. van Loon, W. Jolie, T. O. Wehling, T. Michely, and J. Fischer. My contribution to this work involved performing ab initio DFT and DFPT calculations to establish the downfolding model for monolayer 1H-NbS_2. In this case, model III from the previous publication was used (see Ch. 13). This means specifically that I have calculated the undistorted Wannier Hamiltonian, the force constants, and the electron-phonon coupling. Subsequently, a relaxation study was performed by me to benchmark the model against exisiting relaxed 3×3 *CDW structures from the literature [177].*

14.2. Positioning within the scientific landscape

Isoelectronic and isostructural materials of the TMDC family, such as 1H-MX_2 (M = Nb, Ta; X = S, Se), behave similarly within DFT. More specifically, on the harmonic level, the phonon dispersion predicts instabilities for the phonon wave vector $\boldsymbol{q} = 2/3\,\Gamma\mathrm{M}$, which is commensurate with a 3×3 supercell [82]. Structural optimization on the anharmonic free-energy surface for this supercell yields qualitatively similar distorted CDW ground states for all mentioned H-phase TMDCs. However, on the experimental side, these materials show different CDW physics. For example, in 2H-$NbSe_2$ (bulk) the phase transition temperature towards the CDW was measured to be $T_{\mathrm{CDW}} = 33$ K [184]. Meanwhile, no CDW order was observed in 2H-NbS_2 (bulk) [185–187]. In monolayer 1H-NbS_2, the existence or absence of a CDW appears to depend on the substrate [188, 189].

Here, the current publication reports unambiguous experimental evidence for a CDW in monolayer 1H-NbS_2. The subsequent experimental and theoretical investigations are less dedicated on the origin of the CDW, but rather on the features that come with the presence of the CDW in this material. Interestingly, a CDW gap on the order of ~20 meV opens at the Fermi level, which entails the emergence of low-energy peak features within the gap. The observed peaked structure cannot be attributed to a pure electronic origin, since the gap in the electronic strucutre is on the order of

~100 meV. Instead, combined electron-phonon quasiparticles must play a significant role in the emergence of these peaks. These findings extend the scope of the conventional CDW physics and should be further investigated in the future.

In addition, this publication provides an experimental estimation of the phase transition temperature of the CDW transition, which is determined to be $T_{CDW} = 40$ K. The theoretical determination of this temperature falls within the realm of thermodynamics. Ensemble DFT may have the capability to predict this temperature if electronic entropy were the primary factor. However, for an accurate prediction, lattice entropy and possibly lattice quantum effects are necessary, which is why methods like SSCHA, *ab initio* MD or PIMD are needed.

Furthermore, the discrepancy between the presence of a CDW in the monolayer and its absence in the bulk phase has not been sufficiently explored. This discrepancy between static DFT calculations and experimental observations has been the subject of previous theoretical studies, employing state-of-the-art methods such as *ab initio* MD [177] and the SSCHA [190].

The *ab initio* MD study simulated a monolayer of 1H-NbS_2 on a 3×3 supercell. Both the system size and the simulated time are constrained by the computational expense of performing full *ab initio* calculations of energies and forces, making it impractical to calculate thermodynamic properties. The SSCHA method incorporates the anharmonicity of the free-energy landscape using a self-consistent approach within a trial harmonic Hamiltonian, primarily focusing on vibrational properties such as temperature-dependent phonon dispersion. Consequently, the literature lacks a comprehensive thermodynamic analysis across the CDW phase transition for H-phase TMDCs.

The developed downfolded lattice models, in conjunction with path integral molecular dynamics simulations, could be a valuable tool for addressing these research gaps and shedding light on these complex phenomena.

Unconventional charge-density-wave gap in monolayer NbS_2

Timo Knispel,[†] Jan Berges,[‡] Arne Schobert,[¶] Erik G. C. P. van Loon,[§] Wouter Jolie,[†] Tim Wehling,[¶,‖] Thomas Michely,[†] and Jeison Fischer[*,†]

[†]*II. Physikalisches Institut, Universität zu Köln, Zülpicher Straße 77, D-50937 Köln, Germany*

[‡]*U Bremen Excellence Chair, Bremen Center for Computational Materials Science, and MAPEX Center for Materials and Processes, University of Bremen, D-28359 Bremen, Germany*

[¶]*I. Institute of Theoretical Physics, Universität Hamburg, D-22607 Hamburg, Germany*

[§]*Division of Mathematical Physics, Department of Physics, Lund University, SE-22100 Lund, Sweden*

[‖]*The Hamburg Centre for Ultrafast Imaging, Luruper Chaussee 149, D-22761 Hamburg, Germany*

E-mail: jfischer@ph2.uni-koeln.de

Abstract

Using scanning tunneling microscopy and spectroscopy, for a monolayer of transition metal dichalcogenide H-NbS_2 grown by molecular beam epitaxy on graphene, we provide unambiguous evidence for a charge density wave (CDW) with a 3×3 superstructure, which is not present in bulk NbS_2. Local spectroscopy displays a pronounced gap of the order of 20 meV at the Fermi level. Within the gap low energy features are present. The gap structure with its low energy features is at variance with the expectation for a gap opening in the electronic band structure due to a CDW. Instead, comparison with *ab initio* calculations indicates that the observed gap structure must be attributed to combined electron-phonon quasiparticles. The phonons in question are the elusive amplitude and phase collective modes of the CDW transition. Our findings advance the understanding of CDW mechanisms in two dimensional materials and their spectroscopic signatures.

Interacting electron systems give rise to a diverse array of ordered states at low temperatures, such as superconductivity,[1] magnetism,[2] and charge density waves (CDWs).[3] These ordering tendencies generically stem from the interplay of kinetic and interaction energies with entropy. The ordering-induced energy gains often translate into the opening of gaps in the electronic excitation spectra.[4–7] Spectroscopy of these electronic gaps has been instrumental in understanding the nature of these ordered states: The momentum structure of the gap as well as its response to impurities point toward order-parameter symmetries. Typically, the comparison of gaps with transition temperatures is instrumental in discerning weak versus strong coupling physics, *i.e.*, to distinguish between the BCS (Bardeen-Cooper-Schrieffer) and BEC (Bose-Einstein condensate) limits of superconductivity,[8] between Slater and Heisenberg antiferromagnets,[9] or between Peierls to strong coupling CDWs.[3] Time-dependent gap spectroscopy in pump-probe setups[10–12] offers a means to identify the relevant degrees of freedom associated with a certain type of order. Correspondingly, the analysis of gaps has been widely used to pinpoint which mechanism is responsible for CDW formation.

A well-established CDW mechanism is Fermi surface nesting in the classical Peierls picture,[5] valid for a one dimensional metallic chain developing a periodic lattice distortion. Due to the electronic response of the system, such a distortion is accompanied by an energy gap emerging at the Fermi energy and charge modulation with its periodicity given by the so-called nesting wave vector. CDWs in real materials can deviate from this idealized Peierls picture in several ways. For many materials, the electron-phonon coupling is strongly wave-vector dependent, which becomes the force driving the CDW.[13–15] Instead of gapping out the entire Fermi surface, the wave-vector-dependent electron-phonon coupling can induce partial gaps and changes in the Fermi surface topology.[16] Generally, the change in the electronic structure is not limited to the Fermi energy, like in the classical Peierls transition, but occurs over a broader energy range[3,16,17] — particularly in strong coupling situations.[3] Regardless, however, of strong versus weak coupling scenarios, CDW gap opening is generically explained in a Born-Oppenheimer picture, where electrons move within an effectively static distorted

lattice.

Here, we investigate the CDW in monolayer NbS_2 using scanning tunneling microscopy (STM) and spectroscopy (STS) as well as theoretical *ab initio* based modeling. Within a clear gap in the STS measured dI/dV spectra, a persistent and position dependent fine structure is observed. We demonstrate that the measured unconventional gap with its low energy spectral features reflects the robust presence of collective CDW phonon modes, specifically amplitude and phase modes, which couple to the electrons rather than the opening of a gap in the electronic band structure.

Monolayer NbS_2 was grown *in situ* on single crystal graphene (Gr) on Ir(111) and transferred in ultrahigh vacuum to the STM, see Supporting Information (SI) for details. The STM topograph of Figure 1a displays coalesced monolayer islands covering most of the Gr substrate. (see Figure S1 of SI for a low-energy electron diffraction pattern). The NbS_2 layer conforms to Gr, which itself is continuous over Ir(111) steps running from the upper left to the lower right. The apparent height of NbS_2 is in the range of 0.53–0.64 nm depending on the tunneling parameters. An exemplary profile is shown in Figure 1b taken along the black line of Figure 1a. The atomic lattice of NbS_2 as visible in all STM dI/dV maps of Figure 2 has a periodicity of 0.331(3) nm as measured by STM and low energy electron diffraction. The STS inferred density of states (DOS) in the range of ± 2 eV around the Fermi energy (see Figure S2 of SI) and the dispersion of the Γ pocket measured by STS quasiparticle interference (see Figure S3 of SI) make plain that the monolayer has H-NbS_2 and not T-NbS_2 structure. The measured in-plane lattice parameter and apparent height match with bulk values for 2H-NbS_2[18] and previously measured monolayer values on Gr/SiC(0001)[19] and Au(111).[20]

The sequence of constant-height fast Fourier transform (FFT) filtered dI/dV maps in Figure 2a-c are all taken in the same area and with the same STM tip at sample bias voltages $V_s = -15$ mV, $V_s = 7$ mV, and $V_s = 40$ mV, respectively (see Figure S4 of SI for details on FFT filtering). While the atomically resolved maps in Figure 2a and c display a clear 3×3

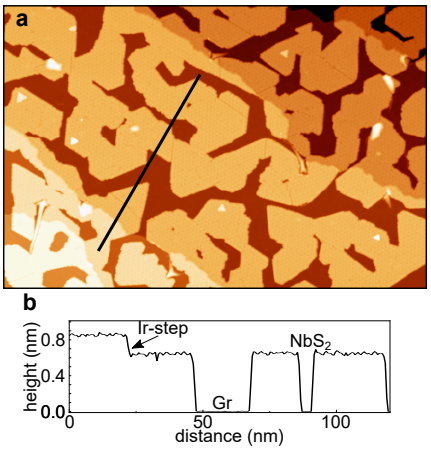

Figure 1: Structure of the NbS_2 monolayer: (a) STM topograph of coalesced monolayer islands of H-NbS_2 on Gr/Ir(111). (b) STM height profile along the black line in (a). Image information: (a) size 250 nm × 166 nm, $V_s = 1$ V, $I_t = 0.1$ nA, $T_s = 1.7$ K.

superstructure, it is absent in Figure 2b, as expected for a map taken within a CDW gap. The intensity ratio $I_{3\times3}/I_{atom}$ [21] of the first order 3×3 superstructure spots and the first order NbS_2 lattice spots is shown as a function of bias voltage V_s in Figure 2d. The plot displays a clear minimum at 7 mV, where the intensity ratio is lower by a factor of 20 compared to the maximum at about −15 mV. The maxima of the 3×3 superstructure shift between the dI/dV maps taken at $V_s = -15$ mV and at $V_s = 40$ mV as expected for a CDW when crossing its gap and as highlighted by the insets of Figure 2d.

Additional insight into the CDW stems from the temperature dependence of the 3×3 superstructure. Figure 2e–g shows a sequence of dI/dV maps measured at sample temperatures of 4 K, 30 K, and 40 K respectively. The superstructure intensity diminishes with increasing temperature and vanishes at 40 K, as obvious from the topographs and their FFT insets. Figure 2h is a plot of $I_{3\times3}/I_{atom}$ as a function of temperature. Based on the data, we estimate a transition temperature $T_{CDW} \approx 40$ K.

Taken together, the existence of a 3×3 superstructure, the $I_{3\times3}/I_{atom}$ intensity ratio minimum next to the Fermi level, the phase shift of the superstructure when crossing the Fermi level, and the disappearance of the superstructure at 40 K sum up to sound evidence for the presence of a CDW in monolayer NbS_2.

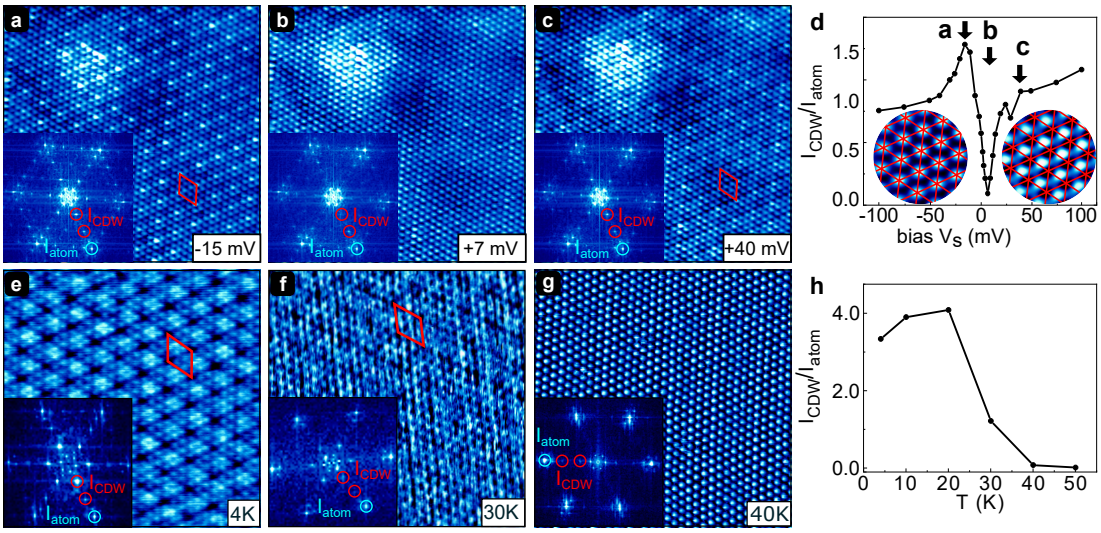

Figure 2: CDW in monolayer NbS_2: (a), (b), and (c) are bandstop filtered constant-height $\mathrm{d}I/\mathrm{d}V$ maps taken at $V_\mathrm{s} = -15\,\mathrm{mV}$, $V_\mathrm{s} = 7\,\mathrm{mV}$, and $V_\mathrm{s} = 40\,\mathrm{mV}$, respectively. Red diamonds in (a) and (c) mark the 3×3 superstructure. The insets are the FFTs of the $\mathrm{d}I/\mathrm{d}V$ maps. Spots of the 3×3 superstructure are marked in red. (d) Intensity ratio $I_{3\times3}/I_\mathrm{atom}$ of the first order 3×3 superstructure spots and first order NbS_2 spots visible in the FFTs as a function of sample bias. The data points for (a), (b), and (c) are indicated. Insets of (d) highlight the lateral shift of superstructure maxima when crossing the Fermi level. The red line pattern is located at the exact same position in relation to the atomic lattice. Only first order 3×3 spots were back-transformed (see Figure S4 of SI for details on FFT filtering). (e–g) Constant-current $\mathrm{d}I/\mathrm{d}V$ maps taken at sample temperatures T_s indicated. The insets are the FFTs of the $\mathrm{d}I/\mathrm{d}V$ maps. Spots of the 3×3 superstructure are marked in red. (h) Intensity ratio $I_{3\times3}/I_\mathrm{atom}$ as a function of temperature. Image information: (a–c) size $12\,\mathrm{nm} \times 12\,\mathrm{nm}$, $V_\mathrm{stab} = 300\,\mathrm{mV}$, $I_\mathrm{stab} = 5\,\mathrm{nA}$, $V_\mathrm{mod} = 5\,\mathrm{mV}$, $f_\mathrm{mod} = 1890\,\mathrm{Hz}$, $T_\mathrm{s} = 4\,\mathrm{K}$, FFT filtered; (e–g) size $9\,\mathrm{nm} \times 9\,\mathrm{nm}$, $V_\mathrm{s} = 100\,\mathrm{mV}$, $I_\mathrm{t} = 0.7\,\mathrm{nA}$, $V_\mathrm{mod} = 10\,\mathrm{mV}$, $f_\mathrm{mod} = 1890\,\mathrm{Hz}$.

Although unambiguous experimental evidence for a CDW in monolayer NbS_2 was missing, our finding is no surprise. While it is well established that bulk NbS_2 does not display a CDW,[22,23] it was pointed out that bulk NbS_2 is at the verge of forming a CDW due to strong electron-phonon coupling.[24] In monolayer NbS_2 on Au(111) no CDW was observed,[20] while on Gr on SiC(0001) the 3×3 superstructure was observed and attributed to a CDW.[19] In subsequent theoretical investigations and using the experimental lattice parameter, the monolayer phonon dispersion indeed was shown to become unstable close to $q_\mathrm{CDW} = 2/3\,\overline{\Gamma\mathrm{M}}$,[25] which is indeed the CDW wave vector corresponding to the 3×3 superstructure observed.

High-resolution $\mathrm{d}I/\mathrm{d}V$ spectra are taken along a high symmetry line in the 3×3 unit cell of the CDW at locations indicated in the $\mathrm{d}I/\mathrm{d}V$ map of Figure 3a and represented in Figure 3b. In all spectra at roughly $\pm 10\,\mathrm{mV}$ (thin dashed lines) the $\mathrm{d}I/\mathrm{d}V$ intensity slopes down forming a trough valley with $\mathrm{d}I/\mathrm{d}V$ intensity reduced by 20–30 % (compare Figure 3c). Inside the trough valley small peaks of $\mathrm{d}I/\mathrm{d}V$ intensity are visible. Despite a strong intensity variation of these peaks, if present, they tend to be at the same bias symmetric locations of $\pm 6\,\mathrm{mV}$ and $\pm 2.5\,\mathrm{mV}$ with a spread of less than $0.5\,\mathrm{meV}$. These locations are highlighted by dashed lines in Figure 3b. Figure 3c shows as black curve the average of 43×43 $\mathrm{d}I/\mathrm{d}V$ spectra taken within the white box in the image of Figure 3a. The flanks of the trough valley are well visible, as are three out of the four inner peaks, while the fourth at $+6\,\mathrm{mV}$ appears as a shoulder. Figure 3c also presents as red curve a $\mathrm{d}I/\mathrm{d}V$ spectrum of NbS_2 with less electrons in the band structure, *i.e.*, on p-doped NbS_2. P-doping was achieved by oxygen intercalation under Gr (see Figure S5 of SI for details), thereby increasing its work functions by around $0.5\,\mathrm{eV}$. Vacuum level alignment implies the build-up of an interface dipole through transfer of electrons out of NbS_2.[26] Comparing the two spectra in Figure 3c makes plain that the width of the trough valley decreased and the peaks at the bottom of the valley changed their position.

While a gap in the measured $\mathrm{d}I/\mathrm{d}V$ spectra located at the Fermi level is often taken as an indication of a gap in the electronic band structure, a CDW gap at the Fermi level is not necessarily reflected in a gap in an STS $\mathrm{d}I/\mathrm{d}V$ spectrum.[16] Although due to a CDW at least partial electronic band gaps will open at the Fermi level, they may be inconspicuous to STS. STS is mostly sensitive to electronic states with small parallel momentum. NbS_2 has no states with small parallel momentum near the Fermi edge (compare Figure S3 of SI).

Indeed, the trough shape of our gap does not appear like a single gap in the spectral function,[27,28] but is more reminiscent to a spectrum resulting from an inelastic tunneling process setting in at about $\pm 10\,\mathrm{meV}$.[29,30] Through the additional tunneling channel the overall tunneling probability increases beyond the onset energy. One might be tempted to

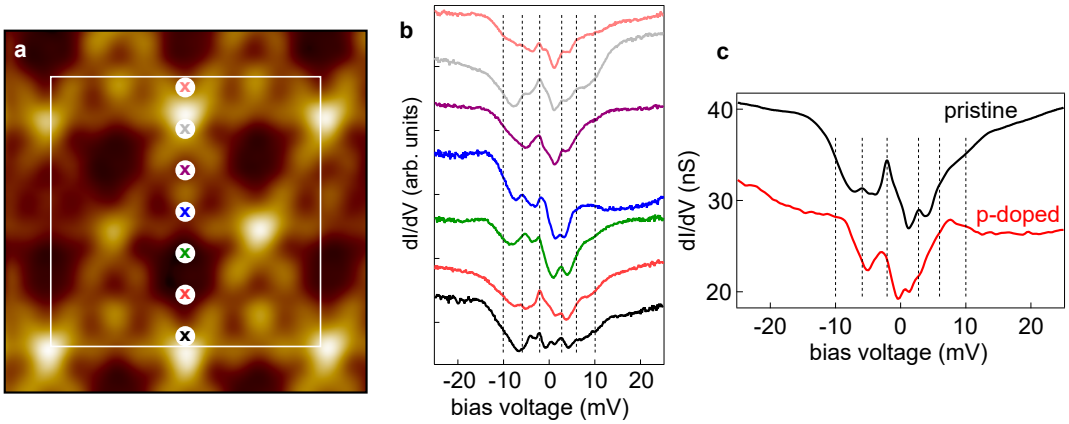

Figure 3: $\mathrm{d}I/\mathrm{d}V$ spectra of monolayer NbS_2 near the Fermi-level: (a) $\mathrm{d}I/\mathrm{d}V$ map of monolayer NbS_2. (b) High-resolution $\mathrm{d}I/\mathrm{d}V$ spectra taken at the points color-coded in (a). Thin dashed lines at $\pm 10\,\mathrm{mV}$ highlight flanks of gap. Thin dashed lines highlight positions of toggling peaks within gap. The $\mathrm{d}I/\mathrm{d}V$ spectra are shifted vertically for better visualization. (c) Black curve: average of 43×43 $\mathrm{d}I/\mathrm{d}V$ spectra taken within the white box in (a). Red curve: $\mathrm{d}I/\mathrm{d}V$ spectrum taken of monolayer NbS_2 grown on O-intercalated graphene on Ir(111). The red $\mathrm{d}I/\mathrm{d}V$ spectrum is vertically shifted down by 5 nS. Image information: (a) size $2.7\,\mathrm{nm} \times 2.7\,\mathrm{nm}$, $V_\mathrm{s} = 100\,\mathrm{mV}$, $I_\mathrm{t} = 1.0\,\mathrm{nA}$, $V_\mathrm{mod} = 15\,\mathrm{mV}$, $f_\mathrm{mod} = 1873\,\mathrm{Hz}$, $T_\mathrm{s} = 0.4\,\mathrm{K}$; (b) $V_\mathrm{stab} = 100\,\mathrm{mV}$, $I_\mathrm{stab} = 4.7\,\mathrm{nA}$, $V_\mathrm{mod} = 0.5\,\mathrm{mV}$, $f_\mathrm{mod} = 311\,\mathrm{Hz}$, $T_\mathrm{s} = 0.4\,\mathrm{K}$; (c) black curve: $V_\mathrm{stab} = 100\,\mathrm{mV}$, $I_\mathrm{stab} = 4.7\,\mathrm{nA}$, $V_\mathrm{mod} = 0.5\,\mathrm{mV}$, $f_\mathrm{mod} = 311\,\mathrm{Hz}$, $T_\mathrm{s} = 0.4\,\mathrm{K}$; red curve: $V_\mathrm{stab} = 50\,\mathrm{mV}$, $I_\mathrm{stab} = 0.5\,\mathrm{nA}$, $V_\mathrm{mod} = 0.5\,\mathrm{mV}$, $f_\mathrm{mod} = 797\,\mathrm{Hz}$, $T_\mathrm{s} = 0.4\,\mathrm{K}$.

assign the inelastic feature at $\pm 10\,\mathrm{mV}$ to bulk phonon modes of NbS_2 expected at $\pm 12\,\mathrm{mV}$.[31] Such modes have been observed in STS of defected bulk 2H-NbS_2[32] and bulk 2H-$NbSe_2$,[33] but displayed no link to a CDW. In addition, the substantial reduction of the gap and its changed internal features upon p-doping rule out this assumption, as bulk phonon modes are not expected to change drastically upon doping.

Worse yet, none of the ideas invoked up to now provide an explanation for the internal fine structure of our gap with tiny peaks at $\pm 2.5\,\mathrm{meV}$ and $\pm 6\,\mathrm{meV}$. However, strong indication that these features are related to the CDW is given by the spatial distribution of the peaks, that retains the periodicity of the CDW (see Figure S6 in the SI).

We note that the gap and its internal peak structure in the $\mathrm{d}I/\mathrm{d}V$ spectra are unchanged through an external magnetic field of up to 8 T. This rules out a superconducting or magnetic origin (see Figure S7 of SI), such as the spin density waves which have been discussed in the theory literature.[34–36]

In search for an explanation for the observed features in the low-energy $\mathrm{d}I/\mathrm{d}V$ spectra, we perform calculations based on density functional theory (DFT) and density functional perturbation theory (DFPT), which provide us with the electronic and phononic properties, respectively. Since DFT and especially DFPT for large systems are computationally costly, we use the downfolding strategy described in Ref. 37 to construct a low-energy model from a single calculation in the undistorted phase. Within this downfolded model, we can then efficiently calculate the (free) energy, forces, and electronic band structure in the distorted phase, which requires a supercell that is several times larger than the original unit cell. Here, we briefly remark on the Marzari-Vanderbilt cold smearing[38] parameter σ, which is used to stabilize the simulation of metals. Varying this parameter illustrates how stable the results are and acts as an indication of the effects of temperature and substrate hybridization[39] (see SI for more details).

The experimentally observed CDW phase involves a distortion of the original atomic lattice into a 3×3 superstructure. A DFPT calculation of the phonon spectrum in the symmetric (undistorted) phase shows several degenerate unstable phonon modes that would result in a 3×3 superstructure. By relaxation of a 3×3 supercell starting from randomized atomic positions within the model, we were able to identify four qualitatively different possible CDW structures, shown in Figure 4 (a). They all feature a significant displacement of the Nb atoms that preserves both the in-plane mirror symmetry and the three-fold rotation symmetry at the points toward or away from which the Nb atoms move. As in Ref. 40 on $NbSe_2$, we label them as T1 (toward S), "hexagons" (toward Nb), T1′ (toward gap), and T2′ (away from gap). The fact that the experimental $\mathrm{d}I/\mathrm{d}V$ maps largely show a single pronounced peak per 3×3 cell and are mainly sensitive to the S atoms suggests that the T1 structure is observed in experiment. Thus, we focus our discussion in the main text on the T1 structure (all other structures are described in the SI). To facilitate the comparison, a smearing $\sigma = 5$ mRy is used unless otherwise noted, since all four structures are stable at this smearing.

As we are trying to better understand the low-energy $\mathrm{d}I/\mathrm{d}V$ spectra shown in Figure 3, we first consider the calculated electronic structure. Figure 4b–d shows the band structure and electronic DOS of the T1 CDW structure. There is a significant reconstruction compared to the high-temperature undistorted structure with several partial gaps opening mainly in the vicinity of the K point. Instead of a sharp gap directly at the Fermi level, there is a rather constant depression of the DOS in an interval of about 150 meV around the Fermi level. Inside this depression region, there are small peaks (Van Hove singularities) whose position is characteristic of the individual CDW structure (see Figures S9, S10, and S11 in the SI for the other three structures) and the displacement. However, these peaks do not fit the experiment energetically and they are not symmetric around the Fermi level. This suggests that the experimentally observed $\mathrm{d}I/\mathrm{d}V$ is not purely electronic in nature.

One possibility is that inelastic phonon excitations could be responsible for the specific signatures in the STS. Thus, we continue with an analysis of the phononic excitations present in the CDW state. Once the system has undergone a CDW transition, signatures of the competing CDW structures remain visible in the phonon spectrum. Figure 4e, f shows the phonon dispersion in the T1 CDW phase. Highlighted in magenta are phonons corresponding to any of the four displacement patterns in Figure 4a, which are longitudinal-acoustic modes corresponding to the experimentally observed 3×3 periodicity. Of these, the mode with the highest energy is the amplitude (or Higgs) mode, where the atoms oscillate toward their undistorted position and back. The other modes are phase (or Goldstone) modes, corresponding to oscillations toward any of the other CDW patterns. The phase modes have a small but non-zero energy in a dynamically stable commensurate CDW. The precise energy of these modes depends on the cold smearing parameter σ. At $\sigma_c = 14.7$ mRy, the undistorted structure is on the edge of being stable, and all highlighted phonon modes have precisely zero energy. For $\sigma < \sigma_c$, as in Figure 4e, f, the system is in a stable CDW phase. Lowering smearing further, the displacement compared to the symmetric state increases, with a corresponding increase of the phonon energies, *i.e.*, the magenta block in Figure 4e

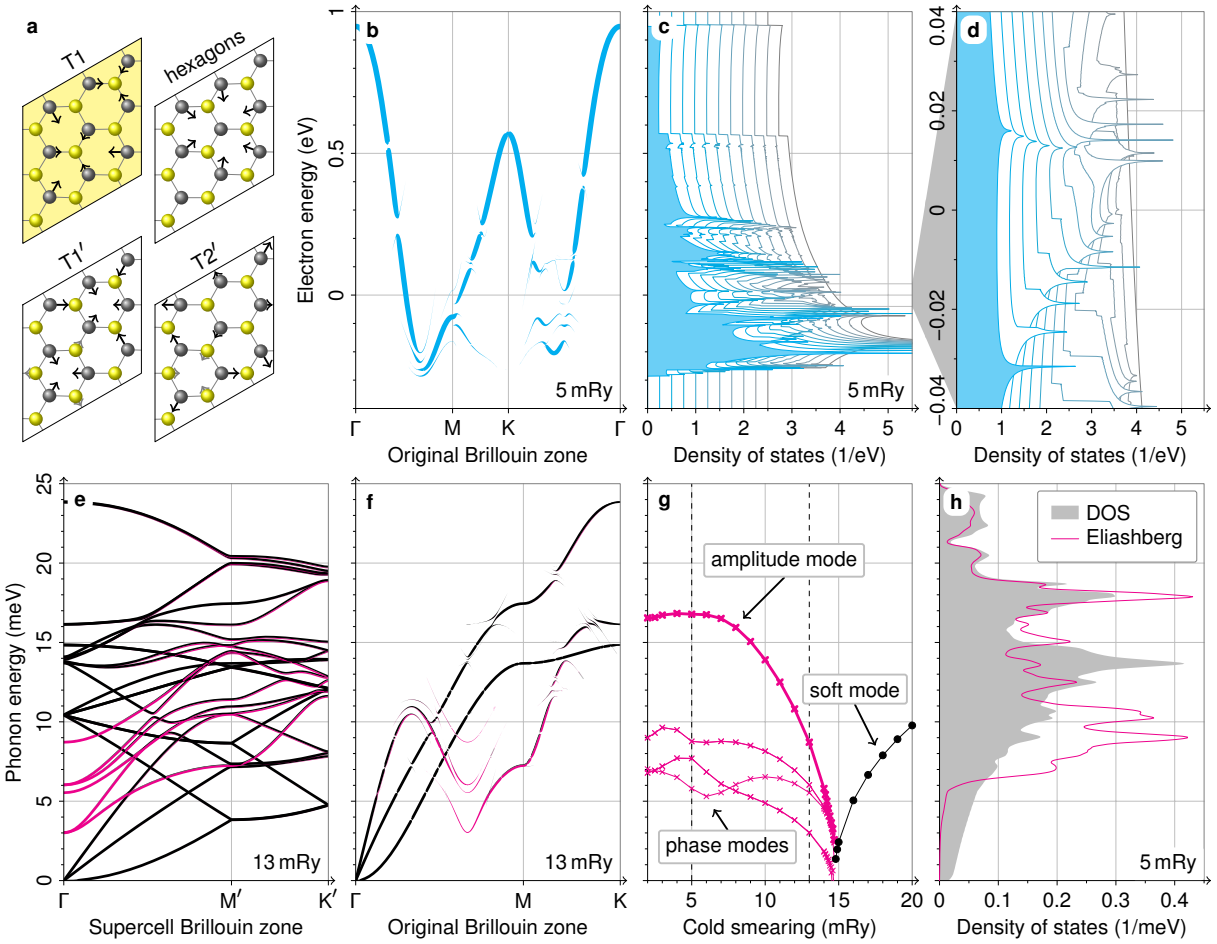

Figure 4: DFT-based low-energy model of NbS_2: (a) Four stable CDW structures. Atomic positions are drawn to scale, Nb in gray and S in yellow. Arrows indicating atomic displacements are scaled by a factor of 15 for visibility. The T1 structure where Nb atoms move toward S atoms is considered in the following (highlighted). (b) Unfolded electronic band structure of the T1 structure. The Fermi level is located at zero. (c, d) Corresponding DOS for CDW displacements scaled by a factor α between 0 (gray, rightmost curve) and 1 (blue, leftmost curve). (d) is a close-up of the low-energy region. (e, f) Phonon dispersion just below the CDW transition. Displacement components belonging to the phase and amplitude modes are shown in magenta. Here, the colored fraction of the linewidth represents the summed squared modulus of the eigenvector overlap. The dispersion in (f) has been unfolded to the Brillouin zone of the symmetric structure. (g) Transition of the softened phonon mode into amplitude (thick line) and phase modes. (h) Phonon DOS and dimensionless (normalized) Eliashberg spectral function. A smearing parameter of 5 mRy is used in (b-d, h), while 13 mRy is used in (e, f). These values are indicated as vertical lines in (g).

moves upwards for smaller σ. Figure 4e, f and the corresponding panels in the SI have a smearing just below the point where the given structure becomes stable, here $\sigma = 13$ mRy, so that the magenta and black modes are clearly separated at $\boldsymbol{q} = \Gamma$. From the point of view of the undistorted structure, the finite energy of the phase modes in the distorted phase is a non-linear phonon-phonon coupling effect. Importantly, if we are sufficiently deep inside the CDW phase, the amplitude and phase mode energies lie robustly within the range of the experimentally observed trough valley (amplitude mode) and the smaller inner-valley peaks (phase modes). This energetic match is generic in the sense that it also applies to the other CDW structures considered in the SI.

To assess the impact of the phonons on the STS, we need to know not only their frequency but also how they couple to the electrons. This is quantified by the Eliashberg function $\alpha^2F(\omega)$ shown in Figure 4h. The electron-phonon coupling appears squared in the Eliashberg spectral function, since the electron needs to emit and absorb a phonon. The Eliashberg function has a clear onset at the energy corresponding to the lowest phase mode. This shows that the modes corresponding to the longitudinal-acoustic modes at $\boldsymbol{q} = 2/3\,\overline{\Gamma\mathrm{M}}$ in the undistorted state still dominate the coupling in presence of the CDW, due to their large electron-phonon matrix elements.[41] On the other hand, the phonon DOS itself has contributions all the way down to zero frequency, coming from the acoustic branches close to $\boldsymbol{q} = \Gamma$, but these are weakly coupled to the electrons, as usual. The Eliashberg function is qualitatively similar in all four CDW structures (see SI for details) with the onset and peak energies matching the STS spectral features qualitatively. Only the precise quantitative energies of the onset differ between the four structures. The absorption and emission of phonons naturally lead to symmetric structures around the Fermi level, therefore offering an explanation for the main experimental observations.

In summary, we present a comprehensive characterization of the CDW in quasi-freestanding H-NbS_2 monolayers grown *in situ* on Gr/Ir(111) by low-temperature STM and STS and by DFT and DFPT calculations. We investigated the electronic footprints and temperature

dependence of the 3×3 modulation pattern and unambiguously link the modulation to a CDW phenomenon. In high-resolution $\mathrm{d}I/\mathrm{d}V$ spectra, we found a gap with additional features inside. We demonstrated that the gap and features are intertwined with the CDW, given by the new bias locations after doping. The most likely explanation of these low-energy features is not purely electronic, but involves combined electron-phonon quasiparticles where the phase and amplitude phonon modes of the CDW couple to the remaining electronic states at the Fermi level. Our finding of an unconventional CDW gap in monolayer NbS_2 provides an alternative perspective on gap opening mechanisms in CDW systems, revealing the role of dynamic effects and lattice fluctuations. These insights underscore the significance of incorporating dynamic lattice effects to accurately interpret the low-energy electronic spectra in CDW or generically ordered systems.

Acknowledgement

We acknowledge funding from Deutsche Forschungsgemeinschaft (DFG) through CRC 1238 (project number 277146847, subprojects A01 and B06) and EXC 2077 (project number 390741603, University Allowance, University of Bremen). JB gratefully acknowledges the support received from the "U Bremen Excellence Chair Program", especially from Lucio Colombi Ciacchi and Nicola Marzari, as well as fruitful discussion with Bogdan Guster. EvL acknowledges support from the Swedish Research Council (Vetenskapsrådet, VR) under grant 2022-03090. JF acknowledges financial support from the DFG SPP 2137 (Project FI 2624/1-1).

Supporting Information Available

Experimental methods (details on the sample growth and STM/STS measurements), low-energy electron diffraction, local DOS ($\mathrm{d}I/\mathrm{d}V$ spectra and band structure calculation) of monolayer NbS_2, band structure of NbS_2 near Γ from quasi-particle scattering, details on

FFT filtering of the dI/dV maps, doping of Gr underlayer effect on NbS_2 CDW, real space visualization of inelastic dI/dV features, magnetic field dependence of the inelastic excitations, details on computational methods, generalized free energy, and computational characterization of all four possible CDW patterns.

References

(1) Qiu, D.; Gong, C.; Wang, S.; Zhang, M.; Yang, C.; Wang, X.; Xiong, J. Recent Advances in 2D Superconductors. *Adv. Mater.* **2021**, *33*, 2006124.

(2) Mak, K. F.; Shan, J.; Ralph, D. C. Probing and controlling magnetic states in 2D layered magnetic materials. *Nat. Rev. Phys.* **2019**, *1*, 646–661.

(3) Rossnagel, K. On the origin of charge-density waves in select layered transition-metal dichalcogenides. *J. Phys.: Condens. Matter* **2011**, *23*, 213001.

(4) Slater, J. C. Magnetic Effects and the Hartree-Fock Equation. *Phys. Rev.* **1951**, *82*, 538–541.

(5) Peierls, R. E. *Quantum theory of solids*; Clarendon Press: Oxford, 1955.

(6) Bardeen, J.; Cooper, L. N.; Schrieffer, J. R. Microscopic Theory of Superconductivity. *Phys. Rev.* **1957**, *106*, 162–164.

(7) Bardeen, J.; Cooper, L. N.; Schrieffer, J. R. Theory of Superconductivity. *Phys. Rev.* **1957**, *108*, 1175–1204.

(8) Chen, Q.; Stajic, J.; Tan, S.; Levin, K. BCS–BEC crossover: From high temperature superconductors to ultracold superfluids. *Phys. Rep.* **2005**, *412*, 1–88.

(9) Schäfer, T.; Geles, F.; Rost, D.; Rohringer, G.; Arrigoni, E.; Held, K.; Blümer, N.; Aichhorn, M.; Toschi, A. Fate of the false Mott-Hubbard transition in two dimensions. *Phys. Rev. B* **2015**, *91*, 125109.

(10) Demsar, J.; Biljaković, K.; Mihailovic, D. Single Particle and Collective Excitations in the One-Dimensional Charge Density Wave Solid $K_{0.3}MoO_3$ Probed in Real Time by Femtosecond Spectroscopy. *Phys. Rev. Lett.* **1999**, *83*, 800–803.

(11) Petersen, J. C.; Kaiser, S.; Dean, N.; Simoncig, A.; Liu, H. Y.; Cavalieri, A. L.; Cacho, C.; Turcu, I. C. E.; Springate, E.; Frassetto, F.; Poletto, L.; Dhesi, S. S.; Berger, H.; Cavalleri, A. Clocking the Melting Transition of Charge and Lattice Order in $1T-TaS_2$ with Ultrafast Extreme-Ultraviolet Angle-Resolved Photoemission Spectroscopy. *Phys. Rev. Lett.* **2011**, *107*, 177402.

(12) Liu, H. Y. et al. Possible observation of parametrically amplified coherent phasons in $K_{0.3}MoO_3$ using time-resolved extreme-ultraviolet angle-resolved photoemission spectroscopy. *Phys. Rev. B* **2013**, *88*, 045104.

(13) Johannes, M. D.; Mazin, I. I. Fermi surface nesting and the origin of charge density waves in metals. *Phys. Rev. B* **2008**, *77*, 165135.

(14) Weber, F.; Rosenkranz, S.; Castellan, J.-P.; Osborn, R.; Hott, R.; Heid, R.; Bohnen, K.-P.; Egami, T.; Said, A. H.; Reznik, D. Extended Phonon Collapse and the Origin of the Charge-Density Wave in $2H-NbSe_2$. *Phys. Rev. Lett.* **2011**, *107*, 107403.

(15) Berges, J.; van Loon, E. G. C. P.; Schobert, A.; Rösner, M.; Wehling, T. O. Ab initio phonon self-energies and fluctuation diagnostics of phonon anomalies: Lattice instabilities from Dirac pseudospin physics in transition metal dichalcogenides. *Phys. Rev. B* **2020**, *101*, 155107.

(16) van Efferen, C. et al. A full gap above the Fermi level: the charge density wave of monolayer VS_2. *Nat. Commun.* **2021**, *12*, 6837.

(17) Hofmann, P.; Ugeda, M. M.; Tamtögl, A.; Ruckhofer, A.; Ernst, W. E.; Benedek, G.; Martínez-Galera, A. J.; Stróżecka, A.; Gómez-Rodríguez, J. M.; Rienks, E.;

Jensen, M. F.; Pascual, J. I.; Wells, J. W. Strong-coupling charge density wave in a one-dimensional topological metal. *Phys. Rev. B* **2019**, *99*, 035438.

(18) Fisher, W. G.; Sienko, M. J. Stoichiometry, structure, and physical properties of niobium disulfide. *Inorg. Chem.* **1980**, *19*, 39–43.

(19) Lin, H.; Huang, W.; Zhao, K.; Lian, C.; Duan, W.; Chen, X.; Ji, S.-H. Growth of atomically thick transition metal sulfide films on graphene/6H-SiC(0001) by molecular beam epitaxy. *Nano Res.* **2018**, *11*, 4722–4727.

(20) Stan, R.-M.; Mahatha, S. K.; Bianchi, M.; Sanders, C. E.; Curcio, D.; Hofmann, P.; Miwa, J. A. Epitaxial single-layer NbS_2 on Au(111): Synthesis, structure, and electronic properties. *Phys. Rev. Mater.* **2019**, *3*, 044003.

(21) Ugeda, M. M. et al. Characterization of collective ground states in single-layer $NbSe_2$. *Nat. Phys.* **2016**, *12*, 92–97.

(22) Naito, M.; Tanaka, S. Electrical Transport Properties in 2H-NbS_2, -$NbSe_2$, -TaS_2 and -$TaSe_2$. *J. Phys. Soc. Jpn.* **1982**, *51*, 219–227.

(23) Guillamón, I.; Suderow, H.; Vieira, S.; Cario, L.; Diener, P.; Rodière, P. Superconducting Density of States and Vortex Cores of 2H-NbS_2. *Phys. Rev. Lett.* **2008**, *101*, 166407.

(24) Heil, C.; Poncé, S.; Lambert, H.; Schlipf, M.; Margine, E. R.; Giustino, F. Origin of Superconductivity and Latent Charge Density Wave in NbS_2. *Phys. Rev. Lett.* **2017**, *119*, 087003.

(25) Bianco, R.; Errea, I.; Monacelli, L.; Calandra, M.; Mauri, F. Quantum Enhancement of Charge Density Wave in NbS_2 in the Two-Dimensional Limit. *Nano Letters* **2019**, *19*, 3098–3103.

(26) van Efferen, C.; Murray, C.; Fischer, J.; Busse, C.; Komsa, H.-P.; Michely, T.; Jolie, W. Metal-insulator transition in monolayer MoS_2 via contactless chemical doping. *2D Mater.* **2022**, *9*, 025026.

(27) Ryu, H. et al. Persistent Charge-Density-Wave Order in Single-Layer $TaSe_2$. *Nano Lett.* **2018**, *18*, 689–694, PMID: 29300484.

(28) Wan, W.; Dreher, P.; Muñoz-Segovia, D.; Harsh, R.; Guo, H.; Martínez-Galera, A. J.; Guinea, F.; de Juan, F.; Ugeda, M. M. Observation of Superconducting Collective Modes from Competing Pairing Instabilities in Single-Layer $NbSe_2$. *Adv. Mater.* **2022**, *34*, 2206078.

(29) Zhang, Y.; Brar, V. W.; Wang, F.; Girit, C.; Yayon, Y.; Panlasigui, M.; Zettl, A.; Crommie, M. F. Giant phonon-induced conductance in scanning tunnelling spectroscopy of gate-tunable graphene. *Nat. Phys.* **2008**, *4*, 627–630.

(30) Gawronski, H.; Mehlhorn, M.; Morgenstern, K. Imaging Phonon Excitation with Atomic Resolution. *Science* **2008**, *319*, 930–933.

(31) Nishio, Y.; Shirai, M.; Suzuki, N.; Motizuki, K. Role of Electron-Lattice Interaction in Layered Transition Metal Dichalcogenide $2H - NbS_2$. I. Phonon Anomaly and Superconductivity. *J. Phys. Soc. Jpn.* **1994**, *63*, 156–167.

(32) Wen, C.; Xie, Y.; Wu, Y.; Shen, S.; Kong, P.; Lian, H.; Li, J.; Xing, H.; Yan, S. Impurity-pinned incommensurate charge density wave and local phonon excitations in $2H - NbS_2$. *Phys. Rev. B* **2020**, *101*, 241404.

(33) Hou, X.-Y.; Zhang, F.; Tu, X.-H.; Gu, Y.-D.; Zhang, M.-D.; Gong, J.; Tu, Y.-B.; Wang, B.-T.; Lv, W.-G.; Weng, H.-M.; Ren, Z.-A.; Chen, G.-F.; Zhu, X.-D.; Hao, N.; Shan, L. Inelastic Electron Tunneling in $2H{-}Ta_xNb_{1-x}Se_2$ Evidenced by Scanning Tunneling Spectroscopy. *Phys. Rev. Lett.* **2020**, *124*, 106403.

(34) Xu, Y.; Liu, X.; Guo, W. Tensile strain induced switching of magnetic states in $NbSe_2$ and NbS_2 single layers. *Nanoscale* **2014**, *6*, 12929–12933.

(35) Güller, F.; Vildosola, V. L.; Llois, A. M. Spin density wave instabilities in the NbS_2 monolayer. *Phys. Rev. B* **2016**, *93*, 094434.

(36) van Loon, E. G. C. P.; Rösner, M.; Schönhoff, G.; Katsnelson, M. I.; Wehling, T. O. Competing Coulomb and electron–phonon interactions in NbS_2. *npj Quantum Mater.* **2018**, *3*, 32.

(37) Schobert, A.; Berges, J.; van Loon, E. G. C. P.; Sentef, M. A.; Brener, S.; Rossi, M.; Wehling, T. O. Ab initio electron-lattice downfolding: Potential energy landscapes, anharmonicity, and molecular dynamics in charge density wave materials. https://arxiv.org/abs/2303.07261, 2023.

(38) Marzari, N.; Vanderbilt, D.; De Vita, A.; Payne, M. C. Thermal Contraction and Disordering of the Al(110) Surface. *Phys. Rev. Lett.* **1999**, *82*, 3296.

(39) Hall, J. et al. Environmental Control of Charge Density Wave Order in Monolayer 2H-TaS_2. *ACS Nano* **2019**, *13*, 10210–10220.

(40) Guster, B.; Rubio-Verdú, C.; Robles, R.; Zaldívar, J.; Dreher, P.; Pruneda, M.; Silva-Guillén, J. A.; Choi, D.-J.; Pascual, J. I.; Ugeda, M. M.; Ordejón, P.; Canadell, E. Coexistence of Elastic Modulations in the Charge Density Wave State of 2H-$NbSe_2$. *Nano Lett.* **2019**, *19*, 3027.

(41) Lian, C.-S. Interplay of charge ordering and superconductivity in two-dimensional 2H group V transition-metal dichalcogenides. *Phys. Rev. B* **2023**, *107*, 045431.

TOC Graphic

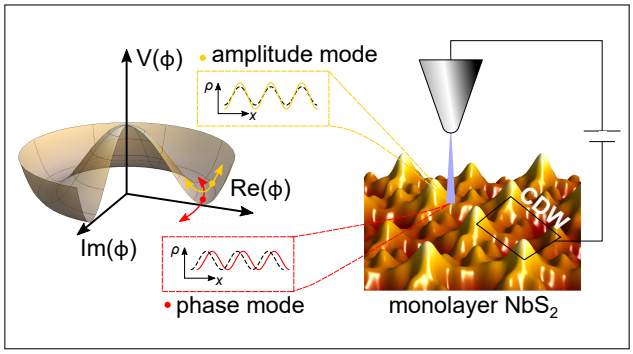
V(ϕ)
amplitude mode
ρ
x
Re(ϕ)
Im(ϕ)
ρ
x
phase mode
CDW
monolayer NbS2

Supporting Information: Unconventional charge-density-wave gap in monolayer NbS_2

Timo Knispel,[†] Jan Berges,[‡] Arne Schobert,[¶] Erik G. C. P. van Loon,[§] Wouter Jolie,[†] Tim Wehling,[¶,‖] Thomas Michely,[†] and Jeison Fischer[*,†]

[†]*II. Physikalisches Institut, Universität zu Köln, Zülpicher Straße 77, D-50937 Köln, Germany*

[‡]*U Bremen Excellence Chair, Bremen Center for Computational Materials Science, and MAPEX Center for Materials and Processes, University of Bremen, D-28359 Bremen, Germany*

[¶]*I. Institute of Theoretical Physics, Universität Hamburg, D-22607 Hamburg, Germany*

[§]*Division of Mathematical Physics, Department of Physics, Lund University, SE-22100 Lund, Sweden*

[‖]*The Hamburg Centre for Ultrafast Imaging, Luruper Chaussee 149, D-22761 Hamburg, Germany*

E-mail: jfischer@ph2.uni-koeln.de

Experimental methods

Sample preparation was accomplished in an ultrahigh vacuum (UHV) system with a base pressure of $p < 2 \times 10^{-10}$ mbar. Ir(111) was cleaned using cycles of 1 kV Ar^+-sputtering and subsequent flash annealing to 1520 K. Graphene (Gr) was grown by ethylene exposure

to saturation, subsequent flash annealing to 1470 K and a final exposure to 800 L ethylene at 1370 K. The quality of the closed single crystal Gr monolayer was checked by low energy electron diffraction (LEED) and scanning tunneling microscopy (STM).

Monolayer H-NbS_2 was grown on Gr/Ir(111) by reactive molecular beam epitaxy (MBE). The substrate was exposed to an Nb flux of 5.8×10^{15} atoms/m^{2}s from an e-beam evaporator in an elemental sulfur (S) background pressure of $p = 1 \times 10^{-8}$ mbar created by a pyrite (FeS_2) filled Knudsen cell. The growth was conducted for 660 s at 300 K substrate temperature. Subsequently, the sample was annealed to 800 K to improve the layer quality.[1] In order to maximize the monolayer coverage, the island seeds were extended to final size by additional growth at 800 K for 660 s.

After synthesis, the H-NbS_2 layer was checked using LEED. Subsequently, the sample was transferred in UHV to the connected UHV bath cryostat STM chamber for investigation. The temperature T_s of STM or scanning tunneling spectroscopy (STS) investigation is specified in each figure and was either 0.4 K using a He^3 cycle, 1.7 K when pumping on He^4, 4 K using He^4 cooling without pumping, or even higher than 4 K by using an internal heater. Dependence of the STS features on magnetic field was checked by a superconducting magnet creating fields of up to 9 T normal to the sample surface.

Both, constant-height and constant-current modes, were used to measure topography and dI/dV maps. dI/dV spectra were recorded only at constant height. Constant-current STM topographs and constant-current dI/dV maps were recorded with sample bias V_s and tunneling current I_t specified in corresponding figure captions. Constant-height dI/dV spectra and dI/dV maps were recorded with stabilization bias V_{stab} and stabilization current I_{stab} using a lock-in amplifier with a modulation frequency f_{mod} and modulation voltage V_{mod} specified in corresponding captions. In case that for a constant-height dI/dV map the sample bias during measurement does not coincide with V_{stab}, the sample bias V_s is specified additionally. When needed, a voltage divider was applied to improve resolution. To ensure a reproducible and flat tip density of states (DOS) for the STS measurements, Au-covered W tips were

used and calibrated beforehand using the surface state of Au(111).[2,3] Details on STM image processing are given in Figure S4.

Low-energy electron diffraction (LEED)

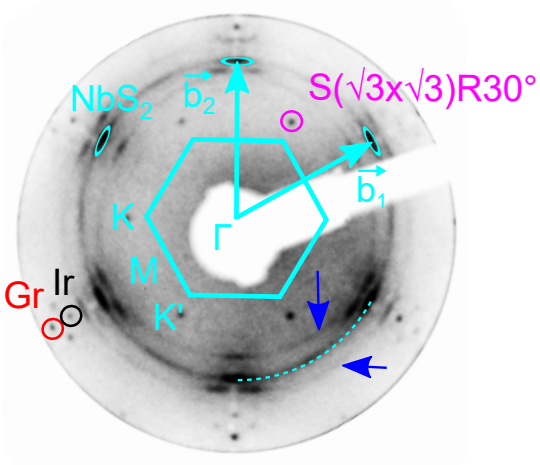

Figure S1: 100 eV microchannel plate LEED pattern. First order reflections of NbS_2 are marked in turquoise, of Gr in red, of Ir in black, and of S intercalated between Gr and Ir in pink. Two faint moiré satellite rings are highlighted by blue arrows. Primitive reciprocal space translations $\boldsymbol{b}_1$ and $\boldsymbol{b}_2$ are indicated.

The LEED pattern corresponding to the STM topograph of Figure 1a displays first order NbS_2 intensity as superposition of (i) prominent elongated spots (several encircled turquoise) reasonably aligned with Gr (encircled red) and Ir (encircled black) and (ii) a diffraction ring due to randomly oriented islands (dashed turquoise segment). Apparently, most islands are aligned with small angular scatter to Gr/Ir(111), while some display random orientation. Additionally, faint off-centered rings are visible (two highlighted by blue arrows). These rings belong to NbS_2, but are each shifted by one moiré periodicity of Gr. S intercalation between Gr and Ir gives rise to a $(\sqrt{3} \times \sqrt{3})$R30° structure with respect to Ir(111) and corresponding reflections, of which one first order reflection is encircled in pink.

Local density of states of monolayer NbS_2

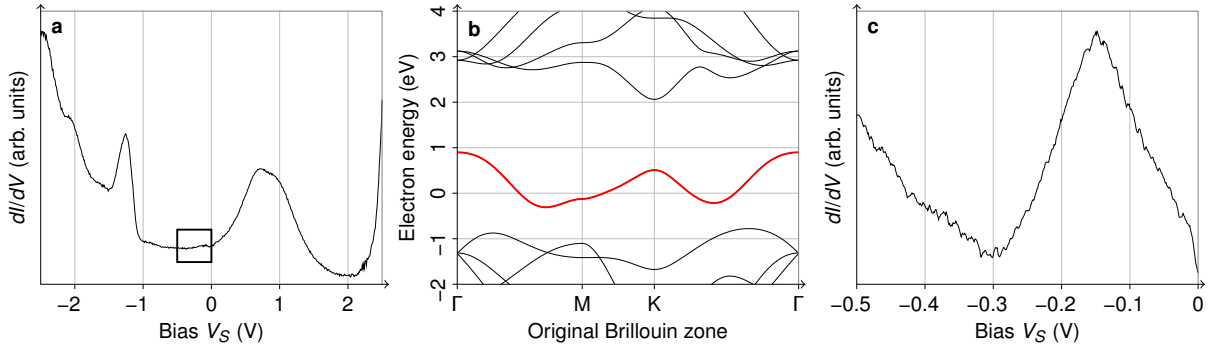

Figure S2: $\mathrm{d}I/\mathrm{d}V$ spectra of monolayer NbS_2: (a) Large-range $\mathrm{d}I/\mathrm{d}V$ spectrum from $-2.5\,\mathrm{V}$ to $+2.5\,\mathrm{V}$. (b) Calculated band structure of freestanding H-NbS_2. (c) $\mathrm{d}I/\mathrm{d}V$ spectrum of boxed voltage range in (a) with tip very close to sample. Spectra parameters: (a) $V_{\mathrm{stab}} = 2.5\,\mathrm{V}$, $I_{\mathrm{stab}} = 1.0\,\mathrm{nA}$, $V_{\mathrm{mod}} = 15\,\mathrm{mV}$, $f_{\mathrm{mod}} = 797\,\mathrm{Hz}$, $T_{\mathrm{s}} = 0.4\,\mathrm{K}$; (c) $V_{\mathrm{stab}} = -0.5\,\mathrm{V}$, $I_{\mathrm{stab}} = 0.5\,\mathrm{nA}$, $V_{\mathrm{mod}} = 5\,\mathrm{mV}$, $f_{\mathrm{mod}} = 1873\,\mathrm{Hz}$, $T_{\mathrm{s}} = 0.4\,\mathrm{K}$.

To gain further insight into the electronic structure, differential conductance $\mathrm{d}I/\mathrm{d}V$ spectra were measured on NbS_2, shown in Figure S2. Figure S2a displays a large-range constant-height $\mathrm{d}I/\mathrm{d}V$ spectrum which can be compared to the density functional theory (DFT) band structure in Figure S2b. We note that (i) Van Hove singularities appear pronounced in $\mathrm{d}I/\mathrm{d}V$ spectra due to the large local DOS (LDOS) associated to them, and (ii) states with large parallel momentum $k_{||}$ are diminished or even suppressed in $\mathrm{d}I/\mathrm{d}V$ spectra, since a large $k_{||}$ is associated with a large decay constant κ, *i.e.*, a rapid decay of the wave function into vacuum.[4,5]

The pronounced peak at $-1.25\,\mathrm{V}$ in Figure S2a is attributed to the three occupied S p-bands with minima or maxima around $-1.25\,\mathrm{V}$ at the Γ-point in Figure S2b. Additional maxima in the occupied states along the $\overline{\Gamma\mathrm{M}}$ or the $\overline{\Gamma\mathrm{K}}$ direction are hardly visible in the $\mathrm{d}I/\mathrm{d}V$ spectrum because of their larger $k_{||}$. The broad and intense maximum with its peak at about $+0.85\,\mathrm{V}$ in Figure S2a is associated to the band maximum of the Nb $d_{\mathbf{z}}$-type hole-like pocket at the Γ-point in Figure S2b, though located at slightly lower energies as in the calculation. The steep rise in the $\mathrm{d}I/\mathrm{d}V$ spectrum at energies above about $+2.2\,\mathrm{V}$ is associated to the empty Nb d-bands with energies above $2\,\mathrm{eV}$ in the calculated band

structure. Figure S2c displays an STS spectrum for the energy range from $-0.5\,\mathrm{V}$ to $0\,\mathrm{V}$ (boxed in Figure S2a). It is stabilized at $-0.5\,\mathrm{V}$, *i.e.*, at an energy with a low DOS as seen in Figure S2a. To pick up the stabilization current of $I_\mathrm{t} = 0.5\,\mathrm{nA}$ the tip moves close to the surface and thus becomes sensitive to less pronounced features in the LDOS. The peak at $-0.15\,\mathrm{V}$ in the resulting spectrum can be interpreted as the Van Hove singularity associated with the toroidal minimum of the Nb *d*-band surrounding the Γ-point.

Band structure of NbS_2 near the Γ-point from quasi-particle interference

Besides the charge density wave (CDW) superstructure, another electronic feature cannot be overlooked in NbS_2 monolayer islands. The $100\,\mathrm{mV}$ $\mathrm{d}I/\mathrm{d}V$ map in Figure S3a displays standing wave patterns at the NbS_2 island edges originating from quasi-particle interference (QPI) of electron waves. Zooming into the island, Figure S3b shows a constant-current $\mathrm{d}I/\mathrm{d}V$ map recorded at $30\,\mathrm{mV}$. At this bias voltage damping of the QPI is weak and the interference pattern is spread out over the whole island. The inset with the fast Fourier transform (FFT) exhibits a ring-like feature, which shows enhanced intensity in the $\overline{\Gamma\mathrm{M}}$ direction. QPI at 30 meV is thus close to isotropic in wave vector, but anisotropic in scattering intensity. The QPI pattern is used to extract the dispersion[7–9] of the *d*-band crossing the Fermi level, discussed in Figure S2b.

In Figure S3c the FFT intensity profiles along the high-symmetry directions in k space are plotted as function of energy. Superimposed to the dispersing feature in the data is the DFT calculated band as dotted-blue line. The bright cut-off toward larger k values agrees reasonably with the calculation.

The dispersion is also determined by analysis of the real space periodicity of the standing waves at NbS_2 island edges. Following the approach of Crommie *et al.*,[7] the standing wave pattern resulting from backscattering at a straight island edge is fitted after proper back-

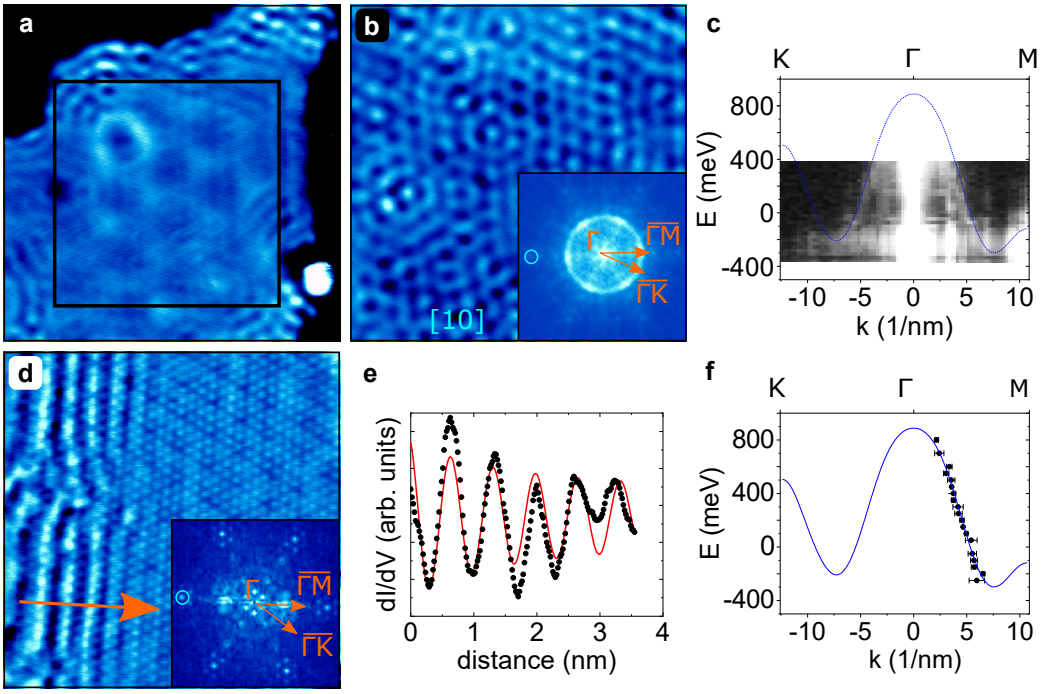

Figure S3: Quasi-particle interference in NbS_2: (a) Constant-current $\mathrm{d}I/\mathrm{d}V$ map. (b) Constant-current $\mathrm{d}I/\mathrm{d}V$ map of the area inside the black square shown in (a). Inset displays the FFT of the $\mathrm{d}I/\mathrm{d}V$ map. An atomic lattice reflection is marked turquoise, the reciprocal space directions marked orange. (c) FFT intensity of the $\mathrm{d}I/\mathrm{d}V$ maps along $\overline{\Gamma\mathrm{M}}$ and $\overline{\Gamma\mathrm{K}}$ as a function of energy $E = eV_\mathrm{s}$. Data extracted from a 200×200 grid of constant-height $\mathrm{d}I/\mathrm{d}V$ spectra in an area of $9\,\mathrm{nm} \times 9\,\mathrm{nm}$ on NbS_2. To represent dispersion, experimental wave vectors are divided by a factor of two.[6] Superimposed as dotted-blue line is our DFT calculated dispersion of the H-NbS_2 d-band. (d) Constant-current $\mathrm{d}I/\mathrm{d}V$ map with the standing wave pattern due scattering at island edge. Direction of the wave vector indicated by an orange arrow. Inset is the FFT of the $\mathrm{d}I/\mathrm{d}V$ map. (e) Line profile along the orange arrow in (d) (black dots) fitted by a Bessel function (red line).[7] (f) $E(k)$ dispersion relation extracted from the Bessel function fits and compared to the calculated band structure also displayed in (c). Image information: (a) size $13\,\mathrm{nm} \times 13\,\mathrm{nm}$, $V_\mathrm{s} = 200\,\mathrm{mV}$, $I_\mathrm{t} = 1.0\,\mathrm{nA}$, $V_\mathrm{mod} = 20\,\mathrm{mV}$, $f_\mathrm{mod} = 797\,\mathrm{Hz}$, $T_\mathrm{s} = 0.4\,\mathrm{K}$; (b) size $9\,\mathrm{nm} \times 9\,\mathrm{nm}$, $V_\mathrm{s} = 30\,\mathrm{mV}$, $I_\mathrm{t} = 0.8\,\mathrm{nA}$, $V_\mathrm{mod} = 7\,\mathrm{mV}$, $f_\mathrm{mod} = 1890\,\mathrm{Hz}$, $T_\mathrm{s} = 0.4\,\mathrm{K}$; (d) size $10\,\mathrm{nm} \times 10\,\mathrm{nm}$, $V_\mathrm{s} = 150\,\mathrm{mV}$, $I_\mathrm{t} = 0.3\,\mathrm{nA}$, $V_\mathrm{mod} = 20\,\mathrm{mV}$, $f_\mathrm{mod} = 1890\,\mathrm{Hz}$, $T_\mathrm{s} = 1.7\,\mathrm{K}$.

ground subtraction through $\mathrm{d}I/\mathrm{d}V[V_\mathrm{s}, x] = L_0[1 - J_0(2kx + \phi)]$. Here J_0 is the zeroth order Bessel function, $L_0 = m^*/(\pi\hbar^2)$ with m^* being the effective mass, ϕ is a phase constant, x the distance from the step edge and k is the wave vector related to the electron energy $E = eV_\mathrm{s}$. Figure S3e exemplifies our approach for a profile (black dots) taken along the orange arrow in the 150 mV $\mathrm{d}I/\mathrm{d}V$ map shown in Figure S3e. The fit is shown as thin red line and yields the k vector for $E = 150$ meV. Figure S3f presents our analysis in the energy range from -250 meV to 800 meV (black dots), which compares favorably with our DFT calculated dispersion shown as blue line.

Details on FFT filtering of the dI/dV maps

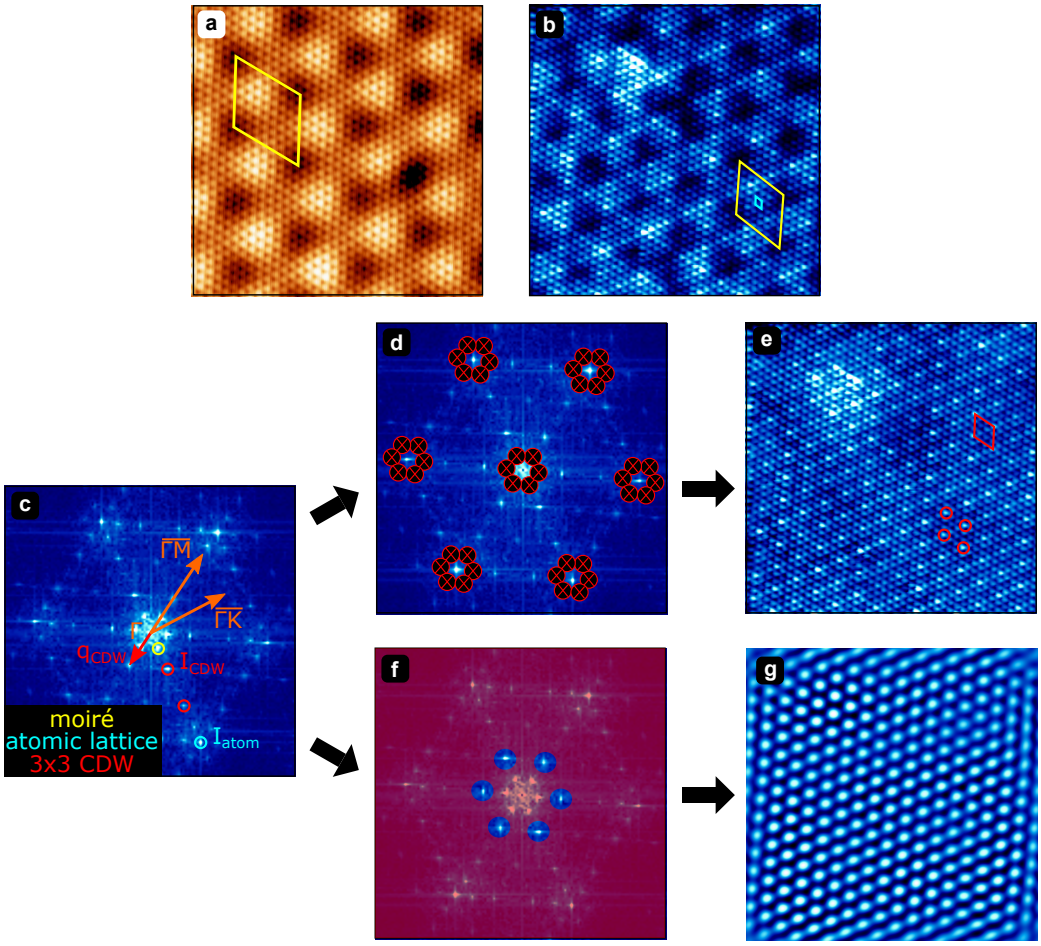

Figure S4: (a) Atomically resolved constant-current STM topograph of monolayer NbS_2. The Gr/Ir(111) moiré unit cell is indicated as yellow diamond. (b) Constant-height dI/dV map. The Gr/Ir(111) moiré and the NbS_2 unit cell are indicated as yellow and turquoise diamonds, respectively. (c) FFT of (b). Spots corresponding to the Gr/Ir(111) moiré, the atomic NbS_2 lattice, and the 3×3 CDW superstructure are encircled yellow, turquoise, and red, respectively. A $\overline{\Gamma M}$- and a $\overline{\Gamma K}$-direction are indicated by orange arrows. (d) The application of bandstop filtering to remove the moiré is visualized. (e) Back transformed moiré bandstop filtered dI/dV map. Red circles and rhomboid in (e) highlight 3×3 CDW superstructure. (f) The application of bandstop filtering to remove all, but the 3×3 CDW superstructure spots is shown. (g) Back transformed bandstop filtered image of (f) leaving only 3×3 periodicity in real space. Images: (a) size 10 nm $\times$ 10 nm, $V_s = 100$ mV, $I_t = 0.7$ nA, $T_s = 1.7$ K; (b) size 12 nm $\times$ 12 nm, $V_s = -15$ mV, $V_{stab} = 300$ mV, $I_{stab} = 5$ nA, $V_{mod} = 5$ mV, $f_{mod} = 1890$ Hz, $T_s = 4$ K.

In the atomically resolved STM topograph of Figure S4a the Gr/Ir(111) moiré (yellow diamond) can be recognized being superimposed on the atomically resolved NbS_2 lattice. The lack of an own moiré between the NbS_2 monolayer and Gr indicates a very weak interaction between the two materials.

The FFT of the $-15\,\mathrm{meV}$ constant-height $\mathrm{d}I/\mathrm{d}V$ map shown in Figure S4b is presented as Figure S4c. The red encircled spots at 1/3 and 2/3 of the distance between the Γ-point and the first order NbS_2 lattice spots (encircled turquoise) are indicative of a 3×3 superstructure. It is obvious that the three equivalent wave vectors related to the superstructure are oriented along the $\overline{\Gamma\mathrm{M}}$-directions. For better visualization of the 3×3 superstructure in real space, the moiré spots are bandstop filtered as shown in the Figure S4d. Upon back transformation, the 3×3 superstructure highlighted by red circles and a rhomboid becomes obvious in Figure S4e. Figure S4e is identical with Figure 2a of the main text. The same procedure was implemented for Figure 2b, c of the main text.

To visualize the CDW without background disturbances all FFT spots except of the CDW spots can be bandstop filtered, as demonstrated in Figure S4f. Upon back transformation only the CDW spots are visible in Figure S4g. This technique was used to obtain the maps of Figure 2d in the main text.

Doping of Gr underlayer effect on NbS_2 CDW

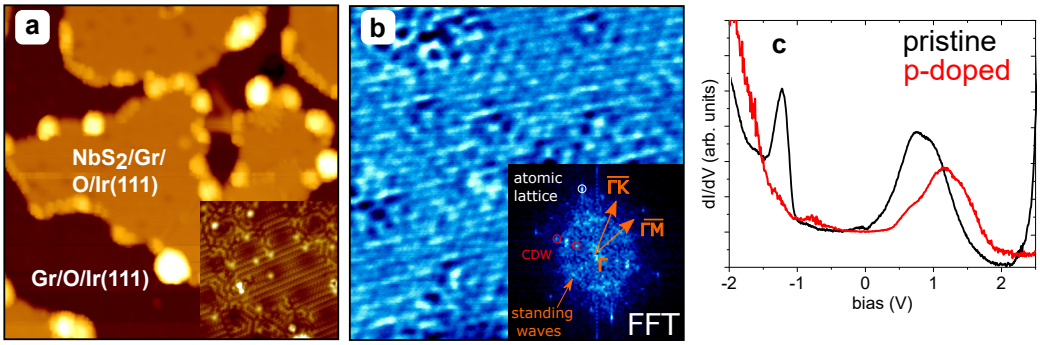

Figure S5: (a) Constant-current STM image of NbS_2 on O-intercalated Gr on Ir(111). Inset: High-resolution topograph of Gr between NbS_2 islands with stripes reflecting the (2×1) adsorption pattern of atomic O on Ir(111) through the Gr layer.[10] (b) Constant-current $\mathrm{d}I/\mathrm{d}V$ map. Inset: FFT of (b) with CDW spots encircled red. (c) Large range $\mathrm{d}I/\mathrm{d}V$ spectra of NbS_2 on O-intercalated Gr/Ir(111) (red) compared to non-intercalated, pristine NbS_2 (black) as in Figure S2a. Image information: (a) size $58\,\mathrm{nm} \times 58\,\mathrm{nm}$, $V_\mathrm{s} = 4\,\mathrm{V}$, $I_\mathrm{t} = 0.1\,\mathrm{nA}$, $T_\mathrm{s} = 1.7\,\mathrm{K}$; (b) size $10\,\mathrm{nm} \times 10\,\mathrm{nm}$, $V_\mathrm{s} = -200\,\mathrm{mV}$, $I_\mathrm{t} = 0.7\,\mathrm{nA}$, $V_\mathrm{mod} = 7\,\mathrm{mV}$, $f_\mathrm{mod} = 1890\,\mathrm{Hz}$, $T_\mathrm{s} = 10\,\mathrm{K}$. Spectra information: (c) red: $V_\mathrm{stab} = 2.5\,\mathrm{V}$, $I_\mathrm{stab} = 1.0\,\mathrm{nA}$, $V_\mathrm{mod} = 15\,\mathrm{mV}$, $f_\mathrm{mod} = 797\,\mathrm{Hz}$, $T_\mathrm{s} = 1.7\,\mathrm{K}$: black: $V_\mathrm{stab} = 2.5\,\mathrm{V}$, $I_\mathrm{stab} = 1.0\,\mathrm{nA}$, $V_\mathrm{mod} = 15\,\mathrm{mV}$, $f_\mathrm{mod} = 797\,\mathrm{Hz}$, $T_\mathrm{s} = 0.4\,\mathrm{K}$.

Figure S5a displays an STM topograph with NbS_2 islands on O-intercalated Gr/Ir(111). Details of the intercalation method are described elsewhere.[11] From Figure S5b it is obvious that the (3×3) CDW superstructure is present. Figure S5c compares the $\mathrm{d}I/\mathrm{d}V$ spectra of NbS_2 on O-intercalated Gr/Ir(111) with the pristine case. The overall $\mathrm{d}I/\mathrm{d}V$ features of p-doped NbS_2 (red curve) are shifted toward positive energy in respect to the pristine case (black curve), in agreement with p-doping.

Real space visualization of inelastic dI/dV features

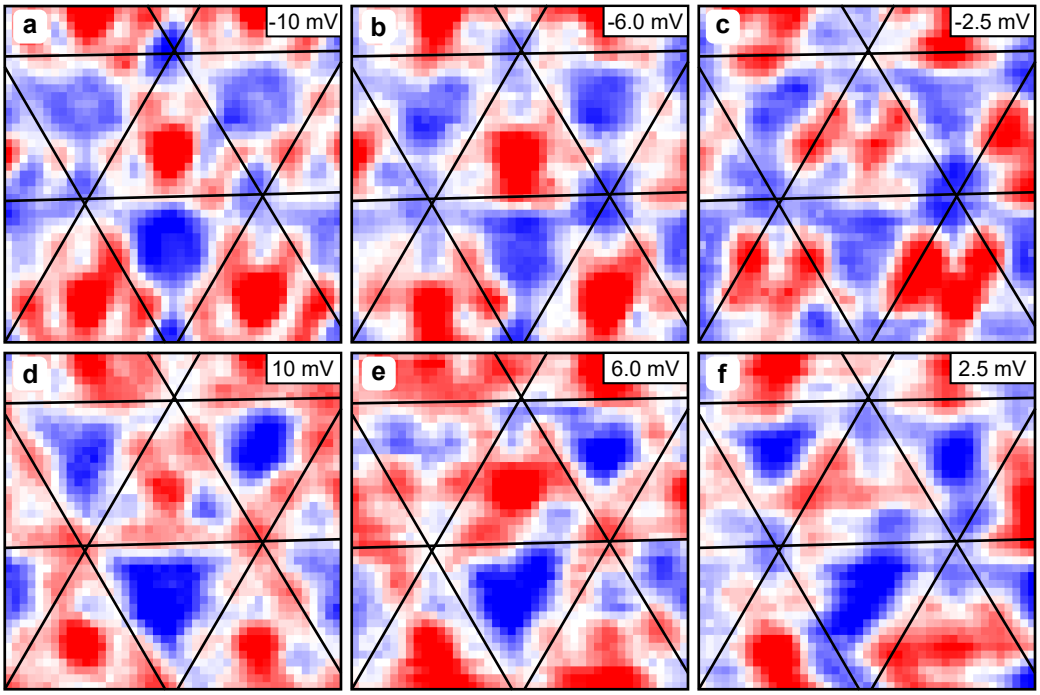

Figure S6: Constant-height dI/dV maps at bias voltages of $-10\,\mathrm{mV}$ in (a), $-6\,\mathrm{mV}$ in (b), $-2.5\,\mathrm{mV}$ in (c), $+10\,\mathrm{mV}$ in (d), $+6\,\mathrm{mV}$ in (e), $+2.5\,\mathrm{mV}$ in (f). The energies are selected according to the energy positions of the inelastic excitations displayed in Figure 3b, c of the main text. The black lines indicate the diamonds of the (3×3) CDW superstructure, which are additionally segmented by them into two triangular areas. Image information: (a–f) size $2\,\mathrm{nm} \times 2\,\mathrm{nm}$, $V_{\mathrm{stab}} = 100\,\mathrm{mV}$, $I_{\mathrm{stab}} = 4.7\,\mathrm{nA}$, $V_{\mathrm{mod}} = 0.5\,\mathrm{mV}$, $f_{\mathrm{mod}} = 311\,\mathrm{Hz}$, $T_{\mathrm{s}} = 0.4\,\mathrm{K}$

The six constant-height dI/dV maps in Figure S6 are taken in the white box of Figure 3a and at the energies indicated by the dashed lines of Figure 3b of the main text. Although the interpretation of the local variation of the dI/dV-intensity is not straight forward and may certainly be affected by details of the tip apex, it is obvious that the intensity variation in all maps reflects the (3×3) CDW periodicity. The down-pointing triangles generally possess lower intensity and the up-pointing triangles higher intensity, the later varying in lateral intensity distribution as a function of energy.

Magnetic field dependence of the inelastic excitations

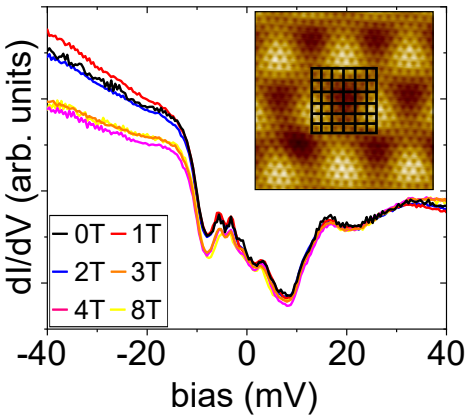

Figure S7: Average spectra at different magnetic field applied normal to the surface, as indicated. Each spectrum in a set of 49 spectra for one magnetic field is taken at a location defined by the grid in the inset. Inset: Constant-current STM topograph of NbS_2. Image information: Inset: size 7 nm × 7 nm, $V_s = 100$ mV, $I_t = 0.7$ nA, $T_s = 1.7$ K. Spectra information: $V_{stab} = 40$ mV, $I_{stab} = 0.7$ nA, $V_{mod} = 0.5$ mV, $f_{mod} = 797$ Hz, $T_s = 0.4$ K.

Figure S7 shows a data set different from the one represented in Figure 3 of the main manuscript. Each point spectrum shown is an average of 49 dI/dV spectra taken on a grid defined by the inset of Figure S7. Again, low energy features within the trough gap are well visible. No change of the average spectra is found as a function of external magnetic field up to 8 T. The somewhat larger dI/dV intensity at negative voltages and fields of 3 T, 4 T and 8 T is presumably a drift effect.

Computational methods

Simulations of metals require a so-called smearing factor for stabilization of the calculations. Here, we use Marzari-Vanderbilt cold smearing.[12] Compared to the Fermi-Dirac distribution with a finite temperature T, this cold smearing has the advantage that the low-temperature behavior (most experimental measurements here were performed at 4 K) can be estimated from electronic structure calculations at larger broadening and therefore sparser Brillouin-

zone sampling. In any case, even using the Fermi-Dirac distribution as the smearing function still disregards thermal motion of the nuclei and therefore overestimates the critical temperature. Furthermore, effects such as hybridization with substrates can have a similar smearing-like influence on lattice instabilities as electronic temperature.[13] In some figures, we show results as a function of the smearing σ to illustrate how stable the results are and as an indication for the influence of temperature. Note that the mentioned smearing values are only used for the structural relaxation, not for the electronic and phononic DOS.

For our downfolding, we consider an effectively noninteracting model with a linearized electron-lattice coupling. Its free energy as a function of atomic displacements reads $F(\boldsymbol{u}) = E^{\mathrm{el}}(\boldsymbol{u}) - TS^{\mathrm{el}}(\boldsymbol{u}) + E^{\mathrm{lat}}(\boldsymbol{u}) + E^{\mathrm{dc}}(\boldsymbol{u})$ with the total single-electron energy E^{el} of the linearized low-energy Kohn-Sham Hamiltonian $H_0^{\mathrm{el}} + \boldsymbol{ud}$, the corresponding generalized entropy S^{el}, as well as the quadratic lattice term E^{lat} and the linear double-counting term E^{dc}, chosen such that the second and first order of the free energy match DFT and density functional perturbation theory (DFPT) for the undistorted system.

The calculations for the undistorted system are done with Quantum ESPRESSO.[14–16] We apply the PBE functional[17] and normconserving pseudopotentials from PseudoDojo[18,19] at an energy cutoff of 100 Ry. A Marzari-Vanderbilt cold smearing[12] of $\sigma_0 = 20\,\mathrm{mRy}$ is combined with uniform 12×12 $\boldsymbol{k}$ and $\boldsymbol{q}$ meshes including Γ. When going to lower values σ on the model level, the number of $\boldsymbol{k}$ points per dimension is scaled by a factor of $\lceil \sigma_0/\sigma \rceil$. Phonon dispersions of the undistorted system for low smearings have been obtained in a computationally efficient way from the data for the highest smearing using the method of Ref. 20, which has proven to yield excellent results for TaS_2.[21] Here, we generalize this method with respect to distorted structures on supercells. To separate periodic images of the monolayer, we choose a unit-cell height $c = 2\,\mathrm{nm}$ and truncate the Coulomb interaction in this direction.[22] The relaxed lattice constant $a = 0.335\,\mathrm{nm}$ is close to the experimental value. The downfolding to the low-energy model in the localized representation of atomic displacements and Wannier orbitals (Nb d_{z^2}, $d_{x^2-y^2}$, and d_{xy}) is accomplished using Wannier90[23] and the

EPW code.[24–26]

Note that including spin-orbit coupling into the calculation leads to a band splitting and thus increases the number of peaks in the DOS. Nevertheless, this does not lead to an explanation of the experimentally observed $\mathrm{d}I/\mathrm{d}V$ spectra.

Generalized free energy

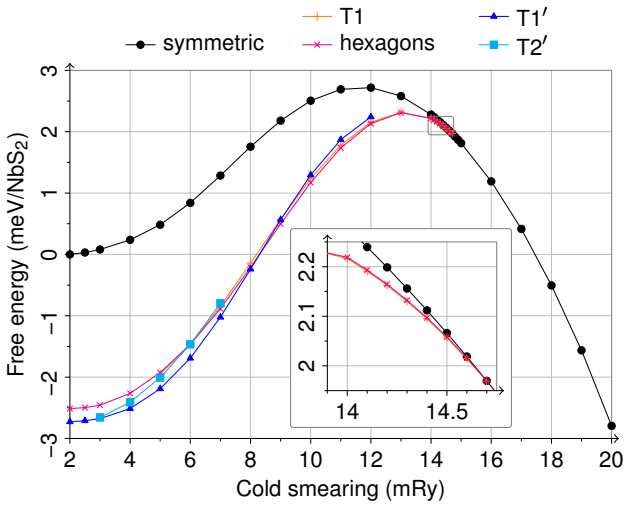

Figure S8: Free energy for different stable (CDW) structures as a function of cold smearing. Inset: Close-up of the region of the phase transition.

Figure S8 shows the generalized free energy for the symmetric and the four distorted phases as a function of cold smearing σ. Here, all colored points correspond to fully relaxed structures. The structure could always be unambiguously classified as one of the four structures shown in the main text, even though the absolute and relative displacements change with the smearing. Below the critical smearing $\sigma_{\mathrm{CDW}} \approx 14.7\,\mathrm{mRy}$, the energy gain from the lattice distortion continuously increases up to about $2.8\,\mathrm{mRy}/\mathrm{NbS_2}$. Here, the energy difference between the different CDW structures is very small, most likely smaller than the expected accuracy of our theoretical approach. Thus, Figure S8 should not be considered the final answer to the question of which CDW structure is observed and we consider all structures in the following. Not all structures are stable at all smearings; “hexagons” and T1 are favored

directly below the CDW transition, T1′ and T2′ for smaller smearings. Only T1 is found for the whole smearing range considered.

Four possible CDW phases

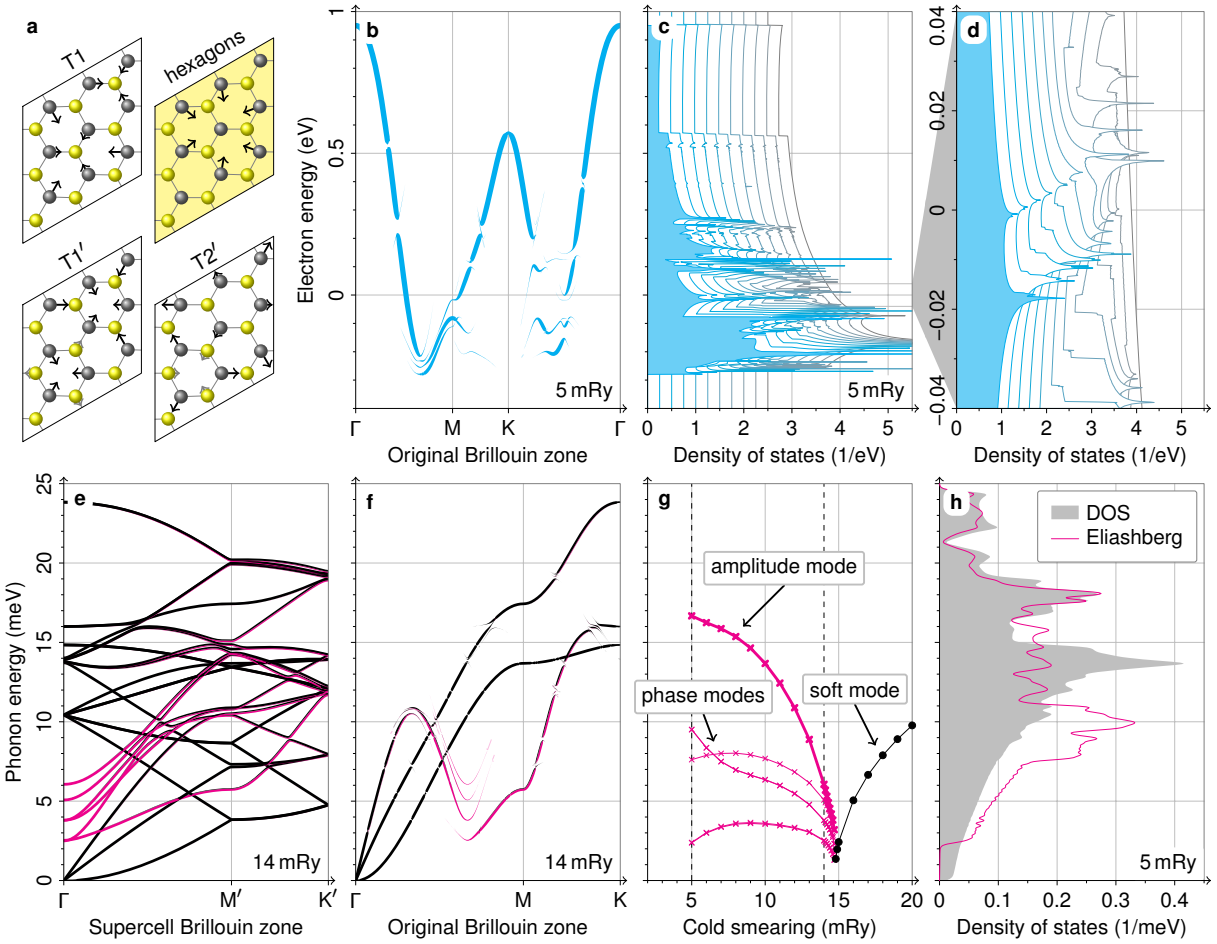

Figure S9: Electronic and phononic properties in the "hexagons" CDW phase, cf. T1 in the main text.

In our calculations, four different CDW phases were stabilized, which we denote as T1, "hexagons", T1′, and T2′.[27] In the main text, we have shown detailed information about the T1 phase. Here, the corresponding results for the other three phases are shown in Figures S9, S10 and S11.

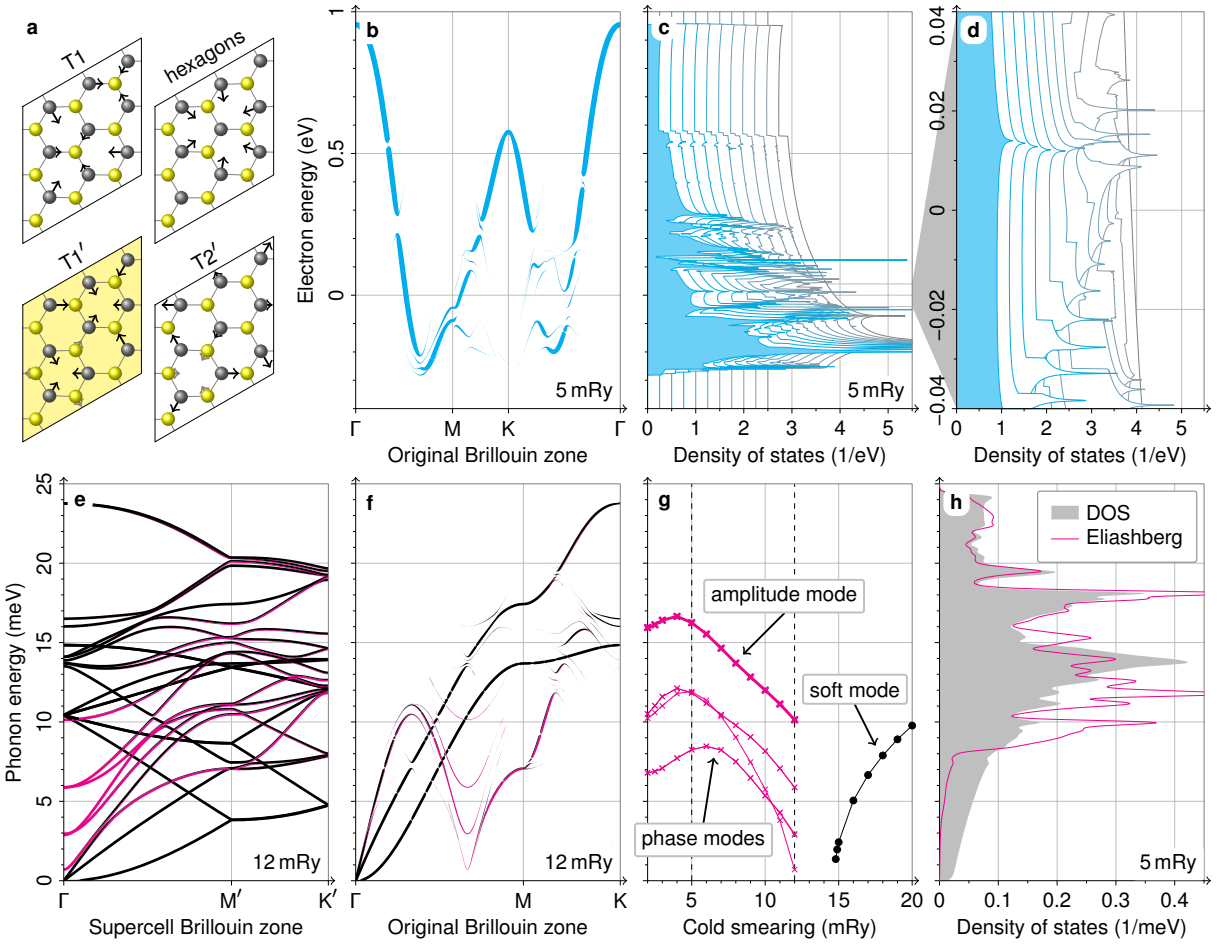

Figure S10: Electronic and phononic properties in the T1′ CDW phase, cf. T1 in the main text.

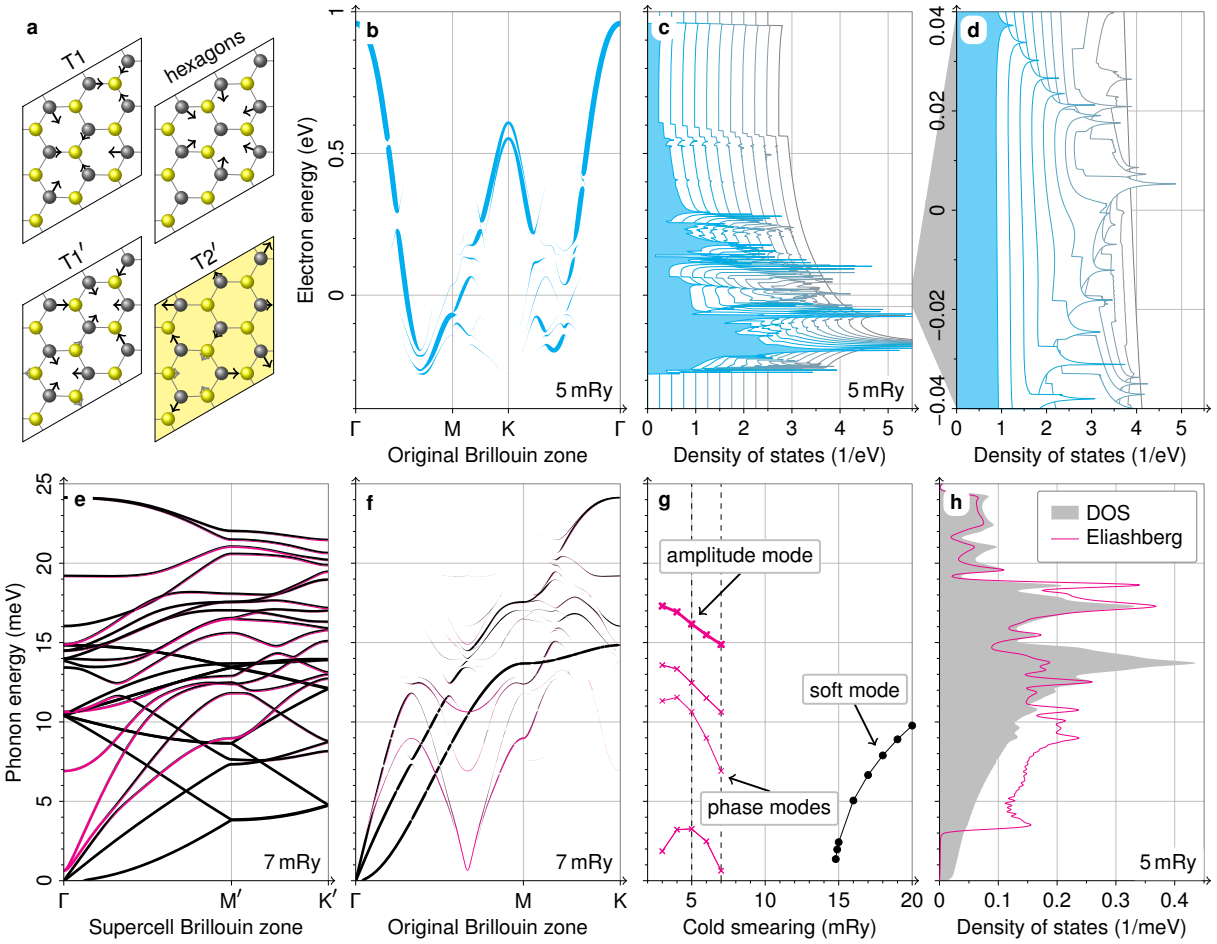

Figure S11: Electronic and phononic properties in the T2′ CDW phase, cf. T1 in the main text.

The electronic band structure and DOS are shown in panels (b–d). For panels (c–d), different displacement amplitudes (with respect to the undistorted structure) are shown, with gray corresponding to the undistorted structure and blue to the fully distorted structure whose band structure is shown in (b). In all cases, the reduction of the symmetry in the distorted phases leads to the appearance of additional bands and additional Van Hove singularities. The position of these Van Hove singularities depends on the displacement, often approximately linearly, and the magnitude of the changes is on the 100 meV scale. Thus, although it is possible to interpret peaks in the experimental STS as Van Hove singularities, fine-tuned parameters are needed to place these peaks at the desired position close to the Fermi level.

Panels (e) and (f) show the phonon dispersions in the supercell and original Brillouin zone, respectively. The magenta marking shows to what extent these phonons correspond to the unstable phonon modes in the undistorted structure. To be more precise, the absolute value squared of the scalar product of the respective displacements determines the fraction of the line that is color magenta. For each plot, the smearing is listed in the bottom right. Panel (g) shows all smearings where the structure can be stabilized and the energies of the phase and amplitude phonons at the Γ point in the supercell as a function of smearing. Figure S11(g) in particular shows that the vanishing energy of one of the phonon modes denotes the end of the stable region in parameter space: at the transition point, a local minimum in the free energy becomes a local maximum. Although their details differ, all four structures have phase and amplitude modes at very similar energy scales of approximately 10 meV. Moving over to panel (h), we show the phononic DOS and the Eliashberg function $\alpha^2F(\omega)$. The amplitude and phase modes at Γ are hardy visible in the phononic DOS, which is dominated by acoustic phonons.

For the formation of polaronic excitations, we need to know both the frequencies at which there are phonons and how strongly these phonons are coupled to the electrons. This can be quantified using the Eliashberg spectral function $\alpha^2F(\omega)$. The electron-phonon coupling

appears squared in this expression since the electron needs to emit and absorb a phonon. The Eliashberg spectral function is shown in panel (h) of the figures. The Eliashberg spectral function has a clear onset at the energy corresponding to the lowest phase mode. This shows that the modes corresponding to the longitudinal-acoustic modes at $\boldsymbol{q} = 2/3\,\overline{\Gamma\mathrm{M}}$ in the undistorted state still dominate the coupling in presence of the CDW, due to their large electron-phonon matrix elements.[28] On the other hand, the phonon DOS itself has contributions all the way down to zero frequency, coming from the acoustic branches, but these are weakly coupled to the electrons and irrelevant for the formation of combined electron-phonon excitations.

References

(1) Hall, J.; Pielić, B.; Murray, C.; Jolie, W.; Wekking, T.; Busse, C.; Kralj, M.; Michely, T. Molecular beam epitaxy of quasi-freestanding transition metal disulphide monolayers on van der Waals substrates: a growth study. *2D Mater.* **2018**, *5*, 025005.

(2) Kaiser, W. J.; Jaklevic, R. C. Spectroscopy of electronic states of metals with a scanning tunneling microscope. *IBM J. Res. Dev.* **1986**, *30*, 411–416.

(3) M. P. Everson, R. C. J., L. C. Davis; Shen, W. Effects of surface features upon the Au(111) surface state local density of states studied with scanning tunneling spectroscopy. *J. Vac. Sci. Technol. B* **1991**, *9*, 891–896.

(4) Feenstra, R.; Stroscio, J. A.; Fein, A. Tunneling spectroscopy of the Si(111)2 × 1 surface. *Surf. Sci.* **1987**, *181*, 295–306.

(5) Tersoff, J.; Hamann, D. R. Theory and Application for the Scanning Tunneling Microscope. *Phys. Rev. Lett.* **1983**, *50*, 1998–2001.

(6) Petersen, L.; Sprunger, P. T.; Hofmann, P.; Lægsgaard, E.; Briner, B. G.; Doering, M.; Rust, H.-P.; Bradshaw, A. M.; Besenbacher, F.; Plummer, E. W. Direct imaging of

the two-dimensional Fermi contour: Fourier-transform STM. *Phys. Rev. B* **1998**, *57*, R6858–R6861.

(7) Crommie, M. F.; Lutz, C. P.; Eigler, D. M. Imaging standing waves in a two-dimensional electron gas. *Nature* **1993**, *363*, 524–527.

(8) Hasegawa, Y.; Avouris, P. Direct observation of standing wave formation at surface steps using scanning tunneling spectroscopy. *Phys. Rev. Lett.* **1993**, *71*, 1071–1074.

(9) Hörmandinger, G. Imaging of the Cu(111) surface state in scanning tunneling microscopy. *Phys. Rev. B* **1994**, *49*, 13897–13905.

(10) Martínez-Galera, A. J.; Schröder, U. A.; Huttmann, F.; Jolie, W.; Craes, F.; Busse, C.; Caciuc, V.; Atodiresei, N.; Blügel, S.; Michely, T. Oxygen orders differently under graphene: new superstructures on Ir(111). *Nanoscale* **2016**, *8*, 1932–1943.

(11) van Efferen, C.; Murray, C.; Fischer, J.; Busse, C.; Komsa, H.-P.; Michely, T.; Jolie, W. Metal-insulator transition in monolayer MoS_2 via contactless chemical doping. *2D Mater.* **2022**, *9*, 025026.

(12) Marzari, N.; Vanderbilt, D.; De Vita, A.; Payne, M. C. Thermal Contraction and Disordering of the Al(110) Surface. *Phys. Rev. Lett.* **1999**, *82*, 3296.

(13) Hall, J. et al. Environmental Control of Charge Density Wave Order in Monolayer 2H-TaS_2. *ACS Nano* **2019**, *13*, 10210–10220.

(14) Giannozzi, P.; others QUANTUM ESPRESSO: A modular and open-source software project for quantum simulations of materials. *J. Phys. Condens. Matter* **2009**, *21*, 395502.

(15) Giannozzi, P.; others Advanced capabilities for materials modelling with QUANTUM ESPRESSO. *J. Phys. Condens. Matter* **2017**, *29*, 465901.

(16) Giannozzi, P.; Baseggio, O.; Bonfà, P.; Brunato, D.; Car, R.; Carnimeo, I.; Cavazzoni, C.; de Gironcoli, S.; Delugas, P.; Ferrari Ruffino, F.; Ferretti, A.; Marzari, N.; Timrov, I.; Urru, A.; Baroni, S. Quantum ESPRESSO toward the exascale. *J. Chem. Phys.* **2020**, *152*, 154105.

(17) Perdew, J. P.; Burke, K.; Ernzerhof, M. Generalized Gradient Approximation Made Simple. *Phys. Rev. Lett.* **1996**, *77*, 3865.

(18) Hamann, D. R. Optimized norm-conserving Vanderbilt pseudopotentials. *Phys. Rev. B* **2013**, *88*, 085117.

(19) van Setten, M. J.; Giantomassi, M.; Bousquet, E.; Verstraete, M. J.; Hamann, D. R.; Gonze, X.; Rignanese, G. M. The PseudoDojo: Training and grading a 85 element optimized norm-conserving pseudopotential table. *Comput. Phys. Commun.* **2018**, *226*, 39.

(20) Calandra, M.; Profeta, G.; Mauri, F. Adiabatic and nonadiabatic phonon dispersion in a Wannier function approach. *Phys. Rev. B* **2010**, *82*, 165111.

(21) Berges, J.; Girotto, N.; Wehling, T.; Marzari, N.; Poncé, S. Phonon self-energy corrections: To screen, or not to screen. https://arxiv.org/abs/2212.11806, 2022.

(22) Sohier, T.; Calandra, M.; Mauri, F. Density functional perturbation theory for gated two-dimensional heterostructures: Theoretical developments and application to flexural phonons in graphene. *Phys. Rev. B* **2017**, *96*, 075448.

(23) Pizzi, G.; others Wannier90 as a community code: New features and applications. *J. Phys. Condens. Matter* **2020**, *32*, 165902.

(24) Giustino, F.; Cohen, M. L.; Louie, S. G. Electron-phonon interaction using Wannier functions. *Phys. Rev. B* **2007**, *76*, 165108.

(25) Noffsinger, J.; Giustino, F.; Malone, B. D.; Park, C.-H.; Louie, S. G.; Cohen, M. L. EPW: A program for calculating the electron–phonon coupling using maximally localized Wannier functions. *Comput. Phys. Commun.* **2010**, *181*, 2140.

(26) Poncé, S.; Margine, E.; Verdi, C.; Giustino, F. EPW: Electron–phonon coupling, transport and superconducting properties using maximally localized Wannier functions. *Comput. Phys. Commun.* **2016**, *209*, 116.

(27) Guster, B.; Rubio-Verdú, C.; Robles, R.; Zaldívar, J.; Dreher, P.; Pruneda, M.; Silva-Guillén, J. A.; Choi, D.-J.; Pascual, J. I.; Ugeda, M. M.; Ordejón, P.; Canadell, E. Coexistence of Elastic Modulations in the Charge Density Wave State of 2H-$NbSe_2$. *Nano Lett.* **2019**, *19*, 3027.

(28) Lian, C.-S. Interplay of charge ordering and superconductivity in two-dimensional 2H group V transition-metal dichalcogenides. *Phys. Rev. B* **2023**, *107*, 045431.

15

Conclusion and outlook

This dissertation focused on the development of downfolded models, which aim to capture the complex intertwined electronic and lattice degrees of freedom. Downfolding, in this context, refers to reducing to the most critical electronic degrees of freedom necessary to describe the relevant physical phenomena of interest. Typically, these critical electronic degrees of freedom reside within the low-energy sector. While this dissertation specifically applies downfolded lattice models to the study of CDWs as an illustrative example of a physical phenomenon, it is important to emphasize that these models possess the capability to describe a broad spectrum of physics beyond CDWs.

In the first publication of this dissertation (see Ch. 11), it was observed that downfolded models can accurately reproduce Born-Oppenheimer potential energy surfaces. This finding was grounded in the simplified and analytically solvable nature of the SSH model. However, this finding may not necessarily apply to real-world systems. Nevertheless, the overarching concept is as follows: The nonlinear response of the low-energy sector to atomic displacements results in anharmonic Born-Oppenheimer potential energy surfaces.

In subsequent research (see Ch. 13), it was demonstrated that these energy surfaces, derived from downfolded lattice models, align with results obtained through DFT calculations. This alignment enables the characterization of anharmonicities, which are inherent in CDWs. Thus, downfolding models can indeed describe CDW physics of real-world materials.

Compared to *ab initio* methods, generating free energy and forces using these models is several orders of magnitude faster, facilitating molecular dynamics simulations on large systems over extended timescales. Molecular dynamics simulations provided access to thermodynamic quantities, such as transition temperatures for structural phase transitions, and will also allow the exploration of vibrational properties, such as temperature-dependent phonon spectra in the future.

In the context of CDWs, it was once more confirmed that real-world materials exhibit more complexity than the simplified Peierls model found in textbooks. Specifically, the notion that a single phonon mode opens a gap in the electronic structure at the Fermi level, leading to an energy gain outweighing the displacement-related energy costs, is overly simplistic. In monolayer 1T-VS_2, both experimental and theoretical investigations revealed that nonlinear mode-mode coupling is necessary to describe the CDW, which results in a complete gap above the Fermi level (see Ch. 12).

Interestingly, another research group with similar team composition published an article asserting a different CDW behavior in 1T-VS_2, which opens a gap at the Fermi level, based on the concept of higher-order Fermi surface nesting. In Chapter 12, it is discussed that the CDWs may appear different initially. Nevertheless, upon comparing the depictions of atomic displacements, the CDWs exhibit striking similarities. Bridging this apparent difference could be achieved through a collaborative

data exchange between the two groups of authors. This illustrates that the work in this dissertation contributes to an ongoing debate in the field of CDW physics.

Furthermore, in the latest publication (see Ch. 14), comprising both experimental and theoretical collaboration, it was definitively established that a CDW exists in monolayer 1H-NbS_2, a matter previously lacking unambiguous confirmation in the literature. This CDW exhibits intriguing features within the electronic gap, attributed to combined electron-phonon quasiparticles. Consequently, this gap is termed unconventional, in contrast to the conventional gap arising from static atomic displacements.

In summary, this dissertation makes a contribution to the field of CDW physics through collaborative efforts encompassing both experimental and theoretical approaches. The theoretical investigations have unveiled intriguing aspects of CDW research, including non-linear mode-mode coupling and unconventional CDW gap behaviors. While the theoretical investigations using *ab initio* methods achieved significant success, the introduction of downfolded lattice models adds another valuable tool for studying the dynamics and thermodynamics of CDWs.

Downfolding models are expected to have a broad impact on materials design, engineering, and dynamic manipulation. By providing a foundational understanding of CDW materials at the atomic level, the creation of new materials with specific electronic and optical properties are enabled. Moreover, this approach opens the door to studying nonlinearly driven systems through computational analysis, where factors such as external electromagnetic fields, lattice configurations, and correlated electrons interact in complex ways.

Looking ahead, the developed downfolding approaches hold potential for investigating the physics of (nonequilibrium) phase transitions involving CDW order [191–199], as well as the interplay of correlations and (dis)ordering [200, 201]. Additionally, these methods offer opportunities to delve into the realm of driven quantum systems [202–204]. This wider range of applications highlights the transformative possibilities of the methodologies outlined in this dissertation.

A

Appendix

A.1. Definitions of electron-phonon coupling matrix elements

In the course of this dissertation different definitions of electron-phonon coupling matrix elements have been used. This section of the appendix should clarify these definitions.

The electron-phonon coupling matrix elements g, used in Eq. (4.13), are defined by

$$g^{(b)}_{\nu n,n'}(\boldsymbol{k},\boldsymbol{q}) = \sum_{\kappa\alpha} \sqrt{\frac{\hbar}{2M_\kappa \omega_{\boldsymbol{q}\nu}}} e^\alpha_\kappa(\boldsymbol{q}\nu) \left\langle n'\boldsymbol{k}+\boldsymbol{q} \left| \frac{\partial V_{\text{ext}}(\boldsymbol{r})}{\partial u^{\alpha_\kappa}(\boldsymbol{q})} \right| n\boldsymbol{k} \right\rangle, \tag{A.1}$$

$$g^{(f)}_{\nu n,n'}(\boldsymbol{k},\boldsymbol{q}) = \sum_{\kappa\alpha} \sqrt{\frac{\hbar}{2M_\kappa \omega_{\boldsymbol{q}\nu}}} e^\alpha_\kappa(\boldsymbol{q}\nu) \left\langle n'\boldsymbol{k}+\boldsymbol{q} \left| \frac{\partial V_{\text{SCF}}(\boldsymbol{r})}{\partial u^{\alpha_\kappa}(\boldsymbol{q})} \right| n\boldsymbol{k} \right\rangle, \tag{A.2}$$

which can be found in Eq. (14) of Ref. [80] and which is almost identical to the definition of Eq. (5.8), except that $\hbar := 1$.

Meanwhile the electron-phonon coupling matrix elements $\tilde{g}$, used for the diagrammatic expression in Eq. (4.14), are defined by

$$\tilde{g}^b_{\boldsymbol{q}\kappa\alpha\boldsymbol{k}mn} = \frac{1}{\sqrt{M_\kappa}} \langle \boldsymbol{k}+\boldsymbol{q}m | \frac{\partial V_{\text{ext}}}{\partial u_{\boldsymbol{q}\kappa\alpha}} | \boldsymbol{k}n \rangle, \tag{A.3}$$

$$\tilde{g}_{\boldsymbol{q}\kappa\alpha\boldsymbol{k}mn} = \frac{1}{\sqrt{M_\kappa}} \langle \boldsymbol{k}+\boldsymbol{q}m | \frac{\partial V_{\text{SCF}}}{\partial u_{\boldsymbol{q}\kappa\alpha}} | \boldsymbol{k}n \rangle, \tag{A.4}$$

which can be found in Eq. (12) of Ref. [81].

A.2. Determining the occupation of the state $|\alpha\rangle$

For the Hartree term, the occupation of the orbital α is needed, which is written as

$$n_\alpha = \langle c^\dagger_\alpha c_\alpha \rangle_{\text{MF}}. \tag{A.5}$$

According to Ref. [205], the ensemble average is given by

$$\langle A \rangle = \sum_i p_i \langle \psi_i | A | \psi_i \rangle, \tag{A.6}$$

which means that the classical ensemble average is determined by the quantum mechanical expectation value weighted with the probability p_i. This occupation can expressed in terms of the occupations of eigenvalues $|n\boldsymbol{k}\rangle$. First, it is necessary to diagonalize the non-interacting Hamiltonian

$$H_{NI}|\psi_{n\boldsymbol{k}}\rangle = \varepsilon_{n\boldsymbol{k}}|\psi_{n\boldsymbol{k}}\rangle \tag{A.7}$$

to obtain the eigenfunctions $|\psi_{n\boldsymbol{k}}\rangle$ and eigenvalues $\varepsilon_{n\boldsymbol{k}}$. Next, these eigenfunctions are represented in the orbital basis

$$|\psi_{n\boldsymbol{k}}\rangle = \sum_{\alpha} \varphi^{\alpha}_{n\boldsymbol{k}}|\alpha\rangle. \tag{A.8}$$

Finally, the occupation of the orbital α is given by

$$\begin{aligned} n_\alpha = \langle c^\dagger_\alpha c_\alpha\rangle_{\mathrm{MF}} &= \sum_{n\boldsymbol{k}} \langle\psi_{n\boldsymbol{k}}|c^\dagger_\alpha c_\alpha|\psi_{n\boldsymbol{k}}\rangle f(\varepsilon_{n\boldsymbol{k}}) && \text{(A.9)}\\ &= \sum_{n\boldsymbol{k}} \left\langle \langle\beta| \sum_{\beta} \varphi^{\beta}_{n\boldsymbol{k}}|c^\dagger_\alpha c_\alpha| \sum_{\gamma} \varphi^{\gamma}_{n\boldsymbol{k}}|\gamma\rangle \right\rangle f(\varepsilon_{n\boldsymbol{k}}) && \text{(A.10)}\\ &= \sum_{n\boldsymbol{k}} \sum_{\beta} \sum_{\gamma} (\varphi^{\beta}_{n\boldsymbol{k}})^* \varphi^{\gamma}_{n\boldsymbol{k}} \underbrace{\langle\beta|c^\dagger_\alpha c_\alpha|\gamma\rangle}_{=\delta_{\alpha\beta}\delta_{\alpha\gamma}} f(\varepsilon_{n\boldsymbol{k}}) && \text{(A.11)}\\ &= \sum_{n\boldsymbol{k}} |\varphi^{\alpha}_{n\boldsymbol{k}})|^2 f(\varepsilon_{n\boldsymbol{k}}). && \text{(A.12)} \end{aligned}$$

A.3. Computational details of incorporated figures

A.3.1. Figure 3.1

The DFT calculations were performed using Quantum ESPRESSO [68, 206]. Uniform meshes 6×6 $\boldsymbol{k}$ points are combined with a Fermi–Dirac smearing of 157.8 K. For a fixed unit-cell height of 15 Å, minimizing forces and in-plane pressure to below $1 \cdot 10^{-5}$ Ry/Bohr and 0.1 kbar yields a lattice constant of 3.39 Å

A.3.2. Figure 4.1

The DFT and DFPT calculations are carried out using Quantum ESPRESSO [68, 206]. The modification that is required for cDFPT is described in detail in Ref. [49]. For the transformation of the electronic energies and electron-phonon couplings to the Wannier basis, we use Wannier90 [207] and the EPW code [208, 209]. The calculation of the phonon self-energies was done with `elphmod` [210].

Acknowledgement

This dissertation reflects my individual effort, but its realization has been a collaborative endeavor involving numerous individuals. In this section, I extend my gratitude to those whose contributions have been instrumental.
Foremost, I acknowledge Tim Wehling, whose visionary conception of this project years ago laid its foundations. His commitment and systematic pursuit of this path have been a major motivation for me.
I express my appreciation to Erik van Loon for creating the design of the initial paper and for his ongoing contributions to all subsequent publications. His insights into the diagrammatic theory and invaluable input in advancing downfolded models have significantly boosted the project. Sergey Brener's involvement in the diagrammatic theory, particularly in incorporating the Coulomb interaction into the models, deserves sincere acknowledgment.
Special thanks go to Mariana Rossi for serving as the second referee and introducing me to molecular dynamics simulations. Her guidance has granted the downfolded models access to thermodynamic quantities. Mariana's enthusiasm for the work and her unwavering support have been a constant source of motivation.
I owe a debt of gratitude to Jan Berges, my predecessor in this project, whose work laid the essential foundation for downfolded models. His expertise in *ab initio* electron-phonon coupling and the development of the fluctuation diagnostics method provided invaluable insights. Jan's introduction to the elphmod code, alongside his guidance through the complexities of physics, was indispensable throughout my PhD journey.
The collaborative efforts with colleagues in Thomas Michely's group in Cologne have been fruitful and merit recognition.
For their proofreading of this thesis, I extend my thanks to Edin Kapetanovic and Jan Berges.
I am grateful to Sarah-Jane Farley and Anna Zharinova for their assistance in navigating organizational and office-related challenges.
Acknowledgment is due to my colleagues – Gautam Rai, Michael Winter, Lennart Klebl, Roberto Mozara, Michael Sentef, Niklas Witt, and Siheon Ryee – for their support in both organizational and physics-related matters.
I am happy that Laura Pätzold continues the trajectory of developing and applying downfolded lattice models.
The results presented in this dissertation and its publications were facilitated by open-source software packages, including Quantum Espresso, Wannier90, EPW, RESPACK, i-Pi, and elphmod. I am grateful to the developers for making these codes available.
Financial support for my PhD phase was provided by the DFG. I am privileged to be compensated for engaging in research, a full-time commitment that requires significant investment. I appreciate the enabling environment for research in Germany and hope for its continuation.
I extend my gratitude to my family. My parents, Karin Krull and Tido Schobert, supported me during my studies and always helped me in time of needs.
Finally, I express gratitude to my wife, Mareka Dirksen, who has been a motivating force during challenging times and a stabilizing presence during moments of stress. I am thankful for sharing this journey with her and I am excited what the future may hold for us.

References

[1] K. Rossnagel. "On the origin of charge-density waves in select layered transition-metal dichalcogenides". In: *J. Phys. Condens. Matter* 23 (2011), p. 213001. DOI: 10.1088/0953-8984/23/21/213001.

[2] Y. Kamihara et al. "Iron-Based Layered Superconductor La[O1-xFx]FeAs (x = 0.05–0.12) with T_c = 26 K". In: *Journal of the American Chemical Society* 130 (2008), pp. 3296–3297. DOI: 10.1021/ja800073m.

[3] M. Imada, A. Fujimori, and Y. Tokura. "Metal-insulator transitions". In: *Rev. Mod. Phys.* 70 (1998), p. 1039. DOI: 10.1103/RevModPhys.70.1039.

[4] R. M. Bozorth. "Magnetism". In: *Rev. Mod. Phys.* 19 (1947), pp. 29–86. DOI: 10.1103/RevModPhys.19.29.

[5] B. M. Richard Van Noorden and R. Nuzzo. "The top 100 papers: Nature explores the most-cited research of all time." In: *Nature* 514 (2014), pp. 550–553. URL: https://www.nature.com/news/the-top-100-papers-1.16224.

[6] A. Migliore. "How To Extract Quantitative Information on Electronic Transitions from the Density Functional Theory "Black Box"". In: *Journal of Chemical Theory and Computation* 15 (2019), pp. 4915–4923. DOI: 10.1021/acs.jctc.9b00518.

[7] S. Andermatt et al. "Combining Linear-Scaling DFT with Subsystem DFT in Born–Oppenheimer and Ehrenfest Molecular Dynamics Simulations: From Molecules to a Virus in Solution". In: *Journal of Chemical Theory and Computation* 12 (2016), pp. 3214–3227. DOI: 10.1021/acs.jctc.6b00398.

[8] E. Pavarini. "Solving the strong-correlation problem in materials". In: *La Rivista del Nuovo Cimento* 44 (2021), pp. 597–640. DOI: 10.1007/s40766-021-00025-8.

[9] M. W. Finnis et al. "Interatomic forces in transition metals". In: *Philos. Mag. A* 58 (1988), p. 143. DOI: 10.1080/01418618808205180.

[10] C. L. Brooks. "Computer simulation of liquids". In: *J. Solution Chem.* 18 (1989), p. 99. DOI: 10.1007/BF00646086.

[11] C. Z. Wang, C. T. Chan, and K. M. Ho. "Empirical tight-binding force model for molecular-dynamics simulation of Si". In: *Phys. Rev. B* 39 (1989), p. 8586. DOI: 10.1103/PhysRevB.39.8586.

[12] L. Goodwin, A. J. Skinner, and D. G. Pettifor. "Generating Transferable Tight-Binding Parameters: Application to Silicon". In: *EPL* 9 (1989), p. 701. DOI: 10.1209/0295-5075/9/7/015.

[13] O. F. Sankey and D. J. Niklewski. "Ab initio multicenter tight-binding model for molecular-dynamics simulations and other applications in covalent systems". In: *Phys. Rev. B* 40 (1989), p. 3979. DOI: 10.1103/PhysRevB.40.3979.

[14] K. Laasonen and R. M. Nieminen. “Molecular dynamics using the tight-binding approximation”. In: *J. Phys. Condens. Matter* 2 (1990), p. 1509. DOI: 10.1088/0953-8984/2/6/010.

[15] R. Virkkunen, K. Laasonen, and R. M. Nieminen. “Molecular dynamics using the tight-binding approximation: Application to liquid silicon”. In: *J. Phys. Condens. Matter* 3 (1991), p. 7455. DOI: 10.1088/0953-8984/3/38/017.

[16] C. Z. Wang, C. T. Chan, and K. M. Ho. “Tight-binding molecular-dynamics study of liquid Si”. In: *Phys. Rev. B* 45 (1992), p. 12227. DOI: 10.1103/PhysRevB.45.12227.

[17] C. Molteni, L. Colombo, and L. Miglio. “Structural Properties of Liquid and Amorphous GaAs by Tight-Binding Molecular Dynamics”. In: *EPL* 24 (1993), p. 659. DOI: 10.1209/0295-5075/24/8/007.

[18] Y. P. Feng et al. “Tight-binding molecular dynamics simulations of semiconductor alloys: Clusters, surfaces, and defects”. In: *J. Phys. Condens. Matter* 9 (1997), p. 4345. DOI: 10.1088/0953-8984/9/21/003.

[19] C.-C. Fu and M. Weissmann. “Tight-binding molecular-dynamics study of amorphous carbon deposits over silicon surfaces”. In: *Phys. Rev. B* 60 (1999), p. 2762. DOI: 10.1103/PhysRevB.60.2762.

[20] J. P. Lewis et al. “Advances and applications in the FIREBALL ab initio tight-binding molecular-dynamics formalism”. In: *Phys. Status Solidi B* 248 (2011), p. 1989. DOI: 10.1002/pssb.201147259.

[21] Z. H. He, X. B. Ye, and B. C. Pan. “Linear scaling algorithm for tight-binding molecular dynamics simulations”. In: *J. Chem. Phys.* 150 (2019), p. 114107. DOI: 10.1063/1.5088918.

[22] M. O’Donovan et al. “From atomistic tight-binding theory to macroscale drift–diffusion: Multiscale modeling and numerical simulation of uni-polar charge transport in (In,Ga)N devices with random fluctuations”. In: *Journal of Applied Physics* 130 (2021), p. 065702. DOI: 10.1063/5.0059014.

[23] A. P. Bartók et al. “Gaussian Approximation Potentials: The Accuracy of Quantum Mechanics, without the Electrons”. In: *Phys. Rev. Lett.* 104 (2010), p. 136403. DOI: 10.1103/PhysRevLett.104.136403.

[24] J. Finkelstein et al. “Quantum-Based Molecular Dynamics Simulations Using Tensor Cores”. In: *J. Chem. Theory Comput.* 17 (2021), p. 6180. DOI: 10.1021/acs.jctc.1c00726.

[25] V. L. Deringer et al. “Gaussian Process Regression for Materials and Molecules”. In: *Chem. Rev.* 121 (2021), p. 10073. DOI: 10.1021/acs.chemrev.1c00022.

[26] Z. Wang et al. “All-Atom Nonadiabatic Dynamics Simulation of Hybrid Graphene Nanoribbons Based on Wannier Analysis and Machine Learning”. In: *ACS Appl. Mater. Interfaces* 14 (2022), p. 22929. DOI: 10.1021/acsami.1c22181.

[27] C. Cheng, S. Zhang, and G.-W. Chern. “Machine learning for phase ordering dynamics of charge density waves”. 2023. arXiv: 2303.03493.

[28] W. M. C. Foulkes and R. Haydock. “Tight-binding models and density-functional theory”. In: *Phys. Rev. B* 39 (1989), p. 12520. DOI: 10.1103/PhysRevB.39.12520.

[29] D. Porezag et al. “Construction of tight-binding-like potentials on the basis of density-functional theory: Application to carbon”. In: *Phys. Rev. B* 51 (1995), p. 12947. DOI: 10.1103/PhysRevB.51.12947.

[30] M. Elstner et al. “Self-consistent-charge density-functional tight-binding method for simulations of complex materials properties”. In: *Phys. Rev. B* 58 (1998), p. 7260. DOI: 10.1103/PhysRevB.58.7260.

[31] B. Aradi, B. Hourahine, and T. Frauenheim. “DFTB+, a Sparse Matrix-Based Implementation of the DFTB Method”. In: *J. Phys. Chem. A* 111 (2007), p. 5678. DOI: 10.1021/jp070186p.

[32] P. García-Fernández et al. “Second-principles method for materials simulations including electron and lattice degrees of freedom”. In: *Phys. Rev. B* 93 (2016), p. 195137. DOI: 10.1103/PhysRevB.93.195137.

[33] Y. Nishimura and H. Nakai. “Dcdftbmd: Divide-and-Conquer Density Functional Tight-Binding Program for Huge-System Quantum Mechanical Molecular Dynamics Simulations”. In: *J. Comput. Chem.* 40 (2019), p. 1538. DOI: 10.1002/jcc.25804.

[34] B. Hourahine et al. “DFTB+, a software package for efficient approximate density functional theory based atomistic simulations”. In: *J. Chem. Phys.* 152 (2020), p. 124101. DOI: 10.1063/1.5143190.

[35] A. M. N. Niklasson. “Density-Matrix Based Extended Lagrangian Born–Oppenheimer Molecular Dynamics”. In: *J. Chem. Theory Comput.* 16 (2020), p. 3628. DOI: 10.1021/acs.jctc.0c00264.

[36] L. Zhang et al. “Equivariant analytical mapping of first principles Hamiltonians to accurate and transferable materials models”. In: *npj Comput. Mater.* 8 (2022), p. 1. DOI: 10.1038/s41524-022-00843-2.

[37] T. Misawa and M. Imada. “Superconductivity and its mechanism in an ab initio model for electron-doped LaFeAsO”. In: *Nature Communications* 5 (2014), p. 5738. DOI: 10.1038/ncomms6738.

[38] N. Witt et al. *No superconductivity in $Pb_9Cu_1(PO_4)_6O$ found in orbital and spin fluctuation exchange calculations*. 2023. arXiv: 2308.07261.

[39] J. Berges et al. “Ab initio phonon self-energies and fluctuation diagnostics of phonon anomalies: Lattice instabilities from Dirac pseudospin physics in transition metal dichalcogenides”. In: *Phys. Rev. B* 101 (2020), p. 155107. DOI: 10.1103/PhysRevB.101.155107.

[40] F. Aryasetiawan and F. Nilsson. *Downfolding Methods in Many-Electron Theory*. AIP Publishing LLC, 2022. URL: https://aip.scitation.org/doi/10.1063/9780735422490.

[41] T. Fujiwara, S. Yamamoto, and Y. Ishii. “Generalization of the Iterative Perturbation Theory and Metal–Insulator Transition in Multi-Orbital Hubbard Bands”. In: *J. Phys. Soc. Jpn.* 72 (2003), p. 777. DOI: 10.1143/JPSJ.72.777.

[42] F. Aryasetiawan et al. “Frequency-dependent local interactions and low-energy effective models from electronic structure calculations”. In: *Phys. Rev. B* 70 (2004), p. 195104. DOI: 10.1103/PhysRevB.70.195104.

[43] F. Aryasetiawan et al. “Calculations of Hubbard U from first-principles”. In: *Phys. Rev. B* 74 (2006), p. 125106. DOI: 10.1103/PhysRevB.74.125106.

[44] K. Nakamura, R. Arita, and M. Imada. “Ab initio Derivation of Low-Energy Model for Iron-Based Superconductors LaFeAsO and LaFePO”. In: *J. Phys. Soc. Jpn.* 77 (2008), p. 093711. DOI: 10.1143/JPSJ.77.093711.

[45] Y. Nohara, S. Yamamoto, and T. Fujiwara. “Electronic structure of perovskite-type transition metal oxides $LaMO_3$ (M=Ti∼Cu) by U+GW approximation”. In: *Phys. Rev. B* 79 (2009), p. 195110. DOI: 10.1103/PhysRevB.79.195110.

[46] K. Nakamura et al. “Ab initio Derivation of Low-Energy Model for κ-ET Type Organic Conductors”. In: *J. Phys. Soc. Jpn.* 78 (2009), p. 083710. DOI: 10.1143/JPSJ.78.083710.

[47] K. Nakamura et al. “Ab initio *GW* plus cumulant calculation for isolated band systems: Application to organic conductor $TMTSF_2PF_6$ and transition-metal oxide $SrVO_3$”. In: *Phys. Rev. B* 93 (2016), p. 085124. DOI: 10.1103/PhysRevB.93.085124.

[48] G. Giovannetti et al. “Downfolding electron-phonon Hamiltonians from ab initio calculations: Application to K_3 picene”. In: *Phys. Rev. B* 90 (2014), p. 115435. DOI: 10.1103/PhysRevB.90.115435.

[49] Y. Nomura and R. Arita. “Ab initio downfolding for electron-phonon-coupled systems: Constrained density-functional perturbation theory”. In: *Phys. Rev. B* 92 (2015), p. 245108. DOI: 10.1103/PhysRevB.92.245108.

[50] Y. Nomura et al. “Exotics-wave superconductivity in alkali-doped fullerides”. In: *J. Phys. Condens. Matter* 28 (2016), p. 153001. DOI: 10.1088/0953-8984/28/15/153001.

[51] E. G. C. P. van Loon, J. Berges, and T. O. Wehling. “Downfolding approaches to electron-ion coupling: Constrained density-functional perturbation theory for molecules”. In: *Phys. Rev. B* 103 (2021), p. 205103. DOI: 10.1103/PhysRevB.103.205103.

[52] M. Kinza and C. Honerkamp. “Low-energy effective interactions beyond the constrained random-phase approximation by the functional renormalization group”. In: *Phys. Rev. B* 92 (2015), p. 045113. DOI: 10.1103/PhysRevB.92.045113.

[53] C. Honerkamp. “Efficient vertex parametrization for the constrained functional renormalization group for effective low-energy interactions in multiband systems”. In: *Phys. Rev. B* 98 (2018), p. 155132. DOI: 10.1103/PhysRevB.98.155132.

[54] X.-J. Han, P. Werner, and C. Honerkamp. “Investigation of the effective interactions for the Emery model by the constrained random-phase approximation and constrained functional renormalization group”. In: *Phys. Rev. B* 103 (2021), p. 125130. DOI: 10.1103/PhysRevB.103.125130.

[55] D. L. Duong et al. “Raman Characterization of the Charge Density Wave Phase of 1T-$TiSe_2$: From Bulk to Atomically Thin Layers”. In: *ACS Nano* 11 (2017), pp. 1034–1040. DOI: 10.1021/acsnano.6b07737.

[56] J. Hall et al. “Environmental Control of Charge Density Wave Order in Monolayer 2H-TaS_2”. In: *ACS Nano* 13 (2019), p. 10210. DOI: 10.1021/acsnano.9b03419.

[57] M. Rösner, S. Haas, and T. O. Wehling. "Phase diagram of electron-doped dichalcogenides". In: *Phys. Rev. B* 90 (2014), p. 245105. DOI: 10.1103/PhysRevB.90.245105.

[58] M. Born and R. Oppenheimer. "Zur Quantentheorie der Molekeln". In: *Ann. Phys.* 389 (1927), p. 457. DOI: 10.1002/andp.19273892002.

[59] G. Czycholl. *Solid State Theory, Volume 1*. 1st ed. Berlin: Springer Berlin, Heidelberg, 2023. DOI: https://doi.org/10.1007/978-3-662-66135-2.

[60] P. Hohenberg and W. Kohn. "Inhomogeneous Electron Gas". In: *Phys. Rev.* 136 (1964), B864. DOI: 10.1103/PhysRev.136.B864.

[61] W. Kohn and L. J. Sham. "Self-Consistent Equations Including Exchange and Correlation Effects". In: *Phys. Rev.* 140 (1965), A1133–A1138. DOI: 10.1103/PhysRev.140.A1133.

[62] D. Rappoport et al. "Approximate Density Functionals: Which Should I Choose?" In: *Encyclopedia of Inorganic Chemistry*. John Wiley & Sons, Ltd, 2009. DOI: https://doi.org/10.1002/0470862106.ia615.

[63] D. C. Langreth and M. J. Mehl. "Beyond the local-density approximation in calculations of ground-state electronic properties". In: *Phys. Rev. B* 28 (1983), pp. 1809–1834. DOI: 10.1103/PhysRevB.28.1809.

[64] J. P. Perdew et al. "Atoms, molecules, solids, and surfaces: Applications of the generalized gradient approximation for exchange and correlation". In: *Phys. Rev. B* 46 (1992), pp. 6671–6687. DOI: 10.1103/PhysRevB.46.6671.

[65] J. P. Perdew, K. Burke, and M. Ernzerhof. "Generalized Gradient Approximation Made Simple". In: *Phys. Rev. Lett.* 77 (1996), p. 3865. DOI: 10.1103/PhysRevLett.77.3865.

[66] J. P. Perdew, K. Burke, and M. Ernzerhof. "Generalized Gradient Approximation Made Simple [Phys. Rev. Lett. 77, 3865 (1996)]". In: *Phys. Rev. Lett.* 78 (1997), 1396(E). URL: https://doi.org/10.1103/PhysRevLett.78.1396.

[67] J. P. Perdew and K. Schmidt. "Jacob's ladder of density functional approximations for the exchange-correlation energy". In: *AIP Conference Proceedings* 577 (2001), pp. 1–20. DOI: 10.1063/1.1390175.

[68] P. Giannozzi et al. "QUANTUM ESPRESSO: A modular and open-source software project for quantum simulations of materials". In: *J. Phys. Condens. Matter* 21 (2009), p. 395502. DOI: 10.1088/0953-8984/21/39/395502.

[69] C. Herring. "A New Method for Calculating Wave Functions in Crystals". In: *Phys. Rev.* 57 (1940), pp. 1169–1177. DOI: 10.1103/PhysRev.57.1169.

[70] F. Herman and J. Callaway. "Electronic Structure of the Germanium Crystal". In: *Phys. Rev.* 89 (1953), pp. 518–519. DOI: 10.1103/PhysRev.89.518.2.

[71] S. Goedecker, M. Teter, and J. Hutter. "Separable dual-space Gaussian pseudopotentials". In: *Phys. Rev. B* 54 (1996), p. 1703. DOI: 10.1103/PhysRevB.54.1703.

[72] C. Hartwigsen, S. Goedecker, and J. Hutter. "Relativistic separable dual-space Gaussian pseudopotentials from H to Rn". In: *Phys. Rev. B* 58 (1998), p. 3641. DOI: 10.1103/PhysRevB.58.3641.

[73] D. Vanderbilt. "Soft self-consistent pseudopotentials in a generalized eigenvalue formalism". In: *Phys. Rev. B* 41 (1990), p. 7892. DOI: 10.1103/PhysRevB.41.7892.

[74] D. R. Hamann. "Optimized norm-conserving Vanderbilt pseudopotentials". In: *Phys. Rev. B* 88 (2013), p. 085117. DOI: 10.1103/PhysRevB.88.085117.

[75] D. R. Hamann, M. Schlüter, and C. Chiang. "Norm-Conserving Pseudopotentials". In: *Phys. Rev. Lett.* 43 (1979), pp. 1494–1497. DOI: 10.1103/PhysRevLett.43.1494.

[76] M. J. van Setten et al. "The PseudoDojo: Training and grading a 85 element optimized norm-conserving pseudopotential table". In: *Comput. Phys. Commun.* 226 (2018), p. 39. DOI: 10.1016/j.cpc.2018.01.012.

[77] N. Marzari et al. "Maximally localized Wannier functions: Theory and applications". In: *Rev. Mod. Phys.* 84 (2012), pp. 1419–1475. DOI: 10.1103/RevModPhys.84.1419.

[78] G. H. Wannier. "The Structure of Electronic Excitation Levels in Insulating Crystals". In: *Phys. Rev.* 52 (1937), pp. 191–197. DOI: 10.1103/PhysRev.52.191.

[79] S. Baroni et al. "Phonons and related crystal properties from density-functional perturbation theory". In: *Rev. Mod. Phys.* 73 (2001), p. 515. DOI: 10.1103/RevModPhys.73.515.

[80] Y. Nomura and R. Arita. "Ab initio downfolding for electron-phonon-coupled systems: Constrained density-functional perturbation theory". In: *Phys. Rev. B* 92 (2015), p. 245108. DOI: 10.1103/PhysRevB.92.245108.

[81] J. Berges et al. "Phonon Self-Energy Corrections: To Screen, or Not to Screen". In: *Phys. Rev. X* 13 (2023), p. 041009. DOI: 10.1103/PhysRevX.13.041009.

[82] J. Berges. *Many-body instabilities in two-dimensional materials*. 2020. DOI: 10.26092/elib/250.

[83] J. E. Inglesfield. "Bonding and phase transitions in transition metal dichalcogenide layer compounds". In: *Journal of Physics C: Solid State Physics* 13 (1980), p. 17. DOI: 10.1088/0022-3719/13/1/007.

[84] K. Motizuki. *Structural Phase Transitions in Layered Transition Metal Compounds*. 1st ed. Dordrecht: Springer Dordrecht, 1986. DOI: https://doi.org/10.1007/978-94-009-4576-0.

[85] F. Giustino. "Electron-phonon interactions from first principles". In: *Rev. Mod. Phys.* 89 (2017), p. 015003. DOI: 10.1103/RevModPhys.89.015003.

[86] F. Giustino, M. L. Cohen, and S. G. Louie. "Electron-phonon interaction using Wannier functions". In: *Phys. Rev. B* 76 (2007), p. 165108. DOI: 10.1103/PhysRevB.76.165108.

[87] M. Rösner. *Electronic Structure of Novel Two-dimensional Materials and Graphene Heterostructures*. 2016.

[88] H. Bruus et al. *Many-Body Quantum Theory in Condensed Matter Physics: An Introduction*. Oxford Graduate Texts. OUP Oxford, 2004. ISBN: 9780198566335.

[89] G. Mahan. *Many-Particle Physics*. Physics of Solids and Liquids. Springer US, 1990. ISBN: 9780306434235.

[90] X. Ren et al. "Random-phase approximation and its applications in computational chemistry and materials science". In: *Journal of Materials Science* 47 (2012), pp. 7447–7471. DOI: 10.1007/s10853-012-6570-4.

[91] G. P. Chen et al. "Random-Phase Approximation Methods". In: *Annual Review of Physical Chemistry* 68 (2017), pp. 421–445. DOI: 10.1146/annurev-physchem-040215-112308.

[92] D. Bohm and D. Pines. "A Collective Description of Electron Interactions. I. Magnetic Interactions". In: *Phys. Rev.* 82 (1951), pp. 625–634. DOI: 10.1103/PhysRev.82.625.

[93] D. Bohm and D. Pines. "A Collective Description of Electron Interactions: III. Coulomb Interactions in a Degenerate Electron Gas". In: *Phys. Rev.* 92 (1953), pp. 609–625. DOI: 10.1103/PhysRev.92.609.

[94] J. Hubbard and R. E. Peierls. "The description of collective motions in terms of many-body perturbation theory". In: *Proceedings of the Royal Society of London. Series A. Mathematical and Physical Sciences* 240 (1957), pp. 539–560. DOI: 10.1098/rspa.1957.0106.

[95] M. Gell-Mann and K. A. Brueckner. "Correlation Energy of an Electron Gas at High Density". In: *Phys. Rev.* 106 (1957), pp. 364–368. DOI: 10.1103/PhysRev.106.364.

[96] H. Ehrenreich and M. H. Cohen. "Self-Consistent Field Approach to the Many-Electron Problem". In: *Phys. Rev.* 115 (1959), pp. 786–790. DOI: 10.1103/PhysRev.115.786.

[97] G. Onida, L. Reining, and A. Rubio. "Electronic excitations: density-functional versus many-body Green's-function approaches". In: *Rev. Mod. Phys.* 74 (2002), pp. 601–659. DOI: 10.1103/RevModPhys.74.601.

[98] S. L. Adler. "Quantum Theory of the Dielectric Constant in Real Solids". In: *Phys. Rev.* 126 (1962), pp. 413–420. DOI: 10.1103/PhysRev.126.413.

[99] N. Wiser. "Dielectric Constant with Local Field Effects Included". In: *Phys. Rev.* 129 (1963), pp. 62–69. DOI: 10.1103/PhysRev.129.62.

[100] N. Marzari. *Ab-initio Molecular Dynamics for Metallic Systems*. 1996. URL: http://theossrv1.epfl.ch/Main/Theses.

[101] M. M. Melander et al. "Grand-canonical approach to density functional theory of electrocatalytic systems: Thermodynamics of solid-liquid interfaces at constant ion and electrode potentials". In: *The Journal of Chemical Physics* 150 (2018), p. 041706. DOI: 10.1063/1.5047829.

[102] M. Tuckerman. *Statistical Mechanics: Theory and Molecular Simulation*. Oxford Graduate Texts. OUP Oxford, 2010. ISBN: 9780191523465.

[103] J. P. Sethna. "139Free energies". In: *Statistical Mechanics: Entropy, Order Parameters, and Complexity*. Oxford University Press, Jan. 2021. ISBN: 9780198865247. DOI: 10.1093/oso/9780198865247.003.0006.

[104] R. N. Barnett et al. “Born–Oppenheimer dynamics using density-functional theory: Equilibrium and fragmentation of small sodium clusters”. In: *The Journal of Chemical Physics* 94 (1991), pp. 608–616. DOI: 10.1063/1.460327.

[105] R. M. Wentzcovitch and J. Martins. “First principles molecular dynamics of Li: Test of a new algorithm”. In: *Solid State Communications* 78 (1991), pp. 831–834. DOI: https://doi.org/10.1016/0038-1098(91)90629-A.

[106] R. Car and M. Parrinello. “Unified Approach for Molecular Dynamics and Density-Functional Theory”. In: *Phys. Rev. Lett.* 55 (1985), pp. 2471–2474. DOI: 10.1103/PhysRevLett.55.2471.

[107] T. D. Kühne et al. “Efficient and Accurate Car-Parrinello-like Approach to Born-Oppenheimer Molecular Dynamics”. In: *Phys. Rev. Lett.* 98 (2007), p. 066401. DOI: 10.1103/PhysRevLett.98.066401.

[108] W. C. Swope et al. “A computer simulation method for the calculation of equilibrium constants for the formation of physical clusters of molecules: Application to small water clusters”. In: *The Journal of Chemical Physics* 76 (1982), pp. 637–649. DOI: 10.1063/1.442716.

[109] M. Ceriotti et al. “Efficient stochastic thermostatting of path integral molecular dynamics”. In: *The Journal of Chemical Physics* 133 (2010), p. 124104. DOI: 10.1063/1.3489925.

[110] G. C. Wick. “Properties of Bethe-Salpeter Wave Functions”. In: *Phys. Rev.* 96 (1954), pp. 1124–1134. DOI: 10.1103/PhysRev.96.1124.

[111] H. F. Trotter. “On the product of semi-groups of operators”. In: *Proc. Amer. Math. Soc.* 10 (1958), pp. 545–551.

[112] D. Chandler and P. G. Wolynes. “Exploiting the isomorphism between quantum theory and classical statistical mechanics of polyatomic fluids”. In: *The Journal of Chemical Physics* 74 (1981), pp. 4078–4095. DOI: 10.1063/1.441588.

[113] R. H. Swendsen and J.-S. Wang. “Replica Monte Carlo Simulation of Spin-Glasses”. In: *Phys. Rev. Lett.* 57 (1986), pp. 2607–2609. DOI: 10.1103/PhysRevLett.57.2607.

[114] M. C. Tesi et al. “Monte carlo study of the interacting self-avoiding walk model in three dimensions”. In: *Journal of Statistical Physics* 82 (1996), pp. 155–181. DOI: 10.1007/BF02189229.

[115] K. Hukushima and K. Nemoto. “Exchange Monte Carlo Method and Application to Spin Glass Simulations”. In: *Journal of the Physical Society of Japan* 65 (1996), pp. 1604–1608. DOI: 10.1143/JPSJ.65.1604.

[116] Y. Sugita and Y. Okamoto. “Replica-exchange molecular dynamics method for protein folding”. In: *Chemical Physics Letters* 314 (1999), pp. 141–151. DOI: https://doi.org/10.1016/S0009-2614(99)01123-9.

[117] N. Metropolis et al. “Equation of State Calculations by Fast Computing Machines”. In: *The Journal of Chemical Physics* 21 (1953), pp. 1087–1092. DOI: 10.1063/1.1699114.

[118] W. K. Hastings. “Monte Carlo sampling methods using Markov chains and their applications”. In: *Biometrika* 57 (1970), pp. 97–109. DOI: 10.1093/biomet/57.1.97.

[119] I. Errea. "Approaching the strongly anharmonic limit with ab initio calculations of materials' vibrational properties – a colloquium*". In: *The European Physical Journal B* 89 (2016), p. 237. DOI: 10.1140/epjb/e2016-70078-6.

[120] R. Cowley. "Structural phase transitions I. Landau theory". In: *Advances in Physics* 29 (1980), pp. 1–110. DOI: 10.1080/00018738000101346.

[121] I. Pallikara et al. "The physical significance of imaginary phonon modes in crystals". In: *Electronic Structure* 4 (2022), p. 033002. DOI: 10.1088/2516-1075/ac78b3.

[122] I. Leonov et al. "Electronic correlations determine the phase stability of iron up to the melting temperature". In: *Scientific Reports* 4 (Mar. 2014). DOI: 10.1038/srep05585.

[123] U.-G. Jong et al. "Anharmonic phonons and phase transitions in the vacancy-ordered double perovskite Cs_2SnI_6 from first-principles predictions". In: *Phys. Rev. B* 99 (2019), p. 184105. DOI: 10.1103/PhysRevB.99.184105.

[124] J. M. Skelton et al. "Anharmonicity in the High-Temperature *Cmcm* Phase of SnSe: Soft Modes and Three-Phonon Interactions". In: *Phys. Rev. Lett.* 117 (2016), p. 075502. DOI: 10.1103/PhysRevLett.117.075502.

[125] F. A. Lindemann. "Über die Berechnung molekularer Eigenfrequenzen". In: *Phys. Z.* 11 (1910), pp. 609–612.

[126] D. S. Kim et al. "Phonon anharmonicity in silicon from 100 to 1500 K". In: *Phys. Rev. B* 91 (2015), p. 014307. DOI: 10.1103/PhysRevB.91.014307.

[127] F. Knoop et al. "Anharmonicity measure for materials". In: *Phys. Rev. Mater.* 4 (2020), p. 083809. DOI: 10.1103/PhysRevMaterials.4.083809.

[128] A. A. Maradudin and A. E. Fein. "Scattering of Neutrons by an Anharmonic Crystal". In: *Phys. Rev.* 128 (1962), pp. 2589–2608. DOI: 10.1103/PhysRev.128.2589.

[129] R. Cowley. "The lattice dynamics of an anharmonic crystal". In: *Advances in Physics* 12 (1963), pp. 421–480. DOI: 10.1080/00018736300101333.

[130] R. A. Cowley. "Anharmonic crystals". In: *Reports on Progress in Physics* 31 (1968), p. 123. DOI: 10.1088/0034-4885/31/1/303.

[131] R. S. Tripathi and K. N. Pathak. "Self-energy of phonons in an anharmonic crystal toO(δ4)". In: *Il Nuovo Cimento B (1971-1996)* 21 (1974), pp. 289–302. DOI: 10.1007/BF02737485.

[132] M. Calandra, M. Lazzeri, and F. Mauri. "Anharmonic and non-adiabatic effects in MgB2: Implications for the isotope effect and interpretation of Raman spectra". In: *Physica C: Superconductivity* 456 (2007), pp. 38–44. DOI: https://doi.org/10.1016/j.physc.2007.01.021.

[133] L. Paulatto et al. "First-principles calculations of phonon frequencies, lifetimes, and spectral functions from weak to strong anharmonicity: The example of palladium hydrides". In: *Phys. Rev. B* 91 (2015), p. 054304. DOI: 10.1103/PhysRevB.91.054304.

[134] B. Fultz. "Vibrational thermodynamics of materials". In: *Progress in Materials Science* 55 (2010), pp. 247–352. DOI: https://doi.org/10.1016/j.pmatsci.2009.05.002.

[135] A. Erba et al. “On how differently the quasi-harmonic approximation works for two isostructural crystals: Thermal properties of periclase and lime”. In: *The Journal of Chemical Physics* 142 (2015), p. 044114. DOI: 10.1063/1.4906422.

[136] D. J. Hooton. “LI. A new treatment of anharmonicity in lattice thermodynamics: I”. In: *Lond. Edinb. Dubl. Phil. Mag.* 46 (1955), p. 422. DOI: 10.1080/14786440408520575.

[137] N. R. Werthamer. “Self-Consistent Phonon Formulation of Anharmonic Lattice Dynamics”. In: *Phys. Rev. B* 1 (1970), pp. 572–581. DOI: 10.1103/PhysRevB.1.572.

[138] T. Tadano and S. Tsuneyuki. “First-Principles Lattice Dynamics Method for Strongly Anharmonic Crystals”. In: *Journal of the Physical Society of Japan* 87 (2018), p. 041015. DOI: 10.7566/JPSJ.87.041015.

[139] M. Zacharias et al. “Anharmonic lattice dynamics via the special displacement method”. In: *Phys. Rev. B* 108 (2023), p. 035155. DOI: 10.1103/PhysRevB.108.035155.

[140] T. Tadano and S. Tsuneyuki. “Self-consistent phonon calculations of lattice dynamical properties in cubic $SrTiO_3$ with first-principles anharmonic force constants”. In: *Phys. Rev. B* 92 (2015), p. 054301. DOI: 10.1103/PhysRevB.92.054301.

[141] Y. Oba et al. “First-principles study of phonon anharmonicity and negative thermal expansion in ScF_3”. In: *Phys. Rev. Mater.* 3 (2019), p. 033601. DOI: 10.1103/PhysRevMaterials.3.033601.

[142] I. Errea, M. Calandra, and F. Mauri. “First-Principles Theory of Anharmonicity and the Inverse Isotope Effect in Superconducting Palladium-Hydride Compounds”. In: *Phys. Rev. Lett.* 111 (2013), p. 177002. DOI: 10.1103/PhysRevLett.111.177002.

[143] I. Errea, M. Calandra, and F. Mauri. “Anharmonic free energies and phonon dispersions from the stochastic self-consistent harmonic approximation: Application to platinum and palladium hydrides”. In: *Phys. Rev. B* 89 (2014), p. 064302. DOI: 10.1103/PhysRevB.89.064302.

[144] R. Bianco et al. “Second-order structural phase transitions, free energy curvature, and temperature-dependent anharmonic phonons in the self-consistent harmonic approximation: Theory and stochastic implementation”. In: *Phys. Rev. B* 96 (2017), p. 014111. DOI: 10.1103/PhysRevB.96.014111.

[145] L. Monacelli et al. “Pressure and stress tensor of complex anharmonic crystals within the stochastic self-consistent harmonic approximation”. In: *Phys. Rev. B* 98 (2018), p. 024106. DOI: 10.1103/PhysRevB.98.024106.

[146] L. Monacelli et al. “The stochastic self-consistent harmonic approximation: calculating vibrational properties of materials with full quantum and anharmonic effects”. In: *Journal of Physics: Condensed Matter* 33 (2021), p. 363001. DOI: 10.1088/1361-648X/ac066b.

[147] C. Z. Wang, C. T. Chan, and K. M. Ho. “Tight-binding molecular-dynamics study of phonon anharmonic effects in silicon and diamond”. In: *Phys. Rev. B* 42 (1990), pp. 11276–11283. DOI: 10.1103/PhysRevB.42.11276.

[148] M. P. Ljungberg and J. Íñiguez. "Temperature-Dependent Classical Phonons from Efficient Nondynamical Simulations". In: *Phys. Rev. Lett.* 110 (2013), p. 105503. DOI: 10.1103/PhysRevLett.110.105503.

[149] D. M. Ceperley. "Path integrals in the theory of condensed helium". In: *Rev. Mod. Phys.* 67 (1995), pp. 279–355. DOI: 10.1103/RevModPhys.67.279.

[150] X. Zhu et al. "Misconceptions associated with the origin of charge density waves". In: *Advances in Physics: X* 2 (2017), pp. 622–640. DOI: 10.1080/23746149.2017.1343098.

[151] J. Wilson, F. D. Salvo, and S. Mahajan. "Charge-density waves and superlattices in the metallic layered transition metal dichalcogenides". In: *Advances in Physics* 24.2 (1975). DOI: 10.1080/00018737500101391.

[152] G. Grüner. "The dynamics of charge-density waves". In: *Rev. Mod. Phys.* 60 (1988), pp. 1129–1181. DOI: 10.1103/RevModPhys.60.1129.

[153] R. E. Thorne. "Charge-Density-Wave Conductors". In: *Physics Today* 49 (1996), pp. 42–47. DOI: 10.1063/1.881498.

[154] P. Monceau. "Electronic crystals: an experimental overview". In: *Advances in Physics* 61 (2012), pp. 325–581. DOI: 10.1080/00018732.2012.719674.

[155] L. Liu et al. "Direct identification of Mott Hubbard band pattern beyond charge density wave superlattice in monolayer 1T-NbSe2". In: *Nature Communications* 12 (2021), p. 1978. DOI: 10.1038/s41467-021-22233-w.

[156] A. J. Berlinsky. "One-dimensional metals and charge density wave effects in these materials". In: *Reports on Progress in Physics* 42 (1979), p. 1243. DOI: 10.1088/0034-4885/42/7/004.

[157] C. van Efferen et al. "A full gap above the Fermi level: the charge density wave of monolayer VS_2". In: *Nature Communications* 12 (2021), p. 6837. DOI: 10.1038/s41467-021-27094-x. arXiv: 2101.01140. URL: https://doi.org/10.1038/s41467-021-27094-x.

[158] H. Li et al. "Rotation symmetry breaking in the normal state of a kagome superconductor KV3Sb5". In: *Nature Physics* 18 (2022), pp. 265–270. DOI: 10.1038/s41567-021-01479-7.

[159] M. Barborini et al. "Excitonic-insulator instability and Peierls distortion in one-dimensional semimetals". In: *Phys. Rev. B* 105 (2022), p. 075122. DOI: 10.1103/PhysRevB.105.075122.

[160] D. Bhoi et al. "Interplay of charge density wave and multiband superconductivity in 2H-PdxTaSe2". In: *Scientific Reports* 6 (2016), p. 24068. DOI: 10.1038/srep24068.

[161] A. A. Balandin, S. V. Zaitsev-Zotov, and G. Grüner. "Charge-density-wave quantum materials and devices—New developments and future prospects". In: *Applied Physics Letters* 119 (2021), p. 170401. DOI: 10.1063/5.0074613.

[162] Z. Y. Liu et al. "Quasi-one-dimensional superconductivity in the pressurized charge-density-wave conductor HfTe3". In: *npj Quantum Materials* 6 (2021), p. 90. DOI: 10.1038/s41535-021-00393-8.

[163] M. D. Johannes and I. I. Mazin. “Fermi surface nesting and the origin of charge density waves in metals”. In: *Phys. Rev. B* 77 (2008), p. 165135. URL: https://doi.org/10.1103/PhysRevB.77.165135.

[164] K. Terashima et al. “Charge-density wave transition of $1T-VSe_2$ studied by angle-resolved photoemission spectroscopy”. In: *Phys. Rev. B* 68 (2003), p. 155108. DOI: 10.1103/PhysRevB.68.155108.

[165] T. Sato et al. “Three-Dimensional Fermi-Surface Nesting in 1T-VSe2 Studied by Angle-Resolved Photoemission Spectroscopy”. In: *Journal of the Physical Society of Japan* 73 (2004), pp. 3331–3334. DOI: 10.1143/JPSJ.73.3331.

[166] V. N. Strocov et al. “Three-Dimensional Electron Realm in VSe_2 by Soft-X-Ray Photoelectron Spectroscopy: Origin of Charge-Density Waves”. In: *Phys. Rev. Lett.* 109 (2012), p. 086401. DOI: 10.1103/PhysRevLett.109.086401.

[167] S. .-. Chan and V. Heine. “Spin density wave and soft phonon mode from nesting Fermi surfaces”. In: *Journal of Physics F: Metal Physics* 3 (1973), p. 795. DOI: 10.1088/0305-4608/3/4/022.

[168] T. Kumakura et al. “Charge density waves and superconductivity in 2H-TaSe2”. In: *Czechoslovak Journal of Physics* 46 (1996), pp. 2611–2612. DOI: 10.1007/BF02570292.

[169] Y. Nomura et al. “Exotics-wave superconductivity in alkali-doped fullerides”. In: *J. Phys. Condens. Matter* 28 (2016), p. 153001. DOI: 10.1088/0953-8984/28/15/153001.

[170] R. Arita et al. “Nonempirical Calculation of Superconducting Transition Temperatures in Light-Element Superconductors”. In: *Adv. Mater.* 29 (2017), p. 1602421. DOI: 10.1002/adma.201602421.

[171] W. P. Su, J. R. Schrieffer, and A. J. Heeger. “Solitons in Polyacetylene”. In: *Phys. Rev. Lett.* 42 (1979), pp. 1698–1701. DOI: 10.1103/PhysRevLett.42.1698.

[172] X. Zhu et al. “Misconceptions associated with the origin of charge density waves”. In: *Adv. Phys. X* 2 (2017), p. 622. URL: https://doi.org/10.1080/23746149.2017.1343098.

[173] T. Kawakami et al. “Charge-density wave associated with higher-order Fermi-surface nesting in monolayer VS2”. In: *npj 2D Materials and Applications* 7 (2023), p. 35. DOI: 10.1038/s41699-023-00395-z.

[174] D. Lin et al. “Patterns and driving forces of dimensionality-dependent charge density waves in 2H-type transition metal dichalcogenides”. In: *Nat. Commun.* 11 (2020), p. 2406. DOI: 10.1038/s41467-020-15715-w.

[175] Y. Wang et al. “Evidence of charge density wave with anisotropic gap in a monolayer VTe_2 film”. In: *Phys. Rev. B* 100 (2019), p. 241404. URL: https://doi.org/10.1103/PhysRevB.100.241404.

[176] M. Liu et al. “Multimorphism and gap opening of charge-density-wave phases in monolayer VTe2”. In: *Nano Research* 13 (2020), pp. 1733–1738. DOI: 10.1007/s12274-020-2799-4.

[177] Y. Zheng et al. “Nuclear Quantum Effects on the Charge-Density Wave Transition in NbX_2 (X = S, Se)”. In: *Nano Lett.* 22 (2022), p. 1858. DOI: 10.1021/acs.nanolett.1c04015.

[178] G. Kresse and J. Hafner. “Ab initio molecular dynamics for liquid metals”. In: *Phys. Rev. B* 47 (1993), pp. 558–561. DOI: 10.1103/PhysRevB.47.558.

[179] G. Kresse and J. Hafner. “Ab initio molecular dynamics for open-shell transition metals”. In: *Phys. Rev. B* 48 (1993), pp. 13115–13118. DOI: 10.1103/PhysRevB.48.13115.

[180] G. Kresse and J. Furthmüller. “Efficiency of ab-initio total energy calculations for metals and semiconductors using a plane-wave basis set”. In: *Computational Materials Science* 6 (1996), pp. 15–50. DOI: https://doi.org/10.1016/0927-0256(96)00008-0.

[181] M. S. S. Challa, D. P. Landau, and K. Binder. “Finite-size effects at temperature-driven first-order transitions”. In: *Physical Review B* 34 (1986), pp. 1841–1852. DOI: 10.1103/PhysRevB.34.1841.

[182] W. H. Sio et al. “Ab initio theory of polarons: Formalism and applications”. In: *Phys. Rev. B* 99 (2019), p. 235139. DOI: 10.1103/PhysRevB.99.235139.

[183] W. H. Sio et al. “Polarons from First Principles, without Supercells”. In: *Phys. Rev. Lett.* 122 (2019), p. 246403. DOI: 10.1103/PhysRevLett.122.246403.

[184] D. E. Moncton, J. D. Axe, and F. J. DiSalvo. “Neutron scattering study of the charge-density wave transitions in $2H-TaSe_2$ and $2H-NbSe_2$”. In: *Phys. Rev. B* 16 (1977), pp. 801–819. DOI: 10.1103/PhysRevB.16.801.

[185] M. Naito and S. Tanaka. “Electrical Transport Properties in 2H-NbS_2, -$NbSe_2$, -TaS_2 and -$TaSe_2$”. In: *J. Phys. Soc. Jpn.* 51 (1982), pp. 219–227. DOI: 10.1143/JPSJ.51.219.

[186] I. Guillamón et al. “Superconducting Density of States and Vortex Cores of 2H-NbS_2”. In: *Phys. Rev. Lett.* 101 (2008), p. 166407. DOI: 10.1103/PhysRevLett.101.166407.

[187] M. Leroux et al. “Anharmonic suppression of charge density waves in $2H$-NbS_2”. In: *Phys. Rev. B* 86 (2012), p. 155125. DOI: 10.1103/PhysRevB.86.155125.

[188] H. Lin et al. “Growth of atomically thick transition metal sulfide filmson graphene/6H-SiC(0001) by molecular beam epitaxy”. In: *Nano Research* 11 (2018), pp. 4722–4727. DOI: 10.1007/s12274-018-2054-4.

[189] R.-M. Stan et al. “Epitaxial single-layer NbS_2 on Au(111): Synthesis, structure, and electronic properties”. In: *Phys. Rev. Mater.* 3 (2019), p. 044003. DOI: 10.1103/PhysRevMaterials.3.044003.

[190] R. Bianco et al. “Quantum Enhancement of Charge Density Wave in NbS2 in the Two-Dimensional Limit”. In: *Nano Letters* 19 (2019), pp. 3098–3103. DOI: 10.1021/acs.nanolett.9b00504.

[191] L. Perfetti et al. “Time Evolution of the Electronic Structure of 1T-TaS_2 through the Insulator-Metal Transition”. In: *Phys. Rev. Lett.* 97 (2006), p. 067402. DOI: 10.1103/PhysRevLett.97.067402.

[192] S. Hellmann et al. “Ultrafast Melting of a Charge-Density Wave in the Mott Insulator 1T-TaS_2”. In: *Phys. Rev. Lett.* 105 (2010), p. 187401. DOI: 10.1103/PhysRevLett.105.187401.

[193] M. Eichberger et al. “Snapshots of cooperative atomic motions in the optical suppression of charge density waves”. In: *Nature* 468 (2010), p. 799. DOI: 10.1038/nature09539.

[194] F. Weber et al. “Extended Phonon Collapse and the Origin of the Charge-Density Wave in 2H-$NbSe_2$”. In: *Phys. Rev. Lett.* 107 (2011), p. 107403. DOI: 10.1103/PhysRevLett.107.107403.

[195] E. Möhr-Vorobeva et al. “Nonthermal Melting of a Charge Density Wave in $TiSe_2$”. In: *Phys. Rev. Lett.* 107 (2011), p. 036403. DOI: 10.1103/PhysRevLett.107.036403.

[196] L. Stojchevska et al. “Ultrafast Switching to a Stable Hidden Quantum State in an Electronic Crystal”. In: *Science* 344 (2014), p. 177. DOI: 10.1126/science.1241591.

[197] S. Vogelgesang et al. “Phase ordering of charge density waves traced by ultrafast low-energy electron diffraction”. In: *Nat. Phys.* 14 (2018), p. 184. DOI: 10.1038/nphys4309.

[198] A. Zong et al. “Evidence for topological defects in a photoinduced phase transition”. In: *Nat. Phys.* 15 (2019), p. 27. DOI: 10.1038/s41567-018-0311-9.

[199] T. Danz, T. Domröse, and C. Ropers. “Ultrafast nanoimaging of the order parameter in a structural phase transition”. In: *Science* 371 (2021), p. 371. DOI: 10.1126/science.abd2774.

[200] S. Wall et al. “Ultrafast disordering of vanadium dimers in photoexcited VO_2”. In: *Science* 362 (2018), p. 572. DOI: 10.1126/science.aau3873.

[201] T. Neupert et al. “Charge order and superconductivity in kagome materials”. In: *Nat. Phys.* 18 (2022), p. 137. DOI: 10.1038/s41567-021-01404-y.

[202] D. N. Basov, R. D. Averitt, and D. Hsieh. “Towards properties on demand in quantum materials”. In: *Nat. Mater.* 16 (2017), p. 1077. DOI: 10.1038/nmat5017.

[203] A. Cavalleri. “Photo-induced superconductivity”. In: *Contemp. Phys.* 59 (2018), p. 31. DOI: 10.1080/00107514.2017.1406623.

[204] A. de la Torre et al. “Colloquium: Nonthermal pathways to ultrafast control in quantum materials”. In: *Rev. Mod. Phys.* 93 (2021), p. 041002. DOI: 10.1103/RevModPhys.93.041002.

[205] R. A. Jishi. *Feynman Diagram Techniques in Condensed Matter Physics*. Cambridge University Press, 2013. DOI: 10.1017/CBO9781139177771.

[206] P. Giannozzi et al. “Advanced capabilities for materials modelling with Quantum ESPRESSO”. In: *J. Phys. Condens. Matter* 29 (2017), p. 465901. DOI: 10.1088/1361-648X/aa8f79.

[207] A. A. Mostofi et al. “An updated version of wannier90: A tool for obtaining maximally-localised Wannier functions”. In: *Comput. Phys. Commun.* 185 (2014), p. 2309. DOI: 10.1016/j.cpc.2014.05.003.

[208] J. Noffsinger et al. “EPW: A program for calculating the electron–phonon coupling using maximally localized Wannier functions”. In: *Comput. Phys. Commun.* 181 (2010), p. 2140. DOI: 10.1016/j.cpc.2010.08.027.

[209] S. Poncé et al. “EPW: Electron–phonon coupling, transport and superconducting properties using maximally localized Wannier functions”. In: *Comput. Phys. Commun.* 209 (2016), p. 116. DOI: 10.1016/j.cpc.2016.07.028.

[210] J. Berges et al. *elphmod: Python modules for electron–phonon models*. doi.org/10.5281/zenodo.5919992. 2017. DOI: 10.5281/zenodo.5919992.

Eidesstattliche Versicherung

Hiermit versichere ich an Eides statt, dass ich die vorliegende Dissertation selbst verfasst und keine anderen als die angegebenen Quellen und Hilfsmittel benutzt habe.

Bremen, den 30.11.2023 Unterschrift: Arne Schobert